ATLAS

SemiConductor Tracker Development

and

Physics Simulation

Heidi Sandaker
Department of Physics
University of Oslo
Norway

September 6, 2005

Thesis presented for the degree of Doctor Scientiarum

Series of dissertations submitted to the
Faculty of Mathematics and Natural Sciences,University of Oslo.
No. 458

ISSN 1501-7710

Cover: Inger Sandved Anfinsen.
Printed in Norway: AiT e-dit AS, Oslo, 2005.

Produced in co-operation with Unipub AS.
The thesis is produced by Unipub AS merely in connection with the
thesis defence. Kindly direct all inquiries regarding the thesis to the copyright
holder or the unit which grants the doctorate.

Unipub AS is owned by
The University Foundation for Student Life (SiO)

Til mine foreldre, min søster, min familie

og

Martin

Acknowledgements

Many people, institutes and universities need to be acknowledged for not only the excellent working environment but also the many varied and challenging projects provided for during my thesis. Had it not been for the interest, motivation and generosity of the people I worked with, my thesis would not have been as challenging, rewarding and highly stimulating for learning physics as it has been. For this I can not thank you all enough. In order of appearance:

A very special thanks goes to my main supervisor Steinar Stapnes for his excellent support during my three years as a doctoral student, always available and always ready with an answer. I also thank him warmly for his unquestioned belief in me at times where this was not obvious to myself. My second supervisor, Farid Ould-Saada, receives an equally heartily thanks for his immense patience, calm and for his great effort to supervise over great distances and under tight schedules.

The University of Oslo has been my home institute during the period of my thesis and has not only provided me with a salary and an office, but also a safe haven of physicist friends and an excellent learning environment. Among the people I would like to thank in particular are the whole of the Experimental Particle Physics Group; Alex Reed, Lars Bugge, Torleif Buran, Kjell M. Danielsen, Jørgen Hansen, Børge K. Gjelsten, Torkjell Huse, Yuriy Polypchenko, Sigve Haug, Trond Myklebust, Katarina Pajchel, Esben Lund and the diploma students. In addition I would like to thank in particular Are Strandli for his warm welcome and helpful integration when arriving at CERN. I would also like to thank two professors in theoretical physics Jan O. Eeg and in particular Finn Ravndal for being wonderfully supporting and welcoming from the moment when I arrived as an estranged alien three years ago. A special thanks to Bjørn H. Samset, keep up the very good work.

A warm thanks goes to the SCAND community. In Oslo, a big thank you goes to Ole Dorholt of the Electronics Department; I have always enjoyed our wide-range discussions and to Per Nordahl of the Instrumentation Laboratory for his excellent metallurgical work. In Bergen, I wish to thank Bjarne Stugu and his students Ola K. Øye and Bjarte Moen. In Uppsala, I thank Richard Brenner and Lars Eklund.

How can I possibly thank CERN and the generous people I have met and worked with! Most of all I will have to thank Heinz Pernegger and Pamela Ferrari for their excellent and never-ending teaching, tutoring, advising and laughing. A big hug to both of you! You are a main reason for me enjoying this as much as I do. In addition, great thanks to Shaun Roe, Joleen Paters, Gareth Moorhead, Dave Robinson, Pepe Bernabeu, Sophia Chouridou, Paul Bell, the Geneva girls (Anna Sfyrla, Maria Chamizo Llatas and Bettina Mikulec) and all the other CERN people.

Thanks to the power supply group for their most valuable discussions and co-operation. A most grateful thanks goes to Alex Grillo, Piotr Malecki, Jan Bohm

and Jan Stastny, Edward Górnicki, Stephan Koperny and Martin Morrissay among others, but most of all to Ewa Stanecka. Our stays in England with Pamela would not have been half as nice if we three girls did not have our discussions in dark pubs over a glass of beer and cider.

Another great thank you goes to the Oxford macro-assembly group, which in fact consists of people of many nationalities and from many institutes. Thank you for your warm welcome and heartily instructions during the installation of the DCS but most of all during my long stay last October. Without you, testing these modules would not have been half as fun and rewarding as it has actually been. A warm thank you to: Janet Carter, Georg Viehhauser, Peter Phillips, Alan Barr, Alessandro Tricoli, Abdelouahab Abdesselam, Christopher Lester, Jørgen Dalmau, Bilge Demirkoz and all the other nice people I met in Oxford.

At any time and place the members of the CERN Exotic Group have been ready and willing to help out. Without their help many tasks would have taken more time and effort than necessary. Thank you for sharing with me your expertise and your time. Among others, thanks to Georges Azuelos, Samir Ferrag, Martina Schäfer, Anne-Sylvie Nicollerat.

Last of the official thanks goes to Heidi Bruvoll, Lars Bernhardsen and Sue Geddes and the secretariats in Oslo, CERN and Oxford. I also would like to thank the Electronics and Instrumentation laboratories in Oslo. And finally, an additional thanks goes to all those who has read and commented on my thesis; Steinar, Farid, Martin Jäkel, Alex, Janet, Gareth, Pepe, Shaun, Pamela, Paul and Aldo F. Saaveda.

More than any others I need to acknowledge and thank my family and friends for all their support. Apart from the ones already mentioned, a big embrace to my best friends (also in order of appearance): Marianne, Ina, Eli, Ingerid and Sophie. For your blind support, long talks and your effort of keeping our friendship alive through hardship and over long distances. Not forgotten, thanks to Martins family for opening their home and to all my Austrian friends and my friends at CERN.

Abstract

In spite of the great success of the Standard Model in providing an exact method of describing the particles we know today and their interactions, a number of questions remains. To search for these answers, the future of new discoveries relies on the building of more advanced particle accelerators, as well as larger, faster and more complex particle detectors. Building the A Toroidal LHC ApparatuS (ATLAS) detector at the Large Hadron Collider (LHC) is an adventurous mission into a new realm of detectors necessary to reach new physics. The LHC is a proton-proton accelerator designed to collide particles at 14 TeV centre-of-mass energy. The resulting shower of particles will be used by ATLAS in a variety of Higgs boson, SUSY and Exotic searches as well as searches for quark compositeness and for precision measurements. The aim of this thesis has been to contribute to this work, both by participating in the building of ATLAS and in the preparation for physics studies.

This report presents the accomplished work for the degree of Dr. Scient at the University of Oslo, Norway. The two main fields of contributions have been the development and test of the ATLAS SemiConductor Tracker (SCT) and the ATLAS physics simulation of extra neutral gauge bosons. My contribution to the SCT development has taken the form of several different projects in several stages of the construction. In total they represent a slice of most of the main tasks needed to construct and build one of the ATLAS detectors, covering the development and tests of the SCT detector, from the individual detector module up to a populated barrel structure ready for insertion into the inner tracker. These projects also include module production tests, module testbeam, barrel assembly tests, development of off-detector hardware as well as a close-to-final Detector Control System (DCS) needed to control and operate the final SCT detector. An overview of some of this work has been presented at the STD5 Hiroshima conference during spring 2004 [1]. Several achievements have resulted from this work and new understanding of the detector and the detector operation has been acquired:

The main success of the off-detector electronics development, notably the power-supply development, has been a stable and working system with full functionality and a successful scale-up from the control and supply of one module to a system testing more than 400 modules at a time. This result reflects both the successful supply of all voltages and commands to the modules but also the communication between all components of the power supply system. Part of this work has been presented in [2], but a more detailed report will follow.

Another important outcome has been the success of the DCS, which has been constructed almost from scratch during my stay at CERN. It is a completely new system, based on all the final, or close-to-final, hardware and software components.

It is also a completely integrated system where all DCS parts communicate with each other and with the SCT Data AcQuisition system (DAQ). This software has been installed in all the SCT macro-assembly sites and has been successfully used to manage the power supply hardware as well as the cooling system, environmental system and thermal enclosure during control and testing of the SCT barrels and disks. It has also been integrated successfully into the ATLAS DCS software, which is another achievement of our system architecture. Some of this work has been presented in [1], [3] and [4], in addition a full ATLAS note is under preparation [5], which describes in detail all the functionality of the SCT DCS system.

During the last years the SCT detector modules have been produced and mounted onto larger detector structures. Important development work in this period has been to test the SCT detectors at several stages during this process as well as during testbeam.. Results from both the module production and the macro-assembly as well from the latest testbeam session will be presented in this thesis. The macro-assembly results have been formidable. During 2003, the first barrel cylinder has been populated and tested which has been a great confirmation of the fine work at all SCT sites. It has proven the success of the SCT design, the production and assembly methods as well as the DCS and DAQ software and SCT electronics. Some of this work has been presented in [1]. Among the main testbeam achievements have been the successful calibration of the modules with the close to final equipment, both DAQ and DCS software and hardware, and the full acceptance and inclusion of the SCT detector into the final ATLAS online DAQ and software. The SCT was run successfully both in calibration mode and data-taking mode with its final DAQ and DCS components. An overview of the SCT testbeam results is presented in [6].

Physics simulations have been performed using ATLAS simulation tools. Exotic particles, notably extra neutral gauge bosons (Z') have been studied, which could be one of the first particles to be detected by ATLAS, giving early indications about physics beyond the Standard Model. A first complete analysis of several models has been made for both the decay to electrons and to muons, using final state radiation and interactions. Results are presented for both the expectation reach of the particles mass in the ATLAS detector and of the model discrimination possibilities if discovered. Some of this work has been presented in [7].

This document is divided into four parts. Part I is an introduction to the complete thesis, with background material and general information, explaining the motivation for the physics and detector development as well as my interest in this work. Part II describes the ATLAS SCT development, where the first chapter, chapter 4, is an introduction explaining the specification and the basic framework of the SCT detector, rearranged and reworked to form a basis for this thesis. Chapters 5-9 present my work and contributions. Part III of this thesis will discuss the ATLAS physics simulations. The first chapter of this part, chapter 10, presents the theoretical and practical base of knowledge being needed for the simulations. Chapter 11 presents the simulation results on extra neutral gauge bosons. Finally, part IV closes this thesis with a summary, conclusion, and a short outlook towards the near ATLAS future.

Contents

Part I

Introduction

1
Elementary Particles

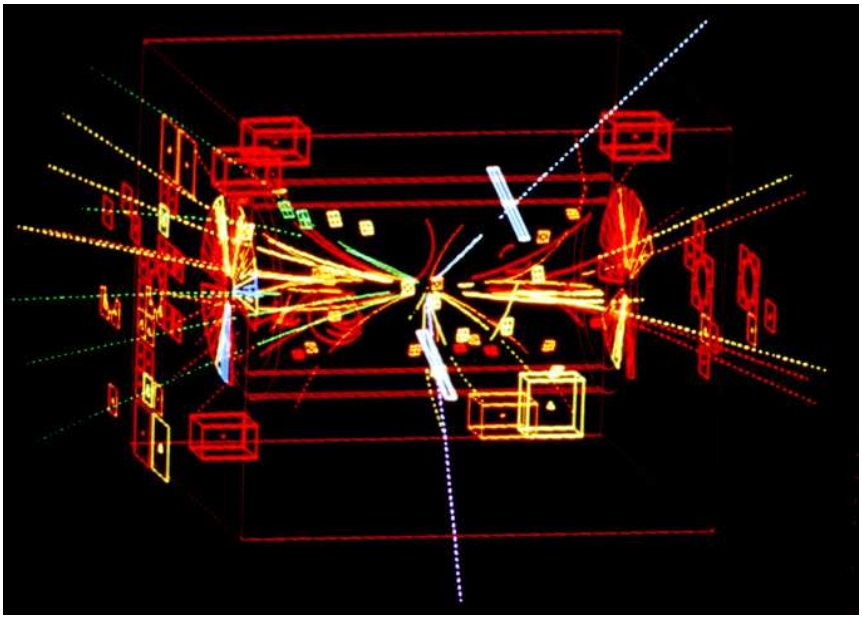

The first Z^0 event recorded by UA1 the 30th of April 1983 [8].

Introduction

Our world as we know it today consists of a multitude of particles with seemingly different properties and interactions. By thorough investigation, one has managed to deduce a set of elementary particles from which all others can be derived. All knowledge about these elementary particles and their interactions has been collected and described by the Standard Model. In all tests, this model has been proven with exceptional accuracy. The only exception is the Higgs mechanism, where current experiments fail to reach the domain of observation. Over the next few years, new experiments will be able to confirm or exclude the Higgs-mechanism as the mechanism behind symmetry breaking and as the one responsible for particle masses.

However, in spite of all the features of the Standard Model, it remains a model which is valid only within a certain range of energies. Because of this, new theories and models have appeared, attempting to explain what happens beyond the Standard Model. The main challenge for these theories consists of joining the three sub-atomic forces and gravity into one force and to understand symmetry breaking and the hierarchy between the forces and elements. Another challenge will be to explain the asymmetry of the world, how some particles seem to prefer a certain chiral direction or why matter dominates the universe.

The following chapter describes the main features of the Standard Model, how the model has been proven experimentally, its limitations and shortcomings and finally our reasons to search for physics beyond the Standard Model. This will also sum up our motivation for building the ATLAS detector, which is part of the main work presented in this thesis (chapters 4-9). Models beyond the Standard Model and how they can be detected in ATLAS will be presented in chapters 10 and 11.

1.1 The Standard Model

The Standard Model (SM) is a highly successful description of elementary particles and their interactions and maybe the most remarkable achievement of modern theoretical physics. Until recently, this model has been able to describe results from our current experiments down to scales of 10^{-18} m and up to energies of around 200 GeV [9]. New experiments are reaching for higher limits and may produce particles with energies just below 1 TeV. The SM started off by establishing quantum electrodynamics (QED), which fused together Quantum Mechanics and Special Relativity and evolved into today's description of the Electroweak theory and Quantum Chromodynamics (QCD)

The Standard Model is a quantum field theory, which describes the weak, electromagnetic and strong interactions of spin 1/2 point-like fermions. It is a gauge theory, based on the $\mathrm{SU}(3)_C \times \mathrm{SU}(2)_L \times \mathrm{U}(1)_Y$ symmetry group. The principle of this theory is that all forces of nature are mediated by the exchange of gauge fields (spin-1 particles) of the corresponding local symmetry group. In this fashion, the SM can be described by three types of fields, the matter field, which gives birth to leptons and quarks; the gauge fields, from which the gauge bosons appear and the

Higgs scalar fields, which describe the masses of particles. Table 1.1 shows the list of the elementary particles described by these fields. In addition, all particles have an antiparticle, which has the same mass and spin as its particle counterpart but the opposite charge and colour.

The interaction between the particles are defined by symmetries in the gauge groups and are the origin of the conservation laws. The conservation of electric charge is related to the U(1) symmetry and the conservation of colour to the SU(3) symmetry. The gauge symmetries are continuous dynamical symmetries, whereas space-time symmetries are continuous or discrete. Typical continuous space-time symmetries are translation in space and time as well as rotation. Typical discrete symmetries are the parity and charge invariance. As an example, parity is conserved for strong and electromagnetic interactions but violated for weak interactions. An elementary particle is also defined by its helicity state which describes the direction of the spin or the particle with respect to its momentum. The helicity of a particle can be either left (L)- or right-handed (R).

SM particles	Type	Spin	Baryon No.	Lepton No.	Electric charge
quarks	u, c, t	1/2	1/3	0	$+2/3$
	d, s, b	1/2	1/3	0	$-1/3$
leptons	e^-, μ^-, τ^-	1/2	0	1	-1
	ν_e, ν_μ, ν_τ	1/2	0	1	0
bosons	γ	1	0	0	0
	W^+, W^-, Z^0	1	0	0	$+1, -1, 0$
	g_i	1	0	0	0
	H^0	0	0	0	0

Table 1.1: The elementary particles and their quantum numbers. The quark and leptons are matter particles whereas the vector bosons are particles which mediate the strong (g_i, $i = 1,..,8$), weak ($W^\pm$, Z^0) and electromagnetic (γ) interactions.

A World of Particles

The matter fields are fermions belonging to the fundamental representation of the gauge group consisting of leptons and quarks. They are spin 1/2 particles described exclusively by spinor fields and their basic unity is the family consisting of three generations (minimal model). Each generation consists of two leptons and two quarks together with their antiparticles, for example the first generation consists of $\{e^-, e^+, \bar{\nu}_e, \nu_e, u, \bar{u}, d$ and $\bar{d}\}$. The other generations have the same composition of particles, with identical properties compared to the particles of the first generation, but with different masses. As can be seen from table 1.1, the electric charges of the three leptons families, e, μ and τ , are equal to -1, but their doublet partners, ν_e, ν_μ and ν_τ, are electrically neutral. The three upper quarks from the doublet, up (u), charm (c) and top (t), have electric charges 2/3 and the lower quarks, down

(d), strange (s) and bottom (b), have electric charge -1/3. An interesting property of the matter fields is that, when taking into account the three possible colours for each quark, the sum of the electric charges in each family vanishes.

Under SU(2) the left-handed fermion field transforms as a doublet, whereas the right-handed fields are singlets. However, since the neutrinos have been discovered to have mass (from the study of atmospheric neutrino fluxes by the Super-Kamiokande[1] experiment and by solar neutrino cross-sections by SNO[2] and Super-Kamiokande), there might be the need to introduce a right-handed neutrino (ν_{eiR}). The left- and right-handed fields can be described in the following fashion, where i describes which family the fermions comes from [10]:

$$l_{iL} = \begin{pmatrix} \nu_{ei} \\ e_i^- \end{pmatrix}_L \quad ; \quad \nu_{eiR}(?) \quad ; \quad e_{iR} \quad ; \quad q_{iL} = \begin{pmatrix} u_i \\ d_i' \end{pmatrix}_L \quad ; \quad u_{iR} \quad ; \quad d_{iR} \Bigg\} i = 1, 2, 3$$

where $e_1 = e$, $e_2 = \mu$ and $e_3 = \tau$ and equivalent for the quarks; $u_1 = u$, $u_2 = c$, $u_3 = t$, $d_1 = d$, $d_2 = s$ and $d_3 = b$. The two doublets describe particles which are linked by the weak interactions. Due to their additional colour, the quarks are triplets under the SU(3) group. The prime of d' is due to quark mixing and is expressed by the relation $d' = \sum_j V_{ij} d_j$, where V_{ij} are elements of the Cabbibo-Kobayashi-Maskawa (CKM) mixing matrix [11]. By ordering the quarks according to their masses, the elements of V_{CKM} can be described by the following 3×3 unitary matrix, where each of the elements V_{ij} is related to the strength of the transition between the up-type and the down-type quark:

$$V_{CKM} = \begin{pmatrix} V_{ud} & V_{us} & V_{ub} \\ V_{cd} & V_{cs} & V_{cb} \\ V_{td} & V_{ts} & V_{tb} \end{pmatrix}.$$

The introduction of neutrino masses can also be described by a 3×3 mass-matrix as explained in [11].

Particle Interactions

The interactions between the fermions described above are mediated by a set of gauge fields which are 12 spin-1 boson fields. They appear when a local gauge invariance is applied to the fermion field. The SU(3) group of the SM gives rise to eight gauge fields which corresponds to eight gluons mediating the strong force, which is responsible for the confinement of quarks into hadrons and mesons. The interactions between the gluons and the quarks are characterised by the coupling constant g_s. The electroweak group $\mathrm{SU}(2)_L \times \mathrm{U}(1)_Y$ gives birth to the four electroweak vector boson fields. The electromagnetic parts describes most of the low energy physics and the weak part is responsible for the radioactive decay of unstable particles. The $\mathrm{SU}(2)_L$ field gives rise to W_μ^i , $i \in \{1, 2, 3\}$ with the coupling g to fermions and the $\mathrm{U}(1)_Y$ group gives rise to B_μ with coupling g' [11].

[1] Solar neutrino experiment in Japan.

[2] The Sudbury Neutrino Observatory in Canada.

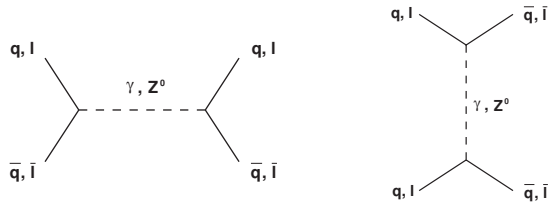

Figure 1.2: Feynman diagram for neutral current decay modes. Left, the annihilation - creation process and right, the scattering process. Time goes horizontally from left to right.

These last electroweak particles are not the particles observed in nature, but are a mixed state appearing from the joint gauge groups. The mass eigenstates observed in nature are the charged W^+ and W^- bosons (weak charged currents) and the neutral Z^0 (weak neutral current, see figure 1.2) and γ bosons (EM current). For the neutral bosons the relation between the mass eigenstates and the symmetry eigenstates is given by the following relation, where the Weinberg angle, θ_W, is the rotation angle:

$$\begin{bmatrix} \gamma \\ Z^0 \end{bmatrix} = \begin{bmatrix} \cos\theta_W & \sin\theta_W \\ -\sin\theta_W & \cos\theta_W \end{bmatrix} \begin{bmatrix} B \\ W_3 \end{bmatrix}.$$

Higgs Mechanism

The third set of SM fields are the Higgs scalar fields introduced by the minimal SM model proposed by Weinberg and Salam based on the Higgs mechanism developed by Higgs in the 1960s. The electroweak $\mathrm{SU}(2)_L \times \mathrm{U}(1)_Y$ symmetry group is spontaneously broken by the existence of a Higgs scalar field with non-zero expectation value. By introducing this field, the masses of the quarks, leptons and intermediate weak bosons emerge. Both the W and Z become massive and the photon remains massless. Without the introduction of the Higgs field these particles would have remained massless. The minimal version of the SM consists of one SU(2) doublet of Higgs scalar fields (spin = 0), which results in one neutral scalar boson, H^0, which is presently unobserved having a mass which can not be predicted from this theory. The possible masses, however, are constrained by current experimental data.

The boson masses can be generated by introducing the Higgs potential V, described by the following relation:

$$V(\phi) = \mu^2\phi^\dagger\phi + |\lambda|(\phi^\dagger\phi)^2, \tag{1.1}$$

where ϕ is the complex Higgs field, μ an arbitrary value and λ the Higgs self-coupling. The electroweak symmetry is broken if the parameter $\mu^2 < 0$. The minimum energy, ϕ_0, also called the vacuum expectation value, reduces the original symmetry. A useful choice of ϕ_0 is given by the following expression with $v = \sqrt{-\mu^2/|\lambda|}$:

$$\phi_0 = \sqrt{\frac{1}{2}} \begin{pmatrix} 0 \\ v \end{pmatrix}. \tag{1.2}$$

Lagrangian

The Lagrangian function describes the particle movement in 4-dimensional space-time, and determines the dynamics of a gauge theory. In the classical limit, it is expressed as the difference between the kinetic, T, and potential energy, U of the system:

$$L = T(\dot{x}) - U(x) = \frac{1}{2}m\dot{x}^2 - U(x), \tag{1.3}$$

where x is a distance and $\dot{x} = \frac{dx}{dt}$ its speed. The equation of motion can be derived from the Euler-Lagrange:

$$\frac{\partial L}{\partial x} - \frac{d}{dt}(\frac{\partial L}{\partial \dot{x}}) = 0 \tag{1.4}$$

$$F = \frac{dU}{dx} = ma, \tag{1.5}$$

where the force, F, is derived as a function of the acceleration, $a = \ddot{x}$.

In field theory, the definition of the Lagrangian of a field, ψ, is given as a function of its density, $\mathcal{L}$:

$$L = \int \mathcal{L}(\psi, \partial_\mu \psi). \tag{1.6}$$

The Euler-Lagrange equation represent the corresponding Dirac equation solution for the wave function and is given by:

$$\frac{\partial \mathcal{L}}{\partial \psi} - \partial_\mu \left[\frac{\partial \mathcal{L}}{\partial(\partial_\mu \psi)} \right] = 0. \tag{1.7}$$

The gauge invariant Lagrangian from the electroweak model (Glashow 1961, Weinberg 1967, Salam 1968 and t'Hooft 1971) consists of several parts and is defined by the following main components [12, 13]:

$$\mathcal{L}_{SM} = \mathcal{L}_{matter} + \mathcal{L}_{gauge} + \mathcal{L}_{Higgs} + \mathcal{L}_{Yukawa} + \dots . \tag{1.8}$$

The matter Lagrangian, $\mathcal{L}_{matter}$, is described by the following representation of the interactions between the gauge bosons and the fermions, as spinor fields, ψ_i, where i represents the three families:

$$\mathcal{L}_{matter} = \mathrm{i} \sum_{i=1}^{3} \bar{\psi}^i \gamma^\mu D_\mu \psi_i, \tag{1.9}$$

and where D_μ, the covariant derivative, is given as the following relation:

$$D_\mu = \partial_\mu - \mathrm{i}gW_\mu^A\frac{\tau^A}{2} - \mathrm{i}g'B_\mu\frac{Y}{2}, \tag{1.10}$$

with Y being the hypercharge, which relates to the isospin and electric charge as $Q = T_3 + \frac{1}{2}Y$, and where the couplings g and g' define the mixing angle $\tan\theta_W = g'/g$. τ_A, with A = {1,2,3} the isospin equivalent of the Pauli matrices which gives the lowest representation of the rotation group.

The second part $\mathcal{L}_{gauge}$ describes the gauge boson part as a function of the two gauge fields W_μ^a and B_μ with the couplings g and g' respectively:

$$\mathcal{L}_{gauge} = -\frac{1}{4}W_{\mu\nu}^a W^{a\mu\nu} - \frac{1}{4}B_{\mu\nu}B^{\mu\nu}. \tag{1.11}$$

The field tensors are expressed in terms of elementary fields:

$$W_{\mu\nu}^a = \partial_\mu W_\nu^a - \partial_\nu W_\mu^a - g\epsilon^{abc}W_{\mu\nu}^b W_\nu^c \tag{1.12}$$

$$B_{\mu\nu} = \partial_\mu B_\nu - \partial_\nu B_\mu\ . \tag{1.13}$$

The ϵ^{abc} are the $\mathrm{SU}(2)_L$ group structure constants. This gauge Lagrangian describes both the kinetic and interaction part of the gauge bosons.

The contribution to the Lagrangian from the Higgs fields are described by the following relation, where the potential V is given by 1.1:

$$\mathcal{L}_{Higgs} = (D^\mu\phi)^\dagger(D_\mu\phi) - V(\phi^\dagger\phi). \tag{1.14}$$

The interaction of the Higgs doublet with the matter fields, which gives the masses to the fermions, is described by the Yukawa Lagrangian;

$$\mathcal{L}_{Yukawa} = \sum_{i=1}^{3}(f_i^l\ \bar{l}_{iL}\ \phi\ e_{iR} + f_i^u\ \bar{q}_{iL}\ \tilde{\phi}\ u_{iR} + f_i^d\ \bar{q}_{iL}\ \phi\ d_{iR}), \tag{1.15}$$

where ϕ is the complex Higgs field and f the Yukawa couplings, and the relation is summed over the family identification, i.

Observables

From the implementation of the Higgs field into the electroweak model one can predict several of the Standard Model observables. For example, the masses of Z^0 and W and the relation between them is given in terms of the gauge coupling g and the weak mixing angle $\sin^2\theta_W$:

$$M_W = \frac{1}{2}vg \tag{1.16}$$

$$M_Z = \frac{1}{2}v\sqrt{g^2 + g'^2} \tag{1.17}$$

$$\cos\theta_W = \frac{M_W}{M_Z} \tag{1.18}$$

$$\rho = \frac{M_W^2}{M_Z^2 \cos^2 \theta_W} , \tag{1.19}$$

where v also expresses the electroweak scale and is a function of the Fermi constant $v = \frac{2M_W}{g} = (G_F\sqrt{2})^{-1/2} = 246$ GeV and where ρ is the relative strength of the neutral and charged current weak interactions. Equations 1.16 - 1.19 allowed physicists to predict the masses of the W and Z^0 bosons to around 80 and 91 GeV for the MSSM with one Higgs boson (with the ratio ρ equal to 1). The Higgs mass is given symbolically by $M_H^2 = -2\mu^2 > 0$ [13]. Due to the high level of precision of the current experiments, radiative corrections need to be taken into account.

1.2 Experimental Results

The first main success of the Standard Model has been the ability to predict theoretically many new phenomena and a large number of new particles with a high accuracy. Successively, these predictions have been successfully verified experimentally in a number of detectors. Last but not least, precision measurements at LEP[3], Tevatron[4] and SLC[5] and many other experiments have proven the SM to an extraordinary accuracy of 0.1% or better [14]. Together, these achievements are some of the most remarkable of modern physics. The recent combined results of the global SM constrained fit taken from the LEP Electroweak Working Group is shown in figure 1.3. As can be seen, most values are measured with an impressive accuracy.

One important success has been the prediction of weak neutral currents and their main properties by the electroweak theory. The discovery of neutral currents at the Gargamelle bubble chamber at CERN PS[6] in 1973 established the weak force mediated by the predicted neutral Z^0. The equally important discovery of the W and Z^0 particles themselves at the SPS[7] accelerator at CERN, at their predicted rates and masses, was announced within a few months in 1983. Both charged and neutral currents, W, Z^0 and their properties were confirmed by other experiments.

Another experimental result from the Z^0 - factories was the determination of the number of light neutrino species resulting in the establishment of the maximum number of families. By defining the invisible width of the Z^0 one can compute the value of neutrino species to be $N_\nu = 2.984 \pm 0.008$ [13] which corresponds perfectly to the observed ν_e, ν_μ and ν_τ.

The SM did not only excel in electroweak measurements but also considerable discoveries were made for the QCD part of the theory. The charmed particles were found by the simultaneous discovery of J/Ψ by SLAC and Brookhaven[8] in 1974. Together with the discovery of its decay predominantly to strange particles, this

[3]Large Electron and Positron collider at CERN, Switzerland.
[4]Tevatron is a $p\bar{p}$ accelerator at Fermi National Accelerator Laboratory (Fermilab), USA.
[5]SLAC Linear Collider at the Stanford Linear Accelerator Center (SLAC), USA.
[6]Proton Synchrotron.
[7]Super Proton Synchrotron.
[8]Brookhaven National Laboratory, USA.

confirmed the Glashow-Iliopoulos-Maiani mechanism from 1970 introducing charm to include the quark section into the electro-weak theories. It also was the first indication that nature shows a symmetry between quarks and leptons.

Soon after, the τ lepton (4000 times heavier than the electron) was discovered at the Mark I detector at the SPEAR[9] e^+e^--collider in 1975, introducing the existence of a completely new family. The prediction of two new quarks to restore the symmetry was proven correct by the discovery of the bottom quark at Fermilab in 1977, but it took 18 more years before the discovery of the top quark completed the third family. This last quark was discovered by the CDF[10] detector at the Tevatron $p\bar{p}$ collider and the results was published in 1995.

1.3 Standard Model Limitations

Although the Standard Model has been highly successful, there are several indications that there will be new physics beyond the SM. The SM contains a large number of free particles (> 19) which need to be determined experimentally and the model does not describe gravity. In addition, when reaching energies higher than 200 GeV, corresponding to scales smaller than 10^{-18} m, one may require new models to describe this new region. A subset of the known indications of new physics are presented below:

Higgs Mechanism

As already mentioned the Higgs boson has not yet been found. If found, it will be the last piece which makes the SM complete for its particular region of validity. However, the Higgs physics needs to be understood. The theory describes a mechanism which explains why fermions and gauge bosons have mass, however this mechanism could already be part of new physics. Neutrino masses may have a different origin altogether, since they are the only known fermions which could be Majorana particles. Majorana particles differs from their Dirac counterparts by being their own antiparticles.

Even though the mass of the Higgs is not predicted by the SM, experimental data have severely constrained the possible mass of the Higgs boson. Direct searches at LEP exclude the Higgs mass up to 114.4 GeV (at 95% confidence level). Indirect searches at LEP together with the combined electroweak results from LEP, SLD[11], CDF and D0[12], give a preferred Higgs mass at 126 GeV$^{+73}_{-48}$ GeV at 68% confidence level. This is shown in figure 1.4 together with the excluded region. The LEP Electroweak Working Group also gives an upper limit of $M_H < 280$ GeV at 95% CL for a SM Higgs since the accuracy of the W and the top mass favours a light Higgs (see figure 1.4, right). As reference, the theoretical constraint of the Higgs

[9]Stanford Positron Electron Accelerating Ring situated at SLAC.
[10]The Collider Detector at Fermilab.
[11]SLAC Large Detector.
[12]D0 is another of Tevatrons detectors.

Figure 1.3: Standard Model results from 2005 [15], showing preliminary constraints based on the summary of results from LEP and other experiments. σ is the cross section at the Z^0 peak for decay into hadrons. $R_f = \frac{\Gamma_f}{\Gamma_{had}}$ is the ratio of the Z^0 partial decay width of fermions and hadrons. $\sin^2\theta_{eff} = (1 + \Delta k)\sin^2\theta_W$, where Δk is the radiative correction. A^f_{FB} is the forward-backward asymmetry for the decay of Z^0 to leptons and quarks.

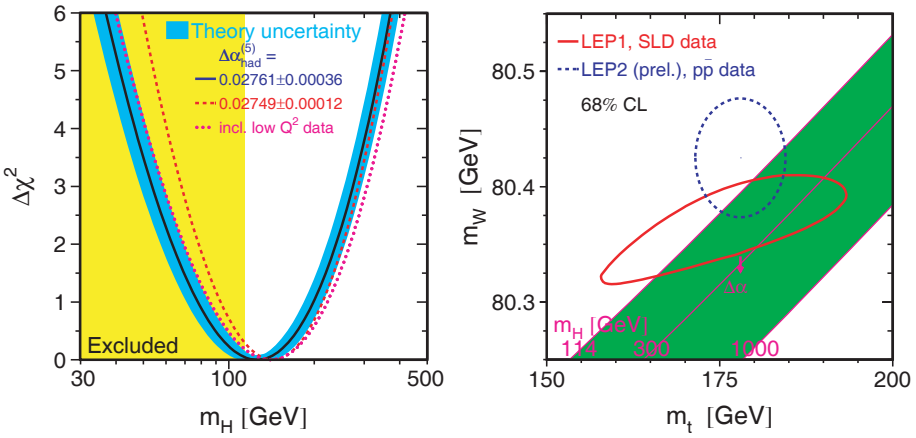

Figure 1.4: Left, Higgs lower limits as of 2005 [15], showing the $\Delta\chi^2$ as a function of the Higgs mass taken by high-Q^2 precision electroweak measurements. This picture shows the preliminary constrained fit to all existing experiments (LEP, SLD, CDF and D0). The minimum of the centre curve shows the preferred mass at 126^{+73}_{-48} GeV at 68% confidence level. Right, a comparison between the W and top masses with the directly measured mass values.

mass requires it to be less than 1 TeV, since the perturbative analysis would break down when approaching this value [13].

Predictions of the Higgs sector have been made, using different models venturing to explain the physics beyond the SM. If a light Higgs exists, then Supersymmetry (SUSY) [11, 16], and on larger scales Superstring theories [11, 17], could be valid. If more than one Higgs particle is detected, new physics will be needed to explain this occurrence since only one Higgs is present in the minimal Standard Model. It could be explained by Left-Right (LR) symmetries [11] or by supersymmetry models, which require several Higgs particles. If the Higgs does not exist, another mechanism for symmetry breaking would be needed which gives mass to the particles.

Unification

Another limitation of the SM is that the $U(1)_Y \times SU(2)_L \times SU(3)_c$ is not a unified theory. After the success of unifying the electromagnetic and the weak theory, it is tempting to do the same with the strong interactions. However, each group factor comes with its own coupling strength and at present energy scales the strong coupling is much higher compared to the electroweak coupling. The situation changes at a higher scale since the strong coupling decreases with the magnitude of the energy-momentum transfer (see figure 1.5, left). Unfortunately, the three couplings do not cross at the same point.

In the context of grand unified theories, the hierarchy problem is our inability to

understand theoretically why the energy scale where the unification of strong, weak and electromagnetic interactions becomes apparent ($\Lambda \sim 10^{16}$ GeV) is so much larger than other energy scales of relevance to particle physics, such as the scale of the electroweak symmetry breaking ($\sim 10^2$ GeV) . For this reason, it is very likely that new physics could appear at energies of around 1 TeV explaining this discrepancy.

Several physics models beyond the reach of the Standard Model attempt to explain the unification of forces and other open questions. Grand Unified Theories (GUT) incorporate larger groups to unifiy the electroweak and the strong force. Chapter 10 will treat in more detail some of the GUT models and their behaviour. Small discrepancies in the SM precision data could be corrected by the introduction of neutral gauge bosons, Z′, or by some other new physic phenomena beyond the Standard Model. This has lately been discussed in [18] and chapters 10 and 11 will illustrate this in more detail.

The Supersymmetric theory provides a powerful solution to the unification of the strong and electroweak interactions. By applying SUSY, the coupling constants cross at one point as can be seen in figure 1.5, right. The SUSY model establishes an additional symmetry between bosons and fermions, a particle-force duality, which results in a set of new supersymmetric particles. These new particles could be detected in new experiments, notably at LHC.

Superstring theory defines particles as 1-dimensional objects (called strings) providing an elegant solution of the main SM problems. By the use of SUSY, superstring theories are able to unify gravitation with the other forces at a much higher scale. However, none of these theories have been experimentally proven or provide clear cut predictions. More theoretical work as well as the discovery of new particles or interactions will be necessary to prove the unification of the other forces with gravity.

Another solution is presented in theories of dynamical symmetry breaking, such as the Technicolour models [19] describing the compositeness of quarks, leptons and gauge bosons. A third model could be that the electroweak force at higher energies becomes strongly interactive and would give rise to WW resonances and multiple production of extra gauge bosons.

Family Problem

One very interesting feature of the SM is the apparent requirement that all families must be complete. As already demonstrated in the past, this makes it possible to predict the existence of new species of particles. Experimentally, there is a constraint on the number of existing light neutrinos ($m_\nu < 1/2\ m_{Z^0}$) deduced from the Z^0 width; they can not be more than three. This also limits the number of families to three, but gives no explanation why not more families exists.

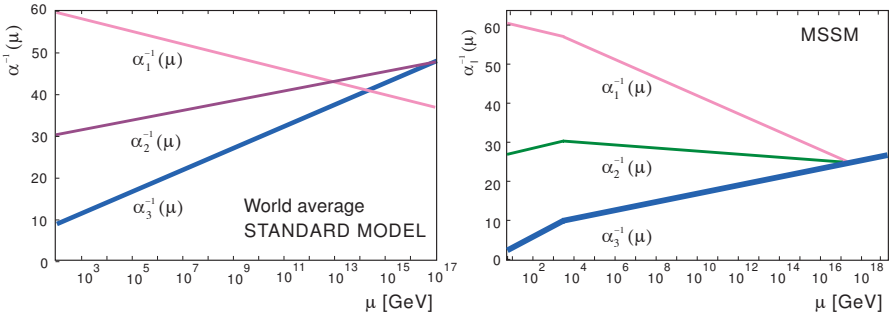

Figure 1.5: The evolution of the inverse coupling costants α_i corresponding to the three SM gauge groups U(1), SU(2) and SU(3) as a function of the energy-momentum transfer, μ. α_i is the hypercharge coupling in the conventional normalisation. The left-hand figure shows α_i without supersymmetry, and right-hand figure with supersymmetry included. The picture is taken from [20].

Conclusion

The construction and development of the LHC accelerator and the ATLAS detector are motivated by these possibilities to complete the SM and to search for new physics beyond its limits. It is expected, as the range and the performance of new experiments improve and approach the 1 TeV scale, that new physics discoveries will be imminent. Even before these scales indirect measurements could give indications of new physics and many unsolved questions of the SM might be answered or we will discover new phenomena which will need our attention.

The high energy and luminosity of the LHC offer a large range of physics opportunities, from the precise measurement of the properties of known objects to the exploration of the high energy frontier. The desire to probe the origin of the electroweak scale leads to a major focus on the Higgs boson and ATLAS is constructed to be sensitive to it over the full range of the allowed masses. Other important goals are to search for signs of new physics such as supersymmetry or technicolour theories or new gauge bosons. The investigation of CP violation in B decays and the precision meaurements of W, top-quark masses and triple gauge boson couplings will also be important tasks of the ATLAS detector.

Quite an effort has gone into the development of the ATLAS detector (as well as the LHC) to be able to investigate the physics envisaged. A demanding program of detector research and development is needed to reach the performance criteria. Chapter 2 describes the main particle interactions with matter and the basic principles of particle detection, most of which are used in the ATLAS experiment.

2
Particle Detection

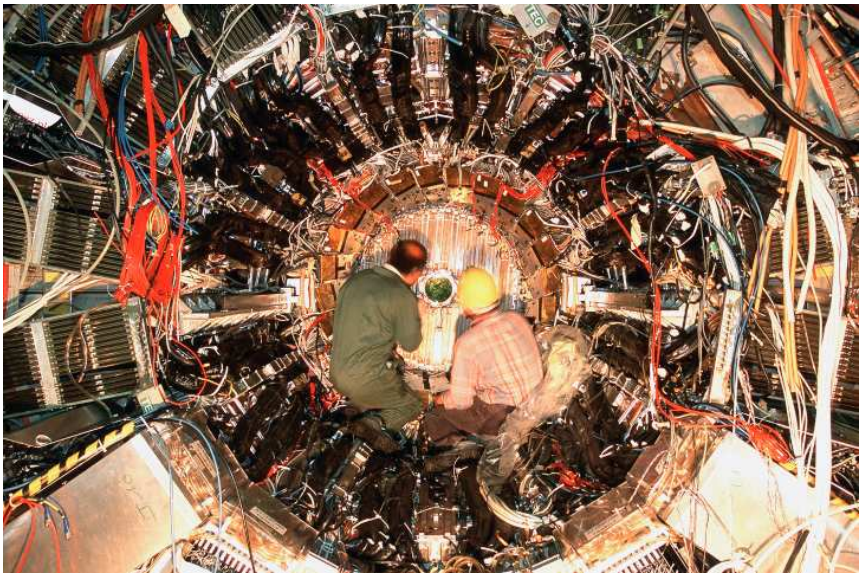

Dismounting the L3 detector at the LEP collider in 2001 [8].

Introduction

To understand elementary particles and the theoretical models describing them, it is important to extend our knowledge about their characteristics and their governing laws. To study these particles it is important to detect, identify and measure them. As the particle physics theories and their experimental requirements advances, increasing demands are put on the research to develop improved detectors and detection methods.

This chapter give an introduction to particle detection by first describing the main relevant particle interactions. The second part describes the principle of the most common detectors types and their performance. It also introduces some of the principles behind the ATLAS sub-detectors, which will be explained in more detail in chapter 3.

2.1 Interaction of Particles

Particles are detected via their interactions with matter. The result of these interactions depends on the incoming particle's charge, mass and energy and as well as on the matter properties. By understanding the interaction processes, the best method to detect and measure a certain particle within a defined energy range can be selected.

Charged Particles

Electromagnetic processes dominate the interactions of incident heavy charged particles (e.g. muons, pions and protons) and light charged particles (electrons and positrons). Their energy is transferred by direct collisions with the electrons or the nucleus of matter atoms. The two main processes, which completely dominate the low energy region, are the following:

- Inelastic collisions with atomic electrons (ionisation)
- Elastic scattering with the atomic nucleus (Coulomb scattering)

Inelastic collisions occur when atomic electrons are excited or freed by the incoming particle. Elastic scattering takes place when the incoming particle is being repulsed by the atomic nucleus and changes its direction, and is slightly less frequent than inelastic collisions. Almost all the energy loss of inelastic collisions is small compared to the total kinetic energy of the particle. However, the energy loss of elastic scattering is even less since the nucleus is mostly large in comparison with the incoming particle [21]. Incident, relativistic light charged particles are also subject to:

- Bremsstrahlung (depends on $\frac{1}{m^2}$)

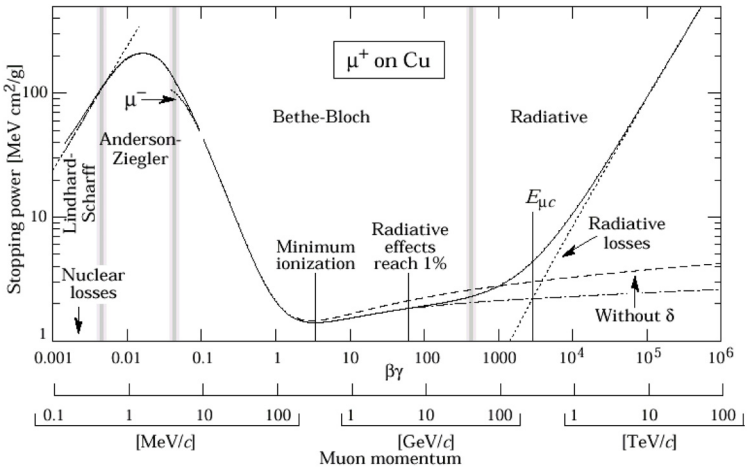

Figure 2.2: The stopping power of positive muons traversing copper, where the solid line indicates the total stopping power. The vertical bands delimit different regions of approximation, for which different processes dominate [11].

Bremsstrahlung occurs when the incident particles, having relativistic energies, are scattered by the matter nucleus. The smaller the mass and the higher the energy of the incident particle, the more likely it is to scatter. Above a critical energy ($\sim$ 10 MeV for electrons) it becomes the dominating process. Other types of radiation processes are those due to the optical properties of the matter:

- Cherenkov radiation ($v_{particle} > c_{matter}$)
- Transition radiation (refractive index $n_1 \neq n_2 \neq ... \neq n_n$)

Emission of Cherenkov radiation occurs when the incoming particles move faster than the speed of light in the medium it moves in. An electromagnetic shock wave (characteristic blue light) is created with a conical shape and with a well defined angle. Transition radiation is another type of medium dependent radiation, which occurs when a charged particle passes from one medium to another with different optical properties.

The effect of an interaction is best described by the energy loss of the incident particle, which is the sum of the energy losses from all processes in play:

$$(\frac{dE}{dx})_{total} = (\frac{dE}{dx})_{collision} + (\frac{dE}{dx})_{bremstrahlung} + \ ... \ . \tag{2.1}$$

For heavy charged particles, the main processes are inelastic and elastic collisions and equation 2.1 can be reduced to its first term, which is best described by the Bethe-Bloch equation. This equation is a function of both the particle and matter

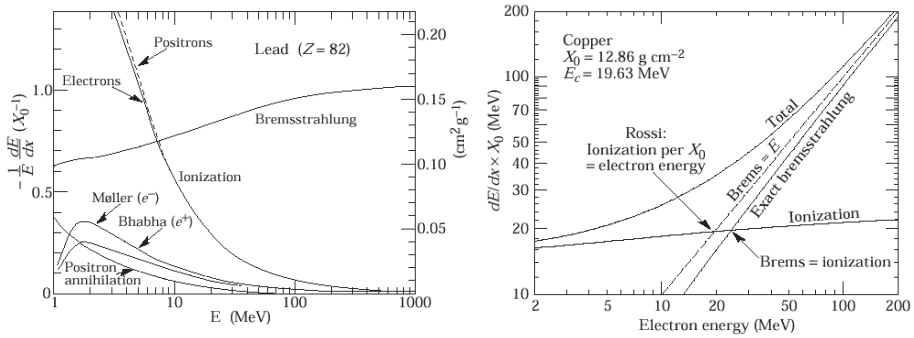

Figure 2.3: Energy loss for light particles as a function of their energy. Left, the fractional energy loss per radiation length in lead for different interactions. Right, a close up on the point of critical energy for electrons traversing copper [22].

properties ($\kappa = 2\pi N_a r_e^2 m_e c^2 \rho \frac{Z}{A} \frac{z^2}{\beta^2}$ where $\beta = \frac{v}{c}$, described in annex A.1) as well as the energy transfer (T), the matter ionisation constant (I) and some correction terms ($\delta/2 + ...$):

$$-\frac{dE}{dx} = \kappa \left[ln(\frac{T}{I}) - \beta^2 - \frac{\delta}{2} + \ ... \right] \tag{2.2}$$

For light charged particles, both terms of equation 2.1 play an equally important role since the bremsstrahlung is increasingly dominant towards high energies. The first term in the Bethe-Bloch equation, needs to be modified to account for the small mass of the incoming particles. Since they are equal to the matter electrons, they are sensitive to their kinematics, spin and identity. In addition, the assumption that the incident particle remains undeflected during the collision process is invalid. The second term of equation 2.1 accounts for the bremsstrahlung effect and is found by integrating the cross-section times the photon energy, where Φ_{rad} is the radiation loss. It can be expressed as a function of the radiation length $X_0 = 1/N\Phi$, where N is the number of atoms/cm^3:

$$-\frac{dE}{dx}_{radiation} = N\Phi_{rad}E \tag{2.3}$$

Figure 2.2 shows the energy loss of an incident muon particle in copper for different energy regions. The solid curve shows the total stopping power, which has a large minimum for $\beta = 0.96$. The amount of energy loss at this minimum varies with the atomic number of the matter particles and the type and energy of the incoming particle. At higher energies, the curve passes through the critical energy, where the energy loss due to ionisation is equal to the energy loss from bremsstrahlung[1].

[1]One of two definitions. Both can be seen in figure 2.3.

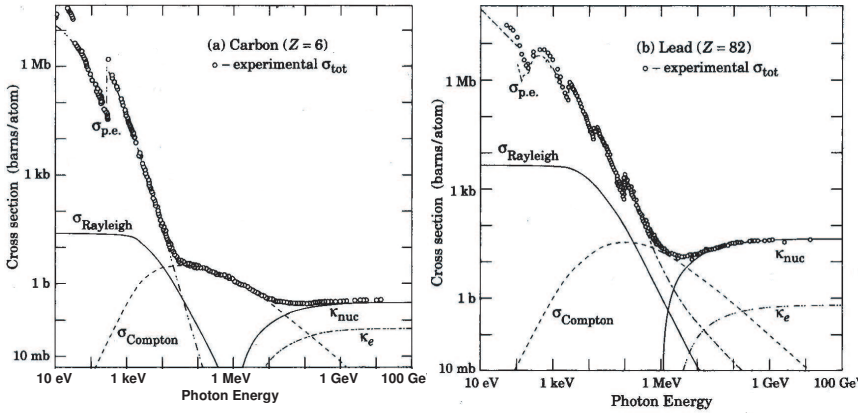

Figure 2.4: The photon energy of carbon (left) and lead (right) as a function of the cross section. The total energy loss is dominated by the photoelectric effect at low energies, Compton scattering at medium energies and pair production (κ) at high energies [11].

Figure 2.3, left, shows the stopping power of light particles as a function of their energy. At low energies, the electrons and positrons loses energy mainly by ionisation, although scattering processes such as Møller scattering, Bhabha scattering and e^+e^- annihilation contribute. As can be seen from figure 2.3 on the left, the bremsstrahlung contribution increases almost linearly.

Neutral Particles

Neutral particles, such as photons, neutrons and neutrinos, are not subject to Coulomb interactions due to their lack of charge. For this reason, it is mostly necessary to first transform them in a reaction process which produces detectable charged particles before they can be detected [21]. Photons are very important since they occur in many interaction processes, not only as primary particles but also as a result of bremsstrahlung and de-excitation. Photons are more penetrating than charged particles due to a much smaller cross-section of the photon processes, of which the most important are the following [22]:

- Photoelectric effect ($\propto Z^5$)
- Compton, Thompson and Rayleigh scattering ($\propto Z$)
- Pair production ($\propto Z^2 + Z$)

The photoelectric effect is the absorption of photons by atomic electrons with the subsequent emission of a bound atomic electron. The cross section for this process

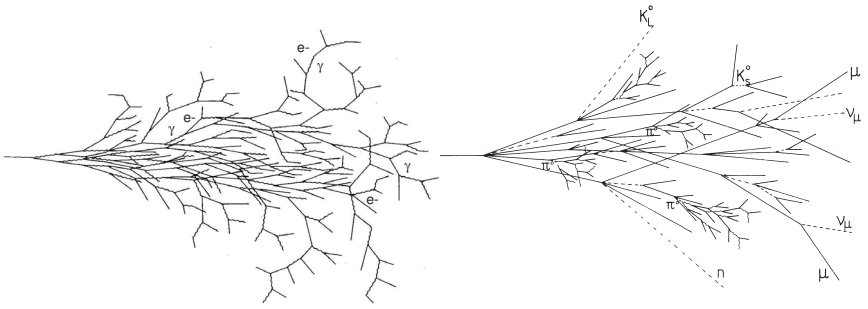

Figure 2.5: Left, an electromagnetic cascade. Right, a hadron cascade in an absorber [23].

is low at high energies but increases towards low energies, with peaks at the shell energies (figure 2.4). Compton scattering (incoherent scattering) is the scattering of photons on electrons which are only loosely bound to the nuclei in the material. Thompson scattering is the scattering of photons by free electrons at the classical limit and Rayleigh scattering is the scattering of photons by the atom as a whole (coherent scattering). Pair production is the transformation of a photon into an electron-positron pair by the presence of a nucleus, at energies higher than 1.022 MeV. Electron screening (how effectively the electrons hide the nucleon charge) influences the strength of this interaction. When only considering pair production the mean free path of the photon is found to be proportional to $9/7\ X_0$ (radiation length).

The neutron mainly interacts with the nuclei of matter via the strong force. This force has a short range ($\sim 10^{-15}$ cm, the diameter of an average sized nucleus), which makes the neutron a highly penetrating particle. When it does interact, it is via the following processes: inelastic scattering (with the atomic nuclei), elastic scattering (from the nuclei), radioactive neutron capture and other nuclear reactions. For energies above 1 GeV these reactions result in a hadronic shower development.

The neutrino reacts extremely weakly with matter. They can still be detected, for example indirectly in closed detectors, by summing up all detectable energy and momentum, attributing the missing energy and momentum to escaping neutrinos.

Showers

By combining several types of interactions it is possible to produce a multiplicative effect which results in a shower or cascade of particles. The following shower types are often used in particle detectors known as calorimeters:

- Electromagnetic showers (bremsstrahlung - pair production)
- Hadron showers (various nuclear processes)

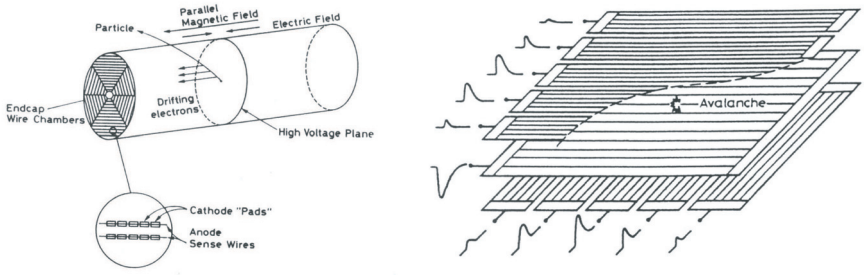

Figure 2.6: Left, the basic principle of a time projection chambre [21]. Right, the schematics of a multiwire proportional chamber [24].

An electromagnetic shower (figure 2.5) can be started at high energies by either a photon produced by bremsstrahlung or from a pair production process in a thick absorber. Alternating pair production and bremsstrahlung create more and more electrons and photons with one split per radiation length, t. The number of tracks increases as $N(t) = 2^t$ and the energy carried by the particles decreases as $E(t) = E_0/2^t$. Hadronic showers are dominated by large transverse momentum transfers in nuclear interactions [23]. A significant loss in hadronic energy is due to the break-up of nuclear bonds and the creation of muons and neutrinos which escape the shower.

2.2 Particle Detectors

Today's elementary particle physics demands the continuous development of a large range of particle detectors to meet the increasing demands of higher efficiency, speed, granularity and resolution. In addition, the detectors have to evolve according to the changes in accelerator designs and cope with higher radiation levels and collision frequencies. The main detector types available are presented below, with emphasis on those relevant to the ATLAS detector.

Ionisation Detectors

The principle of an ionisation detector is to use the signal from ionised particles created by charged particles passing through matter (mostly gas). A simple ionisation detector is a cathode tube filled with gas containing an anode wire. For typical gases, the energy needed to created a charge-anticharge pair is around 30-40 eV [21]. Helium, one of the most frequently used gases also has the highest ionisation potential ($\sim$ 24 eV) which corresponds to $\sim$ 5 primary electrons per cm. The main processes which determine the performance of an ionisation detector are the drift of the ionised particles in the gas and the amplification of the signal.

The typical number of collected ions changes with the level of applied voltage and results in different modes of operation. For low voltages, in the recombination region,

the ions are recombining before the charge collection and no signal is detected. In the ionisation chamber region (< 250 V), there is no mulitiplication and the response is flat. In the proportional counter region (around 250 - 750 V) there is an amplification (gain of 10^4 to 10^6) due to the secondary ionisation produced by the applied electric field. The Geiger-Müller region (> 800 V) is a region where photon emission are the origin of avalanches which appear along the whole wire.

There exists a multitude of ionisation detectors. The simplest one is the drift tube, which was one of the UA1 detectors at SPS used at the discovery of the W and Z^0 bosons. Another type very frequently used is the Multi-Wire Proportional Chamber (MWPC, figure 2.6, right), which uses a set of thin parallel anode wires between two cathode planes to be able to reconstruct tracks in space. Another largely used ionisation chamber is the Time Projection Chamber (TPC), shown in figure 2.6, which has wire chambers at the end of the tube and can provide full 3-D track reconstruction (the z-coordinate is given by the drift time), dE/dx and momentum measurement. Both the ALEPH[2] and DELPHI[3] experiment used TPCs to detect particles. Ionisation detectors will be used for several parts of the ATLAS sub-detectors, for instance in the muon tracker.

Scintillation Detectors

Scintillation detectors are based on another important interaction by charged particles, notably the excitation of the matter electrons as the incident particle passes. This is quickly followed by a de-excitation and the emission of detectable light. Only some materials will emit light and only a small fraction of its energy, around 3%, is released as optical photons. The performance of these detectors depends largely on the material used. Often, it is necessary to add a chain of wavelength shifters before a photon detector, as seen in figure 2.7, to be able to convert the optical signal into an electrical one.

Scintillator materials can be divided into two types; organic and inorganic scintillators. The organic scintillators can be made from crystalline, liquid or plastic materials, which all emit light mostly in the blue to green visible wavelength region. The most popular ones are the plastic scintillators, since they are easy and cheap to produce. The typical light output is about 1 photon per 100 eV of energy deposit. A 1 cm thick scintillator traversed by a minimum ionising particle will yield $\sim 2 \times 10^4$ photons.

Inorganic scintillators differ from the organic ones by having much higher densities ($\sim$ 4 - 8 g/cm^2) of scintillating material which give different properties. Some crystals are scintillators themselves but others requires a dopant such as thallium (Tl) or cerium (Ce) to become fluorescent. The popular inorganic scintillator uses sodium iodide activated with a trace amount of thallium (NaI(Tl)). Typical light output is 40 000 photons per 1 MeV energy loss.

The organic scintillators are fast, reliable and robust, but the light output is

[2]Apparatus for LEP PHysics, one of the four large scale detectors at LEP

[3]DEtector with Lepton, Photon and Hadron Identification, another one of the four large scale detectors at LEP

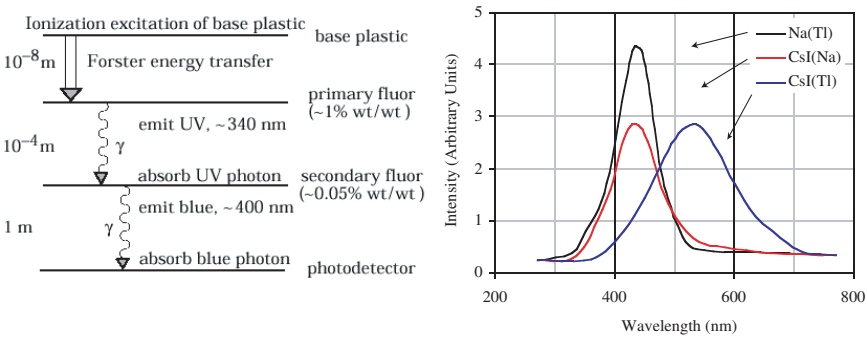

Figure 2.7: Left, scheme of transformation of optical signals into electrical ones. The scintillator material on the top emits light, the primary fluor level shifts this light to UV and the secondary fluor transforms to visible light detected by the photodetector. Right, the light output for different materials [21].

less than for inorganic scintillators. The plastic scintillators are subject to diminishing light yield due to ageing, increasing atmospheric pressure and changes to the magnetic field. Inorganic scintillators, on the contrary, have a high and stable light ouput, which is required for high resolution and precision calibration but are then quite slow. Both types suffer from radiation damage. In ATLAS, scintillators will be used by the hadronic calorimeters.

Calorimeter

Calorimeters are used in most current experiments and will make up a large part of the ATLAS detector. They are composite detectors based on the total absorption of particles to measure the energy and position of incident particles or jets. There are two main types of calorimeters: electromagnetic calorimeters, based on the use of electromagnetic shower, and hadronic calorimeters using hadronic showers.

Electromagnetic calorimeters are often homogeneous crystal calorimeters made of BGO, CsI, NaI and PWO [22], which all have radiation lengths of around 1-2 cm. These detectors are costly and are sensitive to radiation effects and temperature fluctuations. Normally the total energy of the particle is measured and the energy resolution improves with energy and is proportional to $1/\sqrt{E}$. In additon, corrections must be made due to inhomogeneities, cell-intercalibration, non-linearity, electronic noise and pile-up. The shower development is of the order of a fraction of a nanosecond. Sampling calorimeters, made of a combination of absorption material layers (e.g. Pb) and scintillator or ionisation detectors are used in big experiments like ATLAS and only measure a fraction of the energy of the transversing particle.

Hadronic calorimeters are usually much thicker than electromagnetic calorimeters (7-8 hadronic interaction lengths). Some examples of materials employed are

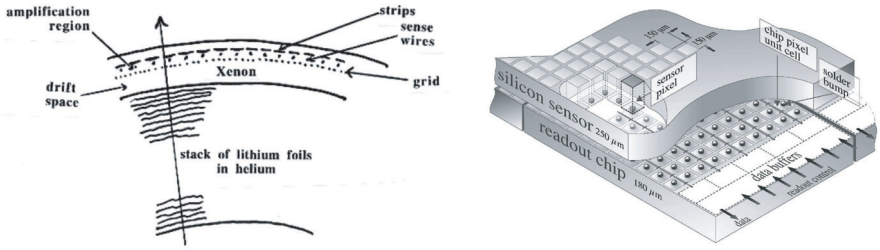

Figure 2.8: Left, schematics of one layer of a transition radiation detector. The particle traverses several layers of foils where photons are produced which are detected in the MWPC [23]. Right, a silicon pixel detector. One layer of sensor pixels is situated on top of the readout chip [22].

H, Be, Si, Fe and Pb. The resolution and the response of hadronic calorimeters are less favourable than for electromagnetic calorimeters due to significant fluctuations in the production of neutral and charged pions. For this reason the design needs to be optimised.

Transition Radiation Detector

Transition Radiation Detectors (TRD) use the production of transition radiation to provide particle identification at highly relativistic energies where ionisation measurements or Cherenkov radiation do not provide useful discrimination. Transition radiation has the advantage that the intensity of the radiation is approximately proportional to γ (where $\gamma = \frac{1}{\sqrt{1-\beta^2}}$), hence it can be used to identify particles with high γ such as electrons.

A typical detector is shown in figure 2.8 and is composed of a stack of radiator foils of low atomic number (e.g. Li, polyethylene, C) to produce a sufficient number of photons in the transition between the vacuum and the dielectric layer. These photons are then detected by special proportional detectors (MWPC) in between a set of foils, containing a high Z gas (e.g. Xe) to absorb the photons rapidly. Typically, at the keV range, the photons are emitted at a small angle $\theta \propto 1/\gamma$. A similar but more complex transition radiation detector will be used to track particles in ATLAS.

Semiconductor Detectors

The principle of semiconductor detectors is the creation of electron-hole pairs in a semiconductor material by the passing charged particles. As described in [25, 26], semiconductor materials have an energy band structure where only a small amount of energy is needed to make them conductive. The energy needed to create an electron-hole pair in silicon is on average 3.6 eV. By doping the semiconductor the number of charge carriers can be augmented and becomes n- or p-type materials if the majority

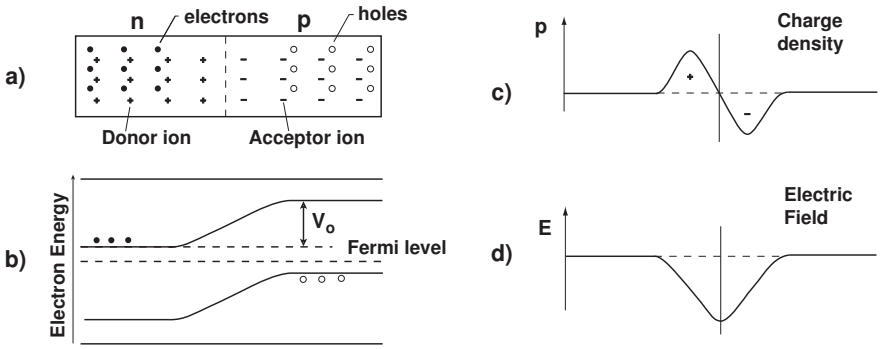

Figure 2.9: a) shows a schematic diagram of a n-p junction, b) a diagram of the energy levels for electrons showing the creation of a contact potential V_0 corresponding to the potential difference across the junction, c) shows the charge density and d) the electric field intensity [21].

charge carriers are electrons or holes, respectively. If a p-type material comes in contact with a n-type material there is initially a diffusion of charge carriers across the materials and the p-region becomes negative and the n-region positive. This creates an electric field gradient across the intermediate region called the depletion zone, which is devoid of all charge carriers (see figure 2.9). This depletion zone is very suitable for particle detection since a passing charged particle will create a current signal proportional to the ionisation.

Silicon semiconductor detectors are mainly used for particle tracking close to the interaction point. Silicon detectors are preferable when detecting charged particles, whereas germanium is a better choice for γ-ray detection, due to its higher atomic number (the photoelectric cross-section is 60 times higher than for silicon). However, germanium needs to be operated at low temperatures because of its smaller band gap, and its cryostat makes it unsuitable for tracking. Silicon detectors have a band gap of 1.1 eV which is well below the average energy of creation and can be operated at room temperature. In an intrinsic volume of 1 cm $\times$ 1 cm $\times$ 300 μm this corresponds to around 4.5×10^8 free charge carriers, but this number is being reduced by depleting the silicon. Different detector shapes are possible of which the two most common ones are pixel (as can be seen in figure 2.8) and multilayer strip readout. As described, the advantages of semiconductor detectors are the self supporting structures, low costs and connectivity. However, since these detectors are often being close to the interaction region, radiation damage is a main concern. The results are increased leakage currents, changes to the depletion voltage and decreased lifetime as well as a decreasing charge collection efficiency. Since their appearance, semiconductor detectors have been very popular and very useful to detect long lived particles and to reconstruct vertices. In ATLAS, the inner tracker will by made of silicon semiconductors, using both pixel and strip layouts.

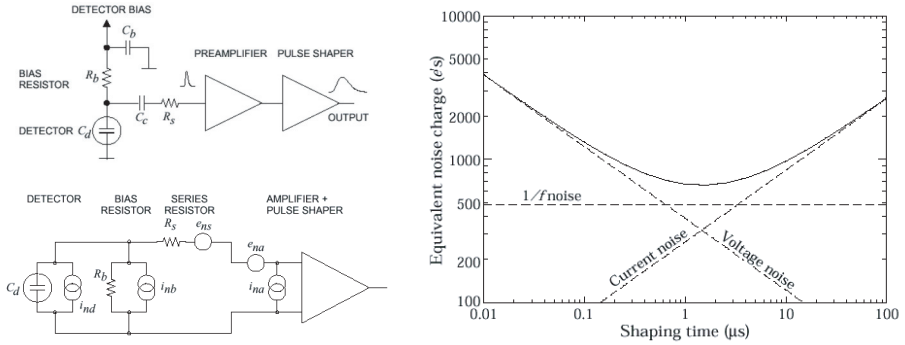

Figure 2.10: Left, typical detector front-end electronics circuit diagram. At the top, the detector representation, at the bottom, the corresponding noise circuit. Right, the total ENC charge is plotted as a function of the shaping time. A minimum can be found which depends on e.g. the detector capacitance [11].

Silicon Front-end Electronics

Low noise electronics is important to achieve optimal detector performances. The detector can be described by the upper circuit diagram in figure 2.10, where the detector is represented as a capacitance, C_d, with a bias voltage, which is applied across a resistance R_b. All resistances at the input path are represented by one resistor, R_s and the signal is coupled through to the preamplifier via a blocking capacitor C_c.

The detector noise can be described by an equivalent circuit (bottom circuit). The current and noise sources are described by i_n and e_n respectively. Figure 2.10 describes the different detector noise contributions. Shot noise and thermal noise have a white frequency spectrum. The 1/f noise is dominant due to trapping and detrapping occuring in various components and provides a constant contribution. At low shaping times the voltage noise is dominant whereas at higher shaping times the current noise is dominant. By increasing the detector capacitance, the voltage noise will increase and the noise minimum shifted to the right. It is thus important to determine the detector capacitance as well as the shaping time, input circuit resistances and the amplifier noise parameters.

2.3 Measurement Characteristics

When detecting a particle, it is often desired to determine not only the type of particle but also its energy, momentum, charge and lifetime. Most detectors provide some of these measurements but often a combination of detectors are needed to fully characterise a particle. Among several possibilites: Transition, ionisation and Cherenkov radiation permit both identification and tracking, whereas calorime-

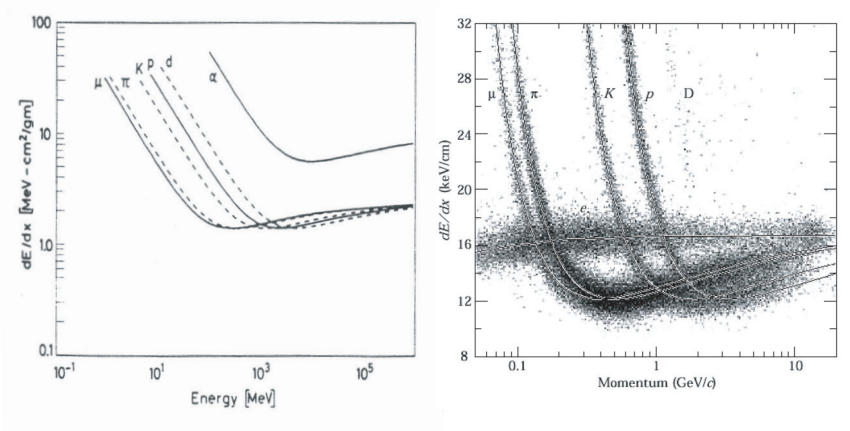

Figure 2.11: The stopping power as a function of the momentum. Left, theoretical values from Bethe-Bloch predictions and right, the measured results. Different particles can be identified by their amount of stopping power. From [22] and [11].

ters are used for energy determination and semiconductor detectors for momentum measurements and tracking.

The identity of a particle is found by determining its charge and its mass. Determination of the energy loss ($\frac{dE}{dx}$) is a powerful tool of particle identification in addition to energy determination. Particles with different mass, but with the same momentum, will have different energy losses as can be seen in figure 2.11. Cherenkov detectors also provide good particle identification by determining the speed of the particle.

Momentum measurements can be done by using the information from a magnetic field. The momentum component transverse to the magnetic field, p, of a particle with charge ze, can be found by measuring the particle curvature, R, and by applying the following relation:

$$p\ cos\lambda = 0.3\ z\ B\ R\ , \tag{2.4}$$

where λ is the pitch angle[4], z the charge and B the magnetic field [11]. It is also important to tag and reconstruct particles from secondary vertices. Precise vertex detectors provide robust tracking close to the interaction area with minimal material in front, to minimise multiple scattering processes.

Conclusion

To detect particles, the ATLAS detector uses layers of several of the detector types described in this chapter, as can be seen in figure 2.12. Closest to the interaction

[4]The angle between the direction of the magnetic field and the particles trajectory.

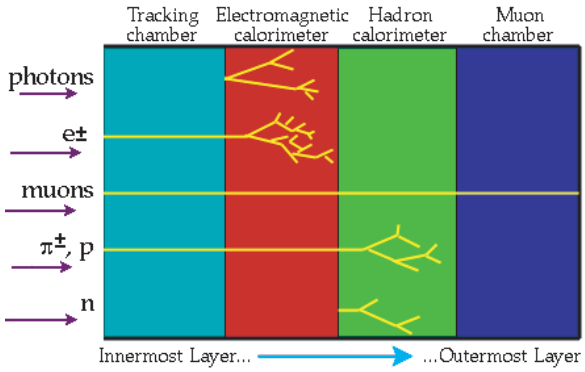

Figure 2.12: Large particle detectors such as ATLAS, consist of a multitude of detectors in layers around the interaction point [27]. Most often, the first layer is used for tracking and momentum measurements, followed by a layer of calorimeters for the measurement of energy followed by a muon chamber.

point are seven layers of pixel and silicon semi-conductor detectors, which permit tracking of charged particles almost from the interaction point. Around these detectors are a layer with a transition radiation tracker, which permit more continuous tracking of charged particles. The next layer consists of both electron and hadronic calorimeters which permit the determination of the energy loss of particles. The very outermost layer consists of a muon spectrometer based on the use of drift tubes among other detectors.

To be able to meet the requirements needed for the LHC runs, all relevant fields of particle detection need to be pushed to new performance levels, including new detector designs, in order to build such a high performance and complex detector as ATLAS. New developments within particle physics instrumentation are a force driving industrial development and often result in important spin-offs in fields such as medical instrumentation. As we will see in the next chapter, new technologies have been successfully developed and high detector performance is to be expected. It will be up to the future to see what physics phenomena ATLAS will discover.

3
LHC and the ATLAS Detector

The ATLAS detector under construction, as of May 2005 [8].

Introduction

New developments of high energy physics experiments are always needed in the search for new particle physics. The scale of large experiments are out of reach of individual research institutes but the European Centre for Nuclear Research (CERN) provides a European facility where researchers from all the world can work together towards new results. Currently a new hadron collider, the LHC is being built in the old LEP tunnel and several new large scale detectors are being constructed at the four interaction points along the beam (see figure 3.2), one of them being the ATLAS detector. The aim of the development is for both LHC and ATLAS to be operational in 2007.

This chapter describes briefly the LHC collider and ATLAS in more detail. Both the physics requirements and the detector specifications will be described as well as the sub-detectors, magnets and trigger implementations. The pictures in this chapter of are mostly schematic drawings of the ATLAS sub-detectors. However, many of these detectors are well on their way to be completed and installed. A brief pictures gallery is found in annex C illustrating the detector development.

3.1 The Large Hadron Collider

The Large Hadron Collider is designed to explore the borders of accelerator physics and the main motivation for its construction is to provide particles needed to investigate the origin of mass and the symmetry breaking. LHC is designed to be a both a proton-proton collider and an ion collider (e.g. Pb-Pb). The following discussion will be focused on the proton-proton collider which will be used in ATLAS. The choice of proton collisions have, from past experiences, proven to be a highly successful tool to discover particles and to perform high precision measurements [28]. In addition, proton collisions are preferred to proton-antiproton colliders since the latter would have difficulties achieving the desired luminosities.

The LHC injector chain can be seen in figure 3.2. Protons, which are produced by a duoplasmatron[1] source in the LINAC2[2] with initial energies of 100 keV are accelerated in the PS Booster, PS and the SPS to 1.4, 25, 450 GeV, respectively before being injected into the LHC. To achieve these energies, these accelerators have been largely refurbished. Among other improvements: the LINAC2 current and the Booster energy needed to be increased and the SPS has a new impedance reduction programme and a new extraction channel. The Pb ions will be produced by the LEIR[3], which has been modified to permit Pb ion cooling and accumulation.

The protons, in bunches, enter the LHC in two beams with separate vacuum pipes, one circulating clockwise and the other anticlockwise in the 27 km circumference tunnel. Each bunch consists of 1.15×10^{11} particles and will have an RMS bunch length at collision of 7.55 cm [29]. Already at 1% of its nominal intensity,

[1] The collisions of electrons and hydrogen free the protons used in the collider.
[2] Linear Accelerator 2
[3] Low Energy Ion Ring, previously the Low Energy Antiproton Ring (LEAR)

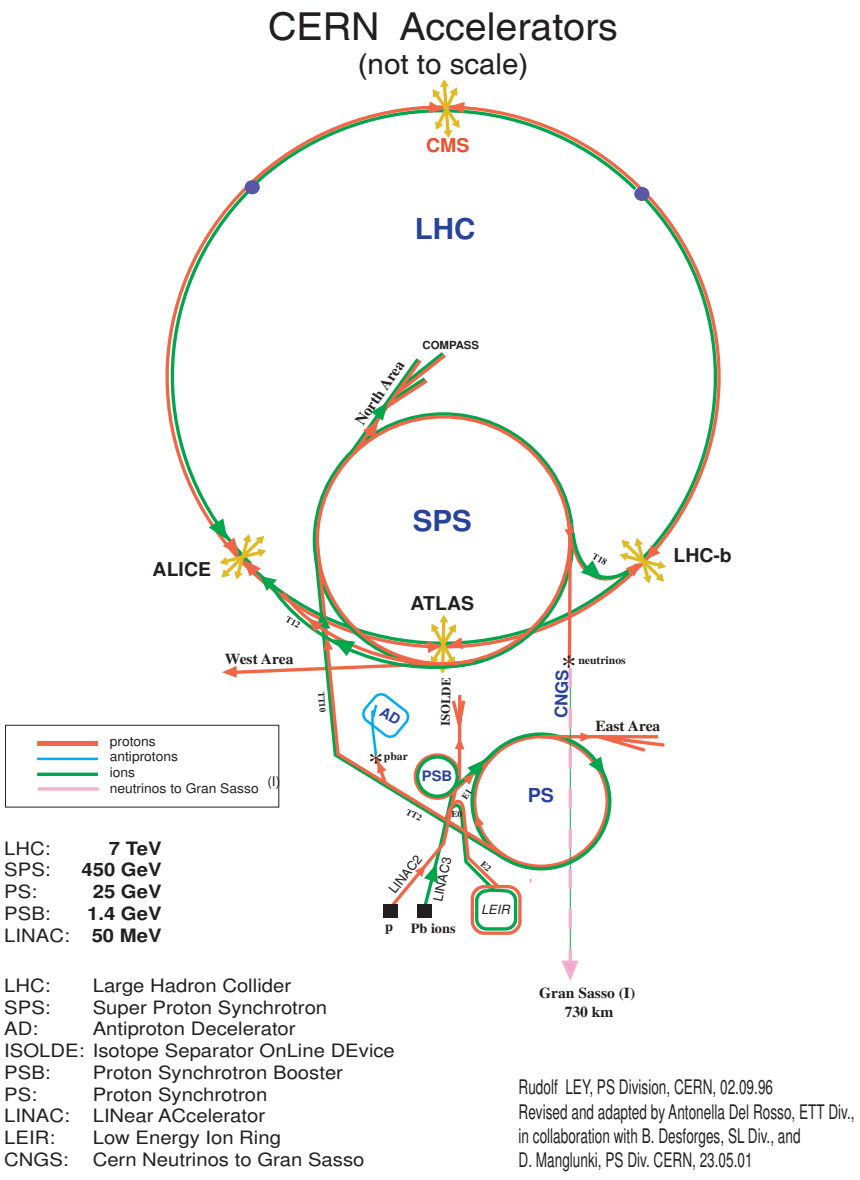

Figure 3.2: Schematic view of the Large Hadron Collider and the injector chain [8]. Protons produced by LINAC2 are accelerated successively in PSB, PS and the SPS before being injected into the LHC tunnel where they accelerate to 7 TeV.

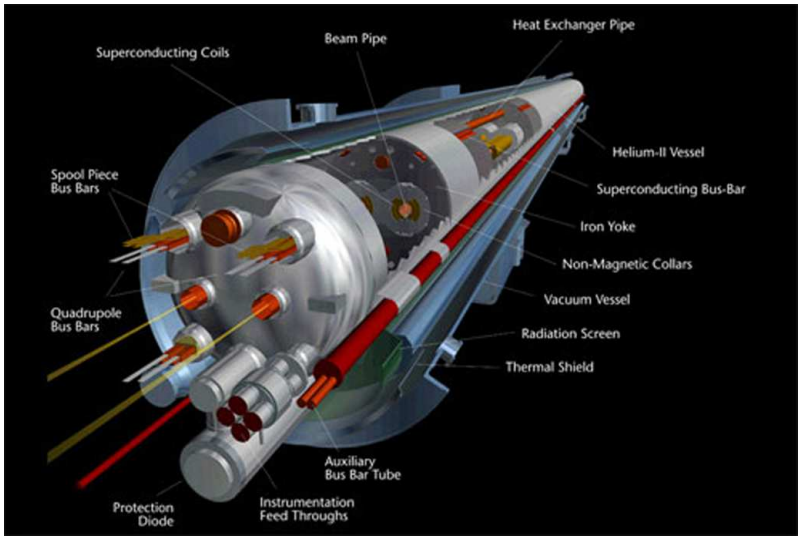

Figure 3.3: The Large Hadron Collider ring with some of its elements: e.g. two beamlines, superconducting coils, cryostats, vacuum tube and supplies [8].

the LHC will enter new territory in terms of stored energy. The beams are stored for 10 hours which corresponds to 4×10^8 revolutions in the machine.

In the LHC, the protons are accelerated up to 7 TeV and are kept in bunches by the use of RF-cavities (16 MV total accelerating voltage per beam at 400 MHz). They are low impedance, high stored energy, superconducting cavities operating at a frequency of 400 MHz and are installed in four areas with enlarged beam separation (42 cm). The protons are kept in the ring and focused by several types of magnetic fields. The relation between the bending power and the beam momentum, p [TeV], is given by the relation 2.4. For the case of the LHC, the beamline radius, R, is 4.5 Km and $\cos\lambda = 1$ and the charge $z = 1$.

The LHC consists of 1232 double aperture superconducting dipole magnets, which are needed for the up to 8.33 T field and more than 500 "2-in-1" superconducting quadrupole magnets operating at more than 250 T/m. They are all situated within the same mechanical structure and cryostat as can be seen in figure 3.3 [29]. In addition, there are more than 4 000 superconducting correction magnets of various types [20]. This gives in total around 40 000 tons of material that has to be cooled down to 1.9 K.

The protons are collided each 25 ns at the four interaction points of the ATLAS, CMS[4], ALICE[5] and LHCb[6] experiments [29]. The collisions have a centre-of-mass

[4]Compact Muon Solenoid detector
[5]A Large Ion Collider Experiment
[6]The Large Hadron Collider beauty experiment

Energy at collision	7	TeV
Energy at injection	450	GeV
Dipole field at 7 TeV	8.33	T
Coil inner diameter	56	mm
Distance between aparture axes (1.9 K)	194	mm
Luminosity	1	10^{34} cm^{-2} s^{-1}
Beam beam parameter	3.6	10^{-3}
DC beam current	0.56	A
Bunch spacing	7.48	m
Bunch seperation	24.95	ns
Number of particles per bunch	1.1	10^{11}
Normalised transverse emittance (r.m.s.)	3.75	μm
Total crossing angle	300	μrad
Luminosity lifetime	10	h
Energy loss per turn	7	keV
Critical photon energy	44.1	eV
Total radiated power per beam	3.8	kW
Stored energy per beam	350	MJ
Filling time per ring	4.3	min

Table 3.1: The main LHC properties.

energy of 14 TeV, which corresponds to around seven times higher energy than the current largest proton collider, Tevatron at Fermilab [30]. The limiting factor to the achievable centre-of-mass energy is the bending power of the magnets as defined by relation 2.4. At the interaction point the magnetic fields and vacuum chambers are shared in a 130 m long common beam pipe.

The peak luminosity at the interaction points of ATLAS and CMS will be of 10^{34} cm^{-2}s^{-1} at 14 TeV centre of mass energy, which is a factor around 100 larger than for previous machines (LEP, Tevatron). This permits the search for particles with mass up to 5 TeV. The cross sections for various centre-of-mass energies are seen in figure 3.4. At design luminosity, each crossing contains on average 25 soft interactions providing an event rate of 10^9 Hz [29], corresponding to an inelastic cross section of around 100 mb. The number of events per second, N_{event}, generated in the LHC collisions, as a function of cross section, σ_{event}, and the machine luminosity (for a Gaussian beam distribution), L, is given by [29]:

$$N_{event} = L\ \sigma_{event}. \tag{3.1}$$

The luminosity is defined as a function of the number of particles per bunch, N_b, the number of bunches per beam, n_b, the beta function at the collision, β^*, the relativistic gamma factor, γ_r, the normalised transverse beam emittance, ϵ_n, the revolution frequency, f_{rev}, and the geometric luminosity reduction factor, F due to the crossing point angle, θ_c, at the interaction point [29]:

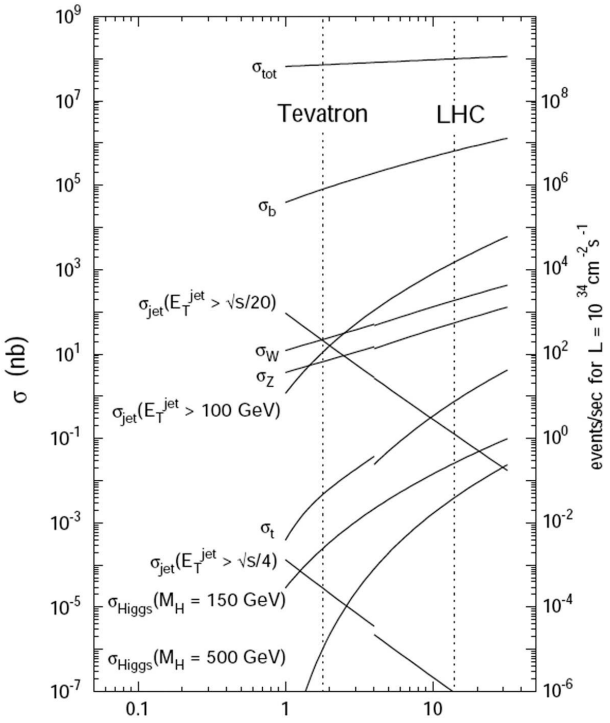

Figure 3.4: Cross sections for different processes plotted as a function of the accelerator energies, for both Tevatron and LHC. The discontinuity of the lines at $\sqrt{s} = 4$ TeV is due to the change from $p\bar{p}$ (Tevatron) to pp (LHC) collider [31].

$$L = \frac{N_b^2 n_b f_{rev} \gamma_r}{4\pi \epsilon_n \beta^*} F. \tag{3.2}$$

The LHC will start operating in two phases. At the beginning of LHC the instantaneous luminosity will be of 10^{33} cm$^{-2}s^{-1}$ (low luminosity) during the first year of operation and will later reach the design luminosity of 10^{34} cm$^{-2}s^{-1}$ (high luminosity). Intensities and emittances of the circulating beams result in a degradation of the LHC luminosity during a physics run, the main cause being the collisions themselves. The initial decay time of the bunch intensity due to this effect, $\tau_{nuclear}$, is given by the following relation with $N_{tot,0}$ being the initial beam intensity, σ_{tot} the total cross section and k the number of interaction points [29]:

$$\tau_{nuclear} = \frac{N_{tot,0}}{L\ \sigma_{tot}\ k}. \tag{3.3}$$

3.2 A Toroidal LHC ApparatuS

A Toroidal LHC ApparatuS (ATLAS) is designed to investigate particles originating from the high energy proton collisions produced by the LHC. It is a general purpose detector optimised to look for a large spectrum of physics signatures, among which some of the most popular comes from the Higgs boson and physics beyond the Standard Model. The ATLAS physics program is described according to [32] and [9] as follows:

- **Higgs search:** The main goal of ATLAS is various Higgs boson searches, from the Standard Model Higgs (H) to the Minimal Supersymmetric extension of the SM (MSSM) proposing a family of Higgs ($H^{\pm}$, h, H and A). For this the detector must discover even the most challenging signatures, which have been used as a first benchmark processes for the setting of parameters that describe the detector performance. High-resolution measurements of electrons, photons and muons, excellent secondary vertex detection for τ-leptons and b-quarks, high resolution calorimetry for jets and missing transverse energy (E_T^{miss}) are essential to explore the full range of possible Higgs boson masses.

- **SUSY search:** Another important physics search may be the search for Supersymmetric particles. To be able to observe the lightest SUSY particles stringent requirements on the hermeticity and the E_T^{miss} capability of the detector, as well as on the b-tagging at high luminosity have been included in the overall design of the detector.

- **Exotics search:** Searches for new physics will include searches for new heavy gauge bosons. W′ and Z′ could be accessible up to 5-6 TeV and would need high-resolution lepton measurements and charge identification in the p_T range as large as a few TeV.

- **Quark compositeness:** Among other signatures of new physics, several would require measurements of very high p_T jets. The signatures charcteristics for quark compositeness have been used to determine the requirements, since they would be observed as deviations in the jet cross-section from the QCD expectations.

- **Precision measurements:** Another important ATLAS task will be the precision measurements of the W and top-quark masses, gauge masses, gauge boson couplings, CP violation and the determination of the CKB unitarity triangle. Already at low luminosities the LHC will be a high-rate b and t quark factory. For these measurements, ATLAS needs to accurately control the energy scale for jets and leptons and to determine precisely secondary vertices as well as the possibility to reconstruct fully final states with relatively low p_T particles and to trigger on low-p_T leptons.

To meet these requirements ATLAS is divided into layers of several subdetectors around the beam pipe, in addition to two big magnets centered at the collision

point, as can be seen in figure 3.5, resulting in the detector performance listed in table 3.2. The resulting event (simulaterd) can be seen in Figure 3.6.ATLAS is around 46 m long, 22 m in diameter and weighs approximately 7000 tons, and has a cylindrical geometry which covers the complete pseudorapidity range of $|\eta| < 2.5$. The pseudorapidity is defined by the following relation with θ being the angle between the particle and the undeflected beam:

$$|\eta| = -\ln \tan \frac{\theta}{2}. \tag{3.4}$$

The detector coordinate system is right handed, the z-axis is pointing in the direction along the beamline, the x-axis points towards the center of the LHC ring and the y-axis upwards but being tilted 0.704 degrees from the vertical one to adjust for the tilt of the tunnel. The parameters z, ϕ, and pseudorapidity η are used to determine the position in the detector. The above listed physics searches translate into the following subdetector requirements.

Inner Detector: Providing efficient tracking of charged particles at high luminosity by the use of a solenoidal magnetic field. This results in high-p_T lepton-momentum measurements, electron and photon identification as well as b, τ and heavy flavour identification, and full event reconstruction capability at lower luminosity. It consists of three parts, the Pixel detector, the SemiConductor Tracker (SCT) and the Transition Radiation Tracker (TRT).

Calorimeter: A very good radiation tolerant electromagnetic calorimetry is needed for electron, positrons and photon identification and energy measurements (e.g. $H \rightarrow \gamma\gamma$). It is complemented by a full-coverage hadronic calorimetry for accurate jet and missing transverse energy (E_T^{miss}) measurements (e.g. SUSY particle decay identification).

Muon Tracker: Provides high-precision muon momentum measurements outside the Calorimeter by the use of the magnetic field generated by the air-core toroidal magnets. It has the capability for accurate measurements at the highest luminosity using the external muon spectrometer alone (e.g. $H \rightarrow 4\mu$).

Trigger System: This system ensures the triggering and measurements of particles at low-p_T thresholds, providing high efficiencies for most physics processes of interest at the LHC.

3.2.1 Inner Detector

The Inner Detector (ID) aims to provide high precision measurements with fine granularity detectors by reconstructing charged particles traversing the detectors in the 2 T magnetic field provided. To achieve this, the Inner Detector is divided into three subdetectors as can be seen in figure 3.7, which combines high resolution elements at inner radii (Pixel and SCT) with continous tracking elements at outer radii (TRT). The ID physics requirements are the following:

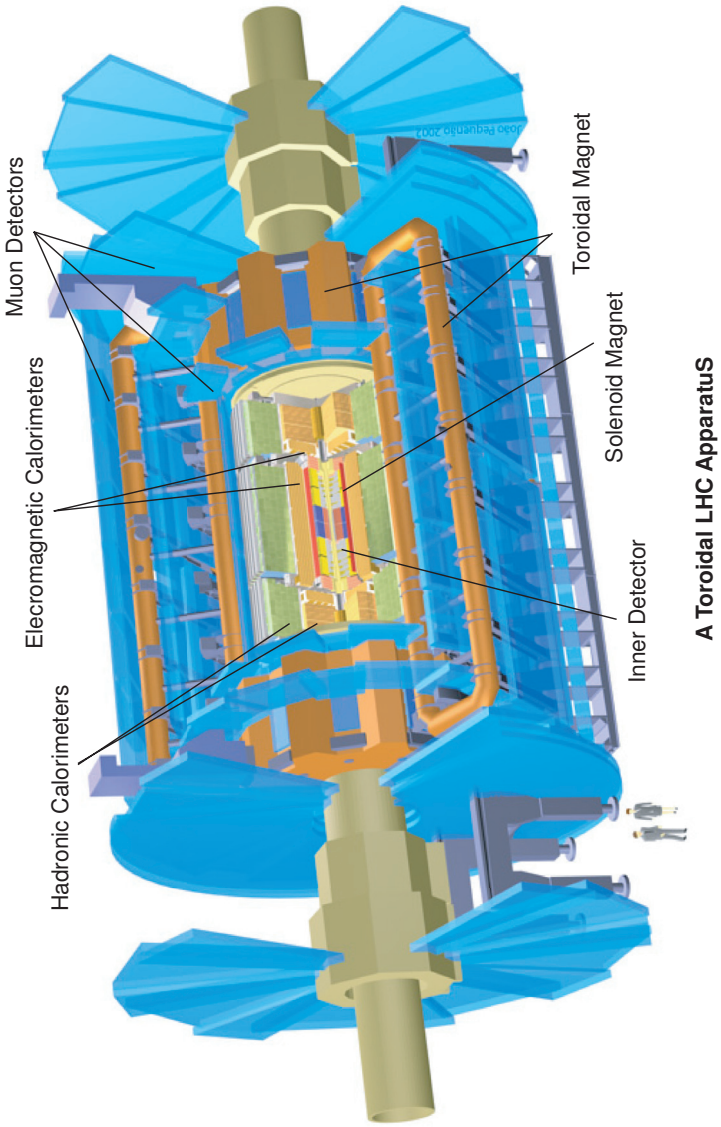

Figure 3.5: The ATLAS detector [8]. The Inner Detector is situated closest to the beam pipe inside the solenoid magnet and consists of three detector parts, the TRT, the SCT and the Pixel detector. Outside the solenoid but inside the toreoidal magnet are the calorimeters, first the electromagnetic Liquid Argon calorimeter (LAr) and then the hadron calorimeter TileCal. Outside of all these detectors is the muon spectrometer.

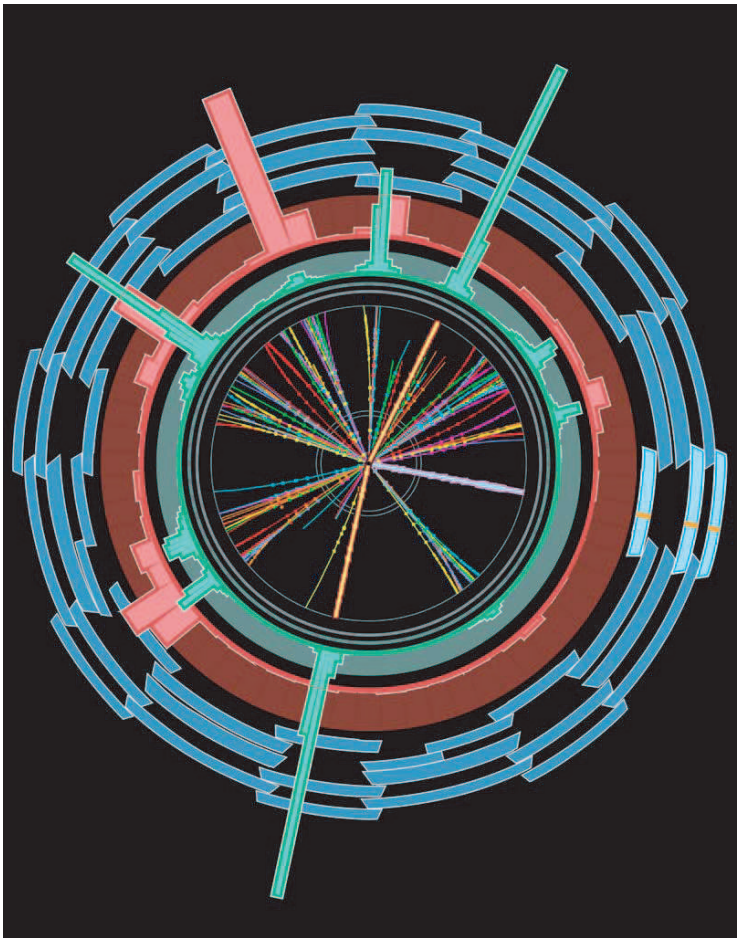

Figure 3.6: ATLAS simulation of one mini-black hole event, viewed along the beampipe [33]. The black centre shows tracks in the Inner Detector, which has been magnified with respect to the other detectors. The thick yellow lines represent the two electrons in the decay of this event. The green band shows the electromagnetic calorimeter and the red area the hadronic calorimeter. The corresponding histograms show the energy deposited by traversing particles. The outer blue area shows the muon spectrometer were one event has been added by hand to show a muon track.

Detector sub-system	Performance
Tracking (Si + transition radiation detector)	$\sigma/p_T \simeq 5 \times 10^{-4} p_T(\mathrm{GeV}) + 1\%$
EM calorimeter (Pb + liquid Ar)	$\sigma/E \simeq 10\%/\sqrt{E(GeV)}$
Hadronic barrel calorimeter (steel + scintillator)	$\sigma/E \simeq 50\%/\sqrt{E(GeV)}$
Hadronic end-cap calorimeter (Cu/W + liquid Ar)	$\sigma/E \simeq 60\%/\sqrt{E(GeV)}$
Muon spectrometer (air toroidal magnet)	$\sigma/p_T \simeq 10\%$ at $p_T \sim 1$ TeV

Table 3.2: Basic performance characteristics of the ATLAS detector [34].

- Precise position measurements to be able to identify particle trajectories, perform momentum measurements and particle identification. Charged particle identification should be provided up to 500 GeV/c.
- Discrimination between electrons and photons in combined measurements together with the electromagnetic calorimetry
- Fast identification of individual particles in dense jets, where the calorimeters cannot resolve them. The electronics must be able to tag bunches which cross every 25 ns.
- Momentum reconstruction in a broad momentum range, especially for the regions where the calorimeter alone cannot perform sensitive measurements.
- The detectors need to be radiation tolerant to be able to survive the ten years of operation. The main fluences will be of charged and neutral particles liberated from the primary interactions and from the walls and the calorimeter.
- The ID material must be minimised to avoid particle scattering, introducing inaccuracies in the measurements of momentum and energy as well as limiting the calorimeter performance.

The ID is the smallest of the ATLAS subdetectors with its 2.3 m in diameter and 7 m length, but it is larger and more complex than similar detectors built in the past. All of the three inner detectors contain three mechanically separated parts, a barrel section ($\pm$ 80 cm in z) consisting of one or more cylindrical layers and two identical end-caps, in which the detector surfaces are perpendicular to the beam line. In total this covers $|\eta| = \pm$ 2.5. The spatial resolutions in the r-ϕ direction are < 14 μm/layer in the Pixels [35], 16 μm/layer in the SCT [9] and 170 μm resolution for charged particle tracks in the TRT [9]. The expected radiation is shown in table 3.3. Because of the high fluences the innermost Pixel layer, the B layer, is built to be exchanged after approximately three years of operation. The distribution of mass in the Inner Detector can be seen in figure 3.8 shown in radiation lengths.

Pixel Detector

The Pixel detector provides three high precision and high granularity space points as close as possible to the interaction point [36, 37]. It is based on the semiconductor

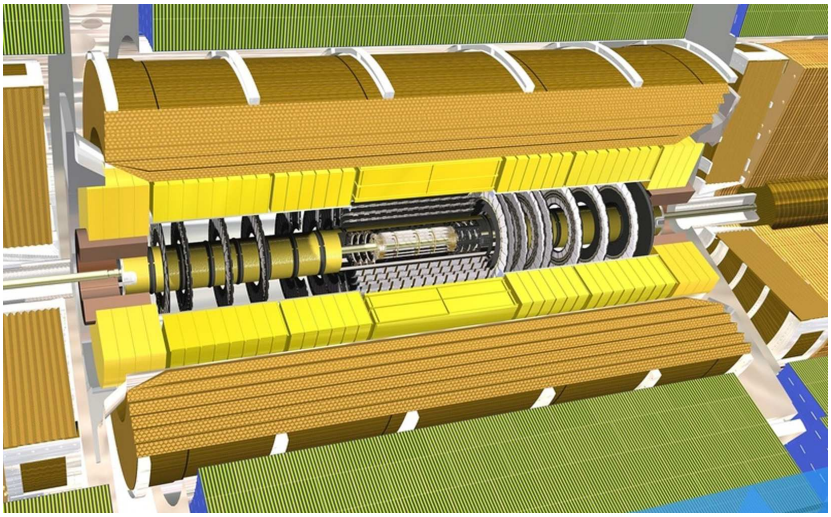

Figure 3.7: A cross section of the Inner Detector consisting of three subdetectors, the Pixel detector closest to the interaction point, then the Semi-Conductor Tracker and outermost the Transition Radiation Tracker [27].

Position	Typical Value / Maximum Value	Typical Value / Maximum Value
	1MeV eq. neutron fluence 10^{13} cm^{-2}/year	Ionising dose kGy/year
Pixel	5 / 50	30 / 300
SCT	1.5 / 2	4 / 10
TRT	0.7 / 1	2 / 6

Table 3.3: The expected fluence and ionisation dose for the three ID subdetectors [36]. Recently, updated and more detailed values have been published in [38].

technology as described in chapter 2.2. The purpose of this detector is to provide advanced pattern recognition in high multiplicity environments, excellent transverse impact parameter resolution and very good 3D-vertexing capability in addition to excellent b-tagging and b-triggering capabilities. The full acceptance permits the determination of the impact parameter resolution and the ability to find short lived particles (e.g. b-quarks and τ-leptons). To achieve three pixel hits in the full rapidity range, the detector is composed of three barrels (radial positions 5.5 mm, 88.5 mm and 122.5 mm) and three end-cap disks on either side (radii of 11 to 20 cm). The distance of the B-layer from the collision point is set by the beamline vacuum system.

A total of 1 744 Pixel modules populates the barrels and the disks. The modules are overlapped to give hermetic coverage. Each Pixel module consists of a silicon sensor bump bonded to a 16 front-end chips un-packaged flip-chip assembly permit-

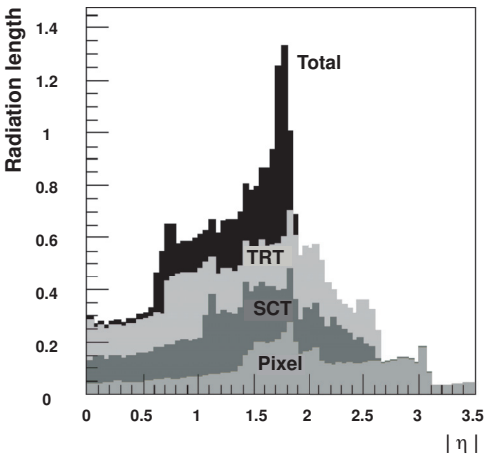

Figure 3.8: The radiation length of the different ID subdetectors as a function of $|\eta|$. The total radiation length has a peak at around $|\eta| = 1.7$, which is due to the accumulation of material in the services to the barrels [9].

ting the sensor readout. Each sensor is a 16.4 × 60.8 mm silicon wafer containing 46 080 pixels, which gives a total of around 80 million pixels for the three barrel layers. The pixel size is limited by the smallest cell available during production, which was 50 μm × 400 μm The front-end electronics of the Pixel detector dissipates more than 15 kW into the detector volume (0.8 W/cm^2) which is removed by evaporative cooling.

SemiConductor Tracker

The SCT detector is the main topic of this thesis. It is based on semiconductor technology (as described in 2.2) and consist of four cylinders around the interaction point and 2 × 9 disks at each end-cap. This detector will provide momentum measurements, impact parameters, vertex position and good pattern recognition. A detailed description of this detector and its performance will be the topic of chapters 4-9.

Transition Radiation Tracker

The TRT, is the outer tracker of the ID. It will provide high performance measurements at high occupancy and high counting rate, which permits a continuous tracking within the detector and a good pattern recognition. The TRT contributes to the accuracy of the momentum measurements and provides discrimination between electrons and hadrons.

The TRT, is a combined straw tracker providing drift time measurements and a transition radiation detector (see section 2.2). It provides on average 36 two-dimensional measurement points for charged particle tracks within $|\eta| < 2.5$ and with $p_T > 0.5$ GeV. Each straw is a proportional drift tube with a diameter of 4

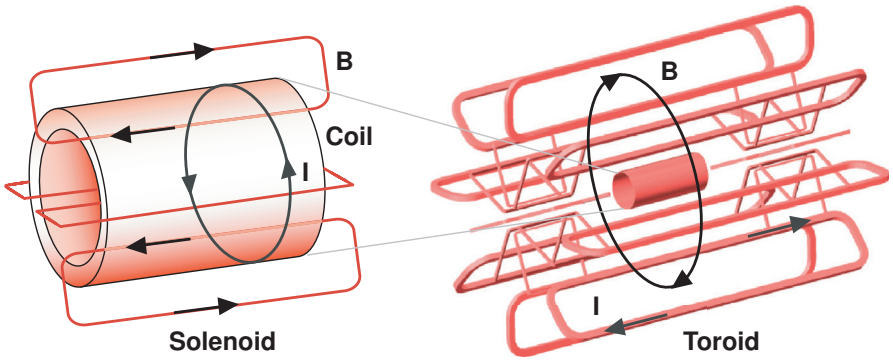

Figure 3.9: Left, the magnet solenoid situated around the Inner Detector with a magnetic field parallel to the beamline [39]. Right, the barrel toroid as part of the muon tracker with a magnetic field perpendicular to the beamline.

mm filled with a 70%Xe-27%CO_2-3%O_2 gas mixture with a gain of 2.5×10^4 and surrounded by a polypropylene/polyethylene fibre radiator in between the straws. Ultra-relativistic charged particles produce transition radiation photons (X-rays) in the passage from the polypropylene to the CO_2 gas which are detected by the straw tracker.

The barrel part of the TRT consists of a total of 52 544 axial straws, contained in modules, in the region of 56 - 107 cm radius. Each barrel module has between 329 and 793 axial straws of about 150 cm length. The straws have been divided in the middle to reduce occupancy by having readout at each end. The end-caps cover the region of radius between 64 - 103 cm and 48 - 103 cm, for the inner and outer end-caps respectively. The end-caps consist of 18 wheels with a total of 319 488 radial straws read out from the outer radius. The total number of electronic channels is 420 000, which are read out by custom made front-end electronics.

3.2.2 Magnets

Two large superconducting magnets permit the measurements of the momentum of charged particles: the solenoid and the toroidal magnet. The central solenoid is surrounding the Inner Detector and provides a 2 T field at the centre and 2.6 T at the windings. It differs from other magnet systems by being situated inside the electromagnetic calorimeter. This has been done to limit the mechanical and technological constraints of the calorimeter and to reduce the lateral spread of the electromagnetic showers. With this structure however, the magnet needs to minimise its material not to decrease the detector performance by introducing additional showers starting before the active part of the calorimeter.

The toroidal magnet generates the magnetic field needed for the Muon Spectrometer and consists of one Barrel Toroid (BT) and two End-Cap Toroids (ECT). Both types consists of eight coils (each in separate cryostats) providing 3.9 T ($|\eta| \leq 1.3$)

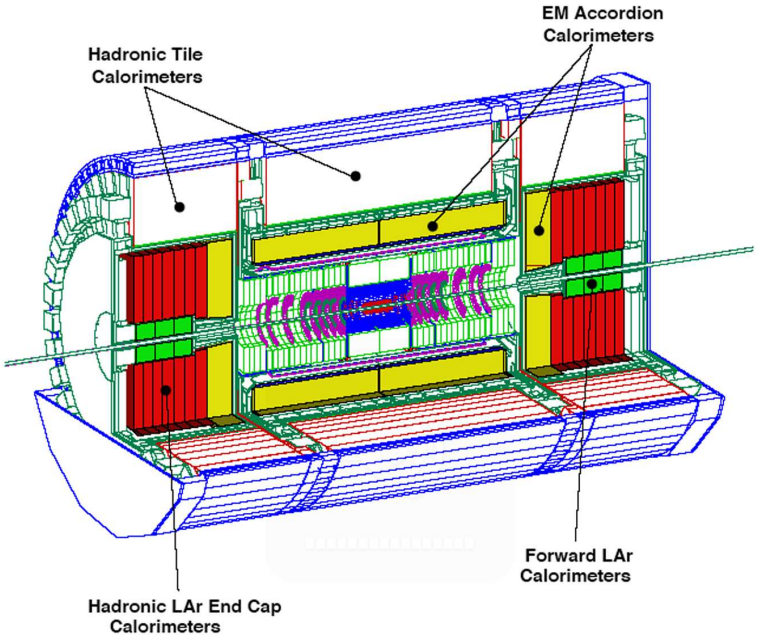

Figure 3.10: The complete calorimeter structure. Closest to the interaction point is the EM calorimeters, outside in the end-cap region are the LAr calorimeters and around all of them are the hadronic Tile calorimeters [40].

and 4.1 T ($1.6 < |\eta| < 2.7$) fields, almost perpendicular to the incident particles, for the BT and the ECT respectively. The two ECTs are inserted into the BT at each end to provide radial overlap between $1.3 < |\eta| < 1.6$ where the bending power is lower. Figure 3.9, left side, shows a drawing of the solenoid magnet and the barrel toroid, displaying also the current flow and the magnetic field lines. Both types of magnets have to be cooled to 4.5 K during operation. The outer dimensions of the magnet system are 26 m in length and 20 m in diameter.

3.2.3 Calorimeter

Situated directly outside the solenoid are the calorimeters. The innermost layer consists of an Electromagnetic CALorimeter (ECAL) made of liquid argon, whereas the outer layers consist of hadronic calorimeters, the Tile Calorimeter (TileCal) and the Liquid Argon calorimeter (LAr) (see figure 3.10). The calorimeter requirements are to provide particle identification, energy resolution and direction measurements in addition to trigger functionality.

The ECAL covers the pseudorapidity range $|\eta| < 3.2$ ($|\eta| < 1.475$ for the barrel and $1.375 < |\eta| < 3.2$ for the endcap) and provides electron reconstruction from 102

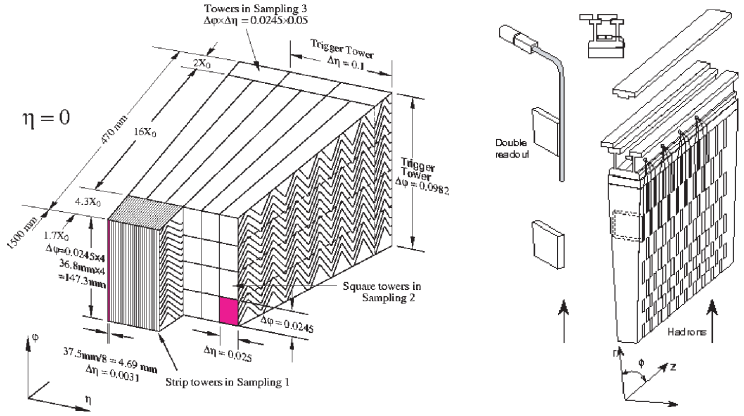

Figure 3.11: Left, an ECAL module consisting of lead-LAr units with accordion shaped kapton electrods. Right, a TileCal module made of iron plates and scintillating tiles. Both from [40].

GeV up to 5 TeV and good energy resolution $\Delta E/E$ in the range 10-300 GeV as well as θ measurements (spread) of the showers and good particle-jet discrimination. Electrons and photons are fully absorbed by the electromagnetic calorimeters. The ECAL is a lead-LAr detector with accordion shaped kapton electrodes and lead absorber plates as can be seen in figure 3.11. The EM calorimeter is $> 24\ X_0$ in the barrel and $> 26\ X_0$ in the forward section.

The hadronic calorimeter covers the range $|\eta| < 5$ and consists of two main detectors. For $|\eta| < 1.6$ it is covered by the Tile Calorimeter. It is a sampling detector which uses iron plates (14 mm) as the absorber material and scintillating tiles (3 mm) as active material (see figure 3.11). Both sides of the scintillating tiles are read out by wavelength shifting fibres (WLS) into two separate photo multiplier tubes (PMT). The LAr Calorimeter covers the range of $1.5 < |\eta| < 4.9$. It consists of a barrel and two end-cap sections built out of different thickness of copper plates and equipped with three electrodes which split into four drift spaces. The thickness of the calorimeters is important for its design. It has to provide good containment for hadronic showers and reduce punch-through into the muon system. Hadron showers are almost absorbed by the hadronic calorimeter.

3.2.4 Muon Tracker

The muon tracker takes up the largest part of the ATLAS volume and is based on the principle of magnetic deflection of muon tracks in the large toroid magnets. In the barrel region the tracks are measured in three cylindrical layers around the interaction point whereas in the end-cap region the chambers are installed vertically. The muon tracker consists of four different chamber technologies; Monitored Drift

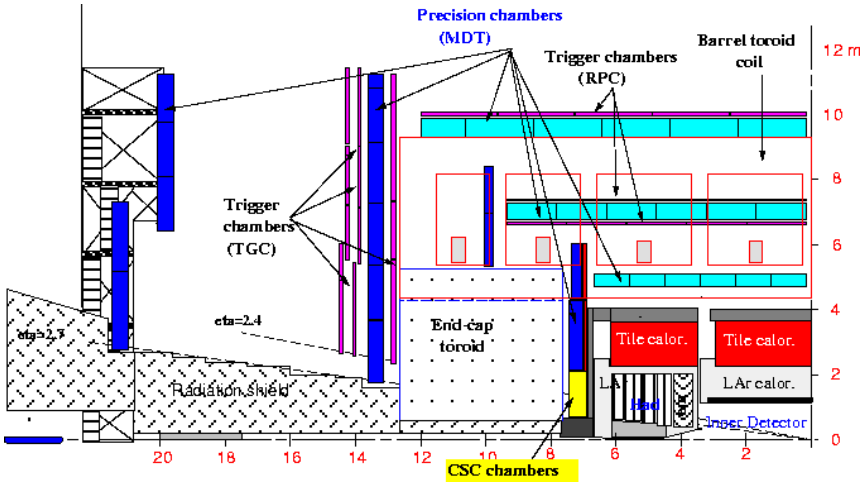

Figure 3.12: The muon detector showing, left, a vertical cut and right, a horizontal cut parallel to the beamline. Both the precision chambers (MDT, CSC) and the thinner trigger chambers (RPC, TGC) are seen [41].

Tubes (MDT) and Cathode Strip Chambers (CSC) for the tracking and Resistive Plate Chambers (RPC) and Thin Gap Chambers (TGC) for the trigger functions (see figure 3.12). The barrel region covers the range $|\eta| < 1$ and consists of three cylinders of radii 5, 7.5 and 10 m. The end-cap covers $1 < |\eta| < 2.7$ and contains four disks at distances 7, 10, 14 and 21-23 m from the interaction point.

The MDT consists of 370 000 drift tubes grouped in 1 200 chambers. Each element is an aluminium tube with 30 mm diameter and a 400 μm wall thickness centered around a 50 μm diameter W-Re wire. The tubes are filled with a non-flammable mixture of 93% Ar and 7% CO_2 at 3 bar, giving a drift time around 700 ns. The CSC detectors are multiwire proportional chambers with cathode strip readout orthogonal to the anode wires. The anode wire pitch is 2.54 mm, the cathode pitch 5.08 mm and the chambers are filled with a non-flammable mixture of 20% Ar, 50% CO_2 and 20% CF_4, which results in an electron drift time of 30 ns.

The RPC is a gas detector and the simplest unit consists of a narrow gas gap between two parallel resisitive bakelite plates separated by insulating spacers. The gas used is based on $C_2H_2F_4$ with traces of SF_6 and primary ionised electrons are multiplied into avalanches by application of a $\sim$ 4.5 kV/mm electrical field. The trigger chamber is made of two such layers each read out by series of pick-up strips one parallel and one orthogonal to the MDT wires. Similar to MWPCs, the TGCs provide signals from the anode wires parallel and orthogonal to the MDT wires, however the anode wire pitch is larger than the cathode-anode distance.

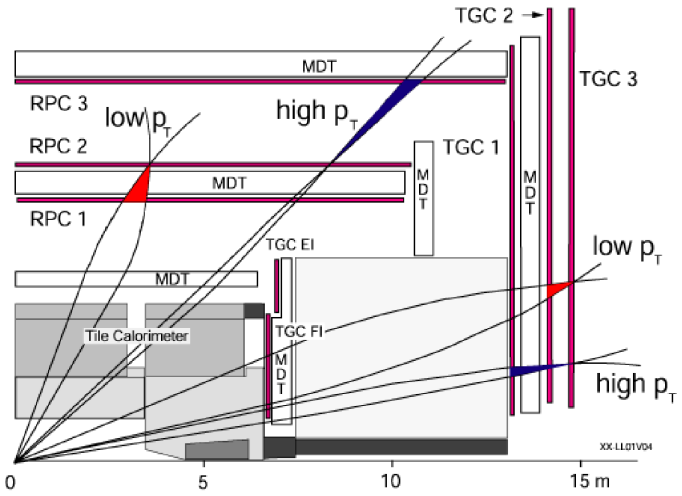

Figure 3.13: Left, the Level 1 muon trigger scheme [42]. The figure shows how the muons will be detected by the various trigger chambers, RPC1-3 in the barrel region and TGC1-3 for the end-cap region.

3.2.5 DAQ and Trigger System

The LHC is a challenging environment for trigger decisions, due to the 40 MHz bunch-crossing rate and the 10^8 read-out channels. In ATLAS, information from both the dedicated trigger chambers of the muon spectrometer (seen in figure 3.13) and from the calorimeters is used. The goal of the ATLAS trigger system is to provide muon selection with $p_T > 6$ GeV at low luminosity and $p_T > 20$ GeV at high luminosity and at a pseudorapidity coverage adequate for Higgs and B-physcis, $|\eta| \sim 2.4$. The calorimeter trigger on isolated electromagnetic clusters with $E_T > 30$ GeV, high energy hadronic jets or large missing E_T. To meet the trigger requirements, three different trigger system are needed for the online event selection, as can be seen in figure 3.14.

The Low Level 1 trigger (LVL1) has to accept a maximum data rate of 40 MHz from the LHC collider. The trigger scheme is based on coincident events in several detectors with a time resolution lower than the bunch crossing interval. This is necessary for the MDT chambers since the 25 ns is much smaller than the detector drift time [43]. The LVL1 selects bunch crossings according to the selection criteria and determines the Region of Interest (RoI) which contains position, momentum and energy data. The output rate of the LVL1 trigger is of around 75 kHz at initial luminosities but can be upgraded to 100 kHz.

The High-Level Trigger system (HLT) consists consists of both the Low Level 2 trigger (LVL2) and the Event Filter (EF). The LVL2 trigger is designed to reduce the 100 kHz data rate of the LVL1 trigger to $\sim$ 1 kHz. To achieve this the LVL2 analyses the data from the triggering detectors, including tracking information from

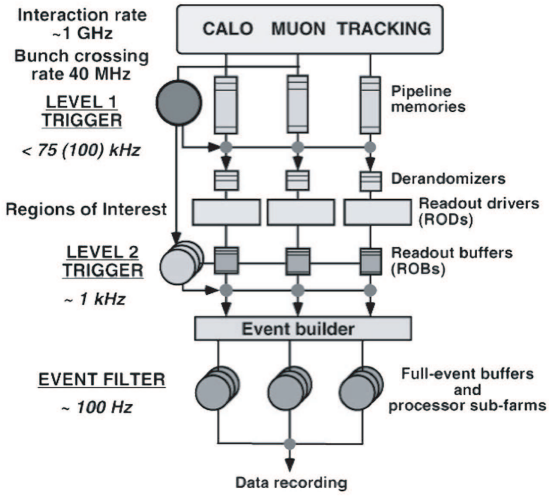

Figure 3.14: The ATLAS Trigger DAQ (TDAQ) system showing the software and hardware components needed to run ATLAS, including the three levels: LVL1, LVL2 and EF [42].

the Inner Detector in the RoI.

The EF gets data at the LVL2 trigger rate of around 1 kHz and makes a final selection of events. This reduces the event rate further to $\sim$ 100 Hz. The selected events are written to mass storage at $\sim$ 100 MB/s.

Conclusion

The development of the ATLAS detector has been challenging the different technologies in use to provide one of the most advanced and complex detectors of today. Its complexity and functionality will provide new opportunities to perform precision measurements of the Standard Model and to search for physics beyond its reach. As well as being an important tool in the search for the Higgs particle, covering a large range of signatures, it will also focus on SUSY searches and searches for exotic particles among others. Weather these theories will be confirmed or dismissed it is clear that the ATLAS detector, when operational, will be an important tool for this work since it will be able to detect particles produced by the LHC, which almost from the start will be within a new and yet unknown energy range. Even though my work has been on a small part of the ATLAS detector, it has been a privilege to be present in a time of construction and seeing so many parts being successfully completed. New detector designs and techniques are all about to be finished, tested and assembled, and the final ATLAS detector starts to take shape. First indications of the performance are positive and preparations for the first cosmic radiation runs are being planned. The next few years will be an exciting time both in finishing the detector and successively to start the search for new physics.

Both the possibilities to work on the largest detector under construction today

within one of the most challenging technological environments as well as physics simulation studies of the ATLAS performance serves as the two main motivations for work of this thesis and will be presented in Part II and III. Part II describes the construction of one of the ATLAS sub-detectors, the SCT. The construction phase, from the smallest unit (module production in the SCAND cluster, chapter 5) to the final assembly of the final SCT cylinders (Barrel Macro-Assembly, chapter 9) will be described. In addition, the construction of support hardware for the SCT detector such as power and cooling as well as the development of a detector control system will be described (chapters 6 and 7). Tests and electrical test results of both barrel and end-cap modules, with a test beam and without, will be presented (chapters 5, 8 and 9). Part III will discuss the possibilities to discover new physics by ATLAS, in particular the detection of extra neutral gauge bosons occurring in several GUT models. This particle is highly interesting since it provides a very clean signal. The ATLAS simulations gives a first estimate about the Z' mass reach and how theoretical model discrimination can be made. Together both parts presents a voyage throught the construction and operation of a slice of ATLAS, taking as example the SCT detector and the Z' particle.

Part II

ATLAS SCT Development

4

The SemiConductor Tracker

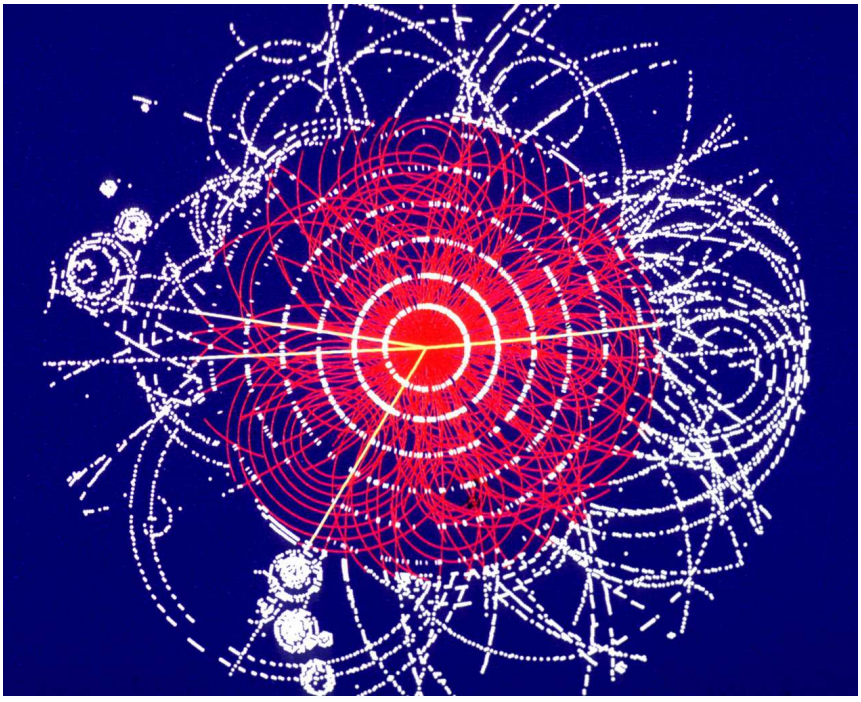

Simulated Inner Detector Tracks (H $\rightarrow$ 4 μ) [8].

Introduction

The main task of the SCT detector is the tracking of charged particles close to the interaction point. Being one of the innermost detectors in ATLAS imposes strong constraints on the construction and performance of this detector. It needs to contain as little material as possible to minimise the influence on particles which will be examined by outer sub-detectors and it needs to be radiation hard since the radiation levels close to the interaction point are very high.

This chapter presents the choice of technology and the detector design. It also describes the hardware requirements, components and the read-out chain of the SCT detector, which are the basis for the work presented in this thesis. Finally, it describes some of the main detector electrical tests needed to accept and configure the SCT detector modules. It also acts as an introductory chapter to part II of this thesis. Most of the technology and development choices described in the successive chapters are based on the requirements described in this chapter and will be referred to as such.

4.1 The SCT Detector

The ATLAS SemiConductor Tracker is one of the largest silicon systems to be completed during the next few years. In comparison with previous semiconductor trackers, for example at LEP and at Tevatron, the increase in scale is significant. For this reason, a serious effort was needed both to produce component silicon modules and to assemble them into larger detector parts. As described by the technical design report [36] the overall size of the detector is more than 10 times larger than earlier similar experiments. The luminosity experienced by the SCT detector is around 10^{34} cm^{-2}s^{-1}, which is 10-20 times higher than previous applications, and the active silicon area of ~ 63 m^2 is more than 50 times that of any existing vertex detector. Another new constraint is that there will be few opportunities to replace the central tracking layers during the 10 year expected lifetime of the detector, and in addition access to detector for repairs will be restricted.

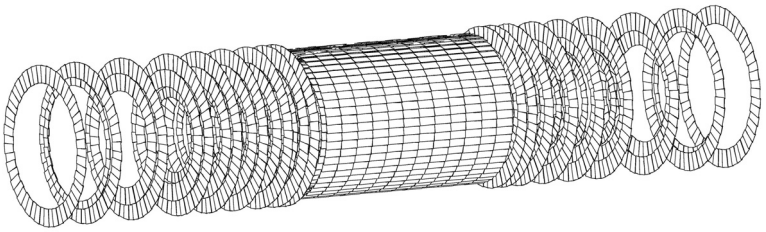

Figure 4.2: The SCT detector consists of four concentric barrels centred around the interaction point and nine disks at each forward region.

4.1.1 Physics Requirements

As introduced in chapter 3, the SCT detector is designed to provide four space points per charged particle track up to a pseudo-rapidity of ±2.5. For this to be possible, there are several demands set by the physics, which give the framework for the development of the detectors themselves and their on- and off- electronics. The following list summarises some of the most important physics criteria for the ID sub-detectors [36]:

- Minimum 6 tracking points from SCT and Pixel to be able to reconstruct isolated leptons of $p_T < 5$ GeV at an efficiency of $|\eta| < 2.5$.
- Efficiency > 95% over the lifetime of the experiment for good tracking and trigger efficiency.
- r-ϕ resolution of ~ 20 μm to meet the $(\Delta p_T/p_T) < 0.3$ requirement at $p_T = 500$ GeV.
- 2-track resolution < 200 μm at R = 30 cm to minimise track losses in b-jets.
- Radiation length < 0.2 X_0.

To meet these Inner Detector requirements, the SCT has been constructed, to comprise four co-centred barrel layers with radius between 30 and 52 cm, and nine disks in the radial range between 26 and 56 cm, as shown in figure 4.2 and listed in table B.1 (in annex). The barrels are numbered from B3 to B6 and the disks from D1 to D9 of each end-cap (A or C). More detail about the barrel composition will be described in chapter 9. The barrels and end-cap structures are populated with a total of 4 088 SCT modules, which will be described in section 4.1.5. Each modules consists of a sandwich of four silicon sensors ordered into two planes with a hybrid for electrical read-out. A detailed description of the barrel and endcap modules can be found in [44] and [45].

4.1.2 Sensor Properties

The SCT detector is made with silicon microstrip detector technology where the main challenges are the radiation damage and scale. As can be seen in figure 4.3, the SCT sensors consist of a bulk silicon material (n-type) with aluminium read-out strips over the p-doped areas. The other side of the silicon is doped with n-type material covered by aluminium. The sensors are passivated on both sides using silicon oxide (not shown in the picture). By applying sufficient bias voltage between the aluminium strips and the backplane of the detector, the doped region is depleted. When a charged particle passes through this depleted region, electron-hole pairs will be produced and collected by the read-out electronics.

The size of the barrel sensor is 3.6×64.0 mm^2 with an active area of 61.6×62.0 mm^2, which is the maximum size that can be produced from a four inch wafer. The strips, in total 768, are 18 μm wide and 62 mm long with 80 μm pitch, and permit

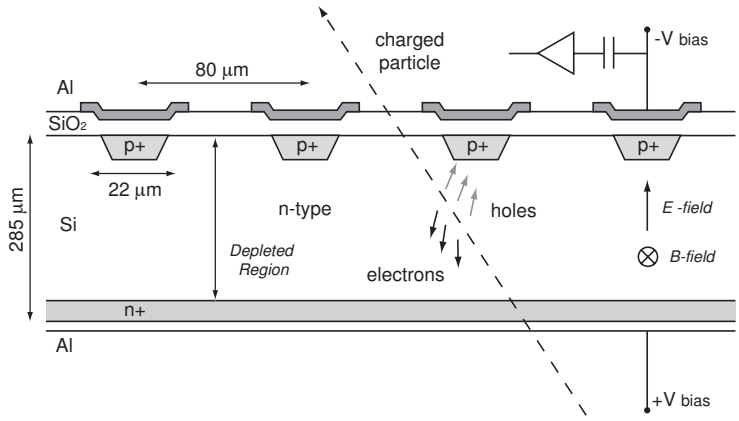

Figure 4.3: The SCT silicon sensor consists of a silicon n-type bulk material with p-doped strips on one side, which are used for charge collection (electrode) while the other side is doped with n+ charges (cathode). By applying a bias voltage across the sensor it becomes depleted. When a charged particle passes the depleted region, electron-hole pairs are produced and the charge is collected.

the read-out of the sensor. The end-cap sensors are similar but made with five different wedge geometries with a pitch equal to 80 μm on average. The thickness of the detector should not exceed 285 $\pm$ 15 μm with a uniformity of 10 μm. Due to the 2 T solenoid magnetic field, the barrel sensors needs to be tilted $\sim 11^\circ$ to avoid an increase of drift time of the electron-hole pairs due to the Lorentz effect (see figure 4.4).

The voltage necessary to deplete the sensor of this thickness will be typically between 40 and 100 V. It has been decided that 150 V will be the starting operating voltage, since this value is considered to be sufficiently above the limit to be sure that all sensors are totally depleted [46]. The leakage current requirements for unirradiated modules has to be less than 20 μA per sensor, or 80 μA per module, measured at 350 V [47]. According to [36], the corresponding maximum bulk leakage current for irradiated modules at -7°C should be less than 500 μA and not exceed 2 mA, with a maximum of 2 μA per channel.

4.1.3 Radiation Effects

A constraint on the SCT operation conditions comes from attempting to minimise the radiation damage from the LHC, as introduced in chapter 3. Even though the estimated annual integrated luminosity of 10^{41} cm^{-2} includes a 50% safety factor, taking into account the uncertainty of the actual dose, special care has been taken for the detectors to be sufficiently radiation resistant. Figure 4.5 shows the expected fluences for the Inner Detector as of [38]. Nonetheless, the radiation effects on the

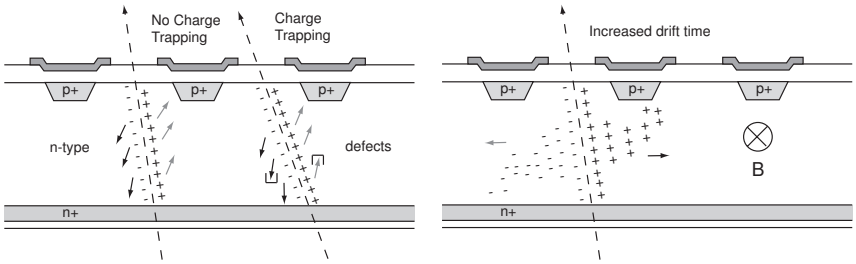

Figure 4.4: Left, charge trapping will change the effective doping. Right, the magnetic field will increase the drift time of the electron-hole pairs in the silicon (Lorentz effect). For this reason the SCT sensors will be tilted ($\sim 11^{\circ}$) in their final position to minimise the collection time.

silicon sensors are expected to induce a continuous degradation of the sensors properties. The main effects expected, which are largely independent, are the following:

- A change in the effective doping over time, which results in a type inversion (from the initially n-type bulk material to p-type).
- A decrease in charge collection efficiency (charge trapping).
- Increase in leakage current.

Radiation will increase the trapped charge on the surface, which results in higher electric fields and breakdown at lower voltages. It will also increase the number of bulk defects, which will again increase the leakage current and thus change the effective doping. The changes to the doping will require higher bias voltage to deplete the sensor. Additional charge trapping will result in a signal degradation. According to [48], the relation between the effective silicon dopant concentration and the depletion voltage is given by the following relation:

$$|N_{\text{eff}}| = \frac{2\ V_{\text{dep}}\ \epsilon_o\ \epsilon_s}{e\ d_{\text{dep}}^2}, \tag{4.1}$$

where, ϵ_o, is the permittivity of space, ϵ_s the relative dielectric constant, d_{dep} the width of the depletion layer and e the electron charge, and where N_{eff} is dependent on time, radiation history, fluences and silicon temperature. After 10 years of operation the change is so dramatic that type inversion is expected and an increase in depletion voltage from the initial value of 150 V up to the design limit of 500 V may be required. Typical IV curves will be shown in chapter 5 and 8. Current sensors are designed to avoid current breakdown, mostly due to microdischarge, below 500 V.

The leakage current not only depends on the radiation effects and microdischarge but also on the detector temperature. An increase in leakage current results in an increased sensor temperature which again increases the leakage current. If this thermal runaway is not controlled, the current can increase rapidly and damage the detector.

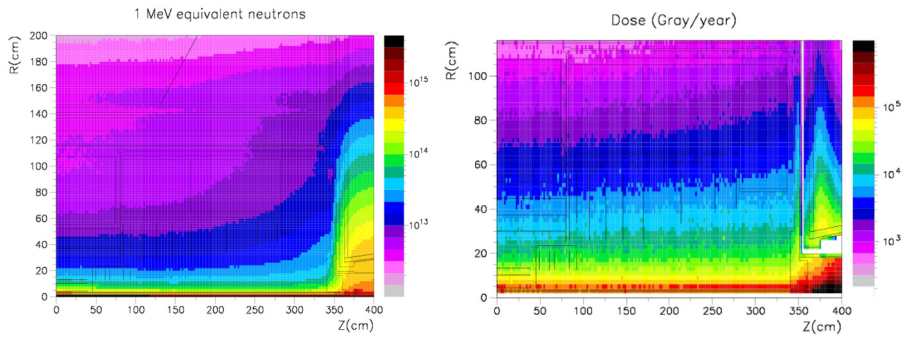

Figure 4.5: Left, the yearly 1 MeV neutron equivalent fluences and right, the annual dose in Gray/Year. Both plots assumes a time of 10^7 s at high luminosity [38].

4.1.4 Electrical Read-out

The silicon sensors are read out by a binary read-out architecture due to moderate spacial resolution requirements as described in [49]. It permits significant data reduction, which results in a reduction of material required for the data transmission and simplified off-detector readout electronics. It was also the most cost-effective implementation meeting the physics requirements. The module read-out is performed by 12 ABCD3TA ASICs, which are manufactured in the radiation hard DMILL process and mounted on a copper/kapton hybrid[1] [50]. Each chip reads out 128 strips (channels). Due to the overall ATLAS requirements, the read-out speed is defined by the $\sim$ 100 kHz trigger rate of the level-1 trigger, which permits the tracking data to be used for level-2 trigger decisions [43].

Figure 4.6 shows the principle of the signal read-out. The analogue signal collected by one of the silicon strips is transmitted to the front-end integrated circuits, which will amplify and shape this signal before comparing it to an externally adjustable ("trimmed") threshold value. The preamplifier uses a bipolar transistor as the input device. The original single-ended signal is converted to a differential one before entering the discriminator circuit. The trimming consists of comparing the signal to a common discriminator threshold (one per chip) by using a single 8-bit DAQ in addition to a specific 4-bit trim DAQ which compensates for channel to channel variation by applying individual threshold corrections. If the signal is above the adjusted threshold value, it goes trough an analogue edge-sensing part of the front-end which suppress the trailing edges and reduces the pulse length to one clock cycle. After this, the signal is transmitted to the 132 cells deep binary pipeline where it will be buffered.

The buffer output will be released on ATLAS L1 trigger request (L1A), which initiates the read-out of this specific beam crossing to a de-randomising buffer which

[1]Six layer copper-polymid flex circuit on a substrate

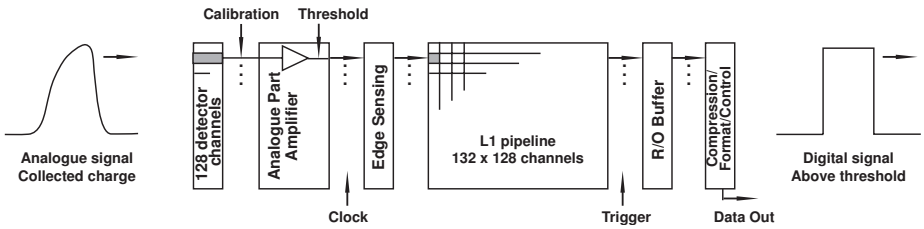

Figure 4.6: The on-detector read-out chain. The analogue signal is converted to a digital signal by being amplified, compared to a threshold value, edge sensed, passed through a pipeline, buffered, formatted and compressed before being transmitted to the off-detector read-out system.

can store up to eight events. If the data is valid, it is compressed and formatted and transmitted to the off-detector electronics for further processing. The compression software acts as a filter and only events which passes the set compression criteria (e.g. any event, X1X, 01X[2]) will be read out.

In addition to the 12 chips, each hybrid consists of surface-mounted components (connectors, resistors, capacitors) including one (end-cap) or two (barrel) thermistors, which permits module temperature reading during operation. If any chip fails, the redundancy scheme permits this chip to be bypassed. The calibration of the detectors are made by the use of a dedicated calibration circuit. By injecting a known charge to the amplifier, the performance of the detectors can be tested. A mask permits to shut off individual channels, which are subject of some hardware defect (e.g. bonding failure) or which show too high noise or occupancy levels.

The detector information is transferred to and from the back-end data acquisition system via optical communication, chosen because of its low mass and lack of electrical pick up. It has to be radiation resistant since some of the fibres are inside the detector volume. The clock (40 MHz) and command signals are transmitted to each individual module and data is read back using two optical streams (link0 and link1), one for each detector plane. Electrical and optical signals are converted by means of Digital Optical Receiver Integrated Circuit (DORIC4) and VCSL[3] Driver Chip (VDC) ASICs. The redundancy is provided by transmitting all data from the 12 chips via one link only, thus allowing for the failure of read-out components for either side. Clock and control redundancy is provided by an electrical connection between neighbouring modules. Any module can be clocked and controlled from its neighbour should its own clock and control link fail.

The low voltages and detector bias voltage are routed to the detector using conventional twisted pair cables outside the detector volume and a thin aluminium on kapton technology within the detector volume, where the need to minimise the mass while maintaining an acceptable voletage drop is critical. These low mass

[2]X stands for any signal, 0 for no hit and 1 for hit. A hit is defined as a value above threshold.
[3]Vertical Cavity Surface Emitting Laser diode

tapes (LMT) are connected to a module via a dogleg[4] for the barrel or directly to the hybrids for the end-caps. Each detector module has independent power paths to make the system more robust against single failures and to allow for individual adjustments of the powering of the modules, which will be required due to variations in the received radiation dose. The SCT grounding is "groundless" [51, 52], which provides a maximum of isolation between modules and minimises ground loops and pick-up.

Electronic noise is one of the main problems when it comes to signal detection. The noise occupancy, or noise hit rate, needs to be less than 5×10^{-4} for it not to affect the data transmission rate, pattern recognition or track reconstruction. The corresponding noise level, from the front-end electronics, should be less than 1500 ENC[5] before irradiation and the channel-to-channel threshold matching. After an irradiation of 3×10^{14} 24 GeV protons per cm^2 the accepted noise level is of 1800 ENC. This corresponds to a gain value of around 50 mV/fC. The noise levels are also dependent on the temperature and increases with ~ 5 ENC/$^\circ C$ according to [53].

4.1.5 Module Description

As already mentionned, due to different sensor geometries the SCT detector consists of several module designs. All barrel modules are identical and aligned precisely parallel with the beam direction. The end-cap sensors have five different radial geometries depending on their radial locations on the disks. Chapters 5 and 9 will present results for the barrel modules whereas in chapters 6 and 8 end-cap modules were used.

The SCT barrel silicon module [55, 56, 57], as can be seen in figure 4.7, consists of two single-sided p-on-n microstrip sensors bonded together and glued back-to-back to another pair at 40 mrad stereo angle to provide bi-dimensional track reconstruction. The small stereo angle reduces the number of ghost hits in a high multiplicity event in comparison with orthogonal strips. This gives each module a 6×6 cm^2 sensor area of parallel strips with 12.32 cm total active length. The hybrid is mounted at the module centre and this centre-trapped design minimises the effect of strip resistance and fan-out capacitance. In between the two sensor pair there is a highly thermally conductive baseboard, made by thick film technology based on a thermo pyrolytic graphite (TPG) substrate, with Beryllium Oxide (BeO) facing. The material has been chosen for its high thermal conductivity and long radiation length. Good thermal contact between the baseboard and the cooling pipes is needed to limit the thermal runaway of damaged silicon detectors.

The end-cap modules, as seen in figure 4.8, use a very similar but wedge-shaped construction of either four or two sensors. The total strip number remains 768, since the strips of each two sensors are bonded together. The hybrid is for the end-cap modules mounted at the sensor edge, and the baseboard is replaced with a spine-shaped TPG piece and Aluminium Nitride facings (AlN).

[4] A dogleg is a l-shaped low mass tape with the opto-package mounted on it

[5] Equivalent Noise Charge, e^-

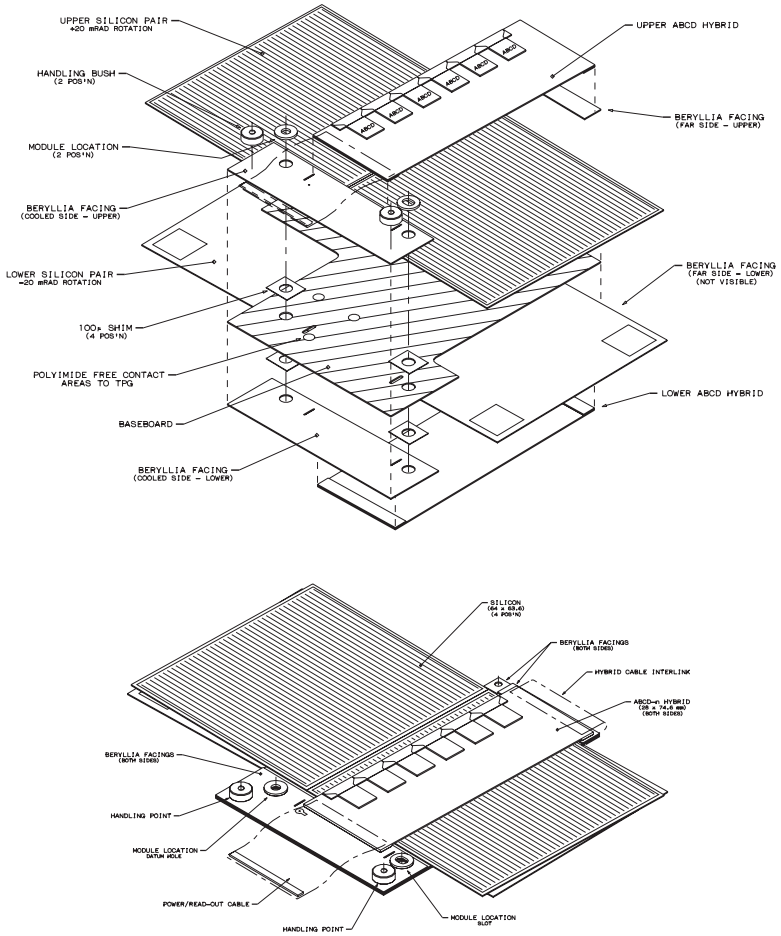

Figure 4.7: The barrel module before (top) and after assembly (bottom). The layers starting from the top are; top part of the hybrid, two silicon sensors, baseboard, two sensors faced down, the bottom part of the hybrid faced down. The sensors are glued together onto the baseboard, while the hybrid is wrapped around both planes and attached to the baseboard only [54].

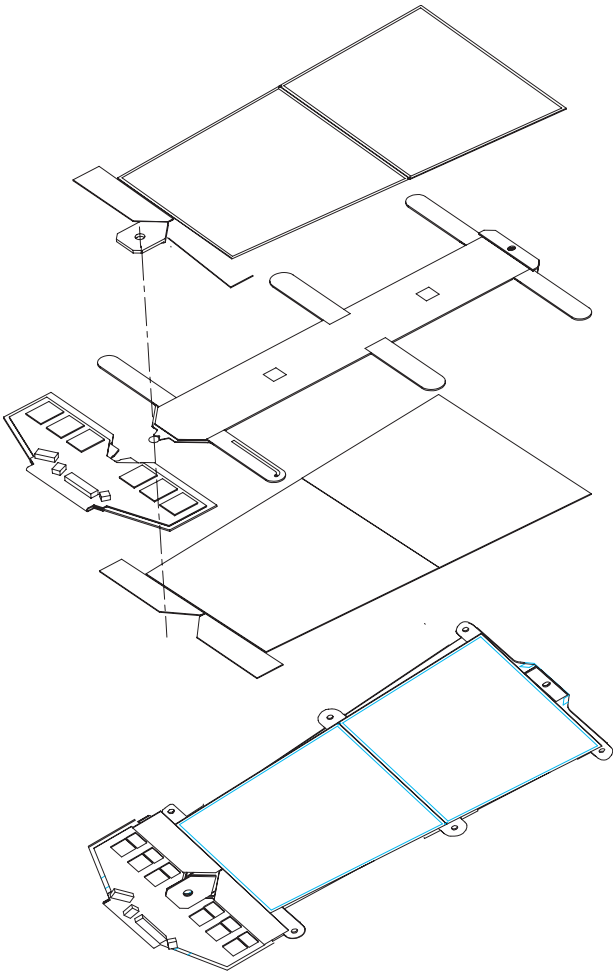

Figure 4.8: The end-cap module before (top) and after assembly (bottom). This end-cap module represent one of the four radial geometries. The layers starting from the top are; the hybrid mounted at the end of the module, two silicon sensors, spline and two sensors faced down. The pictures are from the end-cap community.

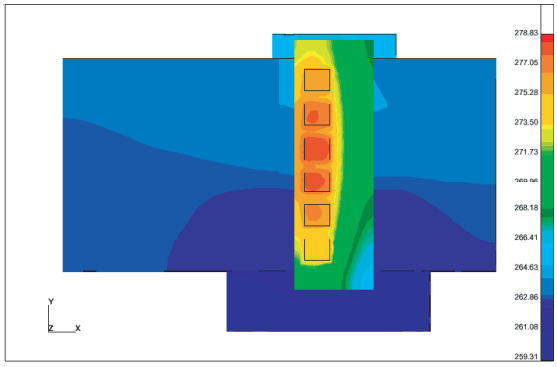

Figure 4.9: The temperature profile of the SCT barrel module at a cooling temperature at -14°C [55]. The highest and lowest temperatures of the module are +5.7°C (hybrid) and -13.8°C (baseboard). The ASICs are the main heat contributors.

Assembled, an unirradiated barrel module will dissipate around 5.6 W, where 5.4 W comes from the electronics. After 10 years of operation this value is expected to increase to 10 W, with 7.4 W coming from the electronics. For this reason the SCT will operate at -7°C in a dry nitrogen atmosphere. Cooling is needed to avoid an increase in leakage current and the changes of the radiation induced doping, as well as to remove heat generated by the chips and DC voltage drops (with the expected power consumption as described in 4.1.3). Figure 4.9, taken from [57], shows the temperature profile of the SCT barrel module when cooled to -14°C.

4.1.6 Barrels and Disks

After assembly, the modules are mounted onto support structures; barrels in the centre region and disks in each forward region. The four barrels, from the centre, have a radius of 299, 371, 443 and 514 mm respectively and are populated by 384, 480, 576 and 672 modules. Chapter 9 will describe more about the innermost of these barrels, barrel 3. The 1976 end-cap modules are mounted onto nine disks are placed at different z-distances, between z = 835 and 2778 mm.

The support structures themselves are made of carbon fibre skin and honeycomb core composite which has a coefficient of thermal expansion close to zero. These structures are constructed to have a minimal deformation during temperature variations of 30°C. The modules are mounted with an overlap to permit hermetic coverage and with a tilt in ϕ to avoid signal spread (as previously explained). The cooling tubes (Cu-Ni for barrel and Al for end-cap), the optical fibres and the kapton tapes are attached to the outside of the carbon structures.

Three back-end systems of detector control and monitoring are required to operate the SCT detector. The data aquisition system (DAQ) permits the calibration of the SCT modules and the physics data taking. The DCS supplies the modules

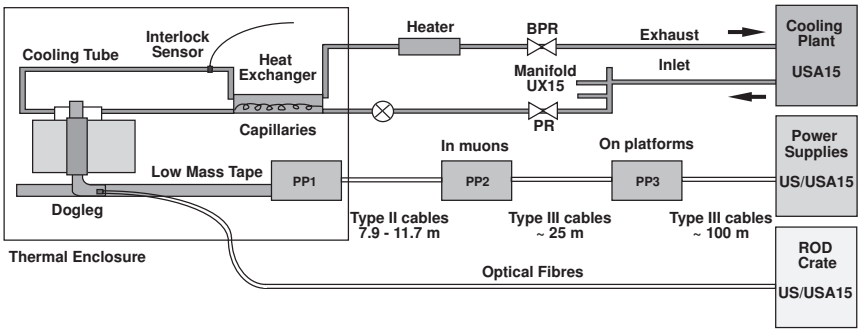

Figure 4.10: The minimal read-out and control unit for SCT barrel modules. The main parts of the SCT supplies can be seen. The ROD crate is part of the DAQ system and issues clock and commands and reads back data. The power supply crate provides the SCT with power and the cooling system cools the detector to the operating temperature. The latter systems are both part of the DCS.

with power and cooling and monitors the operating environment of the detectors. It also provides safety operations and issues slow control commands. In addition, the ATLAS trigger, timing and control system (TTC) is needed to trigger the SCT read-out. Figure 4.10 presents the DAQ and DCS system needed for one barrel module (similar for end-cap). The DAQ, and a subset of the TTC systems, will be described next whereas the DCS system will be described in detail in chapters 6 and 7.

4.1.7 Detector Requirements

To summarise, the physics requirements of the ATLAS detector translate into the detector specification shown in table 4.1. These parameters play an important role in the design of the manufacturing quality control as well as for the DCS system for the final ATLAS. Some grouping of the requirements can be made: some are more important for the DAQ system or the DCS system and some are important for the building of detector module and the assembly of modules to barrels. However, all requirements are equally important when testing and calibrating the modules. Both during the barrel module production (chapter 5) and the barrel assembly (chapter 9) the modules have been carefully tested against these parameters to ensure that the modules are good enough for taking physics data. The testbeam modules (chapter 8) were, for various reasons of availability, not of the same standard as the modules intended for ATLAS.

Type	Parameter	Specification
LHC	Bunch crossing tag resolution	1 bunch crossing
	Occupancy (physics hits)	1% of physics hit occupancy
	Total radiation dose	2×10^{14} n/cm^2, 10 Mrad
DAQ	Tracking Efficiency	99%
	Occupancy (noise hits)	5×10^{-4}
	Noise	$<$ 1500 e-
	Maximum L1 trigger rate	100 kHz
	Maximum L1 trigger spacing	2 bunch crossings
	Double pulse resoultion	50 ns (for two 3.5 fC signals)
	Large charge recovery time	1 μs (3.5 fC signal after a 80 fC signal)
DCS	Operating temperature	-7°C $\pm$ 2.5°C
	Functional temperature range	-15°C to 30°C
	Voltage compliance	$\pm$ 5% of nominal
	Power dissipation	$<$ 3.8 mW / channel
	Leakage current	$<$ 80 mA at 350 V

Table 4.1: A summary of some of the most relevant SCT module requirements.

4.2 Data Acquisition System

The SCT DAQ system permits the read-out and calibration of each individual SCT detector strip (channel). These tests have been crucial to verify the success of the barrel module production process, to check for shipping damage and to qualify the barrel structure assembly. The same is true for the end-cap production and assembly. During the SCT development and construction, the DAQ has been subject to a consistent evolutions, going from a prototype VME set-up to a close-to final system of hardware and software. The latter system, as well as some of the most frequently used tests, will be described in the following section. When not specifically stated otherwise (for instance in chapter 5), all test results in the rest of this document were made using this latest hardware and software system.

4.2.1 ATLAS Framework

The SCT DAQ handles the readout of SCT modules within the ATLAS DAQ framework [43]. When a Level-1 trigger (LVL1) request is received by the sub-detectors, as described in chapter 3, events are transmitted from the front-end pipelines as serial data stream at 40 Mbps and are buffered in the Read Out Drivers (ROD). As already mentionned, the design maximum L1 rate is 100 000 events per second but will be limited initially to 75 000 events per second. The data is transferred to the Read Out Buffers (ROB) [58] via a S-link interface [59] and stored until a Level-2 (LVL2) request is broadcasted. Several ROBs are grouped into one Read Out System (ROS).

The ROD translates the data from its input 320 Mbytes/s to its output band-

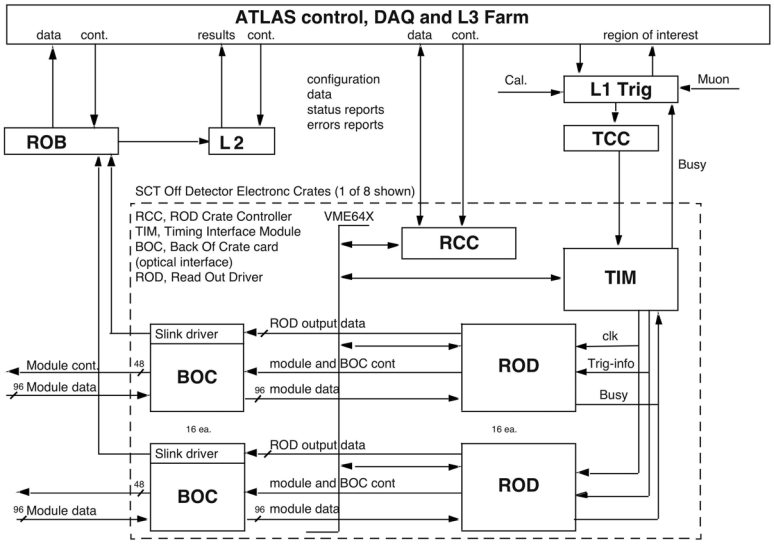

Figure 4.11: The DAQ hardware architecture showing the relation between the different subparts, such as ROD, BOC, RCC and the trigger systems [60].

width if 100 MBytes/s by using a zero suppressing scheme. A system of Sub Farm Interfaces then builds the events under supervision of Data-Flow Managers and passes it to the Event Filter which selects events for archiving. At this point on-line analysis and reconstruction can be initiated. The common ATLAS DAQ system is mostly based on standard computers and ethernet switches, and the bandwidth depends on this choice of technology; however, the capacity limitations at the ROS and beyond can be addressed by adding more duplicate components.

For correct tracking reconstruction, every hit has to be associated to a specific bunch crossing. This means a requirement on the timewalk of less than 16 ns, where the timewalk is defined as the maximum time variation in the crossing of the comparator threshold at 1 fC over a signal range of 1.25 to 10 fC. The fraction of output signals shifted to the wrong beam crossing is required to be less than 1%.

4.2.2 Hardware System

Each sub-detector readout system uses custom ATLAS VME hardware operation requirements. The SCT responsibility is to translate the SCT specific protocol used by the front-end electronics and to transmit events to the ROBs in a way that conforms to the ATLAS standard protocol [43]. The SCT hardware architecture is outlined in figure 4.11.

The Rod Crate Controller (RCC) [61] controls the operation of the crate and monitors its status. The Timing Interface Module (TIM) [62] receives the clock and

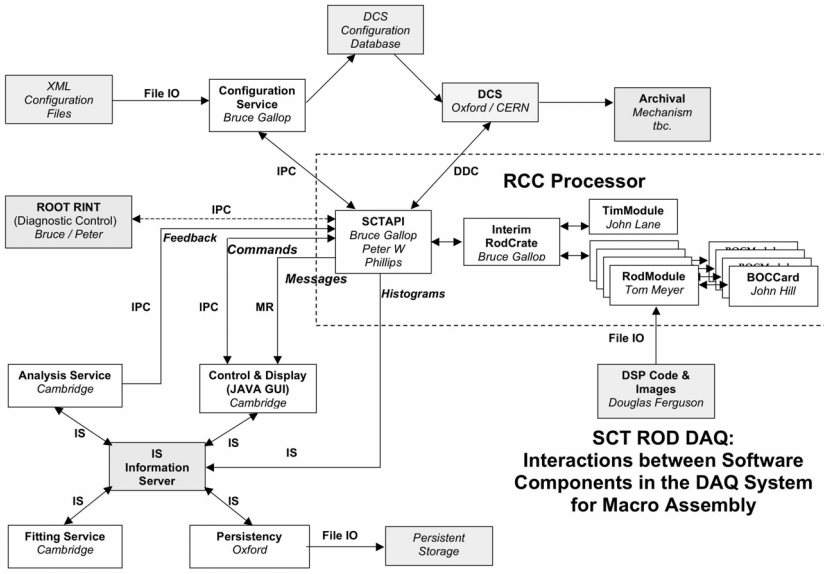

Figure 4.12: The SCT DAQ software architecture and the communication between the different software units. The interface of the SCTAPI to the ROD hardware and the SctGUI user interface can be seen [63].

trigger information from the ATLAS TTC system and makes these signal available on the ROD crate backplane. Each pair of ROD and Back of Crate (BOC) cards provides a DAQ interface for 48 modules. The ROD generates the command streams required to configure each detector module and distributes the TTC signals received from the TIM. Data returned by the modules are buffered, then formatted for S-link transfer. The RODs also histogram the returned data, as required during calibration operation, and help with several error handling tasks. The interface between electrical and optical signals is implemented on the BOC, which also houses the S-link interface. These links are custom 40 MHz links which have been developed specifically for this application.

4.2.3 Software System

In addition to the ability to support normal running of the SCT in ATLAS, the SCT ROD DAQ software must provide extensive support for the configuration and calibration of the detector modules. The resultant architecture of the software is shown in figure 4.12. The DAQ software consists of mainly of two parts. The SCTAPI communicates directly with the ROD and performs the histograms and scans, whereas the SctGUI provides online data analysis and display of results.

At startup, SCTAPI [64] initialises the RODs and detector modules in accordance with information obtained from the Configuration Service. The user can then

control the system from the SctGUI, for example, to request a threshold scan to be performed. Scans are managed by SCTAPI: once a scan has been completed, the histogrammed data is published to the information service (IS). The fitting service takes histogrammed data from IS and performs channel by channel (s-curve) fitting, publishing the result back to IS. Any data that has been published to IS will be archived by the persistency service and may be viewed by the user by means of the SctGUI. Mostly summary data, occupancy histograms and descriptive meta-data is transferred to the IS. Raw event data is mostly not transferred to the IS due to its much larger bulk.

4.3 Electrical Tests and Calibration

Due to the choice of a binary architecture, there is a need to derive analogue performance indirectly. Typical tests of SCT detector modules consist of one or more scans. Each scan represents a series of bursts separated by programmed changes in at least one variable, and each burst represents a number of triggers sent to the modules, with the returned data being histogrammed on the ROD. The tests included as part of the SCT ROD DAQ package build upon those developed for the SCTDAQ software written for the first generation of SCT DAQ hardware [65].

The electrical testing of the SCT modules uses the internal calibration circuit of the ABCD chips to determine parameters such as gain, noise, threshold spread and defects. Chip or hybrid damage may also be detected. The results of these tests are a set of parameters defining the performance of the module as well as a number of channel defects or failure modes. Channels with defects, such as being dead, stuck, unbonded or noisy, are masked off. A subset of the most frequent tests are presented below, based on the work presented in [65, 66].

Digital Tests

A A *Hard reset* of the modules is issued from the DAQ to the DCS system which then performs the task of setting the hard reset line high and then low. The chips lose their configuration and respond with a CLK/2 signal on each datalink. This command is sent from the DAQ system, but as will later be described, is executed by the DCS system.

B The *Redundancy test* checks if the clock and command signals from both the primary and the redundant lines are received correctly.

C The purpose of the *FullBypass test* is to exercice all data/token passing between the chips with the chips in different configurations.

D *Pipeline test* verifies that the contents of each of the blocks within the pipeline is free of defects.

Analogue Tests

Most analogue tests are started by scanning the different threshold value at a fixed calibration charge, 1 fC. For each of the four TrimDAQ settings the channel discriminator offsets are scanned to find the values which minimise the variations of noise occupancy across the channels. Figure 4.13, left, shows an example of the resulting s-curve. The threshold value, vt50, is given by the 50% value of the slope. By scanning the channels for each vt50 for different calibration charges in the range of 0.5 to 8 fC a response curve is determined as shown in figure 4.13, right, and the output noise is measured. From this scan the gain can be determined from the slope of the polynomial fit of this curve and the input noise is determined by dividing the output noise by the gain. These operations are divided into the following analogue tests:

E The *Strobe delay* scan is performed first to determine the timing of the charge injection pulse. The corresponding delay is called the Strobe Delay and has to be set to be at the peak of the shaper response.

F The *3Pt Gain* test is a short response curve where the threshold is scanned for three fixed injected calibration charges. The front-end gain, threshold offset and input noise are calculated.

G *Channel trimming* is done to determine the correct TrimDAC settings for each detector channel. For a fixed injected charge the common chip threshold is varied. At each threshold point another scan of the channel-to-channel DAC settings are made.

H After the channel corrections, the *NPt Gain* test (or *response curve*) is performed. It is a longer response curve with 10 different injected charge values and again the noise, gain and offset values are determined. Figure 4.13, right, shows an example of such a curve.

I The *Noise Occupancy* is the rate of events generated due to noise and is determined by a high statistics threshold scan at the nominal ATLAS trigger rate (100 kHz) with no injected charge. It thus gives a direct measurement of the noise occupancy per channel as a function of the threshold. Channels with high noise occupancy are masked.

J The *Timewalk* test consists of a series of strobe delay tests with varying input charge to determine the time variation in the threshold crossing of 1 fC signal over a range of 1.25 to 10 fC.

Conclusion

To summarise, the SCT detector is subject to rather stringent conditions. The minimising of material, the use of radiation hard technology and other mechanical

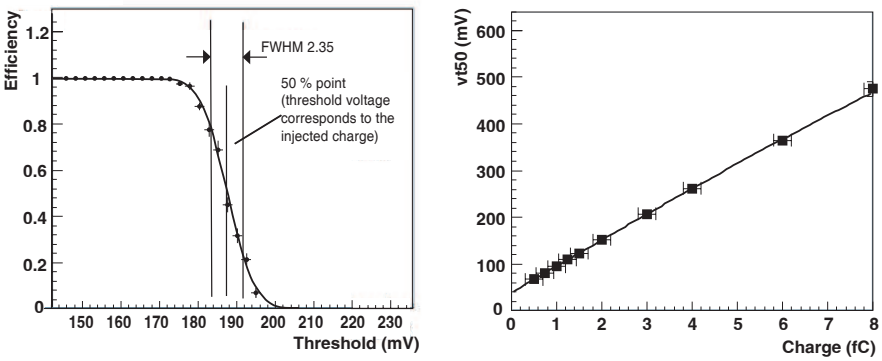

Figure 4.13: Left, a typical s-curve used to determine a 50% point. Right, a typical response curve showing several 50% points as a function of the charge injected for each s-curve. The plots are taken from the output of the SCT ROD DAQ sofware from tests done at CERN.

constraints, results in the construction of a SCT detector as described in this chapter. The read-out of the detector provides, in addition to the collection of physics data, a calibration unit which permits the detector, to a certain extent, to compensate for channel specific degradation and differences in operational conditions.

The following five chapters will discuss most aspects of the SCT from a construction and testing point of view. The production of modules and the assembly of modules to barrel cylinders are all critical processes which threaten to damage the detectors or degrade their electrical performance. As will be seen, both these delicate operations have been completed successfully up to the scale of one barrel structure. To confirm the success of the technology and the various assemblies the modules are tested at several stages during production and in testbeam. The construction of a control and read-out system hardware is needed to provide an optimal operating environment for the detectors in order to ensure the electrical perfomance. The most important parts are the provision of analogue and digital power to each individual module and the cooling of the detectors to avoid overheating, which results in a separate detector environment from the outer ATLAS sub-detectors. The construction of a safe operating software, for both end-cap and barrel modules requires good knowledge of the detector requirements and performance.

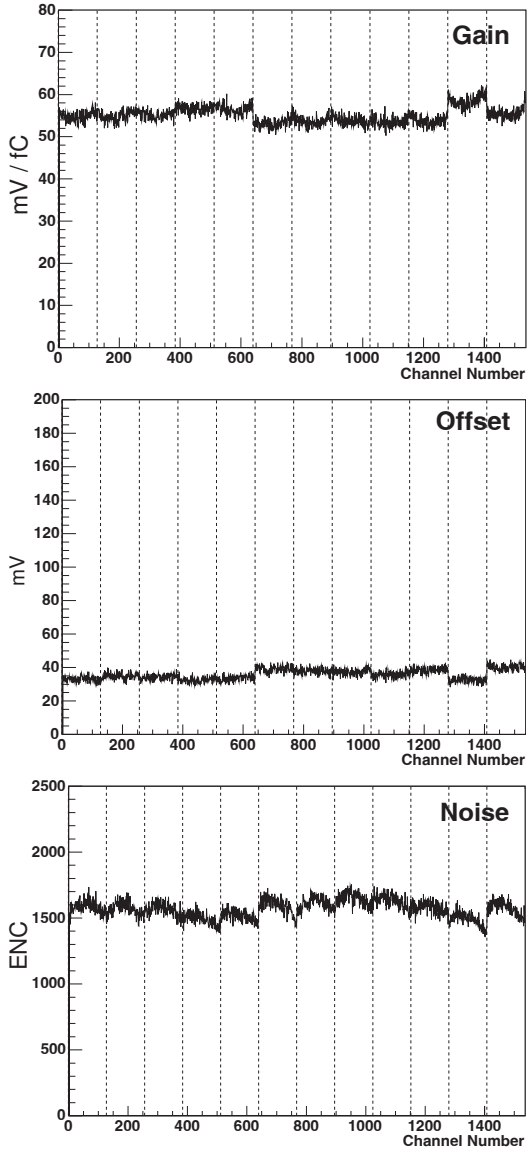

Figure 4.14: Examples of typical test results from the response scan, showing the values for all channels of one module for gain, offset and noise. The small differences in average values between the ASICs can be seen. The plots are taken from the output of the SCT ROD DAQ sofware from tests done at CERN.

5
SCT Module Production

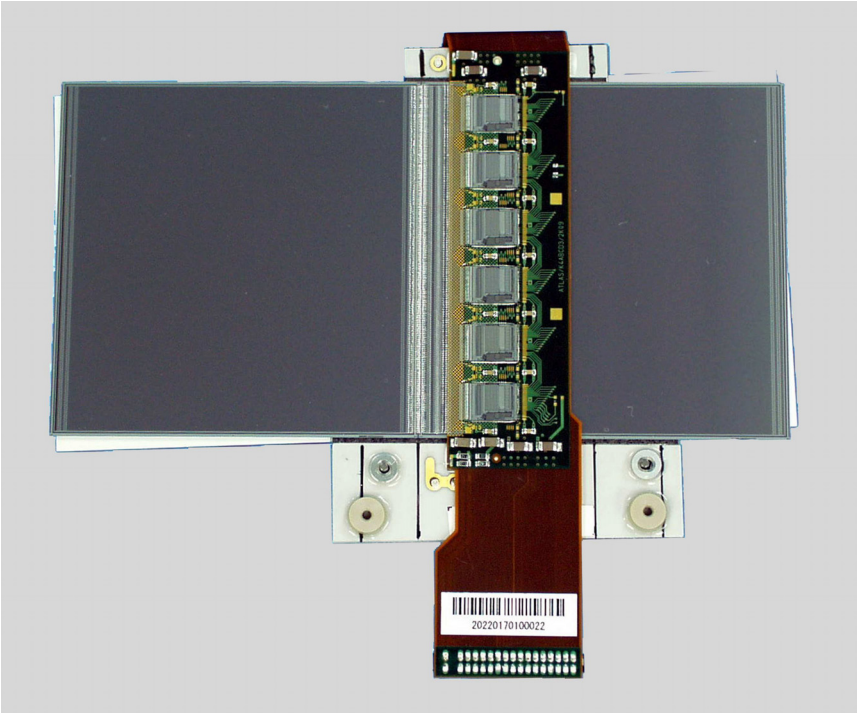

One SCT barrel module [67].

Introduction

The production and tests of large quantities of silicon detector modules for the ATLAS project at CERN are in its final phase. The end-cap production is still ongoing, whereas the barrel production finished in 2004. The University of Oslo has built and tested around 320 of these barrel modules together with the Universities of Bergen and Uppsala. These three institutes form the Scandinavian Cluster (SCAND) for module production. The number of detectors produced by SCAND is relatively small in comparison with other production clusters, yet it is an important contributor to the SCT detector.

My personal contribution to this work has been to construct a test-setup in Oslo for testing IV-curves after module mechanical assembly and to realise an electrical test set-up for the final production tests, including cooling, DAQ and DCS. I also tested some of the preproduction modules produced by the SCAND cluster with this set-up before moving to CERN.

This chapter presents successively the SCAND production site, the IV-curve measurement setup, the cooling system, DCS, DAQ and resulting tests. Overall, one can conclude that the set-up was working and provided results comparable with the other sites. Since the barrel module production is now completed and the first modules are assembled and tested on barrel 3 (see chapter 9), the conclusion is that the SCAND contribution to the barrel module production has been a success.

5.1 SCAND Barrel Module Production

Figure 5.2 shows the SCAND cluster and how the construction work was divided between the sites. In Oslo, the mechanical assembly of the modules took place. The silicon sensors were made by the company Hamamatsu and arrived in Oslo via Bergen where they had been tested for defects and overall performance. The baseboards were fabricated and tested at CERN before shipment. In Oslo, all four silicon sensors of one module were positioned and glued to the baseboard by using

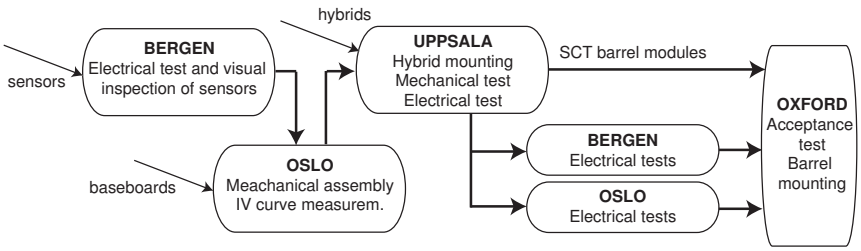

Figure 5.2: The SCAND production sequence. The sensors were assembled mechanically in Oslo before the hybrids were mounted and bonded in Uppsala. The Uppsala, Bergen and Oslo sites were all equipped to perform electrical tests on the produced modules.

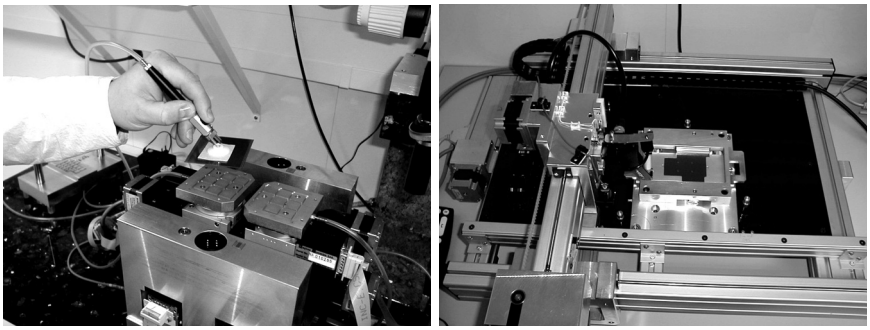

Figure 5.3: Left, placement of the silicon sensors onto the alignment jig. One sensor was lowered onto the rig using vacuum. Right, the glue dispenser which distributed the epoxy onto the baseboard. The baseboard was placed in a frame as can be seen in the middle of the picture. Both pictures have been provided by O. Dorholt.

a dedicated assembly system shown in figure 5.3 [57].

Two modules were positioned on the assembly table of the mounting tool and temporarily fixed by applying vacuum to the back of the silicon sensor. On the table, the sensors were rotated in the x-y plane by step motors with micrometer resolution until they were correctly aligned. The alignment process was done by a pattern recognition program, which used a microscope to read fiducial marks on the silicon sensors [68] (see figure B.1 in the annex). The aligned sensors were transferred to a pick-up jig (produced by the Instrument Workshop in Oslo) by lowering the jig onto the aligned sensors and then transferring the vacuum to the jig (see figure 5.3, left). This procedure was repeated for the other pair of sensors, which went onto the back of the baseboard.

To fasten the sensors to the baseboard, the baseboard was first positioned onto a 3-axis dispensing workstation, which distributed drops of glue in a pre-defined pattern across the surface of the baseboard (see figure 5.3, right). The glue was a high viscosity adhesive mixture of Araldite-2011 with boron nitride to achieve thermal contact. To permit electrical connection between the baseboard and the sensor back-side, an epoxy containing silver (Eotite p-102) was applied at two dedicated spots per sensor. After the application of the glue on both sides, the baseboard was picked up by the pick-up jig and attached to both sensor planes. During this action, two positioning pins guided the baseboard in its correct position. Spacers between the jig and the baseboard ensured the correct module thickness. Finally, the module was cured for 24 hours at room temperature before a three hour finish at 30°C. Before shipment of the modules to Uppsala, their leakage currents were tested up to 350 V and verified to be below the limit (see chapter 4) and not more than 1 μA different from the value recorded in Bergen.

In Uppsala, the assembled modules first underwent a mechanical survey of the module metrology parameters. As many as 13 parameters (listed in table B.2 in

annex) had to be controlled during the mechanical assembly to achieve the correct alignment and detector thickness. Each silicon sensor pair had to be in plane, and each of the two sensor planes had to be aligned to each other. In addition, all sensors were aligned to a common module reference point. Also, the hybrids, arriving from Japan or USA with the ASICs mounted and bonded, were tested electrically to uncover any defects.

If a module passed these reception tests, the hybrid was mounted using special jigs which wrapped it around the sensors without touching their surfaces. The hybrid was glued to the baseboard, cured and visually inspected before the bonding process was started. The bonding was done using a dedicated high density wire-bonder. First the HV and ground lines were bonded, then the 768 channels were bonded in two steps: between the two sensors and between the pitch adaptor and the sensor. In addition to the bonds already on the hybrid, this resulted in a total of 4 608 bonds per module [57].

Several quality tests were done after a module was finished. First another mechanical survey was performed, including the hybrid specifications. Then an electrical test was made to confirm full functionality of the module before starting the thermal cycling and the long term test, which permitted the discovery of any major faults. The details of the electrical tests are basically the same as those described in chapter 4 and some example of these tests on SCAND modules will be presented later in this chapter and in chapter 9.

5.2 IV Measurement System

The IV-curve measurements of all four silicon sensors after the mechanical assembly was one of the main verifications of the module, before shipment to Uppsala for hybrid mounting. For this reason a dedicated IV measurement system was designed for the production site in Oslo. During construction of the IV-system, the main challenge was to construct a light-tight box which allowed easy access and operation, whilst at the same time ensuring the safety of the module during testing. The box needed to be operational for both right and left-handed operators. At my arrival in Oslo the choice of the outer dimensions of the box had already been made but the construction of the measurement rig itself was yet to be designed and constructed.

The IV test box was designed as shown in figure 5.4. The outer box had several layers of overlapping aluminium on two sides to provide light-tight corners. By removing its foot, a microscope (Carl Zeiss), could be fitted into the back of the box and fixed in the appropriate height for observation. In front of the microscope an adjustable table was constructed with a frame for the safe placement of the module. As can be seen in figure 5.4, the table could be moved in the x-y-direction, on two sets of rails, to optimise the detector position. Four screws permitted the user to fix the table in the most suitable position.

The two current-probes (Swissboy, Rudolf Grauer AG) were placed upon a support table which was mounted around the microscope. To stop the probes from sliding during operation and possibly damaging the sensors, they were held to the

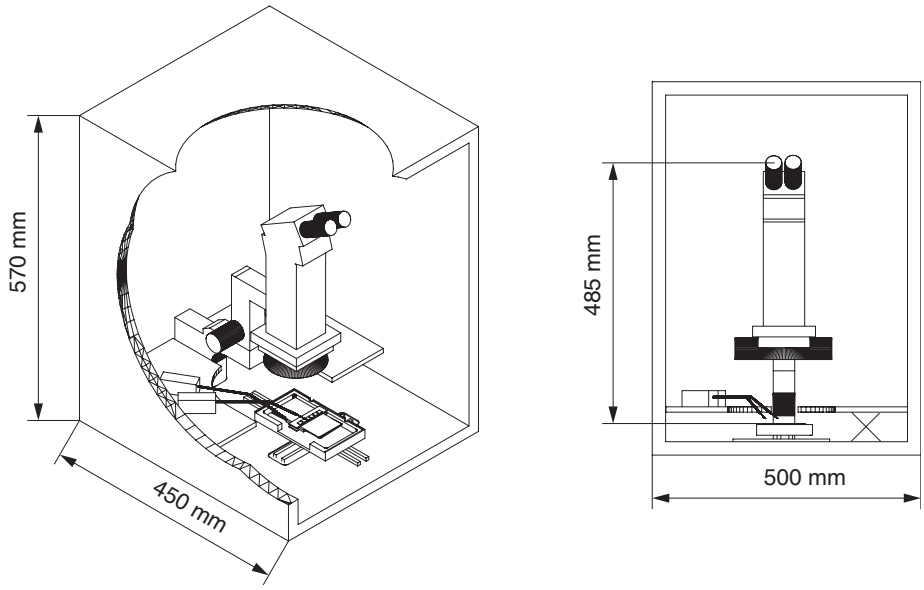

Figure 5.4: The IV-box for leakage current measurements after mechanical assembly.

table by the application of low pressure. Each probe had a long arm with a needle at the end, which had to be placed on the sensors surface to be tested (see figure 5.5). To measure the leakage current of one sensor, the needle of one of the probes had to touch its bias ring pad and the other the back of another silicon sensor (or ground pad of the same sensor). In this way it was also a check of the baseboard contact. All four sensors were measured individually. Several sets of cables entered the box and light-tight connectors had to be provided for those. Black tubes were used preferentially for the low pressure tubes.

A picoamperemeter (Keithley model 6487 Picoamperemeter/Voltage Source) was used for the measurements of the leakage current with 10 fA resolution and provided the bias voltage needed in a range from 0-500 V. The sensor current was expected to be of the order of hundreds of nA. Figure 5.5 also shows how the amperemeter was connected to the IV-probes. The amperemeter was read by the computer via a GPIB interface. A program written by the Bergen group for their sensor tests was used to perform the IV-measurements and to store the values. The start and stop voltage as well as the stepsize could be chosen before the start of the program. The output was written to a text file in a format which could be uploaded to the SCT production database. The current values measured were converted to the normalised value for temperatures of 20°C by using the following formula, where k_B is the Boltzman constant and I_T the current measured at a temperature T:

$$I_{20} = I_T(\frac{293.2}{T+273.2})^2 e^{-\frac{E_g}{2k_B}(\frac{1}{293.2}-\frac{1}{T+273.2})}.$$

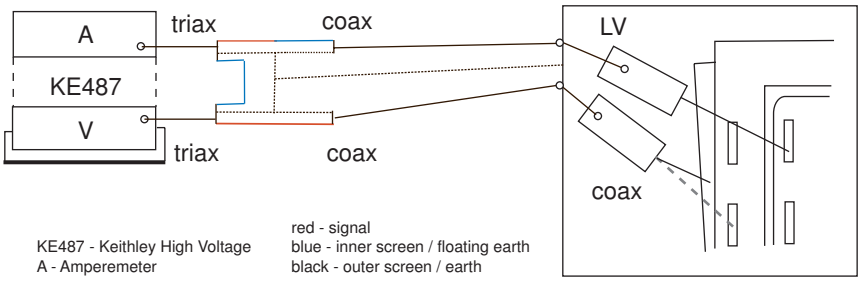

Figure 5.5: Schematic drawing of the cabling of the picoamperemeter and its voltage source. At the left one can see the probe connections to the sensors.

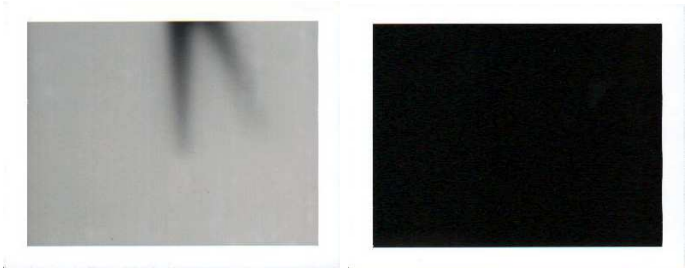

Figure 5.6: Left, a reference picture of a pair of scissors in the laboratory for four seconds by a small lamp. Right, the exposed picture inside the IV-box to check for light leaks. As can be seen, it was not possible to distinguish any differences and the IV-tests could start.

To determine if the IV-box constructed was providing sufficient light-tightness, a quick test was performed using the detection of photons by Polaroid film as can be seen in figure 5.6. One reference exposure, left-hand picture, shows a pair of scissors on top of the film for four seconds in the darkened laboratory. Then the film was exposed inside the closed IV-box for one minute with a fully lit laboratory. Half of the film was closely covered with a sheet to check for shade differences. From the completely black picture it was concluded that the box was sufficiently light-tight and that it was safe to proceed with the first sensor measurements.

The first IV measurements were performed successfully with a very early prototype module. The second series of tests were made with one of the SCAND preproduction modules to determine the quality of the IV system compared to the other measurement systems in the SCAND cluster. This module had been slightly damaged during shipping, but was still suitable for IV-curve measurements. Figure 5.7 shows the results of these tests for two of its sensors. One sensor was measured successfully up to 500 V, the other, with the damage, had current breakdown from around 300 V. The solid lines shows the Oslo results and the dashed lines the mea-

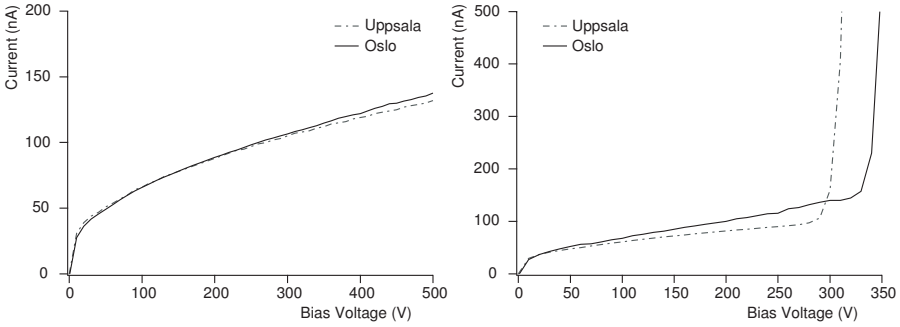

Figure 5.7: Comparison of IV curve measurements performed at the set-up in Oslo and the set-up in Uppsala of the same prototype module having one damaged silicon sensor due to shipping. Both sensors are situated in the top plane of the module and the measurements are all taken with a five second interval. The solid lines show the result from the Oslo site and the dashed show the measurements from Uppsala.

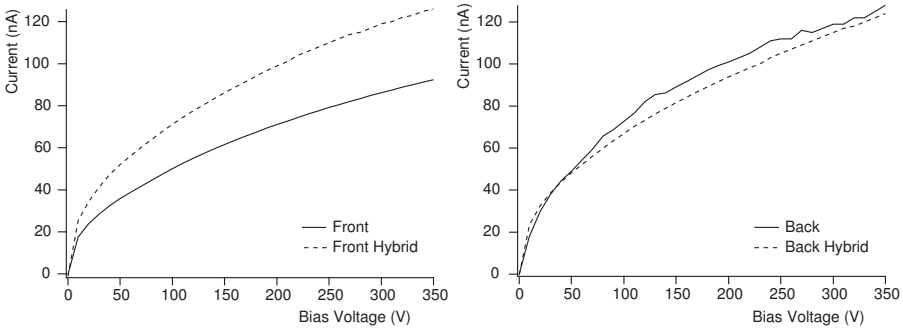

Figure 5.8: IV-measurement of a SCAND production module (20220480112327) taken with the Oslo setup. Left, the curves for the two frontal sensors and right, the two sensors on the back. These sensors, tested after the mechanical assembly, are well within the specifications.

surements from Uppsala. The damaged sensor shows a slightly earlier breakdown in Uppsala then in Oslo. However, it was concluded that there was good overall agreement for two set-ups. Figure 5.8 shows the typical V-curves on both sides for one good SCAND production module taken during production. The bias current of this module show expected values up to 350 V for all four sensors.

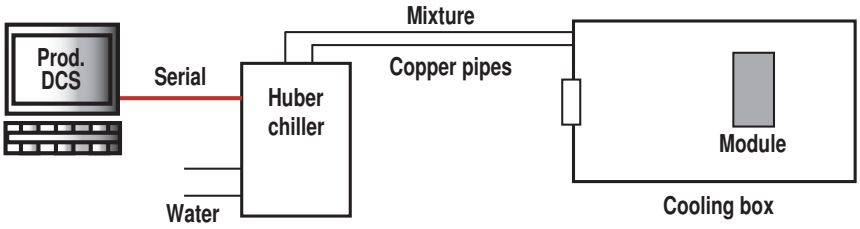

Figure 5.9: Overview of the cooling system. A DCS program permitted to start and stop a predefined chiller cooling cycle. The module was cooled by contact to the bottom of the box via its mounting frame.

5.3 Electrical Test System

To be able to perform electrical tests of the completed module it was necessary to construct both a small DAQ- and DCS- system as well as a cooling system. Among the main challenges was to ensure a safe operation conditions of the modules and low noise measurements. Because of the long duration of the tests, it was not clear how many of the SCAND sites were needed for the tests and for this reason, all three SCAND sites prepared this test set-up. In the end, the capacity of only two sites proved to be sufficient.

5.3.1 Module Test Box

For the production tests it was required that the modules were tested cold in a nitrogen environment, with a temperature as close as possible to the module operating temperature (-7°C), which means that the system ideally must be able to cool down to -25°C. To achieve this, a cooling system was constructed in Oslo consisting of a module test box flushed with nitrogen and cooled by a Huber chiller as can be seen in figure 5.9.

The construction and conception of a first prototype box, seen in figure 5.10, had already started before my arrival in Oslo. My work consisted of helping to conclude the design, provide the cables for electrical readout and to test the box when it was finished. The box was fabricated by the Instrument Workshop at the Physical Institute of the University of Oslo. It was made by two layers of aluminium plates around the isolation and one layer of copper tubes inside, in which the coolant circulated. The tubes went through all sides of the box and the lid. As can be seen in figure 5.10, the nitrogen could circulate via two inlets from the back.

Two modules, mounted in their support frames, could be fixed to the bottom of the box onto an electrically insulated copper plate. The cables for the powering and the readout of the modules (via a signal condition board) were flat cables and entered through the isolation between the lid and the box. The DCS cables entered through a hole at the left side. After the placing of the various sensors, this hole was filled with glue to seal the box and thus avoid nitrogen leakage.

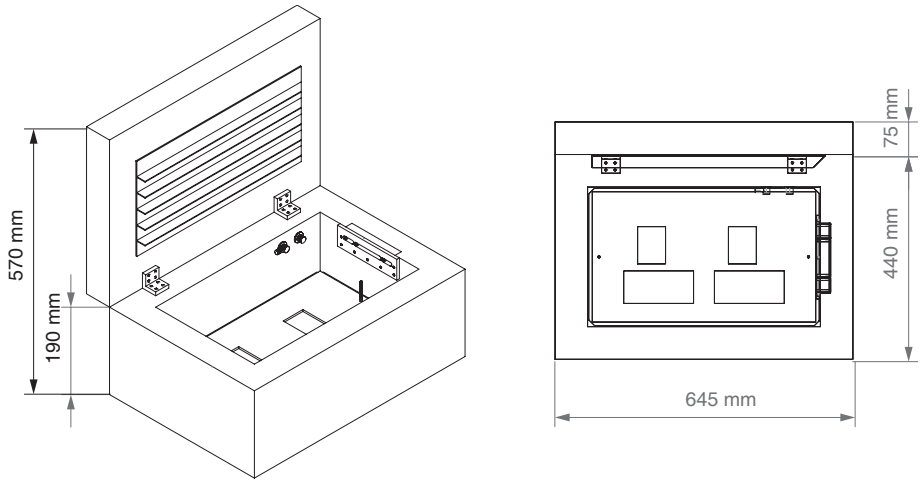

Figure 5.10: A 3D view (left) and a top view (right) of the prototype test box.

The prototype box was connected to a Huber chiller via copper tubes. The pump could run both manually or by using a DCS program written by the Uppsala group, which controlled the Huber from a PC via a serial port. All tubes were coated with isolating foam to avoid condensation. The cooling liquid used for this setup was 2% Metylisobutylketon (Etanol, 4-Metyl-2-Pentanon) from ARCUS, which was chosen because it fitted the Huber criteria, and also due to its availability at the lab.

Figure 5.11 shows the first results of the cooling of this box taken with the DCS system described in section 5.3.2. As can be seen, it performed rather poorly, the response was very slow and did not reach below -5°C in the coldest spot of the box after two hours of cooling. The spread of the temperatures read by the sensors was partly due to their placement inside the box, however some effect was present from the fact that the temperature sensors were not yet glued to the bottom of the box during this test period. It was concluded that the cooling capacity was not sufficient.

The design of the final box was made to improve the cooling capacity and to provide for the possibility to test six modules at a time. This new cooling box was constructed from styrofoam plates of 60 mm thickness covered on the ouside and inside by laminate plates giving an inner volume of 1200 × 350 × 120 mm. Inside the box, the modules were mounted to an aluminimum plate. Inside the plate a capillary copper tube was installed where the coolant could circulate. The modules were electrically isolated from the cooling system. The cabling system from the prototype box could still be used, it only had to be adjusted to the increase in number of modules.

Even though the two tests performed were not entirely identical, it was clear that the final box performed much better as can be see from figure 5.12. The best temperature sensor shows a temperature after two hours of around -22°C. Even the

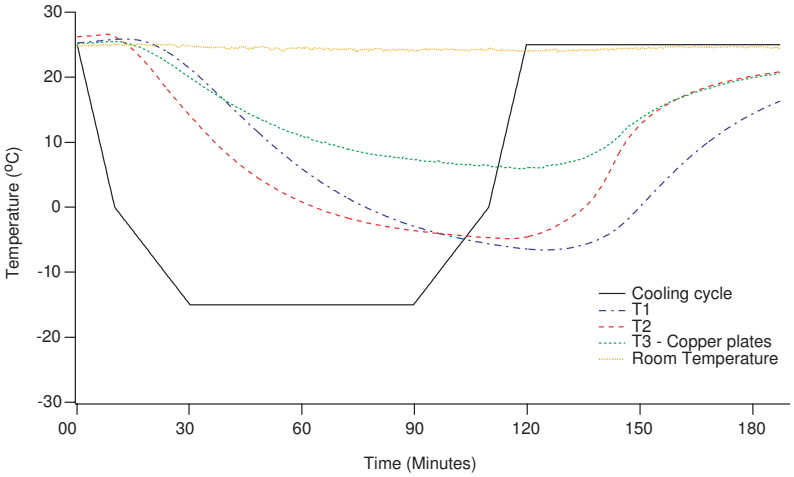

Figure 5.11: The performance of the prototype cooling box. The temperature sensors was placed in various position in the box, and one measured the ambient temperature outside the box. All other sensors were taped to the bottom copper plate. As can be seen, the minimum temperature close to the inlet tubes of the coolant shows around -5°C after two hours of cooling.

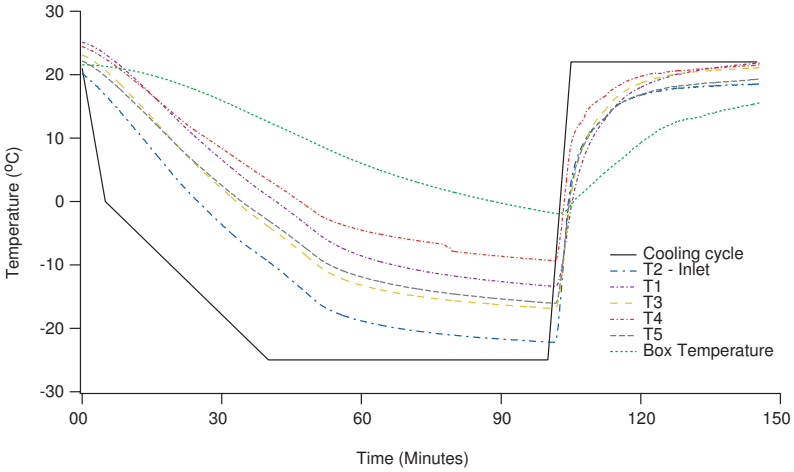

Figure 5.12: The performance of the final cooling box. The temperature sensors were placed in various positions in the box, and one measured the ambient temperature inside the box. All other sensors were taped to the aluminium plate. As can be seen, the minimum temperature close to the inlet tubes of the coolant shows considerably less than -20°C after one hours and 30 minutes of cooling.

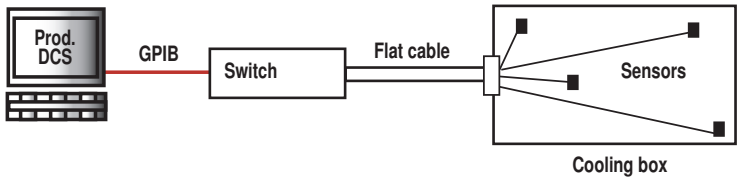

Figure 5.13: Overview of the production DCS system.

temperature sensor showing the temperature of the air inside the box went below 0°C. This performance was considered sufficient for the module production tests.

5.3.2 DCS for Modules Testing

Temperature, humidity and oxygen sensors were used to measure the environment of the modules during testing. To monitor these sensors a small DCS system was developed consisting of a software program reading the sensor values via a switch unit over a GPIB bus (see figure 5.13). The system was calibrated before being used to test the cooling system (as seen in section 5.3.1) and for the modules tests. A flexible architecture was needed to permit easy changes of the number, type and placement of the sensors.

Monitoring Sensors

The temperature sensors were placed at different positions inside the box and were used to monitor the detector temperature and the cooling efficiency. The sensors are Platinum Resistance Temperature Detectors (PRTDs) of 100 and 1 kΩ resistance at 0°C (Heraeus M-KF 1020), which are designed for large volume applications and are known for their long term stability and accuracy over a large temperature interval.

As already mentionned, the temperature sensors were initially connected to the cooling box with tape, but were to be glued to the box during production tests, using thermally conducting glue. Calibration of the sensors, displayed in figure 5.14, was made by using a reference sensor calibrated to 0°C by using a bath of a mixture of ice and water. Before calibration, all sensors from one batch (production series) differed by less than 0.2 degrees but all being around 3°C from the reference temperature of $\sim$ 21°C. After calibration, all sensors were found within 0.2 degrees of the reference value.

One humidity sensor was used to monitor the humidity inside the cooling box. The air inside the box was changed to nitrogen during testing to avoid condensation on the surface of the detectors. The sensor used was a HIH-3605 monolithic integrated circuit from Honeywell. The sensor was powered with a stable DC 5 Volt power supply and its output was a voltage measured by the Agilent switch unit. The humidity measured was a relative humidity, which had to be converted to the absolute humidity (%) taking into account the temperature dependency. The calibration of the sensor was performed by comparing its value with the known value in air at a

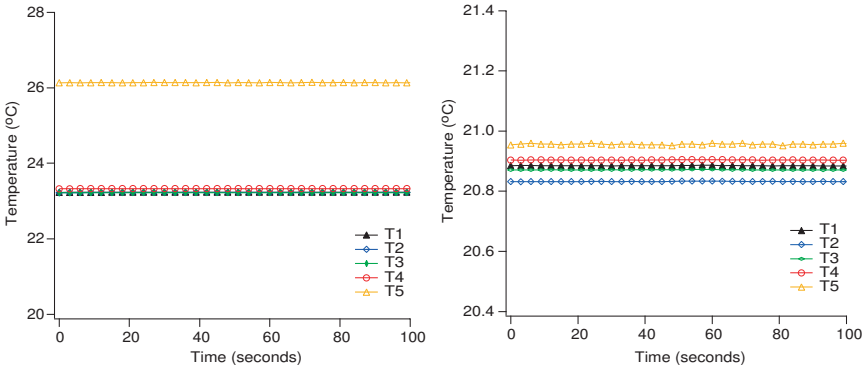

Figure 5.14: Calibration of the temperature sensors. Left, the sensor values before the calibration can be seen and right, after the calibration.

certain temperature and comparing it to the independent calibrated humidity sensor already in use controlling the laboratory air conditions.

An oxygen sensor was implemented outside the box for the safety of the users. When handling large amounts of nitrogen gas in a small room, one had to pay attention to the oxygen level. If it dropped due to nitrogen leakage, the sensor would give the user a possibility to correct the failure or evacuate the room.

The sensor used was a typical oxygen sensor from the company Electrovac for oxygen levels up to 20.9%. It consisted of a zirconia electrolyte cell which, when voltage applied, transferred ionized oxygen molecules providing a current signal. This current was proportional to the oxygen level in the close environment of the sensor. Powered by an external source of 5 V, the signal was read through a signal conditioning unit made by the Electronics Laboratory at the University of Oslo. Care had to be taken to avoid self heating of the sensor (0.1 K/mW at 0°C). The zero level (calibration) was checked by filling the cooling box with nitrogen completely and measuring the concentration inside. Some differences in the reaction time were noticed due to various gains, as can be seen in figure 5.15. A gain of 2.5 was chosen as appropriate taking into account the offset to the calibration value of air.

All sensors were connected via a flat cable to an Agilent switch unit, which permitted to readout the signal via a GPIB bus to the computer. The switch unit provided some conversion of the parameters and permits to read the temperatures directly in degrees Celsius. However, this functionality was not used since it was more accessible via the LabView interface. A dedicated DCS computer running a Windows NT environment and equipped with an GPIB-PC-card from National Instrument (NI-488.2) analysed the values received by the switch unit.

DCS Software

A LabView program was written to monitor the DCS system and was made flexible and modular to accept a growing number of sensors and changes to the sensor types.

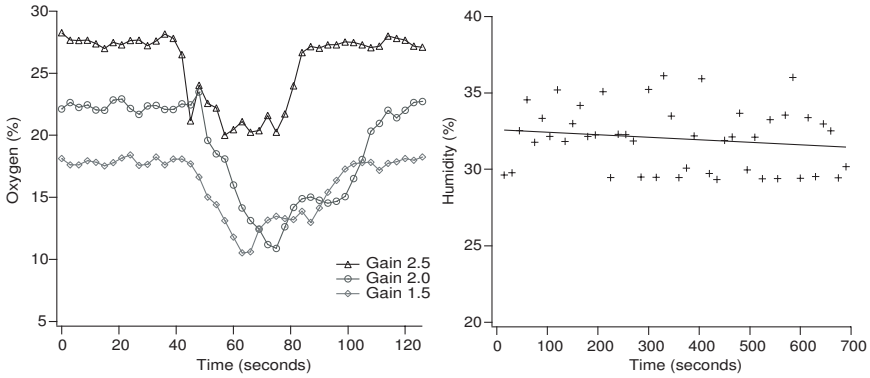

Figure 5.15: Left, typical gains of the oxygen sensor in air. The dip in the middle corresponds to taking one (human) breath out towards the sensor. Right, typical values of the humidity sensor. Some averaging is needed to limit the spread of the values.

A ready LabView driver, controlling the switch unit, was provided by the Uppsala University and integrated into the Oslo setup. Figure 5.3.2 shows the hierarchical structure of the program. A main program took care of calling the appropriate subroutines (e.g. "get data", "convert data", "calibrate data" and "store data") and presenting the data on the screen. It had an initial start-up sequence which permitted the user to change the setup in the case of hardware changes or to skip this process by pressing the start button. The main routine then started in a sequence, where the first frame was used to handle and sort all initial sensor information and the second to handle the continuous reading of values, the presentation and saving of data.

The subroutines were either part of the Agilent server routines, internal LabView functions or custom functions programmed specific for this DCS system. The Agilent Server routines permitted easy access to all of the sensor values whereas the LabView functions provided standard routines for reading, storing and displaying values. The custom routines consisted mainly of one calibration function and one conversion function. The calibration function called a set of calibration factors for the different sensor values, stored as text files, taken during a dedicated calibration run. The conversion function consisted of a set of mathematical formulas to convert the different sensor raw data to their physical values. The correct conversion value was changed automatically according to the initial user choice of sensor type. For the oxygen sensor the measured current value had to be converted into %, for the temperature sensors the resistance measured was converted into temperature and for the humidity sensor voltage was converted into relative humidity.

The functionality of the program was basically the monitoring of the sensors. However, the sensors themselves could be manipulated in the following fashion:

- Each sensor could be disabled and enabled

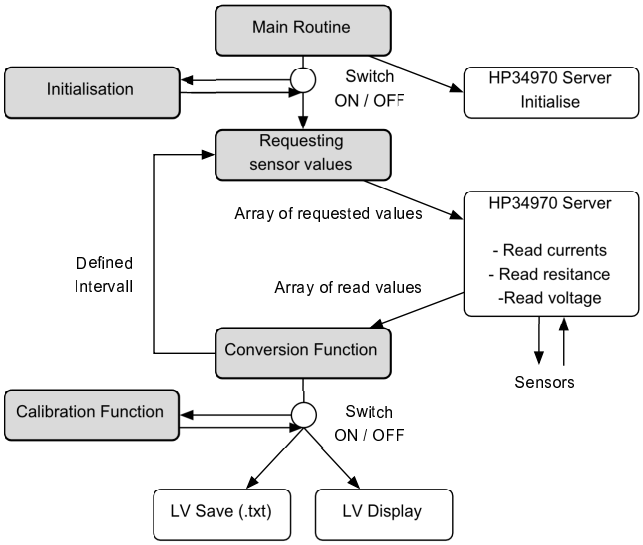

Figure 5.16: The DCS program hierarchy.

- The position (Agilent entry number) of each sensors could be changed
- The type of sensor could be changed

The options for the sensor types was *Temp. 1 kOhm*, *Temp. 100 Ohm*, *Humidity* and *Oxygen*, but this list could be easily extended via the program.

5.3.3 Production DAQ

Figure 5.17 shows an overview of the production DAQ system. A PC running the SctDaq software described in [65], controlled the electrical readout and testing of the SCT modules. This is a custom designed software for the SCT module production based on the use of custom VME components. The hardware consisted of a CLOAK [69] VME card distributing a 40.08 MHz clock to the system and generating fast commands such as Level 1A (L1A) trigger signals. A SLOG [70] card received these signals and distributed them to the modules (12 maximum). It also generated the slow command data needed to configure the modules. A MuSTARD [71] unit received the data from the modules (6 maximum), decoded it and created histograms. Powering of the modules was provided by SCTLV3 (LV3) [72] cards for the low voltages and an old custom made external High Voltage (HV) supply for the detector bias voltage (made by the Electronics Laboratory at the University of Oslo).

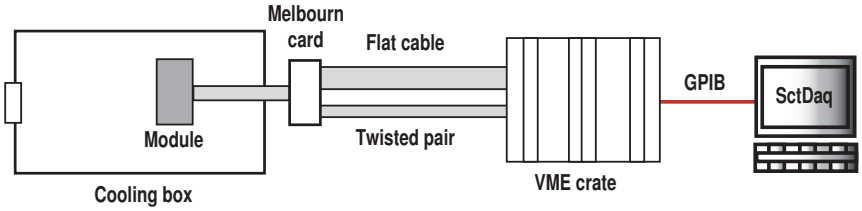

Figure 5.17: Overview picture of the productino DAQ system. The modules, placed inside the cooling box, were read out via a patch card from Melbourne, by two flat cables to a VME crate containing the SCT DAQ hardware. The system was controlled by the SctDaq program running in a PC reading the values over a GPIB bus.

All signals and power were distributed to the modules by two cables via a Melbourne patch card which transformed and redistributed the signals to be conform with the detector requirements. All cables were shielded with aluminium and different grounding schemes were tested to find the operation condition with the lowest noise. The grounding scheme chosen was to ground the module box at as low impedance as possible and to connect it to the module ground (AGND/DGND) on the patch card. The cable screens were connected to the AGND on the LV3 card.

The DAQ software permitted the following functions in accordance with the description in chapter 4, but by using this older model of the SCT DAQ system as described above. Two sequences of tests, the characterisation sequence and the confirmation sequence were needed for the module qualification. The characterisation sequence performed a complete determination of the module performance. The confirmation sequence was a shorter version to be used more often, for instance after mounting or shipment, to verify more rapidly that no damage had occurred. From the tests described in chapter 4 and listed in table 5.1, the two sequences contained the following sub-test:

- Characterisation Sequence = A, B, C, D, E, F, G, H, I , J
- Confirmation Sequence = A, B, C, D, E, F

5.4 Electrical Test Results

Three relatively good modules were tested to verify the functionality of the electrical test setup. One of the modules, 20220380200043, was from the SCAND preproduction series and was shipped from Bergen. The other two modules 20220380200015 and 20220380200016 were both pre-qualification modules from the SCAND cluster. The first of the prequalification modules was tested cold (with a hybrid temperature of 7°C) and the second rather warm (with a hybrid temperature of 20°C) and their results are presented in table 5.1. The module requirements for cold tests, as listed in chapter 4, permits no more than 1% of the read-out strips to be

Modules		QA Module	QA Module
SN		20220380200015	20220380200016
RUN		155	166
A. Hard Reset		passed (0)	passed (0)
B. Redundancy test		passed (0)	12 defects
C. Full bypass test		passed (0)	passed (0)
D. Pipeline test		passed (0)	passed (0)
E. Strobe Delay		passed (0)	passed (0)
F. 3PtGain		passed (0)	passed (3)
G. TrimRange		passed (0)	passed (3)
H. ResponseCurve	Unit	passed (25)	passed (4)
vt50	e^-	142.6 - 147.4	149.0 - 151.5
Gain	mV/fC	52.3 -56.9	52.1 - 55.3
Noise	ENC	1304 - 1552	1486 - 1630
I. NoiseOccupancy		passed (0)	passed (37)
NO	-	2.5E-6 - 6.2E-5	1.6E-5 - 9.1E-4
J. Timewalk		passed (0)	passed (0)
T0 / T1	°C	7 / 7	20 / 20

Table 5.1: Electrical test results from two modules tested in Oslo from the pre-qualification series made by the SCAND cluster as part of the production qualification procedure.

faulty and requires a low occupancy at 1 fC threshold (5×10^{-5}) with a noise less than $\sim$ 1500 ENC.

As can be seen from the results the module 20220380200015 passed almost all of these criteria. The values obtained is within the limit of testing and very compatible with the values measured in Uppsala. For example the noise values are within 50 ENC of the Uppsala values. However the response curve showed 25 failed channels, three due to high gain and the rest detected as partly bonded. Due to a limitation of time and the fact that this module was put on hold due to other reasons further investigation was not pursued further in Oslo. The second preproduction module, 20220380200016, was tested warm and as can be seen from the results also passed most of these criteria. Both the measured values and the few defects present, well below the limit of 15 defects, are good and comparable with the Uppsala values and defects. The slightly high noise values and the high number of strip errors during the noise occupancy test was due to the fact that this module was tested warm. Previous and later cold tests of this module shows that both these errors and the redundant errors disappears and that the module can be considered to be good.

According to [65] the channel defects are divided into two categories: lost channels are the ones having zero efficiency and faulty channels have reduced efficiency. Channels which are dead, stuck, unbonded or noisy are regarded as lost channels, channels which are inefficient, with low gain or being partially bonded are regarded as faulty. According to [73] the produced modules will be divided into the following

categories to be used for the selection of modules to go on different barrels:

- **Good:** Modules that meet all mechanical and electrical specifications. This category is divided into two sub-categories, where one contains the modules suitable to go on all barrels, while the other contains those only suitable to be mounted on barrel 5 or 6.
- **Passed:** Modules which pass all mechanical or electrical specifications except for that it just misses one or more of the mechanical ones. Here the modules are also divided into passed for all barrels or passed-2 for only B5 or B6.
- **Hold:** Modules which are outside the pass limits and are hold up during production. One example of a module on hold is module 20220380200015, which having one mechanical parameter (midfy) value out of the specification is not yet considered for mounting on barrels.
- **Fail:** Modules which are broken or not working and which could never go into ATLAS.
- **Rework:** Modules which could be made usable by performing the necessary changes.

Conclusion

The SCAND production site has successfully contributed to the barrel module production. As already mentioned around 320 modules have been produced and tested by the Scandinavian cluster. Some of the modules have already been mounted and tested on a barrel structure and the performance is in good agreement with modules from other production sites.

A considerable effort was needed to arrive at a set of assembly and test systems which met the high standards of the SCT module production and fitting to the locations of the SCAND sites. Challenging logistics and close cooperation between the sites have been some of the achievements of the groups. In Oslo, an assembly system and alignement procedure, to a large extent self-designed, has permitted the mechanical assembly of the detector. Several test systems as presented in this chapter has been successfully constructed to tests both the mechanical modules and the finished electrical barrel modules. As an example the IV-curve system has been used to successfully test more than 4×320 silicon sensors.

6

SCT Detector Control System - Power, Cooling and Control Hardware

Power supplies in SR1.

Introduction

A large number of hardware systems are needed to control the SCT detector and to supply it with the necessary power and cooling. One of the main tasks of the SCT work during the last couple of years has been to provide such systems, including both the necessary off-detector electronics, control firmware and software necessary for the safe operation of the SCT. One of the main challenges during this development has been to make all DCS hardware parts to work independently and together forming in the end one hardware system for the power and control, one system for the cooling as well as one for the environmental monitoring and a system for the thermal enclosure monitoring.

My contribution has mainly been the testing of power supply hardware and firmware, both with and without dummy modules as well as with real detector modules, both at CERN and in Oxford. I have also contributed to the discussions and development of the communication protocol between the back-end DCS and the crate controller firmware. In addition, I have briefly participated in the development and technology choice of the power pack system.

This chapter starts by introducing the ATLAS framework for the DCS hardware development and continues describing the different DCS hardware parts which are needed to run the SCT detector. The second part of this chapter describes the power supply testing and development which has taken place at CERN. The main goal of this work has been to support the developers in their work. The back-end software described in chapter 7 is based on the hardware and hardware development presented in this chapter.

6.1 ATLAS DCS Front-End Framework

A common front-end system has been developed by the ATLAS DCS group to permit easy implementation of the different sub-detector DCS elements into one common system. This front end I/O system is based on the Embedded Local Monitor Box (ELMB) [74] which has been constructed to simplify the sub-detector development effort. The communication between the back-end and front-end system uses a standard CAN fieldbus and a custom OPC CANopen server, which will be described in more details in chapter 7. A powering device, permitting to power and reset the CAN bus, is also provided by the LHC DCS group. The hardware needed for the detector system is the responsibility of each sub-detector group and the SCT DCS uses the recommented ELMB units, either in the standard edition or in a customised version. Figure 6.2 shows the principle distribution of such a system as proposed by the ATLAS group.

6.1.1 Embedded Local Monitoring Board

The embedded local monitoring board (ELMB) [75] is a general purpose low cost standardised plug in board [76] based on the main AVR micro-processor ATmega128L. A CAN controller manages automatically the communication using the CAN bus

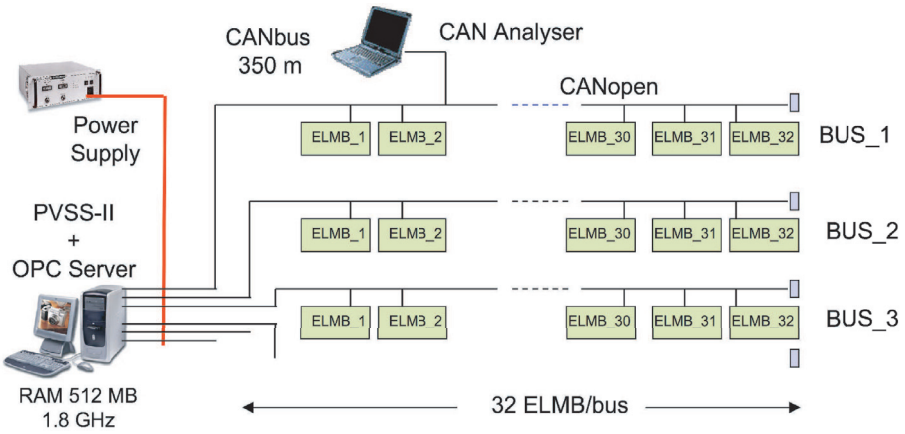

Figure 6.2: The ATLAS front-end framework consists of a PC communicating with multiple ELMBs on several CAN buses. The ELMBs are connected to the sub-detector sensors or other equipment via a dedicated motherboard, either directly using specially developed adaptors or a customised patch card. This picture is taken from [60].

protocol. The ELMB board has a radiation tolerance of up to around 5 Gy and 3×10^{10} neutrons/cm^2 which corresponds to a period of 10 years of operation in the ATLAS cavern. It contains no components sensitive to a magnetic field up to 1.5 T. The ELMB has been designed to have low power consumption and high processing performance, which permits the use of remote power supplies via the CAN bus connector. Three low-drop-out power regulators, with current limitation, are used as filters for the different voltages needed.

The ELMB provides a standard library for monitoring and control of the four differential 16 channel ADC inputs, one 8 bit bi-directional digital I/O, one 8 bit digital output port and one 8 bit digital input port. Mounted on a standardised motherboard, the ELMB can directly read out front-end electronics via a KVASER PCI CAN Card Interface. The motherboard can be equipped with standard adapters such as 4-wire Pt100 sensors (Pt1000), two-wire resistive sensors and differential voltage attenuators. The ELMB library can be used directly or it can be fully reprogrammed within the CANopen protocol, as it is done for the power supply system described in chapter 6.2.1.

6.2 Hardware Controlled by the SCT DCS

The hardware controlled by the DCS has as function to provide the operating conditions of the SCT detector as well as to control some detector functionalities needed by the DAQ. The main operation conditions described in chapter 3, which put the

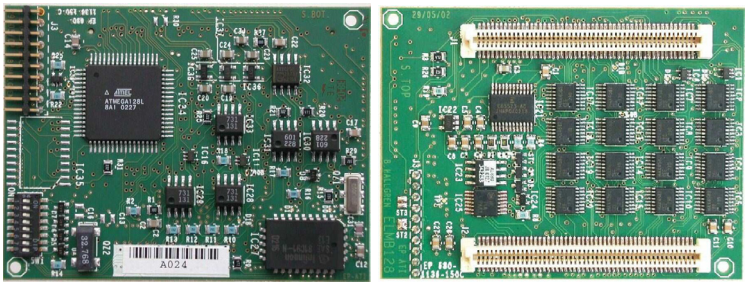

Figure 6.3: The ELMB electronics board. Left, the front side with the address switches in the bottom left corner. Right, the back of the board where one can see the two white connectors, which permits the ELMB to be plugged into the motherboard. Both pictures are from [74].

largest constraints on the hardware development, are the provision of a changeable bias voltage from 150 V up to 500 V due to radiation effects and the cooling of the detectors down to −7°C.

Figure 6.4 is a schematic overview of the different hardware parts, which the SCT DCS controls. The low voltage and high voltage powering and detector control are taken care of by the power system that consists of two parts: The power supply system (PSS) providing the various powers and control signals to the modules and the power pack system (PPS) providing both the steady 48 V needed for the PSS and additional rack monitoring. A cooling system (CS) takes care of the SCT (and Pixel) detector cooling, down to the operating temperature. The sensors of the environmental system (ENV) measure various temperatures and the humidity within the SCT volume. Finally, the Thermal Enclosure (TE) ensures the cold operation of the Pixel and SCT detectors and the warm environment of the TRT. The cooling temperature sensors are also connected to a hardwired interlock system (IS) providing additional safety for the SCT detector.

All SCT hardware subsystems are developed independently of one another within the SCT collaboration at different sites in Europe. For instance the detector cooling system is developed at CERN and the power supply system is mainly developed by the two SCT institutions in Krakow and Prague with the help of other sites. For most systems, a standard ELMB solution is used, except for example for the power supply system (and the final thermal enclosure) where a customised ELMB version is needed.

6.2.1 Power Supply System

The largest and most complex part of the SCT hardware is the power supply system [77]. Each SCT module receives its power and slow control signals by two completely separate, independent and floating power supplies (analogue and digital, insulated with respect to ground and to each other); one for High Voltage (HV)

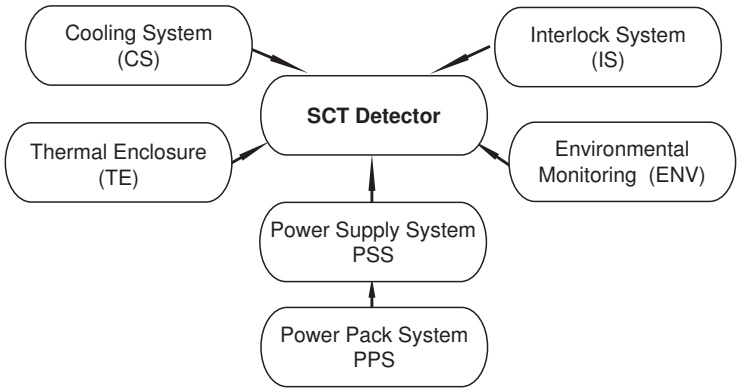

Figure 6.4: Schematic overview of the hardware controlled by the DCS, consisting of the detector cooling system, the interlock system, the power supply system, the power pack system as well as the thermal enclosure. All parts are needed to provide a safe operational environment for the SCT detector.

and one for the Low Voltage (LV). The power supplies are referenced to a common ground on the detector. The connection between the power supplies and the modules are done by a set of cables and patch panels as described in chapter 4.

Figure 6.5 shows a diagram of the power supply system. It consists of 22 racks, each containing four crates, which each power 48 modules. When fully equipped, these 22 racks will provide all power and slow control signals for the whole SCT detector. One crate consists of 12 LV cards [78] with four output channels and 6 HV cards [79] with eight output channels, one crate controller (CC) [78] and one system interlock card (SIC) [80] which interfaces to the interlock system. The communication between the cards and the CC is done via the crate backplane [81]. The LV and HV cards are all provided with power delay circuits, which permit faulty cards to be exchanged without turning off the power to the entire crate, however the channels of the faulty cards should be turned off. All parts of the power supply system follow the ATLAS grounding scheme described in reference [51] and [52].

Both the HV and LV cards are highly complex systems and the development effort has been considerable. The main complexity of the HV card is to provide for a large operational voltage range. For the LV cards, the complexity lies mainly in the many and demanding operational functions needed for the SCT operation. It has been a great effort by the hardware developers to make the power supply system work as well as it does.

High Voltage Cards

The HV card provides the detector bias voltage between 0 - 500 V for a current range of 10 nA to $\sim$ 5 mA. The output voltage is set with 1 V precision and the

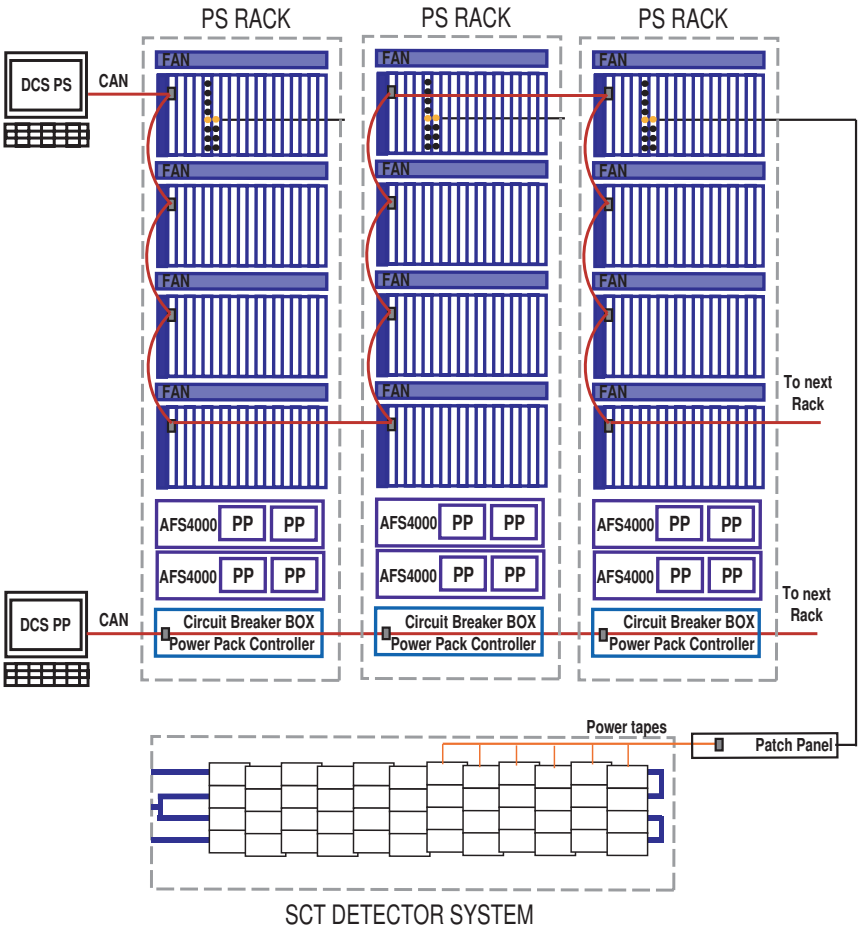

Figure 6.5: The power supply system and the power pack system as installed in SR1. The power supply system comprises the four crates in each rack. The power pack system contains everything else; the four power packs (PP), the circuit breaker box and the four fans. Several crates are connected together and are read out by the same CAN bus system via the crate controller. The power packs systems are readout via a similar CAN bus connected to the power pack controllers. The CAN bus connection illustrated in this picture is only one of several possible solutions.

Probe No.	Resistance	Min. trip limit	Max. trip limit
0	62000 Ω	-	37 nA
1	12000 Ω	37 nA	190 nA
2	2400 Ω	190 nA	970 nA
3	430 Ω	970 nA	5000 nA

Table 6.1: The operating range for the four HV current probes. Each probe permits to read out bias currents in a certain range, from around 40 nA to around 5 μA. This, among other functions, permits the user to read out IV curves.

accuracy of the voltage read-back is better than 1%. Since the detector operation demands a large current range, each output channel is provided with four probes of the ADC (resistor). These are automatically changed according to the current values. The different ranges for each probe are shown in table 6.1. The current accuracy corresponds to the precision of the 10-bit ADC at each current range. The ramp-up and ramp-down speed can be programmed and lies between 5 - 50 V/s. A programmable current trip limit can also be set by the user to protect the module for over-currents up to 5.8 mA, where an absolute hardware protection will automatically reduce the output voltage and trip the module after 1 ms. The HV cards are designed to operate at temperatures between $0 - 35°$C, measured in the rack.

Each HV card consists of a card controller (ADμC812 micro-processor) and eight channel controllers. The main functionality of the card controller is to receive commands from the backplane and transmit them to the relevant HV channels using serial links equipped with opto-couplers. Furthermore, the controller is designed to read back values from the HV channels and, on request, to send them to the crate controller via the backplane. The card controller is also responsible of the enabling or disabling of HV channels (mask). Other tasks of the card controller are to prepare and send the status control byte of the card itself.

All eight HV channels consist of micro-controllers, which read the output voltage and current every millisecond. Each HV channel is responsible for setting the ADC parameters for the requested bias voltage, read the output voltage and current. It also needs to compare the current value with the trip limit, react to interrupts from the card controller, perform internal self-consistency checks and do calibration tests. Table B.3 in annex B.3 shows which HV parameters can be set and read by the DCS system through the crate controller.

Low Voltage Cards

The LV cards provide several logical signals and voltages to the SCT modules. In addition, they provide monitoring of the module voltages, currents and temperatures. Around 25 parameters need to be set or read by the DCS from each LV channel. Details of the LV parameters operated by the DCS software can be found

in table B.4 in annex B.3. The voltages provided by the LV cards are the following four, used both for the opto-packages and for the ASICs:

- *Analogue voltage (V_{cc}):* Provides power to the analogue part of the 12 chip ABCD3T, typically 3.5 V at 900 mA.
- *Digital voltage (V_{dd}):* Provides power to the digital part of the 12 chip ABCD3T, the DORIC4 chip, the VCSEL driver circuit, the VDC chip and other electronic devices, typically 4.0 V at 570 mA.
- *VCSEL voltage:* Provides the VCSEL control voltage for the opto-package, typically 4 V.
- *PIN bias voltage:* Provides the bias voltage of the PIN photo diode in the opto-package of the detector, typically 6 V.

Four sense wires are used to probe remotely these voltages on the hybrid, to detect abnormal voltage drops and to adjust the ASIC voltages at the modules to be stable. The main detector control and monitoring parameters, which permit a safe operation, are the following items:

- *Module Reset:* This signal issues a hard reset command to the module electronics.
- *Clock Select:* This signal line permits the user to tell a module to read the clock and commands from its neighbour module. This link has been provided for redundancy.
- *Temperatures:* NTC thermistors ($R25 = 10\,k\Omega \pm 5\%$) mounted on the detector modules (two for the barrel and one for the end-cap) provide independent temperature readout from -29°C to +70°C.
- *Mask:* Permit to enable or disable modules. If one channel is masked off the detector module connected can not be operated nor monitored.
- *Output on:* This LV card option permits the user to read the module temperatures keeping the module powering disabled.

One LV card consists of one card controller and four LV channels. The card controller receives commands from the crate controller via the backplane and transmits them to the channels. Monitoring values are transmitted back to the DCS system. The card controller can enable or disable the output voltage of each channel, reset and monitor channels and handle interlock signals. If there is a loss of communication to a specific LV channel, the controller switches this channel off and signals a software trip. If the card itself overheats, the controller shuts off the card and signals a card temperature trip. The controller is also responsible for preparing and sending a status control byte of the card itself. After any over-voltage and over-current trip

a reset of the channel must be issued to continue operation. The LV card working conditions are from 10 to 40°C.

Each channel of the LV card consists of two fully separated, floating multi-voltage supplies for the analogue and digital voltage. Each channel is operated by its own micro-controller of the type ADμC812. This controller operates the switching regulator for the main voltage and linear regulators for the VCSEL and PIN bias voltage. Monitoring of the LV parameters is done each 2 ms and stored in the channel controller memory. The controller trips off the channel in case of Vcc and Vdd over-voltage, Icc and Idd over-current and over temperature. Any faulty sensor gives an alarm, and both programmable and hardcoded limits result in trips.

Backplane and System Interlock Card

Communication between cards in the crate is made via the backplane bus [81]. TTL signals allow for 1 byte parallel communication using a custom protocol. All lines are terminated on both sides of the backplane. This provides an interface between the power supply cards and the crate controller. All cards are addressed by their position in the crate; each slot corresponds to one specific address. The custom protocol uses eight bidirectional I/O lines for transmission of data and address, four I/O lines for control of signals and two I/O lines for Reset and Interrupt Request (IRQ) signals shown in table 6.2. The Read and Write cycles are shown in figure 6.6 and differ only by the change in TTL level for the R/W line.

D/AD 0 - D/AD7	data/address 8bit bus
DS	data strobe (active low)
AS	address strobe (active low)
BA0 - BA4	board address defined by position in the crate
ACK	acknowledge (active low)
R/W	read = high, write = low
IRQ	interrupt request (active low)
RESET	reset generated by crate controller

Table 6.2: The backplane signal lines.

Crate Controller

The crate controller (CC) [78] controls all crate operations and translates the 1 byte parallel TTL communication from the backplane protocol to the CANopen protocol and provides an interface between the power supply cards and the DCS software. The CC is made of a general purpose ELMB mounted on a custom made motherboard located in the second slot of each PS crate. The CC card is powered with 12 V from the backplane in addition to the 12 V transmitted via the CAN-bus needed for the CAN-transceiver. In addition, a hardware reset circuit permits safe recovery from the situation when the communication between the ELMB and the OPC CANopen server is lost without interfering with the PS cards.

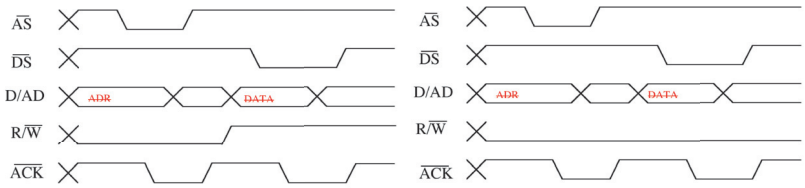

Figure 6.6: The backplane communication. Left a readout command, right a write command, which differs only by the R/W line going high or low. The Address Strobe (AS) goes low to trigger the reading of the address, which is being acknowledged on the ACK line. The data is read or transmitted when the Data Strobe line goes low. These figures are taken from [82].

The crate controller firmware has been written using ICCAVR 6.0 tool from Image Craft. The original code for the ELMB has been substantially modified for our non-standard use of the ELMB. The crate controller program has three main functions. One is to transfer control and monitoring commands via the backplane, another to perform certain safety checks of the system. Finally, all information from the crate is transferred to the DCS system on request, via a standard CAN interface. One of the routines provided by the crate controller is the performance of an IV curve, by scanning the voltage and recording the bias current, for one or more HV channels.

To connect the power supply system to the interlock system, a system interlock card (SIC) is mounted in the first slot of each crate [80]. Thirteen hardwired signals, 12 from the environmental system (cooling temperatures) and one from the ROD system (common for all VCSEL lines of every LV card in one crate), are received by the card from the interlock system and transferred to the backplane. These signals are TTL levels with active low and inactive high which will shut off all VCSEL voltages if the VCSEL line goes high and one of the LV cards if one of the interlock lines lines go high. When an interlock fires, there is no controlled ramp down, the voltage will drop passively according to RC characteristics.

6.2.2 Power Pack System

The main task of the power pack system is to provide the 48 V and 12 V power needed by the power supply system. All power supply racks, as seen in figure 6.5, contain two Artesyn (ASF4000) shelves with two powerpack units each, whose main task is to provide the 48 V $\pm$ 2.5 V DC nominal power at 1 A (fused at 2 A - 40 W maximum) to the four crates of the rack. The powerpacks provide redundant powering by using four parallel powerpack units of which three would have been sufficient. In addition it provides the 12 V needed for the card controllers. The 5 V needed for the the backplane communication is taken from the backplane (48 V) of each and transformed by a DC/DC converter to 5V at 550 mA (fused at 1 A) needed for the backplane communication and the interlock circuit.

In addition, the power signals go through a circuit breaker box, with 12 circuit breakers, situated below the shelves in the rack, which will cut the power in case of over-current to each 1/3 of a crate. This splitting of the 48 V from the power packs into 12 segments has been done to protect the crate backplane lines by limiting the maximum current of each segment. Finally, each rack contains four fans, one for each crate.

To monitor the crate powering, a powerpack controller has been designed which consists of an ELMB mounted in the circuit breaker crate and is connected to the output lines via a minibackplane. This controller continuously reads out the Artesyn power shelf signals such as missing module, AC good, power good, over temperature and current values, so that a failed powerpack can be detected and replaced. The power pack controller will also be used to monitor the fans, door switches and an extra connector is provided for some additional sensors. The power pack controller may control two reset lines, one to each shelf.

All powerpacks will be readout through one or more separate and individual CAN buses. The powerpacks have just been produced and will need to be tested before any final decision on the layout can be taken.

6.2.3 Cooling System

The Inner Detector cooling system [83, 84] will cool down the SCT and Pixel detectors to the needed operational temperature for irradiated detectors of $-7°$C. Warm runs of $+15°$C for initial testing must be permitted. The total system must remove 60 kW of heat and have a stability better than $\pm 2°$C with a minimum of thermal shocks and cycles. To achieve this, the SCT and Pixel circuits will be cooled to $-15°$C using an evaporative fluorcarbon cooling system with C_3F_8 running in thin wall CuNi (SCT) or Al (Pixel) cooling tubes through the detectors with good thermal contact to each module. Independent programmable logical controllers (PLC) control the cooling process.

According to [85], the cooling process in the sub-detectors starts by the delivery of the cooling fluid at room temperature from the condenser to the capillaries, located close to the detector structures. The fluid is non-flammable, non-conductive, radiation resistant and has a good heat transfer coefficient and a small vapour specific volume, which results in minimal tube sizes. When passing through the capillaries, the fluid expands and enters the cooling tubes on the barrels and disks. It remains in a saturation condition (boiling) as it passes the detector modules. The geometrical properties of the capillaries are adjusted to the power dissipation of the module and define the mass flow of the cooling circuit. Heaters are mounted on the exhaust of the detectors to eliminate any condensation on external surfaces and to evaporate any residual liquid still in the system. This also raises the overall temperature above the cavern dewpoint (12° C) before the coolant enters the compressor. Heat exchangers are installed between the warm inlet and the cold return liquid, which increases the efficiency of the system. Higher efficiency permits a decrease of the coolant flow and the amount of insulation needed.

Figure 6.7 shows the schematic drawing of this cooling system. One part consists

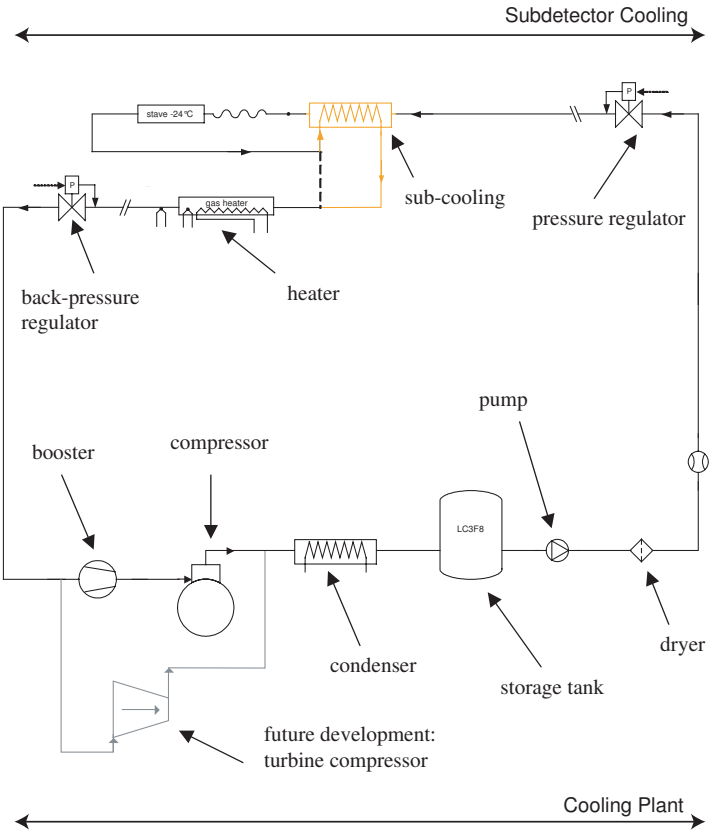

Figure 6.7: The bottom part of this drawing shows the cooling plant and the top part the sub-detector cooling system. The cooling plant consists basically of a compressor, a condenser and a pump, which transforms the vapour from coming from the detector exhaust tubes back to liquid. The liquid then re-enters the detector structure via capillaries and starts boiling. After passing through the detector tubes all liquid has been transformed to gas, any residual liquid is evaporated by heaters at the exhaust. One pressure regulator and one back-pressure regulator regulates the flow and thus the temperature. This picture is taken from [85].

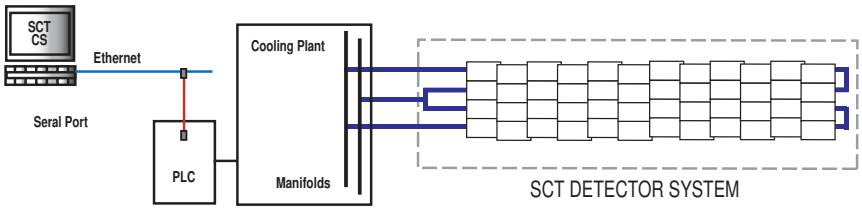

Figure 6.8: The DCS view of the cooling system. The cooling DCS software receives information and issue commands via ethernet connections to the PLC, which controls the cooling plant. In this ways any information to and from the cooling system can be exchanged with the DCS software. The SCT detector tubes are connected to the cooling plant via manifolds.

of a cooling plant with pneumatic and distribution racks. A section of sub-detector manifolds, one for the SCT barrel, two for the SCT end-cap and three for the SCT thermal enclosure, with its back-pressure and pressure regulators are also considered part of the external system. The internal part contains the 244 independent cooling circuits, which are part of the different SCT and Pixel detector structures. Each of these cooling circuits consists of one heat exchanger, 1-3 capillaries, the detector cooling tubes, one heater on the return line and the piping connections to the external system.

Figure 6.8 shows how the cooling system integrates into the SCT DCS back-end system. The DCS is connected to the PLC controller via ethernet. The PLC monitors and controls the cooling plant and gives back status of the cooling system and alarms.

6.2.4 Environmental Monitoring

Environmental monitoring is needed to supervise the running conditions for the SCT detector, in particular the temperatures on the cooling exhaust tubes (176 NTC sensors for the barrels). To measure this, two temperature sensors are mounted for redundancy on the cooling exhaust tube. In addition there are sensors near the edge of the barrel, which measure the temperature changes of the carbon-structure and give an indication of the possible barrel deformation. Both the air temperature and the humidity are measured inside the barrel and are used for the calculation of the barrel dewpoint. The number and organisation of these sensors for the barrel (similar for the end-cap) is shown in table 6.3.

The sensors used to measure the temperatures are negative temperature coefficient (NTC) thermistors with a two-wire readout. The humidity sensors are radiation hard Xeritron sensors, using 6 wires in 3 twisted pairs. Custom ELMBs situated in a BBIM [86] crate are reading out these sensors. Figure 6.9 shows a schematic drawing of the environmental system.

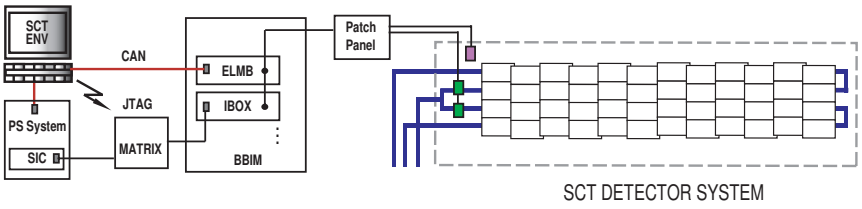

Figure 6.9: The environmental system and the interlock system. The environmental system includes the sensors on the barrel structure and the cooling tubes, necessary patch panels and the readout via several ELMBs mounted in a Building Block Interlock Monitoring (BBIM) crate. The interlock system contains a read-out of the cooling tube sensors only via several IBOXes in the same BBIM crate. The signals are routed to the right power supply cards via an IMatrix box.

Barrel	Cool. Temp.	Mech. Temp.	Air Temp.	Humidity	Total No.
B3	32	9	32	4	77
B4	40	11	32	4	87
B5	48	13	32	4	97
B6	56	15	32	4	107
Total	176	48	128	16	368

Table 6.3: Number of environmental sensors for the four barrels, divided into temperature sensors for cooling, mechanical deformation and air as well as humidity sensors. The number and distribution of sensors are similar for the end-caps.

6.2.5 Interlock System

The NTC sensors on the cooling tubes are also connected to the interlock system which provides a detector safety system purely in hardware. Figure 6.9 shows the different elements of the interlock chain. An interlock box (IBOX, [87]), situated in a BBIM crate, compares each input signal to a fixed threshold, resulting in a digital signal, a two bit pattern representing the different error conditions in negative TTL compatible logic. The SCT detector only uses the high temperature error condition. Hardware modifications are required to change the IBOX operation conditions. The BBIM crates have each 20 slots. Four slots are occupied by ELMB boards (with 64 channels each) and each ELMB is situated between four IBOXes, which gives a total of 16 IBOXes per crate.

After the IBOX, the signal goes to the interlock matrix (IMatrix, [88]), which consists of a map, in the form of a matrix, between the sensors and the module power. The output of the IMatrix is hardwired to the SIC card, one in each crate. 12 of the SIC channels are connected to the 12 LV cards in one crate each corresponding to four modules. In case of a high temperature on one cooling tube, the IMatrix sends the high TTL signal to the SIC card, which distributes it to the cards linked

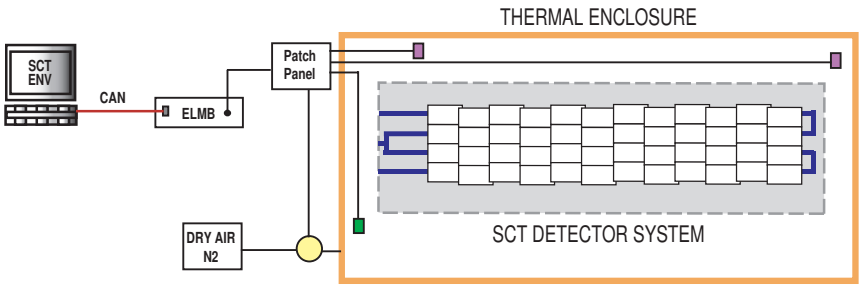

Figure 6.10: The thermal enclosure protects the SCT and Pixel detectors from the TRT environment. It surrounds the two detectors and the DCS software is responsible for reading out the sensors on the inside of the enclosure to monitor its operation. This is done via standard ELMBs reading temperature, humidity, pressure and dry air sensors via a patch panel.

to the 12 modules on this tube. The IMatrix is reprogrammable using a JTAG serial interface [89]. The 13th input is for the VCSEL interlock signal, which will cut the VCSEL power to the modules. Eight other I/O signals are available for additional interlocks.

6.2.6 Thermal Enclosure

The purpose of the thermal enclosure is to provide a thermal shield between the SCT and Pixel detectors which are operated at -7°C and the TRT detector, which operates at +20°C. This is done by a multilayered mechanical structure that consist of a cylindrical support with an inner and outer carbon-fibre wall filled with gas to improve the thermal insulation characteristics. Heater pads will be placed on the external wall to heat it up. Cooling circuits will be attached to heat-spreading foils on the inner surface, which also act as a Faraday cage, to cool this side down.

The temporary thermal enclosure, shown in figure 6.10 which is built for the barrel acceptance tests of the SCT, is monitored by a set of NTC temperature sensors, humidity sensors and differential pressure sensors, with a flow controller for the dry air monitoring. These sensors are read-out by a standard ELMB on a standard motherboard using adaptors to account for the sensor differences. The ELMB channels have been grounded to avoid noise interference.

6.2.7 Hardware Interactions

Figure 6.11 shows an overview of the different hardware parts in a simplified way. The cooling system binds the parts together; whenever it stops working the environmental system will give errors, the interlock system might fire and stop the power supply system. If the power packs are malfunctioning, circuit breakers will stop the power supply system by cutting off its power. Care has been taken during

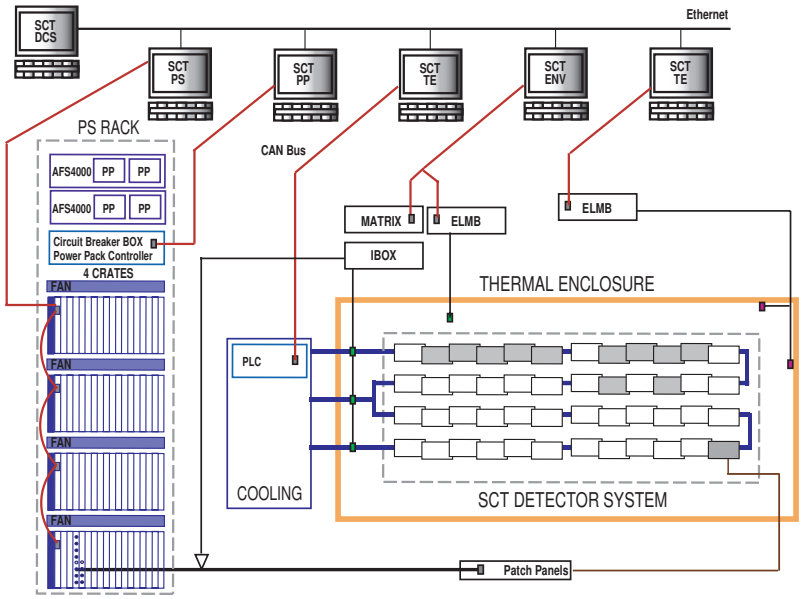

Figure 6.11: Overview of a small subset of the SCT hardware showing the links between the different systems. On the very left hand side is shown a rack with the power supplies and the power pack systems (bottom part). Next to it can be seen a simplified version of the cooling system which is connected to the SCT detector system. The six different hardware systems controlled by the DCS are connected together in the following fashion: The interlock system acts as a hardware interface between the cooling and the power supply system, and can cut the power directly.

development, especially of the back-end system, that all hardware parts function well together and provide the necessary detector protection.

6.3 Power Supply Development

Quite some time and effort during the SCT hardware development have been invested in dedicated tests of the power supplies in order to help the hardware and firmware developers. The discussions with the same developers have also proven highly valuable in the DCS software system development described in chapter 7. As a direct result of the testing, both firmware and hardware of LV, HV, CC and the design of the backplane have been subject to several adjustments and modifications. Some examples are a new backplane design, modification to the HV card design and the implementation of reset lines of both crate and power pack controllers. On the firmware side, the main effort has been to discuss and implement a proper CAN

communication between the back-end system and the CC. A whole new set of crate controller and back-end software operations has been defined.

Power supply tests were mainly done at CERN but also at the Oxford macro-assembly site. The first tests at CERN were made with one crate using a few HV and LV cards and with one module occasionally connected. The last scale-up provided for the barrel testing at Oxford and CERN consisted of eight fully equipped crates using power supplies to test the 384 modules mounted on barrel 3. All tests have been made using the DCS software as described in chapter 7. Continuous modification of this system to adapt to the front-end system is an ongoing process.

A selection of the main test results is presented below. Many of the tests resulted in minor changes, but presented here are some of those which for one reason or another made the power supply development advance significantly and improved the reliability and stability of the system. The results presented are also only those which occurred directly from the CERN or Oxford tests.

The qualification of the hardware has not only come from the dedicated tests but also from continuous module testing and realistic use of the power supplies in both the macro-assembly sites and in Testbeam. This has gone on for more than a year (around 6 months for Testbeam) and has been an important contribution. Results from the Testbeam, which shows the functionality of the hardware presented here will be presented in chapter 8 and the macro-assembly results will be presented in chapter 9.

Noise studies

One of the first studies made was a noise comparison between the old power supply system (LV3 and HV3) and the new ones (LV0 and HV0). Both sets of power supplies were connected to the same data acquisition system running the same software (SctDaq, presented in chapter 5). The module was in the same environment during testing, except that the old power supplies were connected to it with a short cable and the new ones via a patch panel (PP3T) and a long thick cable ($\sim$ 20 m).

After power on, the reception of the clock/2 signal from the module was checked before proceeding with the noise scans. The scans performed on both setups were a 3Pt gain scan and a noise occupancy scan. The result of this test is shown in figure 6.12 and the corresponding values in table 6.4. For both systems, the noise and the occupancy were in good agreement. In addition no particular effects due to the temperature should be present since it was run under identical conditions.

The noise level was between around 1550 and 1800 for both power supplies and the gain between 50 and 55. The noise occupancy was between 3.4 E-5 and 6.3 E-6. The occupancy is slightly higher for the old power supplies than for the new ones. The conclusion of these tests was that the new power supplies were successful, however any improvements in noise levels where not made.

Glitches

One of the first major discoveries of the power supply testing was the finding of glitches on the backplane of the power supply crate. The symptoms of this problem

PS	Gain mV/fC	Offset	Input noise ENC	MeanOcc
LV/HV0	48.7 - 55.0	11.4 - 17.9	1541 - 1788	3.4E-5 - 4.2E-6
LV/HV3	49.6 - 54.9	38.2 - 42.8	1589 - 1764	3.9E-5 - 6.3E-6

Table 6.4: Results from the noise tests of a module with the new and old power supplies.

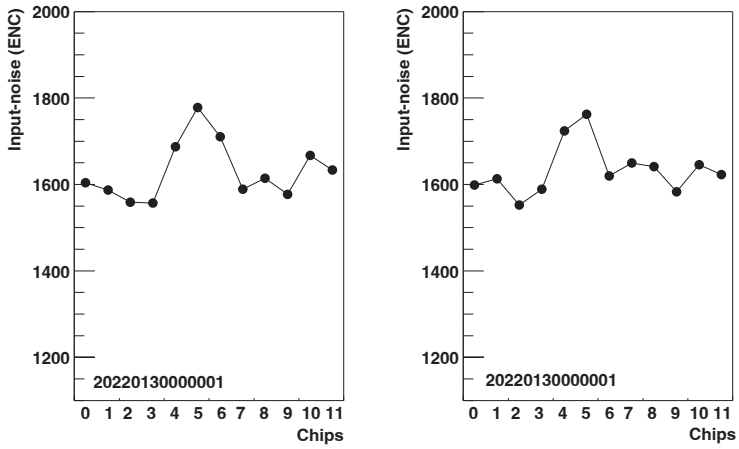

Figure 6.12: Left, ENC noise from the old power supplies. Right, ENC noise from the new power suppliers, at $\sim 28°$C. The plots shows the noise levels for each of the 12 chips. The difference between the two power supply cards can bee seen to be minimal.

were that the LV and HV cards tripped in random fashion without any load on the output. The channels either tripped when the power supplies were turned on or off, during an operation, or when the power supplies were on and stable (between operations). The glitches observed are shown in figure 6.13, top. A logic analyser, connected to the backplane and triggered on pulses shorter than 8 ns, produced this picture. The detected glitches are seen as dashed lines. These glitches resulted in the malfunctioning of the cards since they were detected by the card controllers and disturbing the real commands and addresses.

One solution to this problem was to change the LV firmware to avoid these signals, but the glitches first disappeared when the backplane was redesigned. The new design added a ground plane parallel to the signal lines, and termination, to establish a stable impedance. Figure 6.13, bottom, shows a logic analyser picture of the same test of the modified backplane and as can be seen the glitches have disappeared.

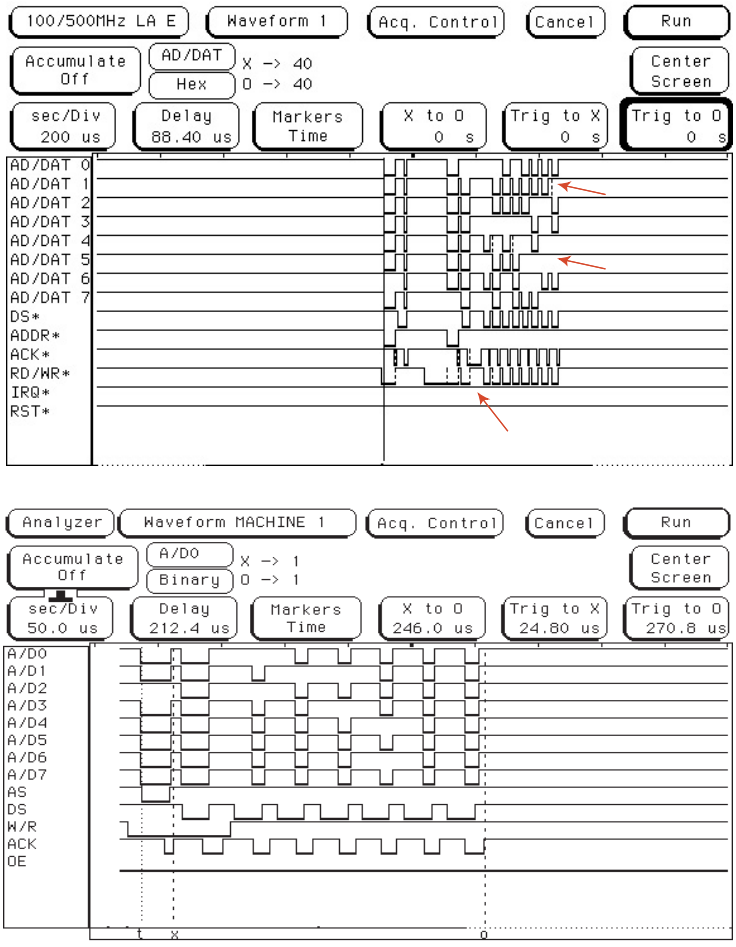

Figure 6.13: Top: Before changes to the backplane were made, we saw sporadic glitches (arrows) between the bits sent on the backplane which clearly disturbed the communication and made both LV and HV channels trip. Bottom: After redesigning the backplane no such glitches could be observed (Here the picture was enlarged to really see if the glitches were gone). The bottom picture is taken from the Krakow group, the top picture was taken by the CERN group.

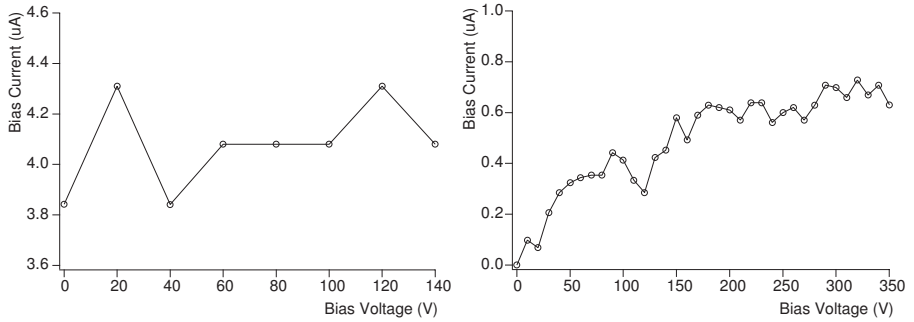

Figure 6.14: Left, an example of an IV curve using original firmware without dynamical change of probe. Right, a typical IV curves after changes to the firmware.

HV current probe

The HV initial firmware implementation of the current probe operation needed to be adjusted. As previously explained, the module bias current is read by the HV card by the use of several probe resistors listed in table 6.1. In the original code, the HV card chose the probe resistor to be used dependend on which current trip limit had been set. If the current dropped or rose a different probe for readout of the current was not automatically changed, which resulted in current readout of the minimum or maximum value of the original probe and not the real value.

This had two problematic effects: first, that there was no reliable bias current readout during ramping and secondly, that IV curves could not be performed. Typical current values during ramping are 1 - 2 μA which are much higher than the typical 4 - 800 nA measured after stabilisation. For an IV-curve, the current values changes typically between 0 and several μA depending on the quality of the module tested, the voltage and the point of sensor breakdown. An example of a malfunctioning IV curve can be seen in figure 6.14, left. Here the IV curve did not start at 0 V but at the minimum value of the set probe. In addition the current oscillated strongly, much more than the current resolution of $\sim$ 50 - 80 nA.

A new firmware solution has solved this problem by adding two new features. First, the chosen probe is no longer linked to the trip limit value set by the user, and secondly it now automatically changes with the actual current readout (dynamical change of probe resistor). When the card reads out a value, which is close to the probe limit, the probe is changed. Figure 6.14, right, shows an example of how an IV curve looks after the changes. There are still some oscillations due to the values being of the order of the HV card resolution. Time averaging of the current values can solve this, however investigation is ongoing to where this should best be made. The easiest implementation could be in the DCS software.

HV transistor failure

After running for a certain amount of time and after running a full rack, the HV channels started to break down. As many as 12 cards with 12 channels broke in SR1 and around three channels broke in H8 on different cards. At the macro-assembly sites also single channels where broken, but not in any operational system. The symptom of the breaking process was that channels tripped because of over-current and the output fixed at around 700 V (672 - 701 V), which is 200 V more than the maximum permitted output value allowed for the modules. Another symptom was that it was not possible to recover from this state. The cards should have had a safety limit at 500 V to protect the modules, but we discovered that this was not the case. After a failure, maximum voltage was transmitted to the module. Finally, two problems were identified; the failing of a channel-specific high voltage Field-Effect Transistor (FET) and the failure of the firmware voltage protection routine.

The reason for the FET failure is still being investigated, but there is reason to believe that they have been caused by poor contact of one or more FET leads by using the wrong solder in the manufacturing process. In addition, the leads are subjects to stress during temperature cycling which could have affected their connection. It has been demonstrated that if a FET has one floating lead it will die. The firmware failure was due to a wrong design of the HV card operation. The original hardware design should have included a clamp or hardware shutdown of the power as to prevent overcurrent spikes. Both the design of the hardware and the firmware was inadequate to handle such a failure mechanism.

A simple protective fix was proposed as a short time solution to be able to continue mounting modules at macro-assembly sites, while working on finding the cause of this problem and to develop a final solution. The hardware fix consisted of replacing one diode on the output of the transistor with two Zener diodes in series to limit the over-voltage. The Zener diodes where chosen such that the maximum bias voltage limited the spikes below 500 V. The firmware has been modified to shut down the channel if an over-voltage condition was detected. The original firmware was not able to do this, because the channel controller, which sensed the over voltage condition, could only shut down the channel via the transistor which had failed. The new firmware transmits the command from the channel controller to the card controller, which can shut down the input power from the channel. Both hardware and firmware temporary fix needed to be installed. Without the firmware turning off the voltage, the Zener diodes would draw too much current and eventually overheat the circuits.

To be able to proceed quickly with detector mounting, the Oxford site quickly produced this clamp circuit on a separate board for immediate use with the old firmware, while waiting for the modified HV boards. So far this has been successful, but the implementation has several disadvantages and care must be taken during testing to a card failure. If the FET fails, the firmware will not protect the modules and the board might overheat which can result in fumes and in the worst case fire. The boards are situated on the detector support structure close to the modules and they might be damaged. Also these boards limit the amount of voltages applied to

the detectors (around 350 V) and add current to the bias current reading, which makes IV-curves no longer accurate.

A final fix for this problem is under preparation. All FETs on the HV boards need to be replaced, the new ones need to be soldered with the correct solder and the leads will be bend to lessen the effect of any mechanical stress. In addition, the clamp circuit will contain extra circuitry to always have a hardware protection in case a HV card fails and the firmware is not working. This gives three levels of safety and is considered to be sufficient to protect the modules. First tests of this final solution have shown promising results and more extensive tests will be made before changing the HV cards.

HV spontaneous ramp up

We also observed, after turning the channel on, that some of the HV channels started to ramp up to some arbitrary values without having received a command to do so. These values where discrete and typical values observed were 38 V, 270 V and 511V. The channels affected were those which were off but with the output enabled. It was noted that the affected channels were randomly positioned in the crate and that the effect occurred randomly over time. Spontaneous ramping also happened with the CC disabled. The solution was indeed found in the HV card firmware and was due to a communication failure between the card controller and the channel controller. The upgraded firmware no longer shows this behaviour.

LV busy problem

During operation of the power supplies we observed that occasionally one or more LV cards would enter busy state (card status 64) and the only way to recover from this situation would be to power cycle the crate. This is not considered to be an acceptable solution since it forces power cycle of the module bias voltage and because it means to power cycle modules which are ok.

The first measure to avoid this, was to implement delays of ~ 50 ms between two commands sent to the LV cards, which is a minimum to avoid the cards to go into busy state. In addition, the CC was made to check the busy status of the LV card before sending it any commands. This improved the situation but did not amend it. It seemed that the proper handshake or time delay were not in place.

Finally, optimising the LV firmware solved the problem. The original implementation did not permit the changing of LV channel parameters when the channel was masked off. When this was tried, the card went to busy state immediately and stayed so permanently. However, the CC has been programmed to do this since it is considered as a safer procedure to first load the values and then to enable the power. The new software has been tested and so far no additional problems have been discovered.

LV communication problems

During operation in H8, it was discovered that if only a subset of the LV channels was masked on during operation, the result was a series of trips reporting Vcc communication error. Due to this single channel operation mode, the communication between the LV controller and the Vcc unit of the LV card was malfunctioning. Apparently, this kind of operation of single channels has been considered non-standard ATLAS operation by the LV card developers and had not been implemented. However, the tests of modules at the macro-assembly sites have proven that this functionality is indeed needed. Changes to the LV firmware have eliminated this problem.

LV startup trips

It was discovered that power supply channels with modules connected to the output often trip at start-up due to the missing clock seen by the module. This is the result of a discrepancy in design between the DORIC operation and the power up of the power supplies. The DORIC design requires all power to be on before the clock is enabled, however the modules requires clock on before receiving the power. When the clock is on before the power, this module occasionally gets into clock/4 mode, which is sometimes difficult to recover from. When power goes on before the clock, the module occasionally trips and has to be masked on and off. In most cases this problem can be avoided by ramping the Vdd in small steps.

Any solution to this problem involves both the DAQ and DCS and their operational states (run states). New SCT run state transition scripts need to be written and tested. For this reason it will be discussed in more detail in chapter 7.

CC and PP reset

During testing it was discovered that there was no reset of the main controller of the CC except to power cycle the crate. This could cause unnecessary power-cycling of the SCT detector, which a remote reset could avoid. By looking at different solutions to this problem, another one was discovered. The custom ELMB provides an automatic reset functionality (watchdog). As shown in figure 6.15, a nodeguarding function resets the digital processor when needed and the digital processor resets the CAN processor via a lifequarding function. In the standard ELMB solution none of the ELMB lines would be affected by this reset and no commands issued. For the CC this is not true, the reset of the digital controller could issue a reset on the backplane (TTL level held high by the CC), which could affect the LV cards. This could not be permitted since this would again cause the LV to be switched off unnecessary.

A new design of the CC was needed, with implementation of a reset line which did not change the crate status. This also had to be added to the concurrent design of the power pack controller. This reset, together with the watchdog functionality, has been tested and proved working.

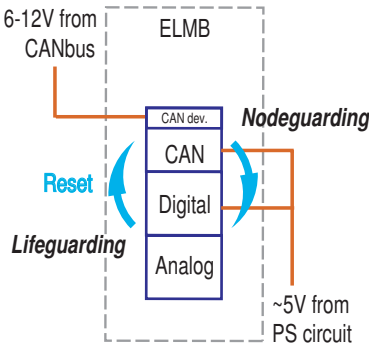

Figure 6.15: The ELMB reset function. The CAN transceiver controls the digital controller by the use of a nodeguarding function. If the latter detects a failure of the the digital ELMB part it will issue a reset. The digital controller uses a lifeguarding function to control if the CAN transceiver is working properly. If not working, the transceiver can also be reset.

Rack temperatures

Figure 6.16 shows the temperature distribution of the cards in one rack. Each line represents one of the four crates, which populates one rack. The temperature lies between 27 - 34°C, where the highest temperature line correspond to the top crate and the lowest to the bottom crate. The racks have been water cooled to 22°C. These temperatures lies well within the LV card specifications (10 - 40°C) but are rather close to the maximum HV card temperature permitted which is of 35°C.

Barrel 3 hardware problems

Some additional problems were discovered during barrel 3 testing in Oxford, and later at CERN, due to the now available high statistics sample. These problems are described in chapter 9, which discussed data taken from this barrel.

Conclusion

Today, a close to final subset of each hardware system has been successfully installed both at CERN, Oxford and the two end-cap sites, Liverpool and NIKHEF. Most, if not all, important aspects of the SCT detector conditions and its challenging operation environment have been provided for. There is still an ongoing development process to improve the hardware and firmware system. Some known failures have still to be resolved and a solution implemented. The power pack system needs to be tested and production started.

The user experience of this hardware system has been very positive. The power supply system has been used for almost two years at CERN and around one year at

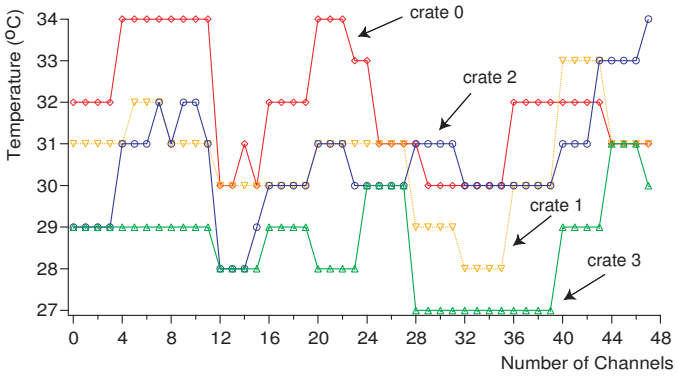

Figure 6.16: The temperature distribution of the cards in one rack. The top crate, crate 0, is the warmest crate due to being furthest away from the rack ventilation. The second crate from the top, crate 1, and the third, crate 2, have both similar temperatures. The coldest crate, crate 4, is the one one the bottom of the rack, closest to the coldest part of the rack fan. This figure was provided by R. Apsimon.

the end-cap sites. Although the development process has been continuous and some important faults have been found during testing, it has been possible to control, monitor and operate modules. Even large scale systems such as a complete barrel have been successfully tested in Oxford. In comparison with the complexity and scale of the power supply system this may be considered as a major achievement.

The cooling has also been successfully installed and operated in Oxford and lately also at CERN. Although the user experience has proven the learning curve of the system in the development phase rather steep, today the cooling system is running stably and can be operated also by relatively unexperienced users in Oxford. The CERN cooling system still has to be tested to its fullest but this is currently being completed with promising results.

Currently, an environmental system has been installed at all sites customised to the need of each user. These sensors are read out continuously and are easily accessed by the users. The interlock system which has been installed first in Oxford have been tested successfully. It has also been proven to function correctly at a few occasions were the cooling system has failed, to the uttermost joy of the barrel operators. A temporary thermal enclosure is in stalled at CERN in SR1 and working impeccably. All these different types SCT specific hardware to be controlled by the DCS has been tested either as prototype or as close to final system and has been working successfully.

7

SCT Detector Control System - Software and Architecture

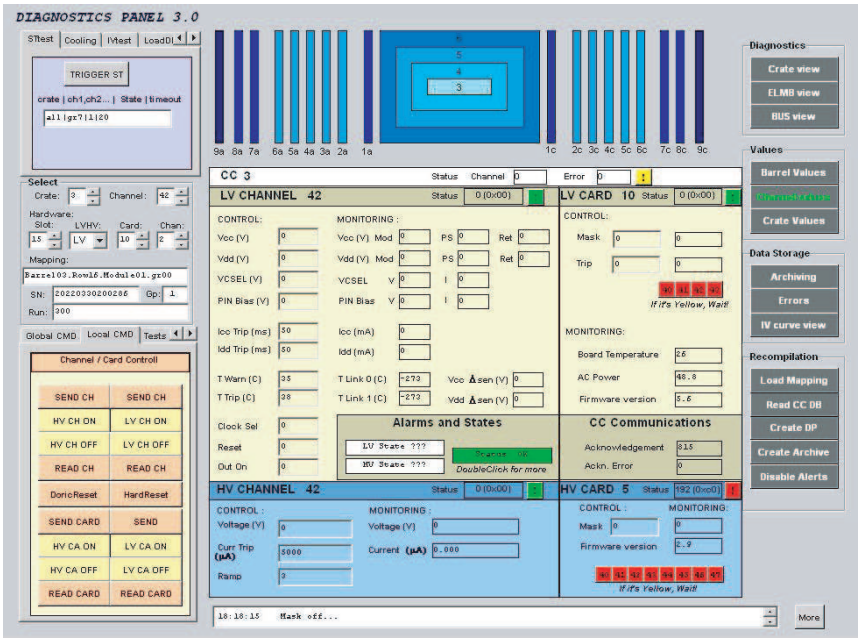

The diagnostic panel of the SCT DCS.

Introduction

Constructing a DCS software for the final SCT hardware has been challenging. Not only is it in charge of supplying the detector with power and cooling, but it also takes care of the detector monitoring and operation. In addition, the DCS needs to ensure that the detector is safe at all time and when it is not, to perform corrective actions initiated either by the software itself or by the user. The process of defining the safe operation conditions, including definitions of the SCT run state transitions and several layers with error conditions, has been a large part of the DCS development. Another important task has been the integration of the SCT specific DCS software into the ATLAS common DCS. During its own development, the final DCS software has simultaneously been used in the development of the power supply system. For this the software needed to be flexible to buffer changes (to the hardware, firmware and software) and providing detailed investigation possibilities. The main responsibility of the software development has been with the SCT DCS group at CERN and Geneva University but with great help and contributions by people from the Oxford SCT Group and others.

During my PhD work I have participated and contributed the SCT DCS from the start of its development. My main contribution has been the design and construction of the main core of this DCS, being responsible for all the control and detector powering (power supply system) together with Pamela Ferrari (CERN), as well as conceptual design for the power pack system and cooling system. I have also contributed to the DCS integration into the overall ATLAS DCS and helped constructing a SCT specific implementation of the DAQ-DCS communication. In addition, I have contributed to the design of both DCS run state transitions and the treatment of SCT error conditions and the safe operation of the system.

This chapter describes the SCT DCS in its current state, however it is a software in constant development, improving as our knowledge about the detector behaviour is increasing. The first part of this chapter describes shortly the framework provided by the ATLAS DCS group. The main part describes the SCT specific software development. Finally, some first estimates of the SCT DCS performance will be made.

7.1 ATLAS DCS Back-end Framework

One important goal of the SCT DCS development has been to implement as much as possible of the ATLAS DCS software architecture to ensure that the final integration will be as complete as possible without compromising the SCT functionality and independence.

The ATLAS DCS is constructed to enable a homogeneous integration of all sub-detectors into a final DCS and to ensure their inter-communication as well as the communication between the DCS and the DAQ. To achieve this, it follows the framework for the back-end system provided by the LHC DCS group based on the recommended front-end electronics. This software consists of a Supervisory Con-

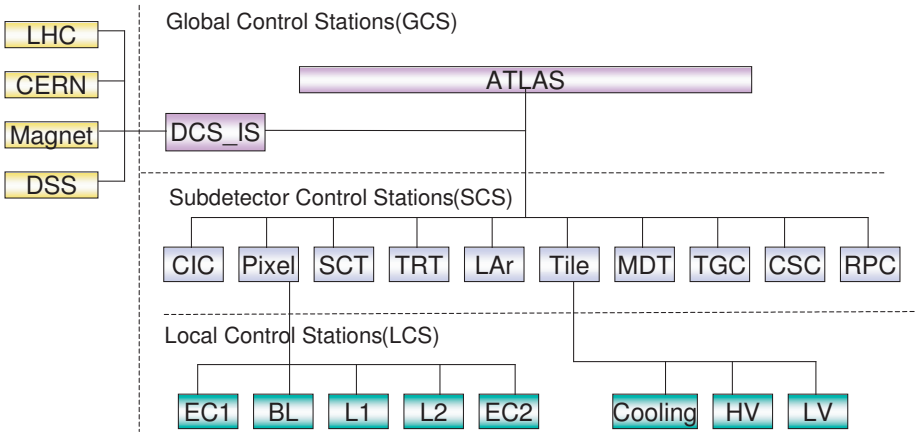

Figure 7.2: The ATLAS DCS system showing the structure of global, sub-detector and local control stations. We can also see the interface to the LHC DCS on the left. This figure is taken from [60].

trol and Data Acquisition program (SCADA) [90], a custom product PVSS II 3.0 from ETM [91], which reads out the CAN bus data using an ATLAS developed CANopen OPC server [92]. The Joint Controls Project (JCOP) [93] provides a software framework, which is tailored to the ELMB front-end solution. This custom solution provides the functionality needed for the ATLAS experiment and a simplified implementation of a large-scale SCADA system. One of its main features, is that it permits updating of values only on change, which limits the amount of data and the traffic on the CAN bus.

Figure 7.2 shows an overview of the hierarchical structure of the ATLAS DCS system by using a finite state machine (FSM) [94]. At the very top is the main control of the ATLAS DCS, which is done by a Global Control Station (GCS) PC. This station controls the overall activity of the ATLAS detector using status messages and alarms and is the interface to the future ATLAS user. The sub-detector control stations (SCS), which consists of one master SCS for each sub-detector, are one level below. These stations are responsible of running the sub-detectors and will validate all commands from the GCS. Some SCS performs additional tasks, such as the Common Infrastructure Control SCS (CIC), which collects information about the overall infrastructure of the experiment. Each SCS controls several local control stations (LCS) per sub-detector. Some LCSs are common for several sub-detectors. For instance, both the Pixel and the SCT are using the ID cooling LCS. One important challenge when developing the SCT specific DCS has been to provide a substructure with its corresponding dependencies, which fits into this overall ATLAS structure.

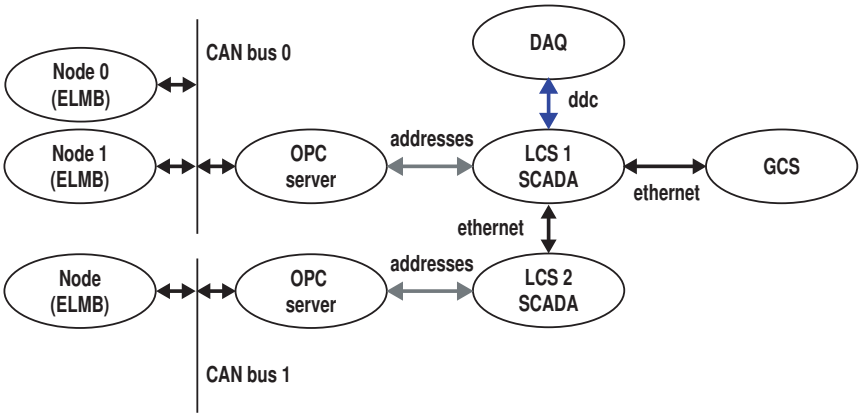

Figure 7.3: The DCS communication chain. One or more nodes on one or more CAN buses (left side) can be read through an OPC server, which transmits the data to the local control stations. DAQ can communicate directly with the lower level LCS, whereas the GCS collects the necessary detector information and displays it for the user.

7.1.1 Software Communication (internal and external)

For all these different DCS system to exchange information within the ATLAS DCS and towards the exterior, such as with the accelerator DCS and the DAQ system, several protocols are used to provide a fast and secure communication. Figure 7.3 shows the different means of communication used within the DCS. There are four types of communication or addressing necessary to run the whole ATLAS detector or one of its sub-detectors such as the SCT; the CAN bus communication, the OPC server to datapoint conversion (address space), the internal DCS to DCS communication and the DDC communication [95] between the DCS and the DAQ. During development of the SCT DCS, a large effort has been put into defining this communication for the SCT detector and to keep it as simple, fast and informative as possible.

According to [96] and [74], the CAN bus communication permits a multi-master hierarchy, broadcast communication and sophisticated error detecting mechanisms. The OPC server application is responsible of requesting and sending messages to the front-end electronics via a PC CAN interface card (KVASER [97]). The protocol used is the CANopen protocol [98] where each parameter on a node on the CAN bus can be accessed via the Devise Object Dictionary (OD) and network management can be performed using the following message types:

- **Administrative message** - Used to perform layer management and network management such as initialisation, configuration and supervision of the network predefined messages.

- **Service Data Object (SDO)** - Provides client access to entries of a device OD by using the objects OD index and sub-index in the first part of the CAN message. This permits transfer of data of any length (in several messages) and the reception of the message is confirmed.

- **Process Data Object (PDO)** - Used for transfer of real-time data from one producer to one or many consumers. Data is predefined and limited to 8 bytes and can be accessed through its CAN identifier.

- **Predefined Messages** - There are several predefined messages used for the network management such as synchronisation (SYNC) messages, time stamps, emergency messages, node and life guarding messages.

All CAN nodes can be reset by the user or the DCS system and go trough the following states while booting: Initialisation → Pre-operational → Operational. Only nodes in Operational state can transfer data to the bus. In addition there are two modes of requesting the nodes to send their data to the OPC server; synchronous mode or asynchronous mode. The first triggers the nodes to send data with a defined time interval either cyclic or acyclic, whereas the second only triggers the sending of data after receiving a remote transmission request.

To transfer the data from the OPC server to the SCADA application, each data value is addressed to point to a variable, called datapoint, in the DCS software. These addresses, used by the OPC server, are stored in a text file database and permit the conversion of the raw data into physical values.

The communication between DCS programs is done by ethernet communication and permits the transfer of status and alarms to other parts of the system and to the main controllers, SCS and GCS. Some effort was necessary to implement this before the release of PVSS II version 3.0 for which it runs smoothly. Now all projects can access the datapoints from all the projects with a minimal effort.

The DAQ-DCS communication (DDC) ensures the coherent operation of the detector and permits a multilevel synchronisation and communication between the DAQ and the DCS system. During physics runs, the DCS will be fully under DAQ control, whereas at other instances the ATLAS GCS will be the uppermost DCS master. The DDC access the DCS at the sub-detector level and its implementation is thus specific for each sub-detector. All control of the DCS through the DAQ will be done via the DDC communication.

The DDC is based on three sets of message transfer, which are shown in figure 7.4. The data transfer facility transfers data using the DAQ Information Service (IS). The operation is bidirectional and it permits synchronisation of configuration/condition parameters. A typical example for the SCT is the need to transmit e.g. temperatures and currents to the DAQ. The message transfer facility transfers messages through the DAQ EPR (Error Reporting Service) unit and is used to transfer alarms and warnings. The DCS command transfer facility is a dedicated run controller which implements the TDAQ finite state machine and permits the transfer of commands from the DAQ to the DCS, such as the change of DCS run state transitions.

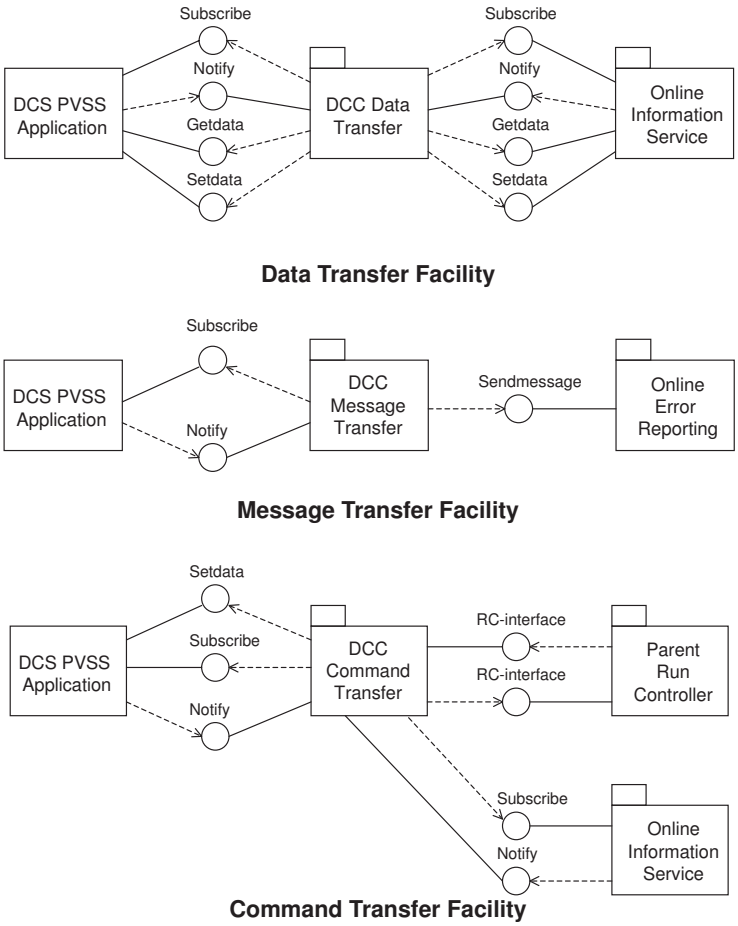

Figure 7.4: The DDC messages. From the top: The data transfer facility takes care of the transfer of data from the DCS to the Information Service, the message transfer facility handles error messages and alarms, the command transfer facility permit the DAQ to take control of the DCS and request certain operations such as the changing of states [60].

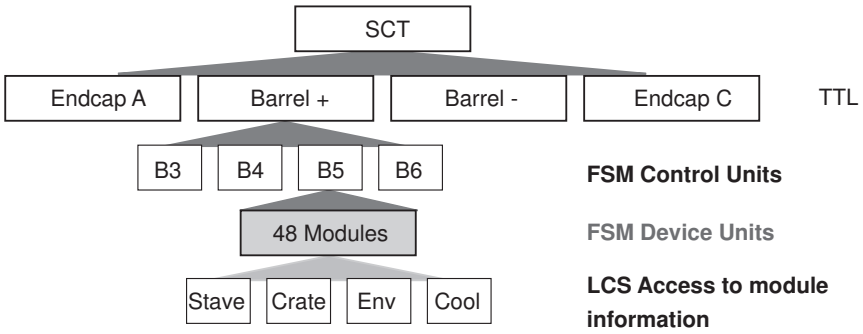

Figure 7.5: The SCT implementation of the FSM. The SCT is divided into several subsystems, which are purely logical on two hierarchical levels. The first levels consists of end-cap A and C and the two barrel sections. Each of the two barrels is divided into four sub-barrels which again are divided into groups of 48 modules.

7.1.2 Software Integration

The JCOP framework started to explore ways of providing a common DCS system for the four LHC experiment. This has resulted in software providing an additional interface between the SCADA projects and the OPC server. The two main achievements of this architecture have been to provide a tailored software for the use of standard LHC components, such as the ELMBs, and as a basis for the FSM introduced in 7.1, which performs the ATLAS top level detector control and management. The FSM permits the sub-detectors or parts of the detectors to be operated in stand-alone mode, which can be needed for calibration scans or separate testing. It also handles user access and the DCS master control (except during physics taking) and it is essential for the coherent operation of ATLAS.

All SCT DCS projects have also been successfully integrated into the FSM and are now running as a sub-detector to a first implementation of a GCS. Figure 7.5 shows this SCT implementation. In the FSM, all objects are divided into control units, which are purely logical devices, and device units, which are directly connected to the front-end system. The SCT detector consists of a hierarchy of control units and is divided into four subdetector parts, one end-cap and half a barrel in both the Z+ region and the Z- region. The barrel and endcap control devices are each divided into 4 barrels and 9 disks respectively. The FSM device units are currently defined as the power supply crate since the CC provides the interface between the module and the readout system. This also represents the transition between device units and control units for the FSM. The operation of the FSM is based on the use of FSM state transitions and error messages which are translated from the SCT specific states and errors. This will be described in detail below.

7.2 SCT DCS Software Development

The DCS system monitors and controls all parameters of the SCT detector system and provides protection for the silicon modules by means of an extensive system of warning and alarms, acting in addition to the hardware interlock system. An alarm will be raised if any monitored parameter, such as temperature or humidity, exceeds a programmable limit. Additional levels of protection are provided within the LV and HV firmware, and the status of the cards is read back by the DCS. Extra functionality has been provided where necessary; for example, enabling and disabling of modules, run state transitions, IV-curves and loading of configuration parameters.

The SCT DCS has been constructed to consist of several local control stations (LCS), each containing one or more DCS projects running simultaneously. As already mentioned, the SCT-DCS will relay on information from many other LCS throughout the ATLAS DCS, such as the CIC DCS and the Beam monitoring DCS. Since the development of an ID cooling DCS has been part of the SCT-groups work, it will be presented here together with all other SCT-specific DCS systems. The SCT DCS have five different subsystems which all have their own dedicated software distributed on LCS machines (Fig. 7.6). One sub-detector Control Station (SCS) is set up as an ATLAS DCS FSM to controls these LCS.

7.2.1 Software Projects

The five subsystems of the SCT DCS all control and monitor certain parts of the detector supplies and are divided into the power supply system, the power pack system, the interlock system, environmental monitoring and the thermal enclosure (see figure 7.6). For all systems a standard ELMB solution is used except for the power supply system (and maybe the thermal enclosure) where a customised ELMB has been developed (as described in chapter 6). All projects provide readout of parameters. In addition, the power supply project is a slow control system, which issues commands to the SCT detector modules. All projects monitor the status of their own communication and issue alarms if it is failing.

The power supply project

The power supply is designed and developed to monitor and control a large number of parameters, which is needed to power and issue slow commands to all SCT modules. The number of parameters per module is around 30, which gives around 1500 parameters per crate or a total of 132 000, which the DCS has to supervise. The hardware details are described in chapter 6. The details of the power supply system and how to run it is described in [99]. Plots showing detector results from using the power supply project will be shown in chapter 8 and 9.

The power supply project monitors and control all power to the module and issue commands via the CC, which either execute a subset of command or transmits the single commands to the power supply cards in one crate. These commands

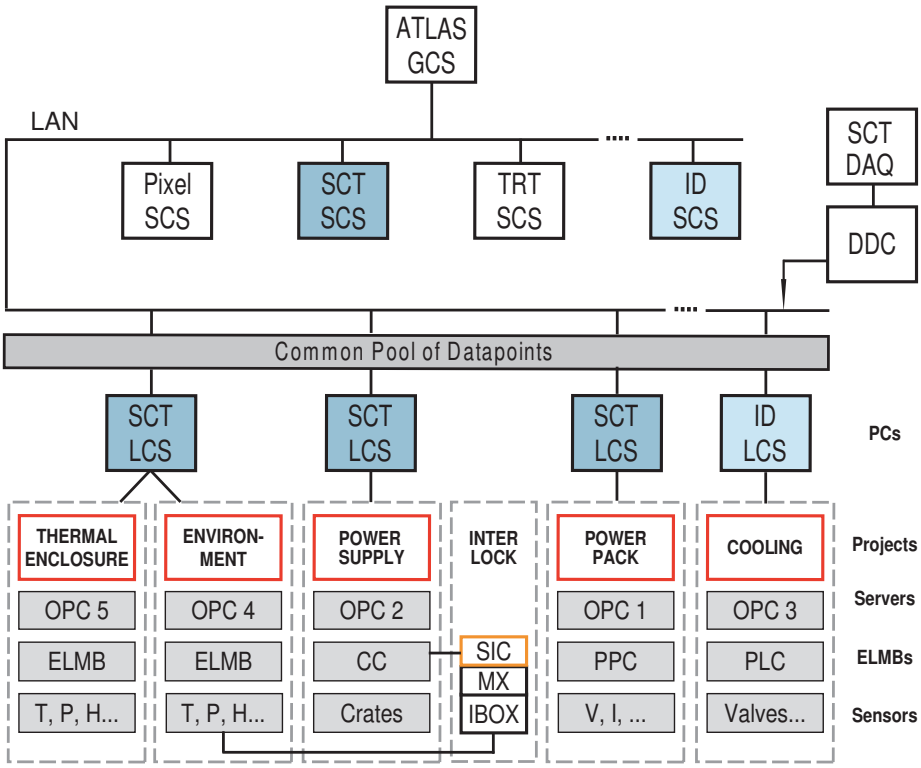

Figure 7.6: SCT DCS overview. On the top is the ATLAS GCS communicating with the SCT SCS through the Local Area Network, which again communicates with the SCT LCS through the same LAN. The datapoint structure of the LCS can be accessed directly, which makes exchanging information simple. The SCT LCS consists of 3 LCSs running four software projects; the thermal enclosure, the environmental project, the power supply project and the power pack project. In addition the SCT uses the IS LCS running the cooling project. This drawing has the interlock system included even though it is purely hardware, but it will affect both the environmental values and the power supply project.

are accessible to the user from the DCS software, either by using panels or by a command line interface and can be addressed to the whole power supply system or to a subset of the system using one of the following structures:

- Individual or a subset of channels.
- Groups of channels (defined by the user).
- Individual or a subset of crates.
- All crates on one bus.

The power supply projects offers two modes to issue commands, either by using the CC database, which is also called the configuration database, or to operate on value-to-value basis. The first one is the most frequently used and with this method the DCS sends operation requests to the CC which then performs the commands using the channel parameters stored in its own EPROM. This limits the amount of data to be transferred on the CAN bus and increases the speed of the system. New parameters can easily be reloaded to the CC database, but care must be taken to avoid reaching the rewrite limit of the CC.

In the value-to-value mode, each value is changed individually by the crate controller following the order as programmed in the SCADA software. The CC only transmits the commands from the back-end software to the right HV or LV channels for execution. This mode permits to change operation values on single modules and has proven useful when module parameters need to be tuned during operation. The parameters which are set in single value mode is not remembered by the DCS system, so if any tuning are proven useful, the values needs to be recorded to the configuration database and loaded into the CC.

The main commands which can be requested through the power supply system are the following, given in the approximately preferred order of initial operation:

- *Load configuration database:* When the configuration database has been changed either by the DAQ or the DCS, the values can be uploaded both to the SCADA software and to the CC EPROM. Both are needed for the configuration database to be fully effective. It is a two-step process, which is done separately for the moment.
- *Set select line:* This permits to use the redundancy link of the requested module, and if set to one, the module will take its clock and command from its neighbour.
- *Set trip limits:* For all currents and temperatures there are hardware limits in the PS cards, which can be set at all times. When these limits are exceeded, the HV or LV cards will shut off the power without ramping (hard shutdown/trip).
- *Set fatal limits:* The CC provides extra protection for certain sensible values, such as the bias current and the module temperature, and a fatal limit can be

set for these values for which the CC shuts down the power by ramping (soft shutdown). The change of these values is done in the same way as the loading of the configuration database.

- *Enable power:* For both LV and HV cards, the power of individual modules can be enabled or disabled, masked and unmasked. In addition, the LV cards have an output parameter that can be set on or off. For an LV channel to power a module it must both be masked on and have output = 1. The HV channel is powered directly when masked on.

- *Set value:* Any parameter of a module can be changed within its range. This can be done both individually and by changing the configuration database. The channel changed is ramped up or down to the new value.

- *Do run state transition:* A change of the SCT power supply state can be requested which changes the cannel, crate or crates to *on*, *off* or *standby*. This is done by using the predefined parameters in the CC database.

- *Read module values:* Most voltages, currents and temperatures can be monitored by the DCS. This can be done both by synchronous and asynchronous readout.

- *Reset module:* This command issues a hard reset to the modules in question.

- *Do IV curve:* The CC can perform an IV curve from 0-500 V. A separate trip limit set by the user will interrupt the IV curve script if the bias current exceeds this value. The output is stored in a text file.

All main functionalities of the power supply project are written as a series of scripts, which can be accessed from a set of trigger datapoints (shown in figure 7.8 at the very left). These scripts translate the actions by setting a sequence of datapoints to certain values. These values are then sent to the requested CAN node(s) and an acknowledgement of the successful execution will be returned. DAQ can access these trigger datapoint via specially developed DDC commands and the SCT GCS can access these directly within the project or via ethernet connection. By default, the monitored values are read back to the DCS software in a synchronous interval defined by the user. If any monitored module value exceeds the operational limits, the power supply will shut itself down, change its status and state and transmit an error message.

The power pack project

The power pack system monitors the condition of the power supply racks e.g. the power to the crates, its current and the redundancy and also checks if the fans are working. In addition, it permits the remote power cycling of the racks. Some additional signals not yet defined can also be monitored. Apart from the rack reset all projects tasks are to monitor the rack functionality. This DCS is currently under

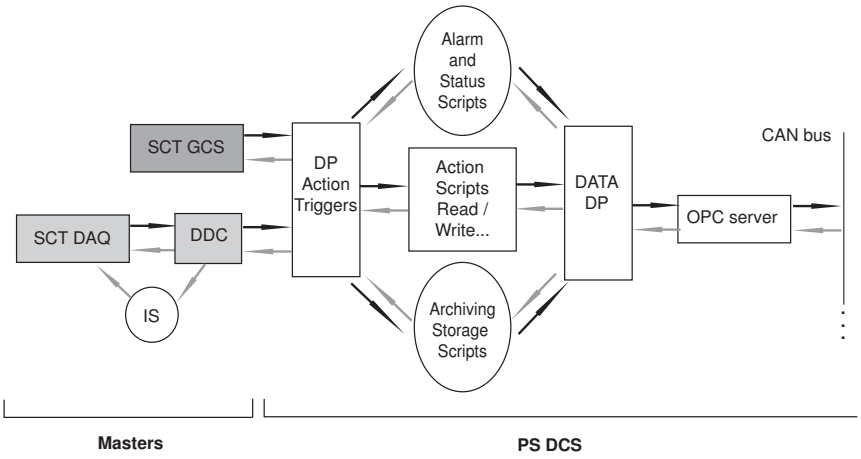

Figure 7.7: The power supply architecture. Both masters, the DAQ and the DCS, access the power supply system in the same fashion, notably via a set of DP Action Triggers (DDC datapoints). When triggered, these datapoints starts certain routines in a set of scripts, which makes up the core of the project. These scripts read and write to the datapoints needed and the commands are transferred to the system through the OPC server.

development. Future functionality will include alarms and warnings if the power or current are exceeding certain alarm levels to give the user possibilities to recover the situation before the circuit breakers shuts the power off completely. If the powering or the fans are not working an emergency message should be sent to the power supply DCS to request a regular shut down of the SCT power.

The cooling project

The cooling project monitors the cooling plant via an ethernet connection to a Programmable Logic Controller (PLC) using a PLC OPC server (produced by Schneider). The principal of this OPC server is similar to the custom OPC server used for all other projects. The cooling project can access all PLC variables e.g. cooling status, cooling alarms, pressures and flow-meter values. For the final system, functionality will be added to command the SCT manifolds, both to start up and shut down the SCT and to regulate the cooling if the module powering is failing. This will be done independent of the Pixel detector cooling. The general idea is that the operation of the cooling system should be completely separated from the detector operation as much as possible. However the operational temperature and back-pressure values needs to be given from the DCS to the cooling plant. At the moment, if any alarms are issued from the cooling plant the cooling projects sends an emergency message to the power supply DCS which will immediately shut off the

module power.

The environmental project

The environmental project monitors a certain set of temperature and humidity sensors described in chapter 6. These sensors are mounted on several places on the detector structure itself and permit the observation of changes to the cooling and temperatures, the carbon-fibre structure deformation and the calculation of the dewpoint close to the modules. The values from the temperature sensors on the cooling tubes and the resulting calculation of the dewpoint are the most critical values during SCT operation. If any of these temperatures exceeds the alarm limit or enters an alarm condition, a messages is send to the power supply system requesting the power to the modules should be shut down immediately. After this, the cooling will be turned off. The power supplies will be shut off when one of the following conditions occurs:

- The temperature on the cooling tubes exceeds the cooling temperature plus 10°C.
- The difference between the temperature on the cooling tubes and the dewpoint is more than 5°C.
- The air temperature is larger than 30°C.
- The mechanical sensors show temperatures less than -10°C or more than 30°C.

Thermal Enclosure

The thermal enclosure project monitors the temperature, humidity and pressure sensors within the thermal enclosure and calculates from this information the dewpoint value. In addition it monitors the dry airflow into the cavity. The main task of the project is to issue alarms if the values exceed the critical values. This is particularly important for the dewpoint value, which needs to be more than 5 degrees lower than the dry air temperature. Any alarms from the thermal enclosure DCS will also result in a request for the power supply DCS to shut down the module power.

7.2.2 Software Architecture

At the core of the DCS is the PVSS datapoint structure. Each project variable, which represents a physical value or a command, is represented by a datapoint. In addition there are datapoints for internal use. Each of the DCS projects has its individual structure which reflects its distribution of the readout and control parameters and in most cases this coincide with the actual hardware structure. The power supply system however has a quite complex internal hierarchy, since each module is provided with power from two cards in one crate, and this structure has been simplified in the PS DCS project.

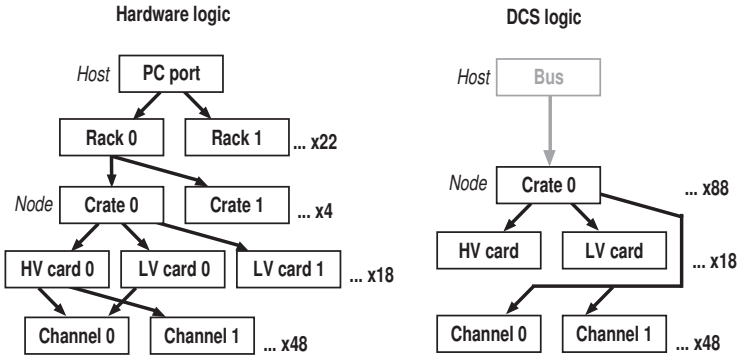

Figure 7.8: The structure of the power supply project. To simplify the software structure the following architecture (right) has been chosen, which does not reflect all the detail of the hardware structure (left) but corresponds more closely to the CAN communication path.

Figure 7.8 shows the hardware structure of the power supply project versus the DCS structure. In this structure, each channel represents fully one module and consists of both HV and LV parameters. The card values are treated as separate card datapoints and the crate controller values as separate CC datapoints. This structure simplifies the programming effort and shortens the path to each variable.

Figure 7.9 shows how this translates into datapoints. All parameters for the 48 modules in one crate are also put under the same crate in the software. There is another set of datapoints specific for each crate controller and a set of datapoints, which are used for internal software purposes.

The JCOP framework operated with predefined datapoints and addresses for the standard ELMB solution and for some commercial hardware, such as the CAEN power supplies. The SCT DCS projects, which are using the standard ELMB versions can thus use the JCOP framework and follow its architecture. Since the power supply system is not based on a commercial solution but on a specially designed hardware and software, it has not been possible to use the JCOP framework for this project. Instead, a dedicated architecture has been constructed, which permits a flexible operation and an easy access to the hardware functionality both for the SCT GCS and the DAQ system. Figure 7.7 shows this power supply architecture.

7.2.3 System Configuration

Since the SCT modules are expected to change over time and with the received amount of radiation, each SCT module has a separate set of required values as well as warning and alarm limits. In addition, the SCT detector will be operated under two different conditions; warm (ambient - testing) and cold (-7° - normal operation) running. All this values and settings are stored in the SCT DCS configuration

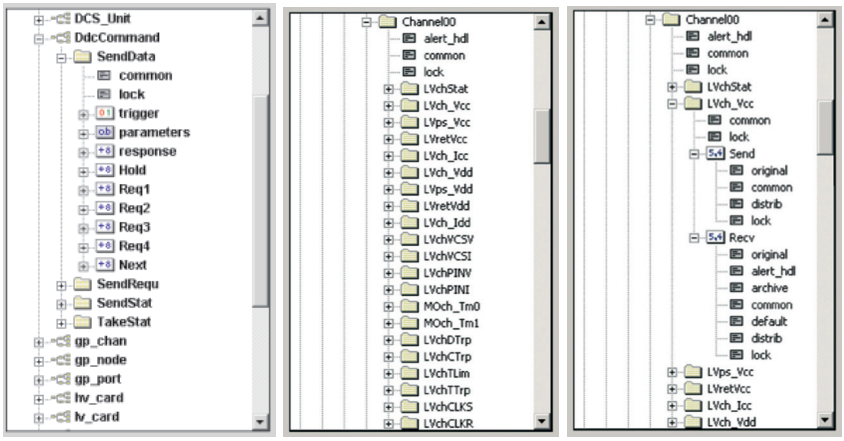

Figure 7.9: The power supply datapoints. Left: the DDC trigger datapoints. Middle: the module datapoints. Right: Detailed view of the module datapoints. For each datapoint there is a certain substructure, which permits to read or write to a value.

database and consist of the following types:

- All values to be set at run state transitions
- Alarms and warnings
- Mapping of cooling staves and channels to detectors (SN)

This database is created by the DAQ in XML format and dumped to the DCS system as a text file before being loaded into the DCS system. The loading consists of two parts; for all relevant projects the new values need to be loaded into the DCS project. In addition, the power supply system needs to load the module values and alarms for different detector states into the crate controller. This loading has to be requested by the DAQ system and the DCS should only update values, which has changed since the last loading because the EEPROM only support a certain number of updates.

7.2.4 Run State Transitions

There are two sets of states, which the SCT detector has to go through to become operational and to be safely shut down. The DAQ has its proper states and the DCS likewise. For the DCS, the SCT detector needs to have several sub-states, in addition to the global FSM states, to be able to power up safely. These states can change slightly in the future but the basic principle will stay the same. Both the SCT FSM states and the SCT sub-states and their (simplified) dependencies can be seen in Figure 7.10.

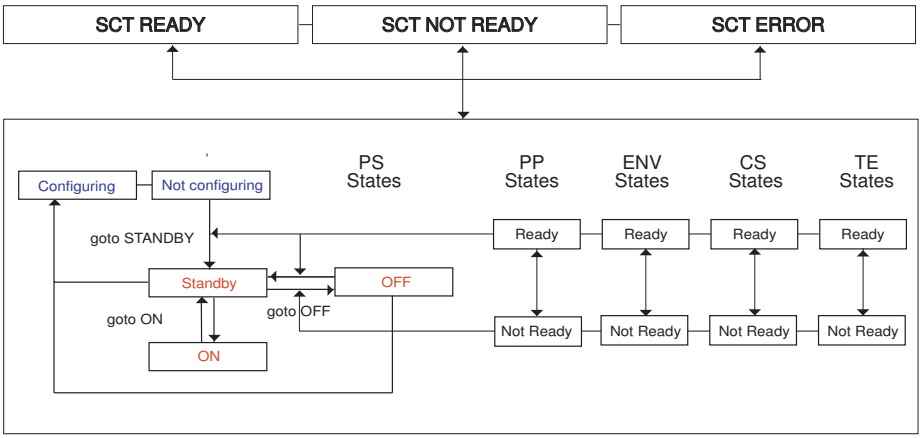

Figure 7.10: The SCT run state transitions are divided into two parts, one set of internal states proper to each project and one set of overall SCT states (READY, NOT READY and ERROR) in which the SCT detector is ready for physics data.

For all project, except the power supply project, the sub-detector states are READY or NOT READY, READY when all values are monitored correctly and within the limits and NOT READY if any errors or alarms has occurred. The power supply project has the following sub-detector states, where the two configuring state shows the state of the CC and the three other states shows the state of the power supplies and the modules:

- NOT CONFIGURING: In this state the CC is already properly configured and the CC is ready to change the state of the modules. If the configuration database has not changed there is no need to reload this and the detector can be operated directly.
- CONFIGURING: In this state the user can load new values to the CC database when the configuration database has changed.
- OFF: The modules are enabled (LV) but not powered, but their temperatures are monitored for safety reasons.
- STANDBY: The modules are enabled and powered to values considered safe. It is not possible to take physics data in this mode but the voltages are kept to minimise the detector noise and to limit the time it takes to get back into physics taking mode.
- ON: Modules are fully enabled and completely powered. The modules are ready to take physics data.

Run States	Description	V_{bias}	V_{cc}	V_{dd}	$VCSEL$	V_{pin}
OFF	HV off	0 V	-	-	-	-
	LV off	-	0 V	0 V	0 V	0 V
	(output off)					
STANDBY	HV standby	20 V	-	-	-	-
	LV standby1 *	-	2 V	4 V	4 V	6 V
	LV standby2 *	-	3.5 V	4 V	4 V	6 V
	(output on)					
ON	HV on	150-350 V	-	-	-	-
	LV on	3.5 V	3.5 V	4 V	4 V	6 V
	(output on)					
Configuring	any values	-	-	-	-	-

Table 7.1: Different alert levels for the detector voltages. *) The standby state is divided in two, to permit the DAQ to configure the SCT modules.

These detector sub-states are then translated into the three FSM states, which are common for the whole SCT detector, namely:

- ERROR: The SCT detector moves to this state when any error occurs
- NOT READY: The SCT detector has no errors but is still not operational
- READY: The SCT detector is ready and can take physics data.

Figure 7.10 also shows which direction the change of run state transitions is permitted. Projects in NOT READY state can go to READY only when no errors are present, and will go back to NOT READY state as soon as any error occurs. The power supply project can only be in ON, OFF or STANDBY state if all other projects are in READY state. If this is the case, the modules can only go to ON or OFF through the STANDBY state. It is not possible to go directly to OFF from the ON state. The STANDBY state is an intermediate state, which also permits the detector to be paused by the DAQ during physics run. In principle, the power supply project can go to CONFIGURING mode from all three main sub-states however it is recommended that the system state be OFF or STANDBY. Table 7.1 shows the main values, which is set at the different power supply states.

Change of run state transition can be made for individual channels, for groups of channels within one or more crate, or they can be done for one whole crate or all. However there is a strict sequence in which the channels can be changed. Modules, which are already in ON state will not be affected by commands that takes channels from STANDBY to OFF or from OFF to STANDBY. This is important since in case of a failure of a few modules not all modules will need to be power cycled for the system to recover. One important principle is that working modules should not be touched if one can avoid it.

For one of the Power Supply states, the change of state is a bit more complex than to just set new values for the output voltages. The STANDBY state includes

several sub-steps, which make sure that the front-end equipment of both DCS and DAQ is not interfering with each other to make the system fail to change transition. The low voltage value for the Vcc needs to be ramped (in steps yet to be defined) when going to ON state.

The reason for this manoeuvre is due to a conflict in the design of the DORIC and the power supplies. The DORIC is designed to require all module power ON before enabling the clock, however in reality the modules often trip (communication error) if they have not received the clock on before the power. If the clock is sent before the modules are powered, sometimes the clock is badly set (in clock/4 mode) and it is difficult to recover (toggling Vdd seems to help) but setting the pin bias before Vdd and Vcc can be useful. To arrive safely in the ON state in table 7.1, the following proposition of a sequence of steps might prove useful:

- LV and HV are ramped to STANDBY, and confirmation message of this procedure is transmitted to the DAQ
- The V_{pin}-value is set
- DAQ configures the modules
- LV is ramped to ON, HV stays in STANDBY
- HV is ramped to ON.

7.2.5 Startup and Shutdown procedure

The start-up and shutdown sequence of the SCT DCS is shown in figure 7.11. The main DCS issue here is that all other projects have to be up and running in the right state and are delivering sensible values without errors before any operation of the power supply project can be permitted. This is to avoid that by accident one or more modules are powered without any monitoring of detector values such as temperature or dewpoint. At shutdown, the power supply project needs to be shut down first, since at no time during operation the system monitoring should be disabled.

7.2.6 Alarm and Error messages

An important aspect of the DCS is to ensure the safe operation of the detector. This implies that whenever a fault occurs, the necessary action taken either by the users or by the system itself. In addition, useful information must be quickly transmitted to the right partitions and propagate upwards in the DCS system and (if considered important) via the FSM to the ATLAS DCS. The information also has to be transmitted to the DAQ, where the decision about whether to stop a physics run will be taken. Within the SCT DCS terminology the names *Alert* describes any alarms and warning which are due to detector problems. The name *Errors* describes the incorrect functionality of the DCS system itself.

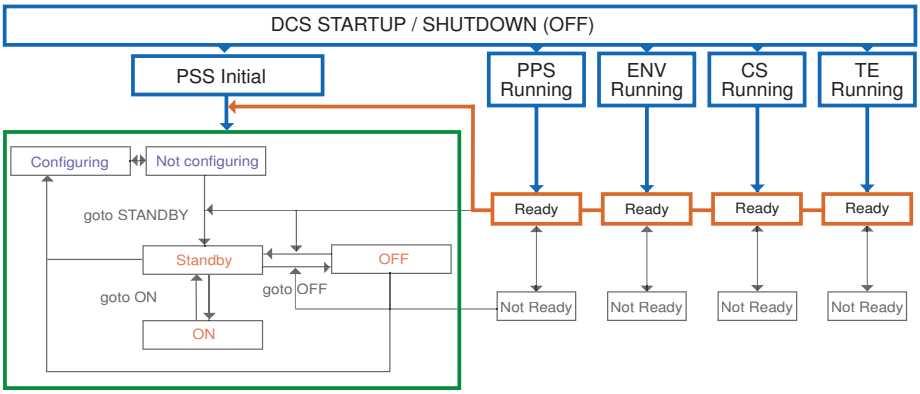

Figure 7.11: SCT DCS start-up procedure. All projects start up initialising their systems. When all projects are in READY state, except the power supply project, the latter can enter its first state. At shutdown, the power supply project terminates first and the cooling project last.

Figure 7.12 shows the alert dependencies of the sub-systems. Any alerts in other projects than the power supply projects results in a change of state from ready to the ERROR state. When this happens, it is considered as a fatal alert for the power supply system and the power of the modules will be ramped down. As described previously, any problems with the cooling, the thermal enclosure and the environmental project could have fatal consequences for the detector modules.

Table 7.2 describes the four types of alerts and the priority they have. The high alerts and the fatales have the highest priority, and it will be necessary for the system or the user shut down the SCT detector. Typical high alerts can occur at over-temperature of the module or when the bias current goes over safe operation limit. All other alarm states are currently used purely for information and the user must take an action if considered necessary. The fatal limits are put on parameters, which are considered the most critical to the SCT system. For these parameters the CC provides an extra protection by using this safety limit.

The actions taken by the DCS for the different alerts and fatals are the following:

1. Alarms/warnings from PS channels, which results in a change of the channel status
   - Channel tripped.
   - Channel over-temperature.
   - Channel communication error.
2. Alarms/warnings from CC, stored in EPROM of the CC and loaded with the configuration

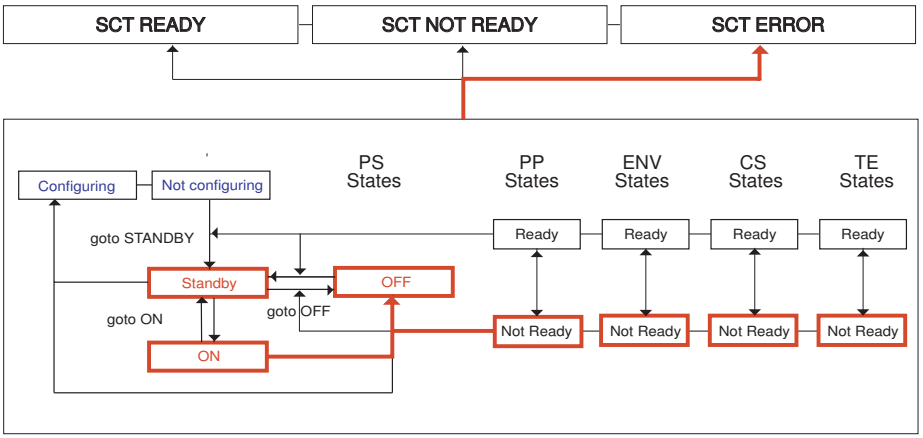

Figure 7.12: The SCT DCS alert dependencies. If any of the projects go into the NOT READY state they will stop the operation of the power supplies. If there are any errors in the ON or STANDBY the power supplies will equally be turned off. If this happens, the whole of the SCT detector will go to the SCT ERROR state, which is read by the FSM.

Alarm states	Description	Priority
Interlock	Power is shut off by hardware	0
High Alarm	Power supplies will trip	1
CC Fatal	CC will ramp down the power immediately	2
High Warning	Mainly DCS information, crate controller will take action for over-temperature and over-current	3
Normal	Expected range of values	
Low Warning	DCS information	4
Low Alarm	DCS information	2
Errors	DCS system errors	1

Table 7.2: Different alert levels and their priorities for the detector operation.

- A channel tripped results in CC switches off high voltage and generates a DCS alarm.
- If the module hybrid temperature exceeds alarm level, CC switches off the HV and LV and sends the DCS alarm.
- If communication between CC and card is lost, CC resets card via back-plane and sends a DCS warning when communication is restored or an alarm if the communication is not restored.
- If in OFF state, the CC checks if the output is on. If so, the CC disables

any power ramp up and generates DCS alarms.

3. Alarms/warnings from cards which changes the card status word

   - card tripped because of rack over-temperature.
   - card power failed.
   - CC power failed.

4. Informative alarms/warnings from DCS software (could easily be linked to an action). It changes the channel status datapoint. And if the conditions are right, it changes the crate status. At the moment any channel alarm/fatal/warning gives crate failure. The number of channels in warning/alarm/fatal is counted for each crate and information is written to the alarm history file (warning came/went, path, number of parameters now in which alert state)

   - Any value exceeding warning or alarm limit.

5. System errors from the OPC server e.g. dead CC, communication lost. The bus, ELMB, CC or PP needs to be reset. If any communication with the ELMB is lost by any project, the power supply project is always informed.

Since the SCT detector will be operated under warm and cold conditions, two sets of the alarms and warnings for all parameters needs to be loaded to the system whenever the running conditions changes. Which values and which parameters that are loaded depend not only on the warm and cold conditions, but also on the state which is currently active. The values corresponding to different states are found in tables 7.3, 7.4, 7.5, 7.6, 7.7 and 7.8.

Archiving and backup

There will be two main databases in the ATLAS system, the configuration database and the conditions database. For the SCT detector the values, which should be stored in the configuration database for each run, are those described previously in this chapter. The ATLAS community has not yet decided upon the final format of this database.

The conditions database will collect all the data from the detectors during data taking which are fundamental for offline reconstruction and analysis. This database will be provided by the LHC Computing Grid [100] applications area project. As a temporary solution, the SCT DCS system uses the archiving system delivered with the PVSS software for storage. In addition, the DAQ stores a set of database values for each scan performed.

Parameter	Units	Norm_Off	WarnH_Off	AlarmH_Off	Fatal
LVchVout	-	0	-	1	F
MOch_Tm0	°C	-20	-3	0	F
MOch_Tm1	°C	-20	-3	0	F
HVchVolt	V	0	5	10	F
HvchCurr	nA	0	400	600	F

Table 7.3: OFF values for SCT cold operation. Dashes indicate that there is no meaningful value to be assigned.

Parameter	Units	Norm_Off	WarnH_Off	AlarmH_Off	Fatal
LVchVOut	-	0	-	1	F
MOch_Tm0	°C	20	10	18	F
MOch_Tm1	°C	20	10	18	F
HVchVolt	V	0	5	10	F
HVchCurr	nA	0	400	600	F

Table 7.4: OFF values for SCT warm operation. Dashes indicate that there is no meaningful value to be assigned.

Parameter	Units	AlarmL	WarnL	Norm	WarnH	AlarmH	Fatal
LVch_Vcc	V	2.0	2.5	3.5	4.0	4.5	-
LVps_Vcc	V	3.1	3.6	3.65	5. 0	9.0	-
LVret_Vcc	V	0.01	0.02	0.08	0.2	0.5	-
LVch_Icc	mA	750	850	950	1050	1100	-
LVch_Vdd	V	3.5	3.7	4.0	4.7	4.9	-
LVps_Vdd	V	3.7	4.0	4.4	6.0	9.0	-
LVret_Vdd	V	0.005	0.02	0.08	0.7	1.0	-
LVch_Idd	mA	450	500	550	600	650	-
LVchVCSV	V	3.5	3.7	4.0	4.2	4.5	-
LVchVCSI	mA	0.01	0.02	2.2	?	?	-
LVchPINV	V	5.5	5.8	6.0	6.2	6.5	-
LVchPINI	mA	0.01	0.02	0.03	?	?	-
MOch_Tm0	°C	-	-15	0	10	33	F
MOch_Tm1	°C	-	-15	0	10	33	F
HVchVolt	V	130	140	150	160	170	-
HVchCurr	nA	?	?	?	150000	200000	F

Table 7.5: ON values for cold SCT operation. The question marks represent values which have not yet been defined. Dashes indicate that there is no meaningful value to be assigned.

Parameter	Units	AlarmL	WarnL	Norm	WarnH	AlarmH	Fatal
LVch_Vcc	V	2.0	2.5	3.5	4.0	4.5	-
LVps_Vcc	V	3.1	3.6	3.65	5. 0	9.0	-
LVret_Vcc	V	0.01	0.02	0.08	0.2	0.5	-
LVch_Icc	mA	750	850	950	1050	1100	-
LVch_Vdd	V	3.5	3.7	4.0	4.7	4.9	-
LVps_Vdd	V	3.7	4.0	4.4	6.0	9.0	-
LVret_Vdd	V	0.005	0.02	0.08	0.7	1.0	-
LVch_Idd	mA	450	500	550	600	650	-
LVchVCSV	V	3.5	3.7	4.0	4.2	4.5	-
LVchVCSI	mA	0.01	0.02	2.2	?	?	-
LVchPINV	V	5.5	5.8	6.0	6.2	6.5	-
LVchPINI	mA	0.01	0.02	0.03	?	?	-
MOch_Tm0	°C	-	15	25	30	33	F
MOch_Tm1	°C	-	15	25	30	33	F
HVchVolt	V	130	140	150	160	170	-
HVchCurr	nA	?	?	?	150000	200000	F

Table 7.6: ON values for warm SCT operation. The question marks represent values which have not yet been defined. Dashes indicate that there is no meaningful value to be assigned.

Parameter	Units	AlarmL	WarnL	Norm	WarnH	AlarmH	Fatal
LVch_Vcc	V	1.0	1.5	2.0	2.5	3.0	-
LVps_Vcc	V	1.1	1.6	2.1	5.0	9.0	-
LVret_Vcc	V	0.01	0.02	0.08	0.2	0.5	-
LVch_Icc	mA	-	-	353.0	1150	1200	-
LVch_Vdd	V	3.5	3.7	4.0	4.7	4.9	-
LVps_Vdd	V	3.7	4.0	4.4	6.0	9.0	-
LVret_Vdd	V	0.005	0.02	0.08	0.7	1.0	-
LVch_Idd	mA	450	500	550	600	650	-
LVchVCSV	V	3.5	3.7	4.0	4.2	4.5	-
LVchVCSI	mA	0.01	0.02	2.2	?	?	-
LVchPINV	V	5.5	5.8	6.0	6.2	6.5	-
LVchPINI	mA	0.01	0.02	0.03	?	?	-
MOch_Tm0	°C	-	-15	0	10	33	F
MOch_Tm1	°C	-	-15	0	10	33	F
HVchVolt	V	10	18	20	22	24	-
HVchCurr	nA	20	40	100	1100	1200	F

Table 7.7: STANDBY values for cold SCT operation. The question marks represent values which have not yet been defined. Dashes indicate that there is no meaningful value to be assigned.

Parameter	Units	AlarmL	WarnL	Norm	WarnH	AlarmH	Fatal
LVch_Vcc	V	1.0	1.5	2.0	2.5	3.0	-
LVps_Vcc	V	1.1	1.6	2.1	5.0	9.0	-
LVret_Vcc	V	0.01	0.02	0.08	0.2	0.5	-
LVch_Icc	mA	-	-	353.0	1150	1100	-
LVch_Vdd	V	3.5	3.7	4.0	4.7	4.9	-
LVps_Vdd	V	3.7	4.0	4.4	6.0	9.0	-
LVret_Vdd	V	0.005	0.02	0.02	0.7	1.0	-
LVch_Idd	mA	450	500	550	600	650	-
LVchVCSV	V	3.5	3.7	4.0	4.2	4.5	-
LVchVCSI	mA	0.01	0.02	2.2	?	?	-
LVchPINV	V	5.5	5.8	6.0	6.2	6.5	-
LVchPINI	mA	0.01	0.02	0.03	?	?	-
MOch_Tm0	°C	-	15	25	30	33	F
MOch_Tm1	°C	-	15	25	30	33	F
HVchVolt	V	10	18	20	22	24	-
HVchCurr	nA	20	40	100	1100	1200	F

Table 7.8: STANDBY values for warm SCT operation. The question marks represent values which have not yet been defined. Dashes indicate that there is no meaningful value to be assigned.

7.3 DCS Performance

Different parts of the DCS system have been in use for almost two years and the first impressions of the performance of the system have been made. Tests have been made of the performance of the different CAN performance of the DCS projects separately. The maximum delay between two messages on the CAN bus should be 0.9 ms for 100% occupancy. However, for safe operation the occupancy should be less than 60%. The maximum number of ELMB nodes on each bus at a baudrate of 125 kbits/s will be of 32 [101, 102].

For the power supply project the maximum busload of 60% corresponds to a maximum delay of 4 seconds between the read-out of two consecutive crates (each 1500 parameters), which gives a minimum synchronous readout time of 3-4 seconds (2700 PDOs every 0.9 ms). As a result of this, a maximum of 11 crates can be connected to the same CAN bus at the same time. There will be a total of 88 crates needed to read out the SCT, which means that 8 buses will be needed for the PS system.

The ramp down speed of one crate is defined by the ramping speed chosen by the user and by the time it takes the CC to send the commands to all the channels. It takes 6 seconds from the first channel starts ramping until the 48th channel starts. Since the crates are all independent, this value does not vary with the number of crates on the bus. For this reason the total time to shut down all crates on one bus is not much more since the total amount of messages will be equal to the number of crates, which gives a maximum of 11 messages.

The intercommunication between the different DCS projects is defined by the ethernet speed. Since the SCT DCS will be on a dedicated local network there should be no reason for this to be slow or fail. However, the PVSS archiving routine is known to slow down the DCS system, and the SCT DCS needs to archive around 16000 parameters every readout cycle (worst case). This can probably be improved by transferring the archiving to a separate PC to avoid this part of the PVSS program to slow down and in the worst case crash the system. However, in the future the values will be stored in the conditions database, which is yet to be defined, and might solve this problem by other means.

Conclusions

A new DCS system for control and readout of the SCT detector has been developed and tested successfully. The system is complete regarding all aspects of the DCS hardware, ranging from power supplies to cooling, software communication and includes functionality, which permits the detector operation within the overall ATLAS framework. Some of the main challenges faced and solved have been to make a unified system, but also to ensure the operation condition and performance providing maximal detector functionality. However, the software is still subject to developments and improvements to provide an up-to-date and optimal DCS as the construction of the SCT detector proceeds.

The SCT DCS have so far been successfully installed and used in a variety of sites with different purposes. It is currently in use both at the three Macro-Assembly sites (Oxford, NIKHEF and Liverpool) and at CERN (both in SR1 and in testbeam). The results of these tests (described in chapter 8 and 9) demonstrate a fully working DCS, which permits DAQ operation, both for calibration and for physics runs. One of the main achievements of the SCT DCS has been the successfully simultaneously operation and monitoring of the ~ 400 modules on barrel 3. This can be seen as a successful qualification and acceptance of this new and close to final back-end DCS system.

The user feedback has been mainly positive and the open architecture of the program permits developers to easily contribute with their own pieces of code, as long as it is done along the basic SCT DCS guidelines. Now, operating for more than a year, and reaching version 4.0, it has become quite advanced, providing an integrated and user-friendly system for all hardware subsystems.

8

SCT system performance - ATLAS Testbeam

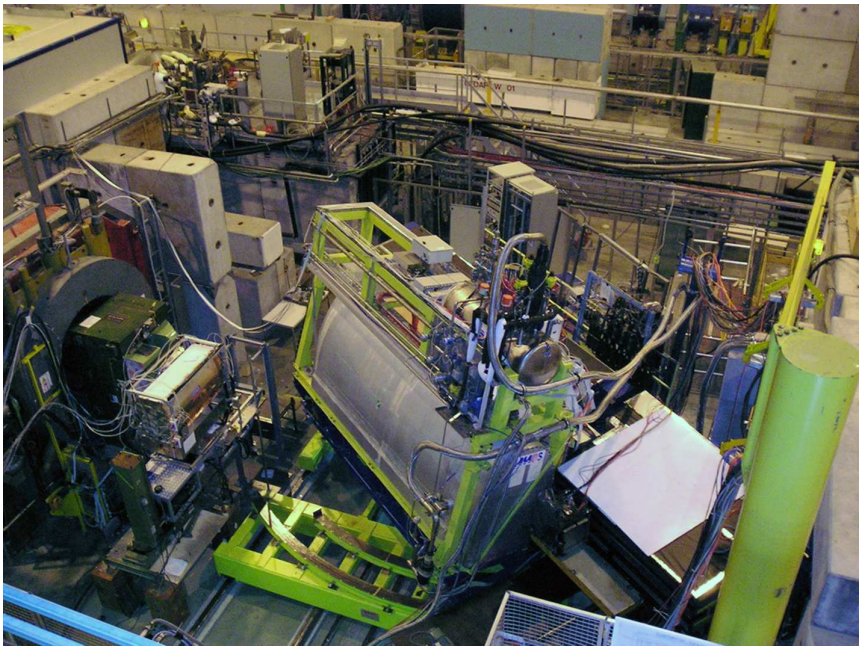

The ATLAS Testbeam May 2004 [103]

Introduction

Tests of the ATLAS detector components in testbeam setups, have over the years given the developers important information about the module design choices and performance. The 2004 testbeam, lasting around eight months, had as its main goal to test the combined operation of most parts of the ATLAS detector. This has been important to prepare for later integration work and to optimise trigger and DAQ performance. In addition, this has provided the opportunity to perform combined offline analysis of alignment and tracking.

My contribution to the 2004 testbeam has been to provide user support, debugging of the SCT DCS system installed and to calibrate the SCT modules. My main motivation for this work has been the possibility to operate the SCT detector in close to ATLAS like conditions, and to use this excellent opportunity to extend my knowledge about the SCT detector behaviour and readout system. Since I was already engaged for the barrel 3 tests in Oxford, I could only stay for the first part of the SCT testbeam session.

This chapter presents an overview of the SCT installation and the calibration data, as taken during my participation. Later changes to the system, such as changes to the setup due to mass tests or the addition of a failing SCT layer, has not been included. Section 8.1 presents both the ATLAS and SCT testbeam setups and Section 8.2 the SCT calibration data.

8.1 Testbeam 2004

As described in [104, 105], the ATLAS testbeam facility is situated at the H8 beam line of the Super Proton Synchrotron (SPS) at the Prèvessin site at CERN. The H8 beam line can provide a 450 GeV primary proton beam as well as muons, pions and electrons in the momentum range 10 - 350 GeV with a maximum intensity between 10^5 and 10^7. In a special very low energy mode also 1 - 9 GeV pions and electrons can be produced. The protons from the SPS collide with typically one or two fixed targets, which are used to produce the correct particles. A magnetic momentum spectrometer permits to select their momentum. In addition the beam is collimated and focused before entering the detector area. The spills into the beam line take several seconds and are repeated in cycles of 14 - 17 seconds.

This year's testbeam have been operated at a few tens to hundreds of particles per second only, which have excluded tests of pile-up and bandwidth extremities. This years run program used the following particles (as described by [106]):

- Electrons and pions have been produced with low energy (2 - 9 GeV) and with high energy 20 - 180 GeV. Studies have been made by varying the magnetic field simulating the ATLAS solenoid between 0 and 1.4 T, with and without extra material to study the effect of services and cables.

- Muons have been produced at high energy only (350 GeV) and tested in a magnetic field simulating the ATLAS toroidal magnet, which has been varied between 0 and 0.33 T.

- Photons with around 30 GeV energy have been produced from an electron beam of 180 GeV.

8.1.1 ATLAS in Testbeam

The main ATLAS motivation for the 2004 testbeam has been the combined data-taking with a slice of all the ATLAS detectors. One of the main tests was the test of the common ATLAS DAQ system. In particular the Data-Flow system [107] including a common LVL1 trigger, individual busy veto, the Event Filter, as well as the ATLAS event format were tested. In addition, the each subdetector had close to final DAQ hardware, for example RODs, which needed to be tested (see chapter 4 for more details on the DAQ system) before being integrated and used for data-taking together with the ATLAS DAQ. Secondly, several dedicated studies of parts of the subdetectors together were made. Combined calorimeter runs were made to study the integration of the different calorimeter parts. The three subdetectors of the Inner Detector was run together, the ID and the muon chambers as well as the ID and the calorimeter, to achieve information on the combined tracking performance.

Figure 8.2 shows a schematic drawing of the ATLAS slice installed in testbeam. This slice approximately maintains the overall distances of the ATLAS detector from the interaction point and out to the muon chambers. The origin of the global coordinate system is the interaction point and common for all detectors. The Inner Detector slice consists of three layers of 6 Pixel modules, four layers of in total eight SCT modules and 1/16th of the TRT barrel. Both the Pixels and SCT systems are situated inside a MBPS[1] giving a horizontal field. The calorimetry system consists of one LAr barrel module with its cryostat and three layers of TileCal barrel modules, all mounted on a common support table. This support table was used during dedicated LAr runs to rotate the detectors to vary the incident angle of the incoming particles. The muon detectors are mounted vertically and consist of one barrel projective tower and one end-cap sector, both containing both MDTs and RPCs.

The ATLAS slice provides the LVL1 trigger signal but in addition, between the LAr module and the TileCal modules, there is a layer of scintillator triggers providing an additional external signal. The scintillators sense the passage of beam particles and send a signal to the detector readout system to trigger the read-out. In ATLAS the readout of the detectors will be synchronised with the bunch crossings, but in testbeam the spills are random within the cycle. During this testbeam, one week of running had concentrated spills around each 25 ns, which verified successfully the detector and trigger functionality. For most other runs the scintillator triggers were used.

8.1.2 SCT in Testbeam

The main goal of previous SCT testbeam tests has been to determine the SCT performance, the module efficiency and the resolution using the testbeam environment

[1] A CERN standard superconducting dipole magnet.

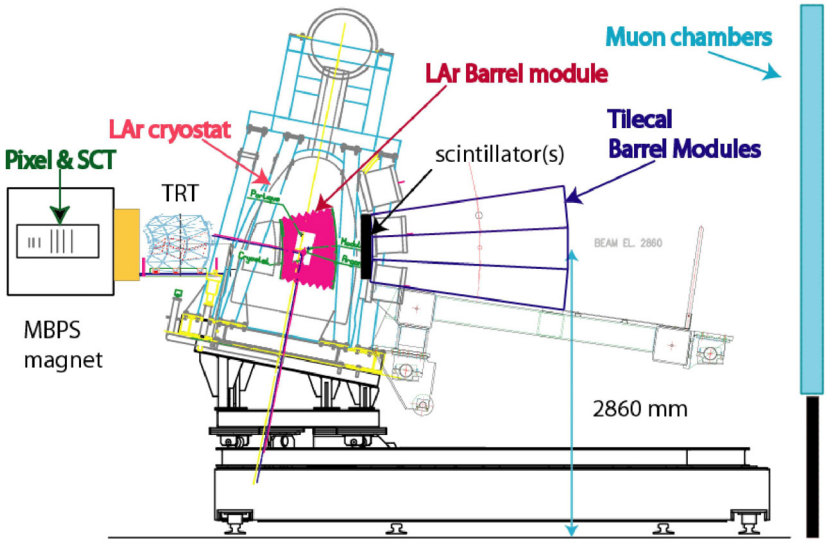

Figure 8.2: The ATLAS slice in the testbeam setup. From the left, three planes of the Pixel detector and four planes of the SCT detector are inside a MBPS magnet. Outside the magnet is the TRT detector, followed by a support structure containing the LAr cryostat and a LAr barrel module. Right of the LAr is a layer of scintillators used as an additional trigger system (distinct from the ATLAS trigger system) followed by TileCal barrel modules. At the very end of the chain, mostly not shown, is the Muon Chambers mounted vertically [103].

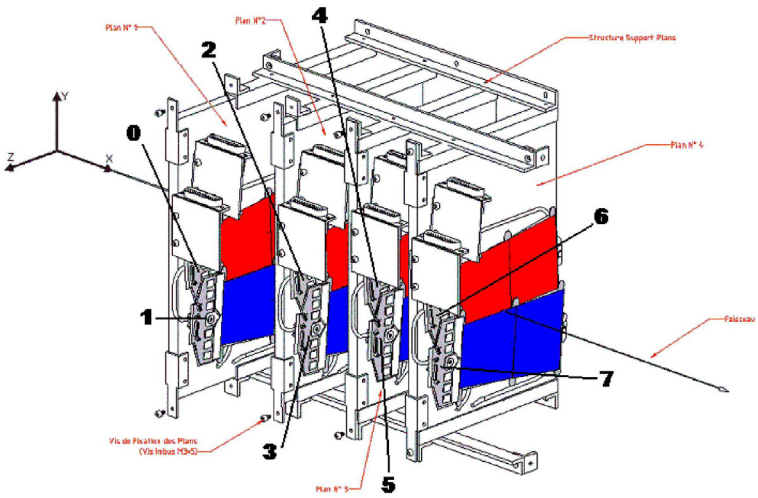

Figure 8.3: The SCT test box with its end-cap modules in a barrel-like arrangement [108]. Four layers of two modules are mounted on a support structure and are separated by same distances as the four barrel cylinders. The structure is enclosed by a box, which is light leak-tight and flushed with chilled N_2. The modules are water-cooled to have an operating temperature around than 30°C.

as a framework for this work. This testbeam has not been used for such a traditional test of the SCT modules since their parameters by now are considered to be well known and are presented in [6]. The main aim has been to operate the SCT in a close to ATLAS like environment and especially to look at issues relevant for the Inner Detector integration and common operation. This translates into the testing of physics compatibility (e.g. noise, cross-talk), the integrity of communication (TTC, control and readout) and the provision of a data set for testing of the software (simulation and reconstruction) with real data. The ID reconstruction comprises alignment tests, calibration methods and momentum resolution of the track parameters. In addition, the ID needs to be integrated with the rest of the ATLAS and an effort has been made to combine reconstruction from the ID and the calorimeter (e.g. Bremstrahlung recovery, π identification) and the muons combining the ID, MDT and RPCs.

To achieve this, the SCT modules needed to be operated with a full and close to final read-out chain, consisting of both the SCT specific ROD system as well as the ATLAS specific ROS setup [109] including the ByteStreamConverter, Online software and conditions database [110]. The SCT setup consists of eight non-irradiated

end-cap outer modules mounted in a test box as shown in figure 8.3. The modules were mostly production modules not meeting quality criteria and showing a high number of electrical defects or minor alignment errors, and thus were unsuitable to be mounted on disks. Otherwise the modules were perfectly good modules. The modules are arranged approximately like the barrel modules on the cylinder structures. The overlap between the modules and the distances between the four layers along the beam axis are similar to the final overlap and radial distances of the barrels. The box is flushed with N_2 to ensure a dry atmosphere and is light-tight and thermally insulating.

The modules are cooled by water/ethanol provided from a Huber chiller keeping the modules at 29°C with the fluid at around 5°C. A second chiller is used to cool the N_2 gas. The box is subject to a horizontal 1.4 T magnetic field from the MBPS magnet, which deflects the particles according to the Lorentz effect and simulates the 2 T Inner Detector solenoid. The field is oriented parallel with the strip orientation.

The modules were read out via optical fibres connected to a SCT DAQ system as described in chapter 4, consisting of one SCT ROD crate containing one single board computer (SBC, Concurrent Technology VP100/10), one ROD (rev. E), a TIM (rev. 2) and a BOC card. The SCT modules have two modes of operations, the calibration mode and the data-taking mode. In the calibration mode, data from the detectors are read by the SBC and transmitted to the SctRodDaq software for further analysis. In the data-taking mode, the amount of data is much too large for the SBC to handle and it is converted and transmitted to the ATLAS DAQ system via a S-link interface (HOLA[2]) connecting to a ROS PC with gigabit ethernet output. From the ROS system the data is handled by the Data-Flow and Online [111] software. To make the SctRodDaq run with the ATLAS software, it needs to be modified from the standard version, which was not compatible with the final ATLAS software development at the start. Considerable effort was made to achieve this in the short timeframe of the testbeam.

During tests, the modules were operated at a fixed threshold of 1 fC and 150 V bias voltage. The modules also had a constant incident angle of the beam with respect to the modules. The modules were powered via power cables connected to a power supply crate via PP3-T[3] filter cards. A fully populated PS crate (1 SIC card, 6 HV cards, 12 LV cards, fan, powerpack) was used although only eight of the channels were connected to modules. The crate was monitored using the SCT DCS software (version 3.0) and back-end system described in chapter 7.

This testbeam did not have silicon telescopes (described in [6]) as previously used, since these are not present in the final ATLAS detector and would have presented an increase in the mass volume. In addition, they were not required for the physics program. The SCT alignment and the track reconstruction were thus achieved by using the data from the Pixel detectors. After the alignment of the Pixel detector with their standard procedure, this data was made available for the SCT group and used to reconstruct tracks in the SCT detector.

[2]High-speed Optical Link for ATLAS
[3]T-shaped patch panel 3

Nb	Module SN	Gain [mV/fC]	Thr.spread @1fC [e^-]	T [$\sim^o$C]	Noise [e^-]	Defect SW	Defect DB
1	20220130000106	56.03	105	28	1650	47	45
2	20220130000079	54.87	92.5	33	1821	47	42
3	20220250000061/L1	54.68	97.4	30	1744	9	9
4	20220130000000	61.04	97.5	30	1442	30	28
5	20220130000134/L0	57.02	100	30	1613	12	1
6	20220130000023	52.39	135	30	1725	36	33
7	20220130000005	57.04	95	29	1550	47	29
8	20220130000011	55.44	92.5	30	1646	35	16

Table 8.1: Summary of module calibration parameters. All values are for link0 except for module 3 which only operated with link1, Defects are given by the number of affected strips, e.g. 47 = 47 strips affected. SW indicated the number of defects identified in situ by the SctRodDaq values and DB the number from the production database.

.

8.2 SCT Calibration

Before starting the measurements for testbeam, but with the SCT modules in their final position, the SCT detector was calibrated to determine parameters such as gain and noise. The noise occupancy was also measured but the data was not retrievable due to some problem not yet identified. The measurement was made in-situ prior to the beam testing. The calibration where performed at the testbeam operating temperature with the hybrid temperature around 30°C. This is warm compared to the expected ATLAS hybrid operating temperature of around 10°C but allowed a much simpler cooling system to be used.

Noise and Gain

The results of these tests are presented in table 8.1 for the data readout link corresponding to the front plane of the SCT module. As described in chapter 4, the SCT module has two readout links, one reading out the front plane (link0) and the other the back plane (link1) of the silicon sensors. During these calibration tests two planes were not operational corresponding to link1 on module 3 and link0 on module 5. Later system improvements permitted the recovery of one plane using calibration data not taken in this session, thus not presented here.

For link0, the overall gain lies between 52 and 61 mV/fC with noise values between 1440 and 1750 ENC and a threshold spread between 92 and 135 electrons. A number of defects occurred were identified during testing and are indicated in the table. It shows both the defects listed by the SctRodDaq software (SW) and the defects registered in the production database (DB). The high number of defects was indicative of the reason why these modules failed quality assurance and were thus available from the production line for the testbeam. Module 5 also has some

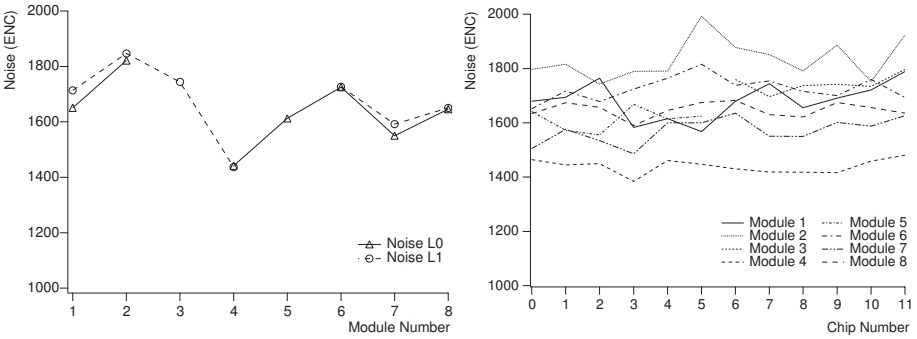

Figure 8.4: Noise distribution in the testbeam cage. Left, the average value per module for the two links. Right, the link0 values for the 12 chips. The noise values lay around 1400 to 1800 ENC, which is acceptable.

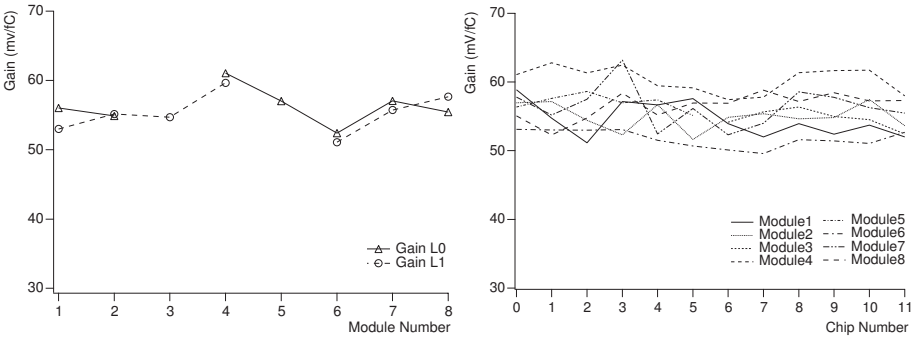

Figure 8.5: Gain distribution in the testbeam cage. Left, the average value per module for the two links. Right, the link0 values for the 12 chips. The gain lies in the band between 50 and 60 mv/fC, which is acceptable.

channels which are reported by the system as untrimmable.

The distribution of the noise and gain values for both planes of a module can be seen in figures 8.4 and 8.5. The noise values range from around 1400 ENC to 1800 ENC for both links. One of the links, link0 shows slightly lower values than link1. However, when looking at the noise values of each chip (link0 only), one can see that they are distributed more or less uniformly across the module with a tendency to be highest at the last chip.

The high noise values are mostly due to the high module operating temperature, accounting for around 80-100 ENC of the excess ENC. Another noise source was the imperfectly optimised grounding and shielding of these modules. All modules showed rather nominal values for warm tests, in accordance with the production tests. sThe gain values are also rather uniform and lie within a band from 50 to 60 mV/fC. As expected from looking at the noise values, the gain of link0 is mostly slightly higher than for link1. The gain per chip, seen in the right hand plot, seems

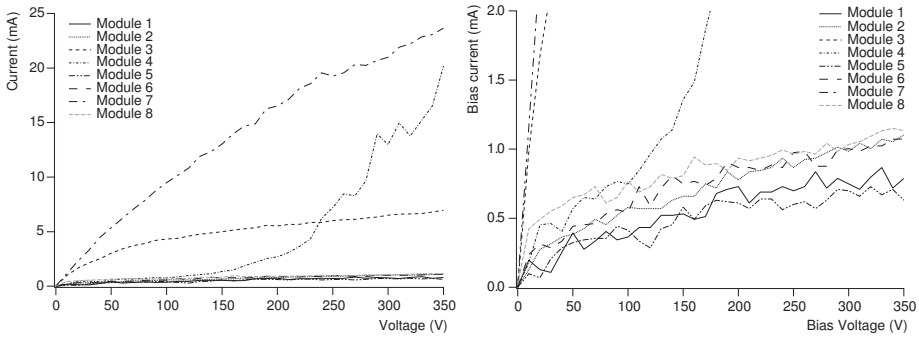

Figure 8.6: IV curves of all eight modules at around 30°C. Some of the modules are just below 1 μA, but three modules have increased leakage current. The graph at the left side is a close-up at the full range shown right.

to decrease slightly from the first chip, 0, to the last chip, 11.

IV-curves

IV curves for the eight SCT modules were made initially using the IV-curve functionality from the SCT-DCS system as described in chapter 7. The temperature during the IV-scans was $\sim$ 30°C. Each IV-scan was run between 0 - 350 V with 10 V intervals and a pause of around 15 seconds in between each step. The scan was performed on one module at the time, but they were all taken successively under the same conditions.

Figure 8.6 shows the results of the IV-curve tests. The left hand plot shows all IV-curves up to 350 V and up to the maximum current which was slightly less than 25 μA. The right hand plot shows the same voltage range but with a close-up of the region of currents less than 2 μA. As can be seen, modules 3, 4 and 7 show significantly higher currents than the others. Module 3 is a preproduction module and is known to have high leakage current but within the acceptance criteria. Its behaviour seems normal just with higher currents than other modules up to around 5 μA at 350 V. Modules 4 and 7 have both been produced with production sensors. Module 7 rises from the start up to almost 25 μA at 350 V, whereas module 4 rises a little later, from $\sim$100 μA reaching 20 μA at 350 V. For these to modules the production database shows IV-curves less than 1 μA at 500 V. The cause of these increased currents is not known and was not subject to further studies, since the currents were sufficiently low for the testbeam test.

Geometric distribution

The geometrical distribution of the noise and gain is shown in figures 8.7 and 8.8. There are some regions with quite different noise and gain than others. The modules

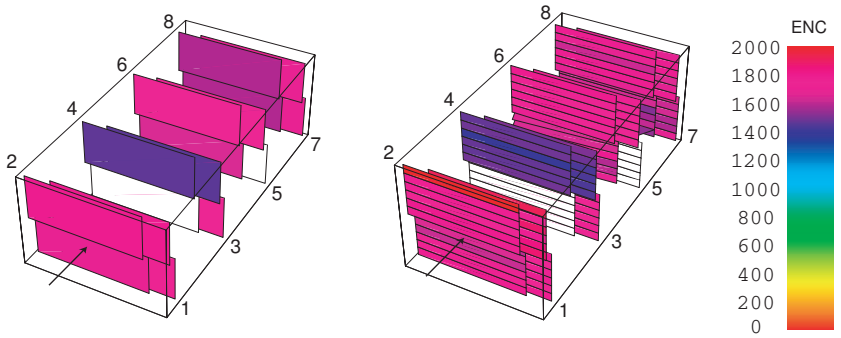

Figure 8.7: Noise distribution in the testbeam cage. Beam from the bottom side, bottom front module is module 1. Left, the average noise per link, right, the noise per chip distribution.

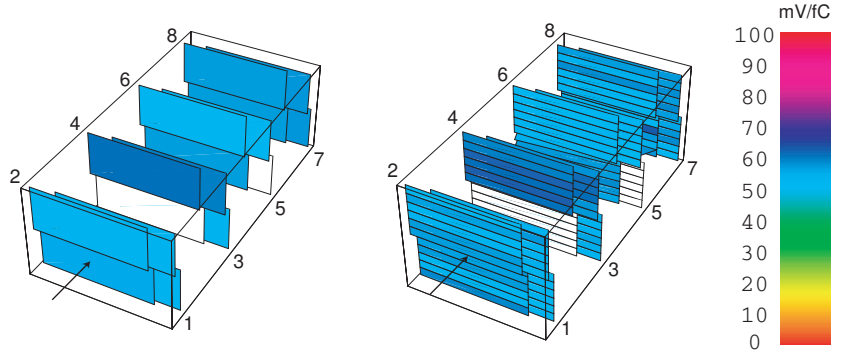

Figure 8.8: Gain distribution in the testbeam cage. Beam from the bottom side, bottom front module is module 1. Left, the average gain per link, right, the gain per chip distribution.

are shown starting with number 1 and 2 at the bottom and top position in the front respectively. The beam is entering from the front side into the picture. The two planes, which were not operational during calibration, are shown in white. The left hand picture shows the average noise per plane, and the right hand picture shows the noise per chip to determine if all the chips had a problem or only a selection of chips.

It seems that for module 4 has overall lower noise and higher gain than the other modules and some single chips on module 7 have lower noise. However, the overall distribution of both noise and gain seems to be uniform across the different positions.

8.3 Testbeam Results

First results from the analysis of the testbeam data of 2004 have been presented in [112, 108, 110]. Many important achievements have been made by the ATLAS as a whole as well as for the different subdetectors, such as the muon spectrometer and the calorimeters. Several improvements, common to all ATLAS detectors, were made to the DAQ system. Both the Event Filter and the Data-Flow system have profited from the results of this testbeam session. A partial demonstration of the TTC chain was made, including tests of the ATLAS trigger if not to its full bandwidth extremities. The LVL1 trigger was produced and a synchronised L1A accept trigger for the subdetectors.

In particular, some of the results, which are particularly relevant for the SCT and its integration into the Inner Detector and ATLAS, can be summarised as follows:

- One of the main SCT achievement of this testbeam has been the demonstration of the full readout chain. Both SCT DAQ and DCS were proved to work satisfactory after the installation and debugging session and made possible the operation of the SCT and the integration with the Inner Detector and ATLAS. The efficiency and resolution of the SCT detector was demonstrated to be conform to results from previous testbeams.

- Another major accomplishment was the successful integration of the SCT into the common Data-Flow system and the taking of data in combined detector mode. This includes constant development of the SctRodDaq software during the length of the testbeam session. From a DAQ software part this has been an important realisation and tests of both of the SCT DAQ and the ATLAS DAQ systems together.

- The SCT contributed with data to the main Inner Detector physics program (low energy runs with e/π, different material studies, magnetic field scans) and to the combined runs with the Muon detector (low energy runs with e/π, different material studies, magnetic field scans). The full reconstruction chain (offline, EF and LVL2), using data from the slices of Pixels, SCT and TRT, have been demonstrated to work and has pushed the development of realistic calibration, alignment corrections (see figure 8.9) and detector imperfections.

Conclusion

The combined testbeam 2004 was successful on many levels. It was a unique opportunity to test common data taking with a complete slice of the ATLAS detectors and to prepare for the first physics run at the LHC. It was also an important test for the sub-detectors and their individual programs. For the SCT, the testbeam results have been used to start the integration work into the ATLAS detector and to test the final read-out and control system.

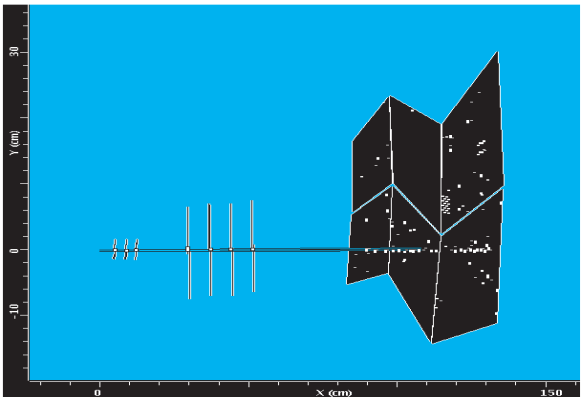

Figure 8.9: This figure shows the reconstructed tracks of the Inner Detector.The middle four points (in four planes) shows the space points reconstructed from the SCT detector [108].

In the future there are no more testbeam sessions planned. For the Inner Detector this means that the next step were particles can be measured will be the cosmic ray tests of the integrated TRT and SCT detectors foreseen in 2005. It will be very exiting to see if larger parts of the SCT detector behave as well as the SCT modules in the testbeam.

9

SCT system performance - Barrel Assembly

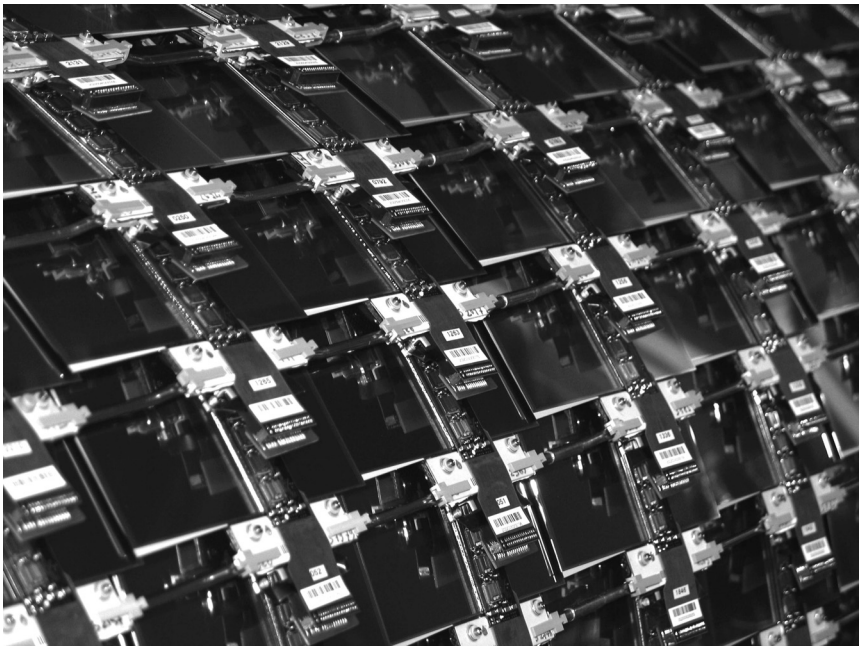

SCT modules on barrel 3.

Introduction

After production and testing, the SCT silicon modules are mounted onto carbon structures to form the complete SCT detector. For the barrel, this work is being done at the Oxford University. Each of the four cylinder structures is assembled there before they are sent to CERN. At CERN each barrel will be inserted into each other into a 4-barrel system and then and into the barrel TRT detector, before being lowered into the pit.

My contribution to the barrel assembly preparation and testing has been the following. First, I have helped setting up a DCS system for macro-assembly tests, notably the power supply DCS (described in chapter 7), which have resulted in the first user experience of the DCS system. In addition, debugging of the Power Supply system has also been done in Oxford in order to have a stable macro-assembly system. Secondly, during one month, I have had the opportunity to participate with the testing of barrel 3[1] (B3) and the first barrel to be produced. One challenge has been to have a reliable test-system ready in time for production, another to find and investigate all problems which occurred after or during mounting, to best understand the quality of the mounting procedure and the performance of the assembled barrel. It has been a pleasure and highly interesting for me to be present during this crucial time of barrel mounting and to participate in these tests which have permitted me to deepen my knowledge about the SCT detectors and of the larger barrel structures.

Finally, I have made a first simple analysis of the barrel 3 assembly data as presented here in this chapter. The results presented are of the post-mounting test sequence made during my visit. Some of the modules were mounted before or shortly after my stay but are still shown here for completion. The data are taken warm, so the barrel specification for equivalent cold runs will not be met. The data presented is to be considered as very preliminary, since the whole detector will be tested again both warm and cold in Oxford (see some examples in annex B.4) and after arrival at CERN. Nevertheless, these first results are very encouraging.

9.1 Barrel Assembly and Test System

Before mounting a barrel module onto the barrel structure [113], the barrel structure itself is installed in the cold room at the macro-assembly site of the Oxford University. This cold room will be used for both the initial warm and later the cold tests of the barrel. All tests presented here will be from the warm operation. The barrel structure consists of a carbon structure with module services connected, such as cooling tubes, harnesses and optical fibres as described in chapter 4. The fixtures have been mounted on the barrel at the University of Geneva and the services at the Rutherford Appleton Laboratory. Figure 9.2 shows the completed barrel and figure 9.4, left, a close up of the barrel services. Figure 9.2 also shows how the barrel structure is resting on two pillars being part of the support structure and which per-

[1]The SCT barrels are numbered from 3 to 6. Barrel 3 is the innermost barrel closest to the Pixel detector with a radius of 30 cm.

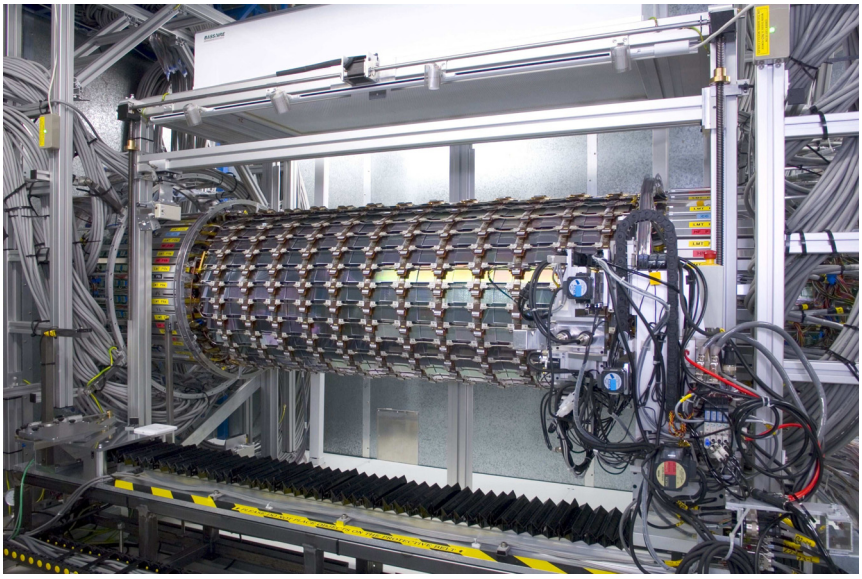

Figure 9.2: Barrel 3 in its mounting position in the Oxford macro-assembly cold room [115]. The mounting robot can be seen at the right side and runs horizontally on the rails at the bottom of the picture. On the very left and right sides are the support wheels and cables to the control room.

mits the barrel to rotate during the mounting process. The cold room is a dedicated closed area, which can be made light tight and where all necessary services for barrel control and readout are installed. Because of this, the barrel can be tested several times during the module mounting process, and any errors detected can be quickly fixed and the mounting process optimised if needed.

The mounting of the detectors is done using a dedicated robot [114], which from a fixed height can access the 12 module positions this corresponds to. Figure 9.2 also shows the robot in its first mounting position and figure 9.3, right, shows a close up of the jaws holding the module. The robot is driven on the rails below the barrel to move from one module mounting position to another in the horizontal direction. To change between the rows of modules in the vertical direction the barrel needs to be turned by the correct angle. A complex alignment software makes sure that the barrel is in the right place before starting the mounting procedure.

The details of this mounting procedure are described in [114]. Six modules are mounted at a time, first the six lower module in every second position, then the six upper modules. First, the operator manually coats the cooling blocks with thermal grease onto which the module is connected, to improve the heat dissipation. Then, the modules are picked up from its protection box by the robot with a pair of jaws and inserted in its position on the barrel structure as shown in Figure 9.3, left.

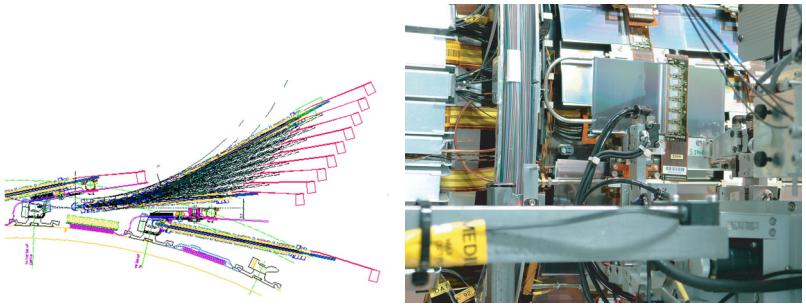

Figure 9.3: Left hand picture shows the insertion motion to be done by the robot to be able to mount the barrel modules [116]. It also shows one module in its final position. Right hand picture shows the grip of the robot of the module [115].

This movement permits the module to enter between its neighbours and into its final position. Two robot screwdrivers are used to fix the module to the mounting bracket and to apply extra securing clips. A sensor pin is attached manually and permits the determination of the precise location of the mounting point. After mounting, the electrical connector on the module is plugged into the one on the dogleg. Finally, for each of the new cooling loops equipped with new modules, the environmental temperature sensors are mounted on the cooling exhaust pipe (see chapter 6.2.4).

Figure 9.4 show a close-up of the structure before and after the modules have been mounted. One can see the carbon structure at the back holding the cooling tube and the cooling blocs, where the module baseboards are connected to the cooling. Vertically, in the front of the cooling blocks, doglegs can be seen with their connectors. As explained in chapter 4, these doglegs route the electrical signals (for command, data and power transmission), from the fibres and the LMTs to the modules. The command and data signals are transformed on the dogleg from optical to electrical signals and from electrical to optical signals respectively. Thin optical fibres can be seen in black entering the carbon structure horizontally.

The monitoring and readout of the barrel during tests are done from the control room situated on top of the cold room. Figure 9.5 shows the cabling from the cold room to the control room. At both ends of the barrel there are two support wheels, which supply each all services to its closest barrel half. This minimises the cable path inside the barrel and thus reduce the amount of material within the detector volume. One half of the barrel is referred to as the Z+ side and the other the Z- side. The cooling tubes on the barrel are connected to the cooling plant via capillaries or exhaust tubes exiting the barrel at the start of the support wheels. Care has to be taken when turning the barrel as not to damage these tubes and the capillaries.

The low mass tapes from the barrel are connected to patch panels on the support wheels, one for each row of modules. From the patch panels the power goes through thick grey cables to the power supplies in the control room. The optical fibres are

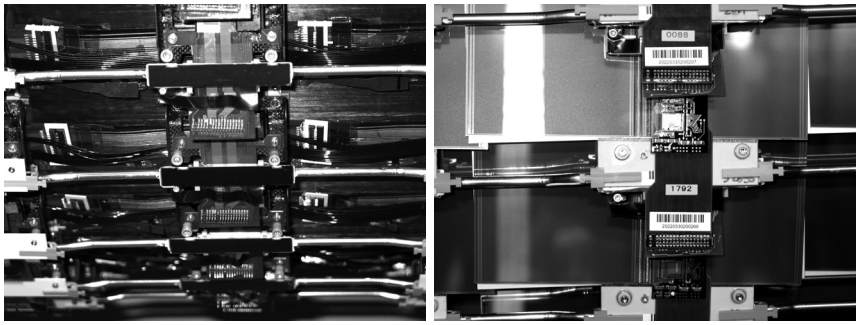

Figure 9.4: Left, the bare barrel carbon structure is shown with cooling tubes, fibre optics and flat power tapes. Right, one can see the barrel structure after the mounting or modules. The cooling tubes, the clips and the dogleg connectors can still be seen in this picture. One can also see how the modules overlap to fully cover the detector area.

guided from the barrel via a vertical support structure between the support wheel and the barrel. The fibres are rolled around this structure a few times (to be able to turn the barrel without damaging the fibres) before going up in bundles to the control room, where they are connected to the BOC at the back of the ROD crate.

Figure 9.6 shows a sketch of most of the Oxford readout system during these preliminary tests. One rack contained the DAQ crate with two RODs, one for the Z+ side and one for the Z- side. Two racks contained one PS crate each with low and high voltage for the modules. One of the racks supplied the Z+ side and another the Z- side. A prototype module interlock system provided a hardware safety system for the barrel, cutting off the power supplies at over-temperature. In addition, an environmental monitoring system, especially adapted to the Oxford system, supervised both coolant tube temperatures and the cold room environment.

The barrel cooling system is connected to the barrel via manifolds, which permits individual cooling loops or a subset of loops run at a time. The principle of the cooling system is the same as described in chapter 6, however the Oxford cooling system is made to run both C_4F_{10} and C_3F_8 for warm and cold tests respectively. The cooling system is monitored by a cooling DCS, which is similar to the one described in chapter 7, but specially adapted to the Oxford system. The coolant is swapped by switches at the send distribution and the return distribution, which permit to switch between the C_3F_8 and the C_4F_{10} plant. In addition the back-pressure has to be regulated to around 1.2 bar for C_4F_{10} and 3 bar for C_3F_8.

Figure 9.7 shows the temperatures of one cooling loop during one cooling cycle using C_4F_{10}. One cooling cycle includes the cool down of the detectors and running DAQ tests before stopping the cooling. As one can see, after the cooling has been turned on, the temperature increases during around 20 minutes by a few degrees before it decreases from 25°C to around -7°C almost instantaneous. This initial

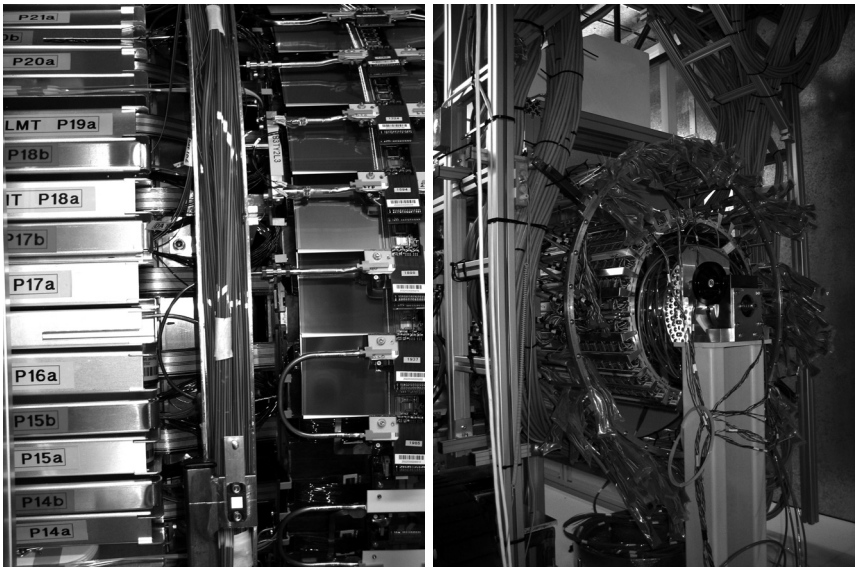

Figure 9.5: The left figure shows how the cables, fibres and tubes go from the detector structure to the support structure. Right, shows the support wheel of the power cables with their patch panel to go from the flat copper tapes to the grey cables.

increase is not well understood but can be because of an increase in heat capacity due to the difference in temperature between the warm gas still in the system and the cold room temperature.

The extra decrease (undershoot) in temperature just after the temperature drop at the beginning and at the end of the cycle is well understood. The reason for this is that the return pipe is not yet full with liquid, the impedance of the output is low and the pressure in the stave is similar to the back-pressure. When the tube is filled, the stave pressure is slightly higher than the back-pressure, which increases the temperature. The same thing, in the reverse order, happens at the end of the cycle. After stopping, the system flow decreases; the pressure of the stave drops to the back-pressure level and so does the temperature.

The oscillations during the cooling cycle are due to the duty cycle of the chiller, which provides the cooling for the condenser. This also changes the condenser pressure over time and defines the back-pressure since no direct regulation of the back-pressure was applied. The temperatures measured of the neighbouring staves, which are not cooled, increases slightly during testing. This is due to the increase in overall heat because of the thermal radiation from the modules, picked up by the neighbouring rows.

After the mounting of a subset of modules, typically 6, 12 or 18, the cold room is evacuated and locked up, dry air is turned on and the light is switched off. For each

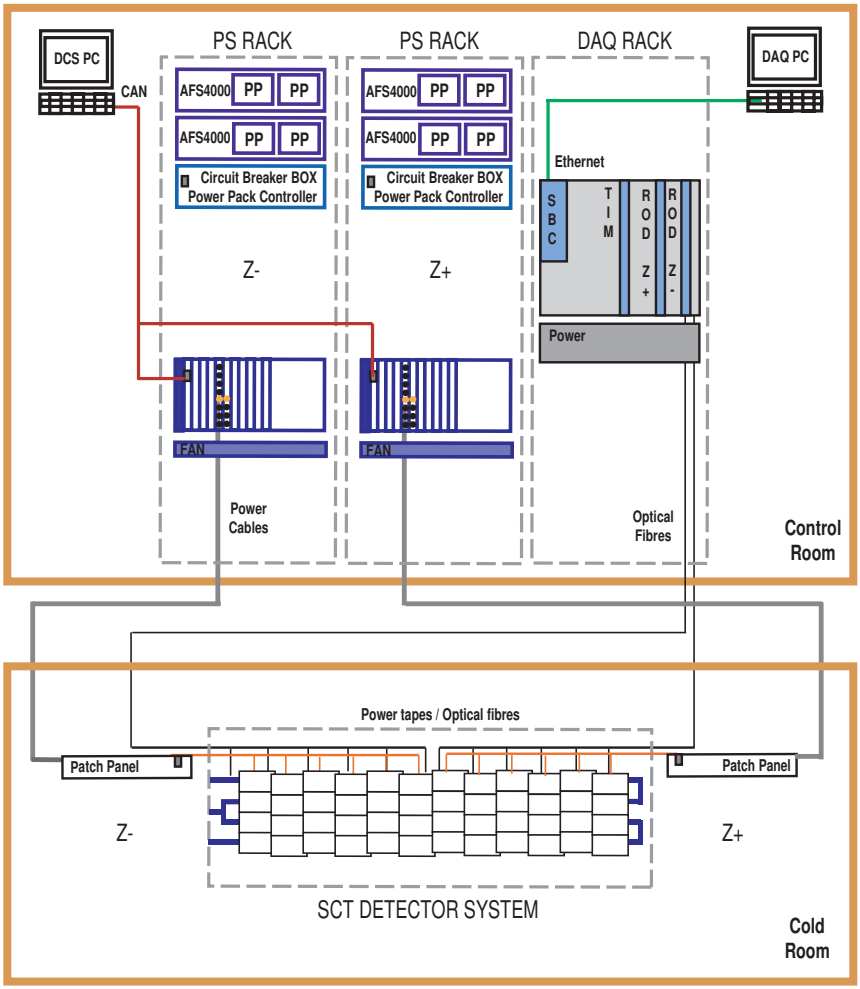

Figure 9.6: The Oxford supply and read-out system, only showing the power supply DCS and the DAQ system. Not shown in this picture are the environmental system, the cooling system and the interlock. The SCT detector is illustrated by a one of its cooling loops.

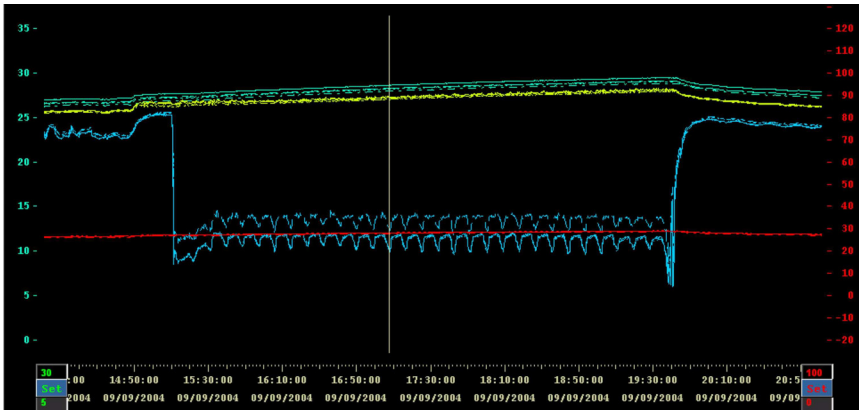

Figure 9.7: Picture from the cooling DCS showing one loop of the cooling system running C_4F_{10}. One can see how the temperatures on the exhaust of the staves goes down at the beginning of the run and how they oscillate during the cooling due to the duty cycle of the chiller. When shutting off the cooling, the values first decrease before they start rising towards the ambient temperature.

turn of the barrel, for which the power cables needs to be disconnected from the patch panels on the support wheels, the cables need to be reconnected before starting the tests. The corresponding fibres of the new modules need to be connected to the BOCs situated in the control room. Dedicated interlocks, both for the lights and the power, ensure safety both for the detector and for the people working in both the cold and the control rooms. Both DCS and DAQ software has to be configured and the module interlock programmed, tested and enabled before starting the system.

9.2 B3 Assembly Test Results (Warm)

As previously explained, the B3 data shown in this chapter are taken from the warm testing of the barrel modules after mounting, the so-called assembly test sequence. The main purpose of the B3 assembly tests was to verify that there was no degradation of the modules after assembly and during mounting. To verify this all assembly tests data were compared with the reference data, which are data of individual modules taken after module production. Most of the reference data used came from the reception tests taken at the arrival of the modules at the Oxford macro-assembly site. This data have all been taken using the SctDaq setup as described in chapter 5.

At the beginning of each test sequence all DCS parameters was checked, in particular the temperature and the leakage current. The module temperatures were checked before the start to investigate if the sensors themselves were working cor-

	Digital tests		Analogue tests
A	Hard Reset	E	Strobe delay
C	FullByPass	F/H	3Pt or NPt Gain
D	Pipeline	I	Noise Occupancy

rectly and to verify that the modules were correctly cooled. The module temperatures, before testing, should only be a couple of degrees higher than the temperature of the cooling tubes. On B3 all temperatures where found to be good after assembly.

The leakage currents were also checked, both at 200 V bias voltage before start, and at 500 V once, to verify that the module was not damaged. The modules chosen for B3 had been selected carefully from the modules which in previous tests had shown no microdischarge at 500 V. All other tests were made at 200 V bias voltage. These tests were made with cooling and HV on. In addition the LV was on at this stage to avoid PPS communication problems. For this reason the hybrid temperatures was typically 20-25°C depending on the coolant temperature. The leakage current is expected to double for an increase of 7°C. The module leakage current was checked to be less than 800 nA at 350 V and less than 1 μA at 500 V, which corresponds to approximate maximum values before the barrel mounting. Being much lower than the SCT requirements but close to the last values measured for the modules, any significant increase over these values could indicate module damage. In addition, one would detect if something were touching the module causing HV shorts.

After these initial tests, all DCS parameters are controlled regularly during testing. Special attention was given to the dew-point value. The dew-point temperature was calculated from the humidity value and should be checked to be no less than 4°C lower than the cooling tube temperature. The values from these DCS tests where for the main part of the tests noted by hand before a software upgrade made it possible to store them electronically. For this reason some of the DCS values will be missing from the plots shown in this chapter.

During assembly tests, the SCT electrical requirements were checked for all modules. For the modules to pass these criteria on the barrel, every module must have noise occupancy less than 5×10^{-4} (at any temperature) and less than 15 defects corresponding to 1% of the channels. For any high noise occupancy values and for all suspicious defects, the values were compared to several sets of reference data to determine if the effects were new or already present after module production. In addition, the noise and gain were checked to be relatively uniform, without discrepancies and consistent with the cold limits of < 1500 ENC and 50 mV/fC respectively. Details of these electrical tests performed are explained in chapter 4. The test sequence performed to determine the success of the assembly is similar to the calibration sequence and includes the following tests, in the same order:

Since only some modules were tested at a time, they have been subject to slightly different operating conditions and therefore the variation in the results will be larger than in the full system. One of the main differences has been temperature variations

of the cooling staves, which depends on the particular module load being tested, the number of loops in use and the operating conditions of the cooling plant. As we will see later this temperature difference was around 2°C during testing for all modules being tested. Since these first warm tests are preliminary and are followed by full barrel tests, both warm and cool, no investigations have been made to determine and correct for these system properties.

9.2.1 About B3

Barrel 3 has been populated with modules from all four production sites: UKB[2], USA, Japan and Scand[3]. UKB modules have been used until the assembly process has been proven successful. Subsequently, modules from all sites have been mounted per row and in accordance with their availability in Oxford. This means that there are 234 UKB modules on barrel 3, 116 US, 22 Scand and 12 Japanese modules.

The modules chosen for barrel 3 had to pass the overall production criteria and they need to be stable up to 500 V bias voltage with no microdischarge. In addition, there must be no visual damage or reduction of the electronics performance due to shipping. For this reason all modules are tested (reception test) on arrival in Oxford. This gives on barrel 3 a total of 384 modules of which 348 are "good" modules (90.6%), 31 "passed" modules (8.1%), 5 "passed-2" modules (1.3%). The criteria for a module to be in the category "good" is that it passes all electrical and mechanical specifications (as described in chapter 5) and in most cases those modules have considerably less than the 1% defects allowed. The "passed" and "passed-2" categories are modules which just barely misses one or more mechanical specifications but which meets all the electrical specifications. "Passed-2" modules are preferred to go onto barrels 5 or 6 at higher radius.

Figure 9.8 shows where the modules from the different sites are mounted onto the barrel. As already mentioned all rows are populated with modules from the same site. The only exception are modules with optical retro-reflectors for alignment purposes[4], which all have been mounted on UK modules. These modules have to be mounted at defined geometrical locations, and thus sometimes occur within a row from another site.

9.2.2 DAQ Results

A first estimate of the overall performance of the barrel 3 can be deduced from the first warm assembly tests. The average noise, gain and noise occupancy levels as well as the overall spread give indications of what to expect when the detector is tested cold. Figure 9.9, 9.10 and 9.11 show the distribution of the module noise occupancy, noise and gain respectively and independent of module position. The modules are sorted by increasing numbers; the first 114 modules are the ones produced in the

[2]UKB, the United Kingdom barrel module production site

[3]The Scandinavian cluster (see chapter 5)

[4]Part of the Frequency Scanning Interferometry (FSI) System, which does in-situ position monitoring of the SCT detector

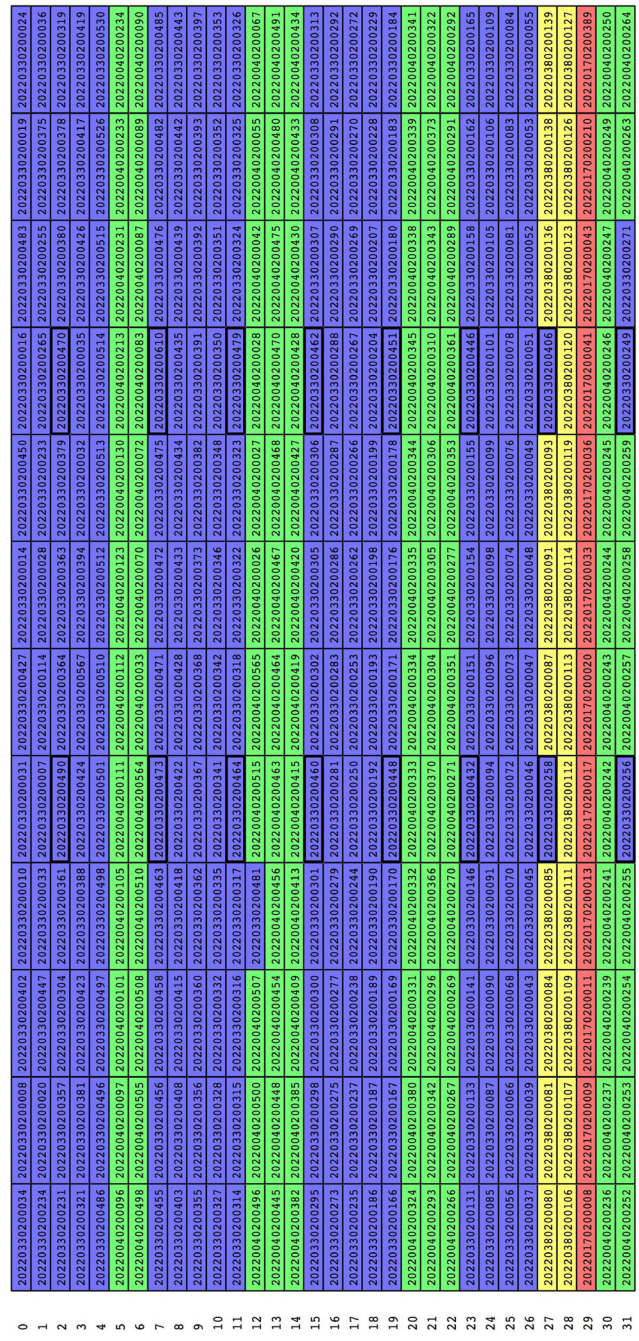

Figure 9.8: Distribution of modules on B3 (serial numbers). The numbers also represent the different production sites; UKB (20220330...), USA (20220040...), Scandinavia (20220380...) and Japan (20220170...).

USA, modules 115 to 127 in Japan, modules 128 to 362 are the ones produced in the UK, and finally the last 22 modules are from the Scand cluster. The right lines indicate the SCT requirements as described in chapter 4. For the noise and gain the lines represents the cold limits.

The characteristics of the plots are listed in Table 9.1. The noise occupancy values are distributed around the average of around 4×10^{-5} within a band of around 1-2 orders of magnitude. With a few exceptions, this seems to be well within the limit for both warm and cold tests. The average noise value is around 1620 ENC and most module noise values lie around $\pm$ 200 ENC of this average. For all modules this is a satisfactory results for warm tests. The corresponding gain values are situated around the average of 53 mV/fC within a band of around $\pm$ 6 mV/fC. Also in this case, the values are good for warm tests. For all three parameters, both barrel data and reference data are mainly in accordance. The few modules, which show differences between the barrel and reference data, have been retraced to show the same behaviour in another set of reference data tests (for instance tests made in Oxford or at the production sites). The distribution of the noise and gain per chip (no averaging per module) can be seen in Figure 9.12 and 9.13 on the left side. Both plots show very promising results, with a low average and small spread around the average value. Most satisfactory is the result that all modules are expected to be well within the cold limits when this will be tested. This shows the success of the construction of the modules themselves and of the mounting procedure.

Parameter	Unit	Average	RMS	Max	Min	Aver. Dev.
Noise occ.	e-	3.78E-5	4.74E-5	1.97E-4	3.87E-6	2.13E-5
Noise occ. Ref.	e-	3.88E-5	4.82E-5	1.51E-4	3.41E-6	2.19E-5
Noise	ENC	1618	1619	1798	1382	52
Noise Ref.	ENC	1616	1618	1830	1450	57
Gain	mV/fC	53.4	53.4	59.4	47.9	1.8
Gain Ref.	mV/fC	55.8	54.8	60.7	48.6	2.2

Table 9.1: Noise, gain and noise occupancy values for barrel 3 and reference data. The average, RMS and average deviation are calculated according to standard methods.

Calibration factor

One important difference between the barrel data and the reference data is the partial implementation of the calibration factor. The calibration factor originates from the difference in wafer properties of the module chips and represents the relative noise difference of the wafers. Most modules have chips which come from the same wafer and thus have the same calibration factors. However, different modules have chips from different wafers and occasionally there are chips from different wafers on the same modules. Between the chips, the calibration factor varies normally between 0.97 and 1.3, where a value equal to 1 is considered not setting it. During the first

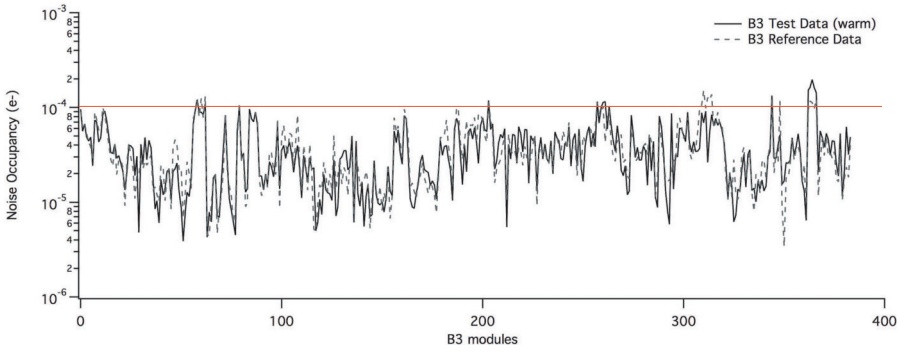

Figure 9.9: Distribution of module noise occupancy. Solid line shows cold upper limit.

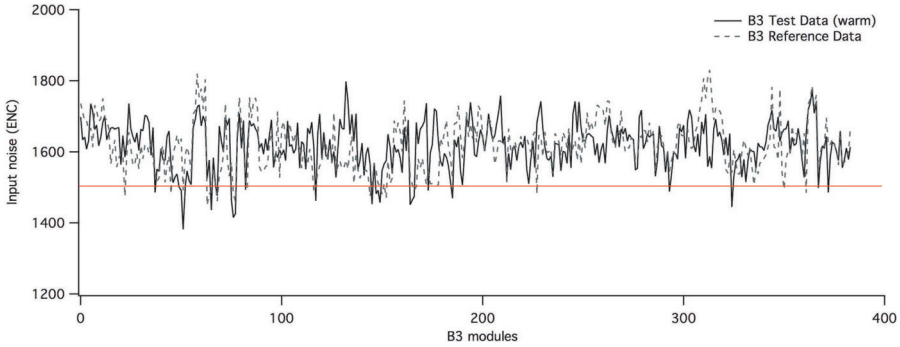

Figure 9.10: Distribution of module noise. Solid line shows cold upper limit.

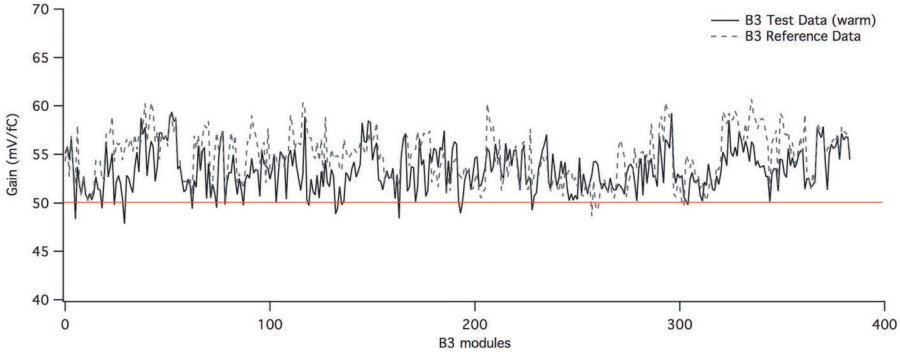

Figure 9.11: Distribution of module gain. Solid line shows cold upper limit.

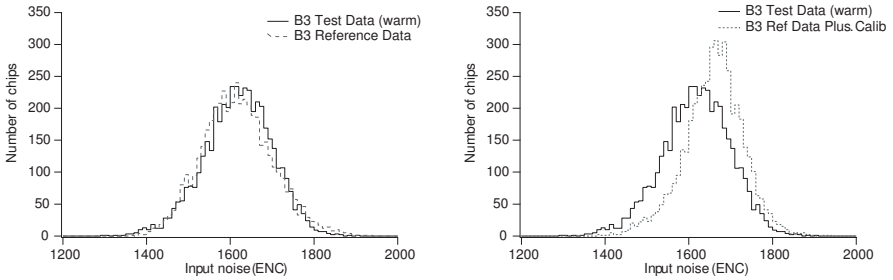

Figure 9.12: ENC noise distribution of the chips. Left, the original data, right, data with most calibration factors included.

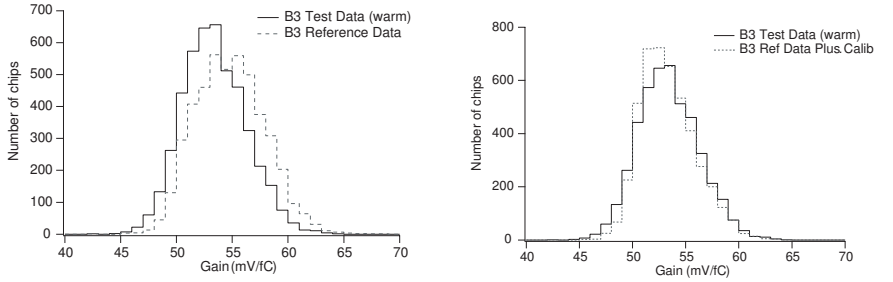

Figure 9.13: Gain distribution of the chips. Left, the original data, right, data with most calibration factors included.

assembly tests and from looking at the wafer data [117] it was not clear whether or not to include this calibration factor. For this reason a large part of the barrel data were taken including the calibration factor, but a certain fraction of the modules did not have it included (set to 1). For the reference data, they were all taken without the calibration factor included. Some of the following plots show reference data with the calibration factor. For these values the calibration factor has been multiplied with the resulting noise and gain after the measurement. If not explicitly stated, the plots shown display the original data of both assembly data and reference data.

Figure 9.12 and 9.13, right hand sides, show the effect of this calibration factor. The figures at the left show the noise and gain as measured (barrel data partially with the calibration factor and reference data without the calibration factor). The right hand figures show the same picture but here the reference data has been multiplied with the calibration factor. As can be seen for the noise values, when the calibration factor is applied, the offset between the two sets of data increases. It is believed that even if this makes the agreement between barrel 3 data and reference data look worse than when using the original data, this effect is due to setup differences and not so much caused by the calibration factor itself. Also, the shape of the distributions

should be narrowed, which can be seen in the two plots, however the barrel data have quite large width compared to the reference data. This can be due to the fact that not all the barrel data were calibrated at this time. For the next tests of the barrel it has been decided that to include all the calibration factors since this a first estimate is that they give more accurate results.

Comparison of the two links

The difference in noise occupancy, noise and gain between the two links on one module should not be too large, since the two links are providing two measurements for the same space point. The modules mounted on B3 has been chosen to have an average temperature difference between the two links of $\Delta T < 2°\text{C}$. As can be seen in section 9.2.3 this criterion is also well met after barrel assembly. Another known phenomenon is the temperature distribution of the chips within one link. Earlier measurements (as can be seen in chapter 4, figure 4.9) have determine the temperature variations within one link to be of around 4°C. It is therefore expected to see a higher noise towards the middle of each link.

Figure 9.14, 9.15 and 9.16 show the average noise, gain and noise occupancy plotted by chip number 0-11, which means that position 0, 5, 6 and 11 are chips at the end of the module. The plots on the left side show the original data and the plots on the left, the data with the calibration factor included for the reference data. For noise occupancy only the original data is shown. From Figure 9.14 one can immediately see the increase in noise towards the middle of the hybrids on both sides. Chips situated in the middle of the two hybrids have higher noise by about 25 ENC compared to the outer chips. For each degree a 5 ENC difference is expected. From this it is reasonable to believe that most of the additional noise comes from the temperature differences between the chips. Some additional, but much less, noise may come from the neighbouring electronics.

The gain in Figure 9.15 shows a slight dependence of the chip placement, probably originating from the noise effects, but washed out. No significant offset between the two links can be seen. For the noise occupancy plot, 9.16 , the difference between the two links is noticeable. The noise occupancy seems to increase with increasing chip numbers for the barrel data. The reference data seems to flatten out towards high chip numbers whereas the barrel data does not. The main conclusion is that the accordance between the two links is very good and that no damage has been done to either side of the detectors.

Site comparison

The modules on B3 have been carefully selected to be all within the criteria independent of the production site on the basis of earlier tests. Figures 9.17 shows the noise and gain distribution per productions site after the barrel assembly. As one can see from these plots, even after the assembly, there are no obvious offsets in degradation specific to a production site.

Most modules on barrel 3 come from the UKB and USA production sites and for these sites the statistics is sufficient. There are few modules from the Scand

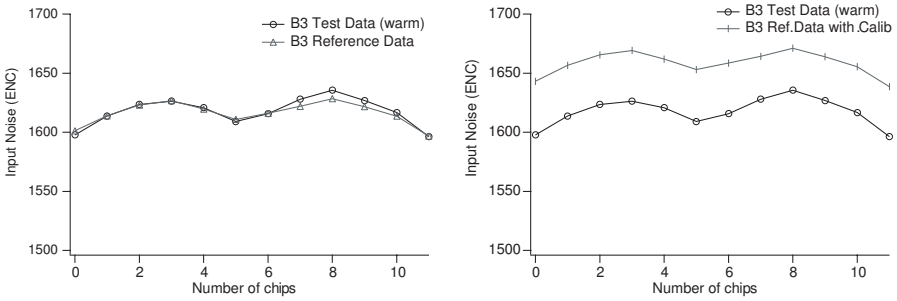

Figure 9.14: Average noise per chip. Left, the original data, right, data with calibration factor included.

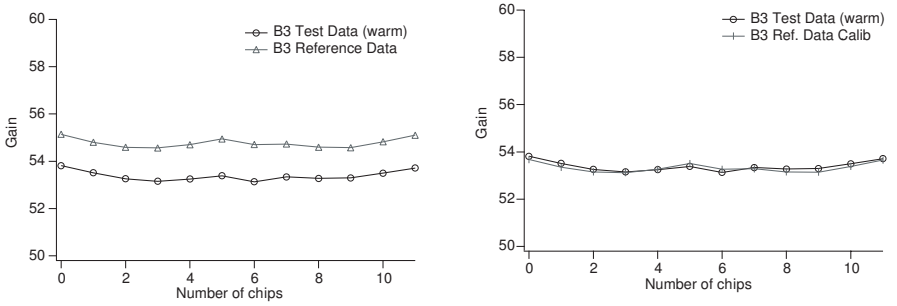

Figure 9.15: Average gain per chip. Left, the original data, right, data with calibration factor included.

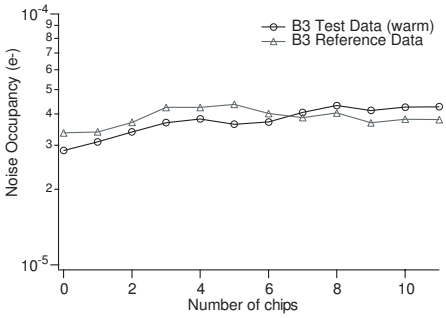

Figure 9.16: Average noise occupancy per chip. Left, the original data, right, data with calibration factor included. Corrected reference data was not available.

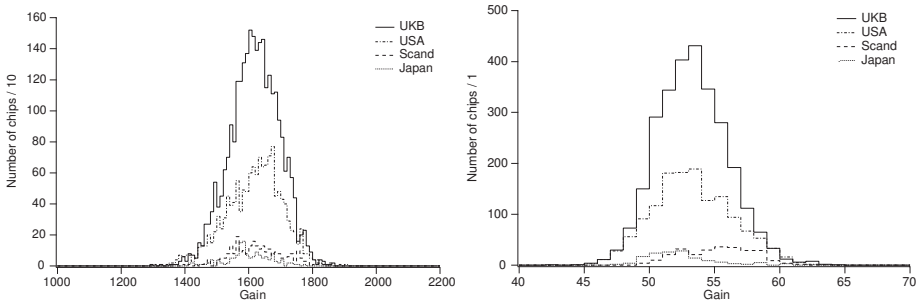

Figure 9.17: Site comparison. The distribution of modules from different sites was due to availability, but all sites should be present with at least one populated row. Most modules on the barrel are from the UKB and USA sites.

and the Japanese site on barrel 3 but the agreement is still good. The Scand modules are so far within the overall specifications and do not show abnormalities compared to modules produced by other sites. This is a very good result and shows the assembly performance of the different production sites. Another major achievement, considering the differences between the production clusters, is that there are no apparent differences between the sites.

Geometric Distribution

Another successful results of the barrel assembly and tests is that there are no apparent or large differences between the modules situated in different areas of the barrel structure. The next set of figures show the geometric distribution of the values described previously and corresponding plots of the defects. The purpose of this is to see if one can recognise areas on the barrel with different characteristics than others. As can be seen on the following figures there are no indications of site dependent differences.

Figure B.7 and B.8 show the noise and gain results from the 3Pt gain measurements. Figure B.9 shows the corresponding defects from this measurement. One can clearly see the missing chip, which is reported as 128 bad channels. For both the noise and gain tables the distribution seems to be random. The defects seem to be slightly higher in the top half part of the barrel if one disregards the disabled chip. However, any effect seems to be minimal. Figure B.10 shows the results from the noise occupancy tests. The defects found in these tests can be seen in Figure B.11. The noise occupancy distribution seems to be random except for in the bottom left corner where the occupancy seems to be a bit high. This also results in a high number of faulty channels in this region on the defect plot due to the same high occupancy. On the overall the noise performance seems to be satisfactory.

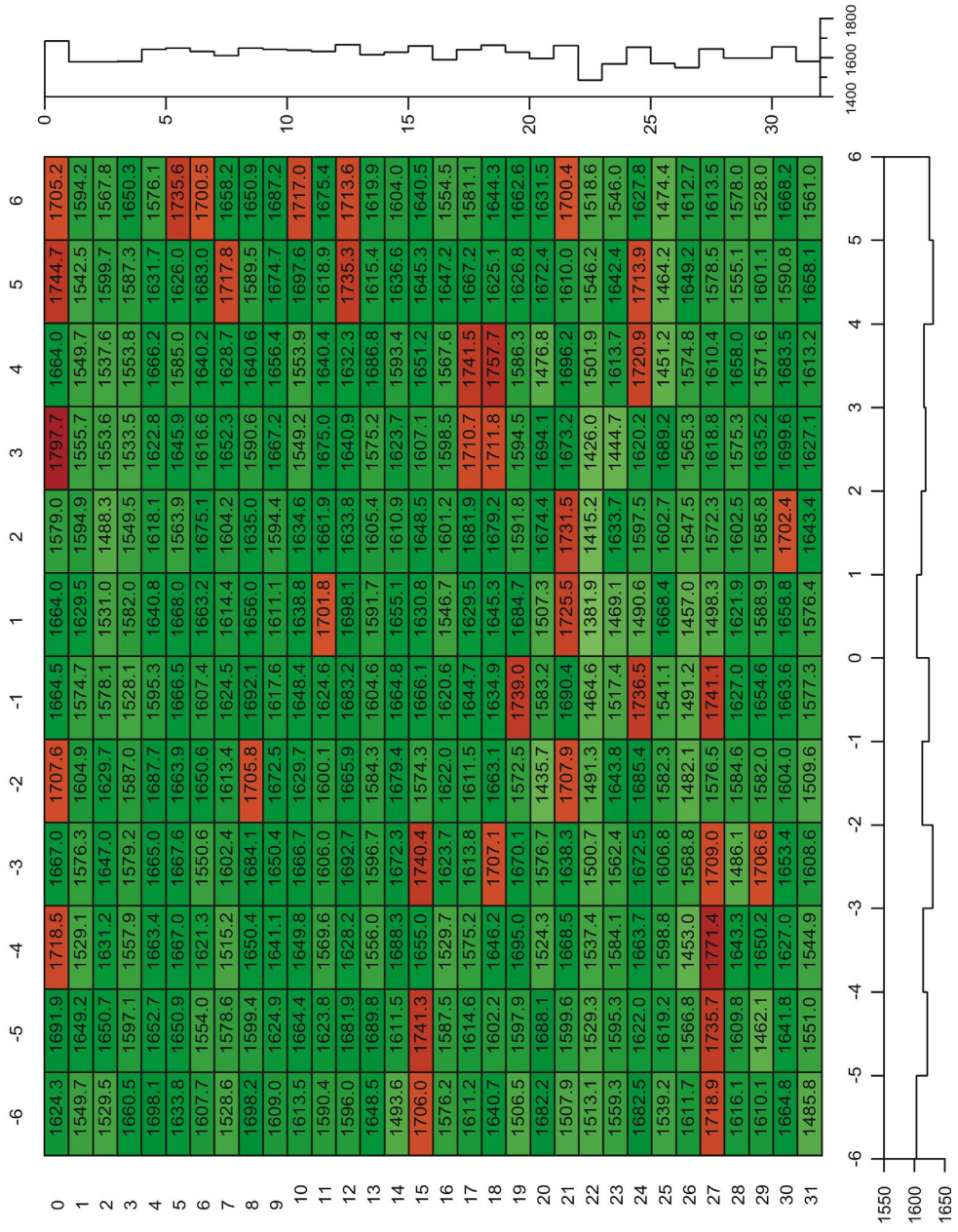

Figure 9.18: Geometric distribution of detector noise. Red indicate values over 1700 ENC. The axes show the average distribution along the beam and vertical to the beam.

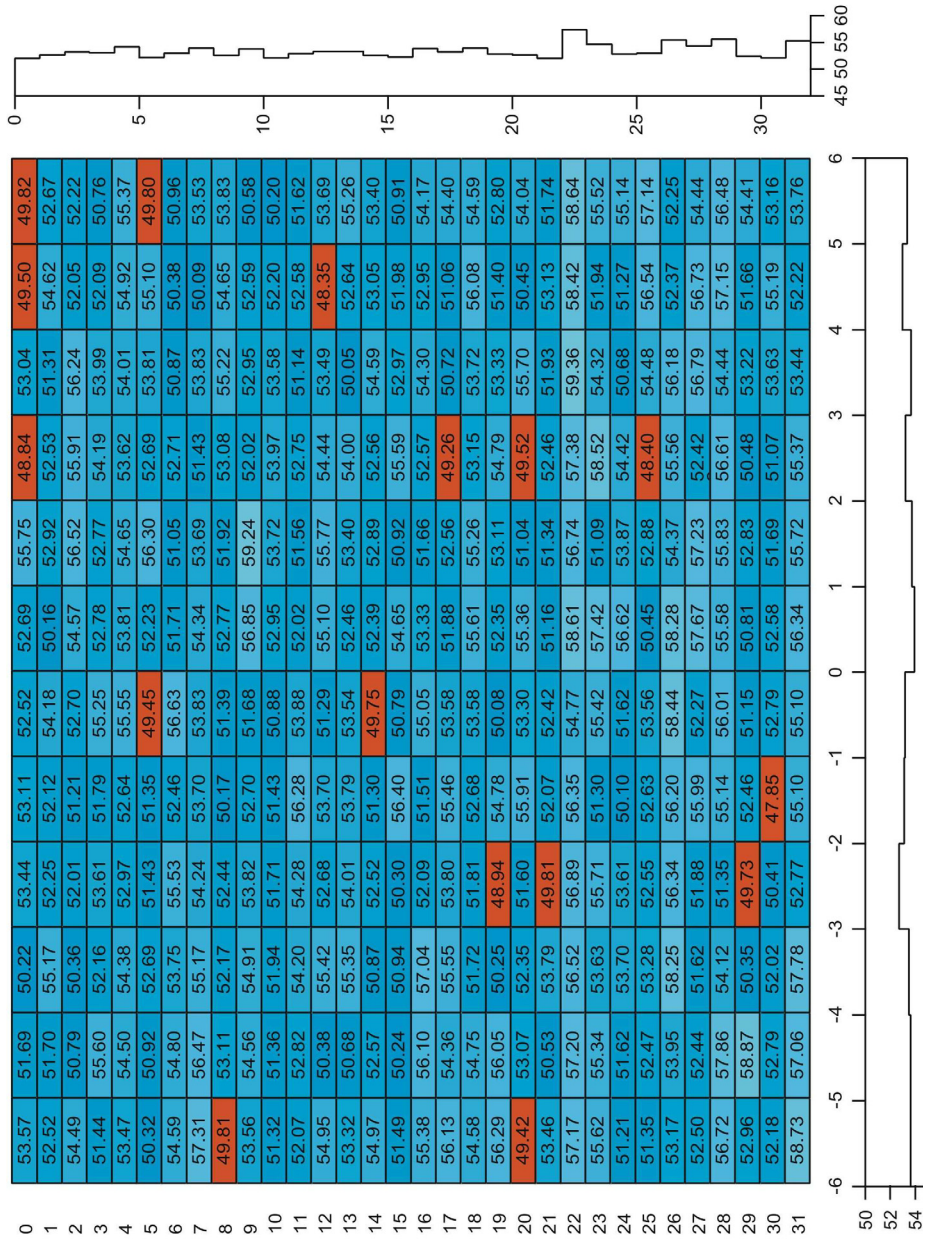

Figure 9.19: Geometric distribution of the detector gain. Red indicate value less than 50 mv/fC.

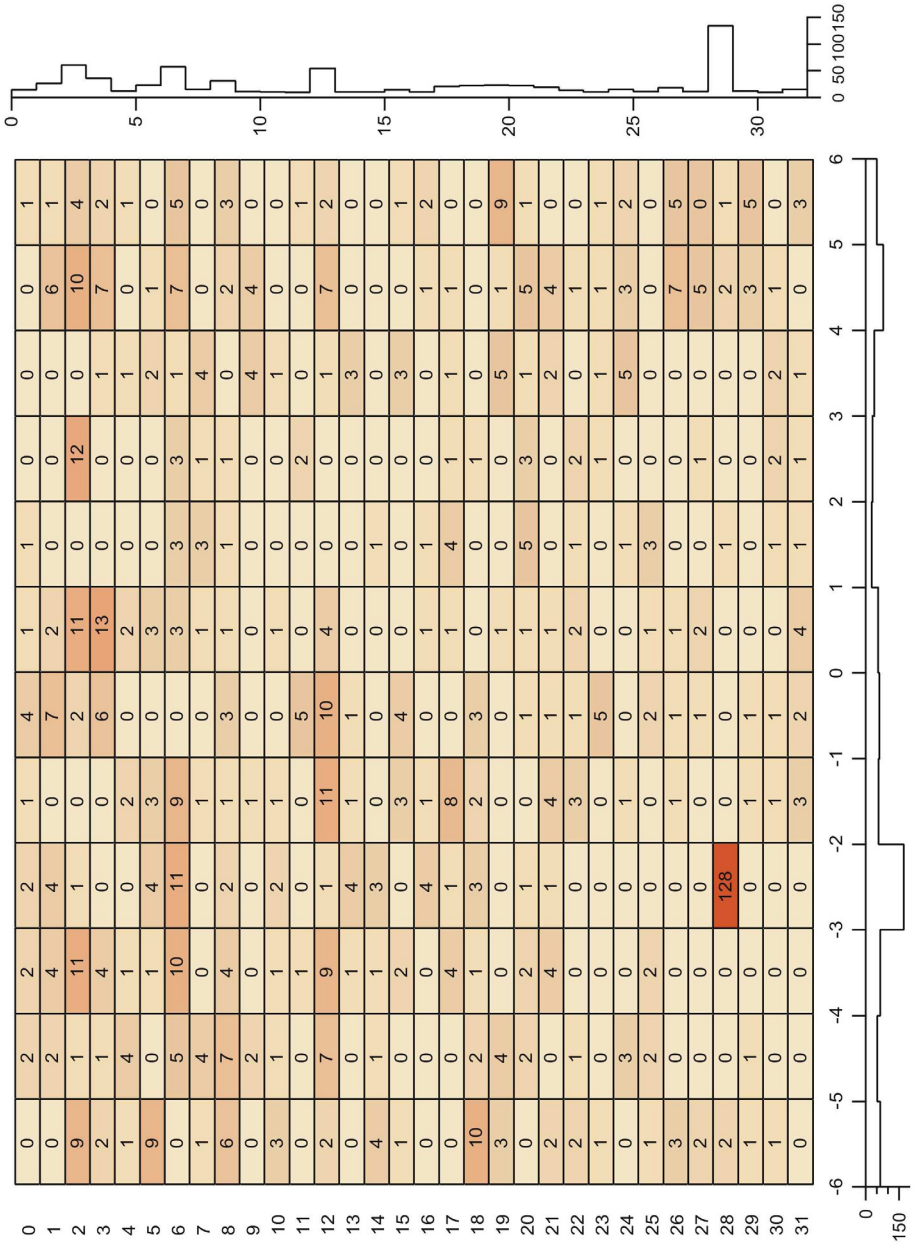

Figure 9.20: Distribution of detector defects for 3Pt gain.

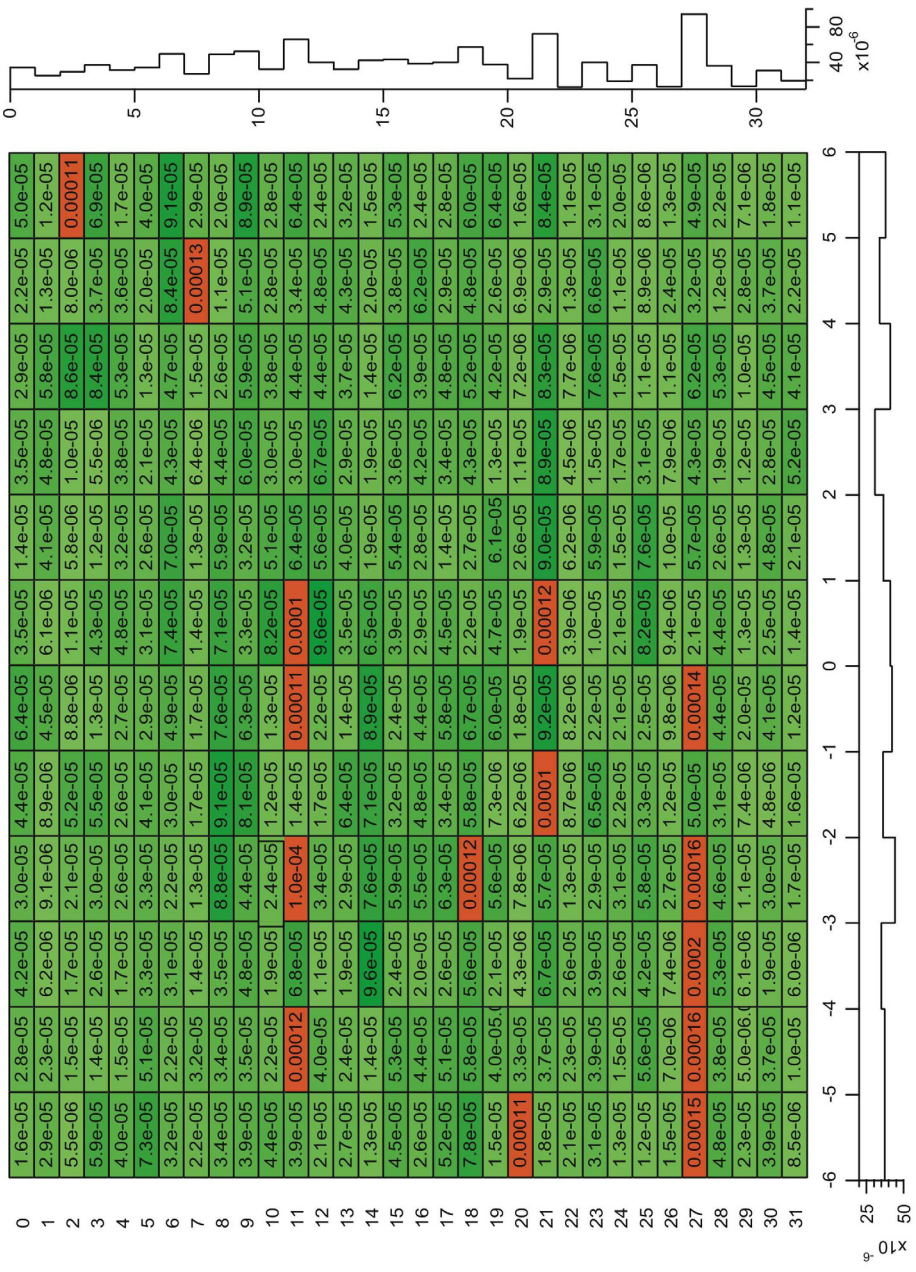

Figure 9.21: Distribution of noise occupancy (ENC).

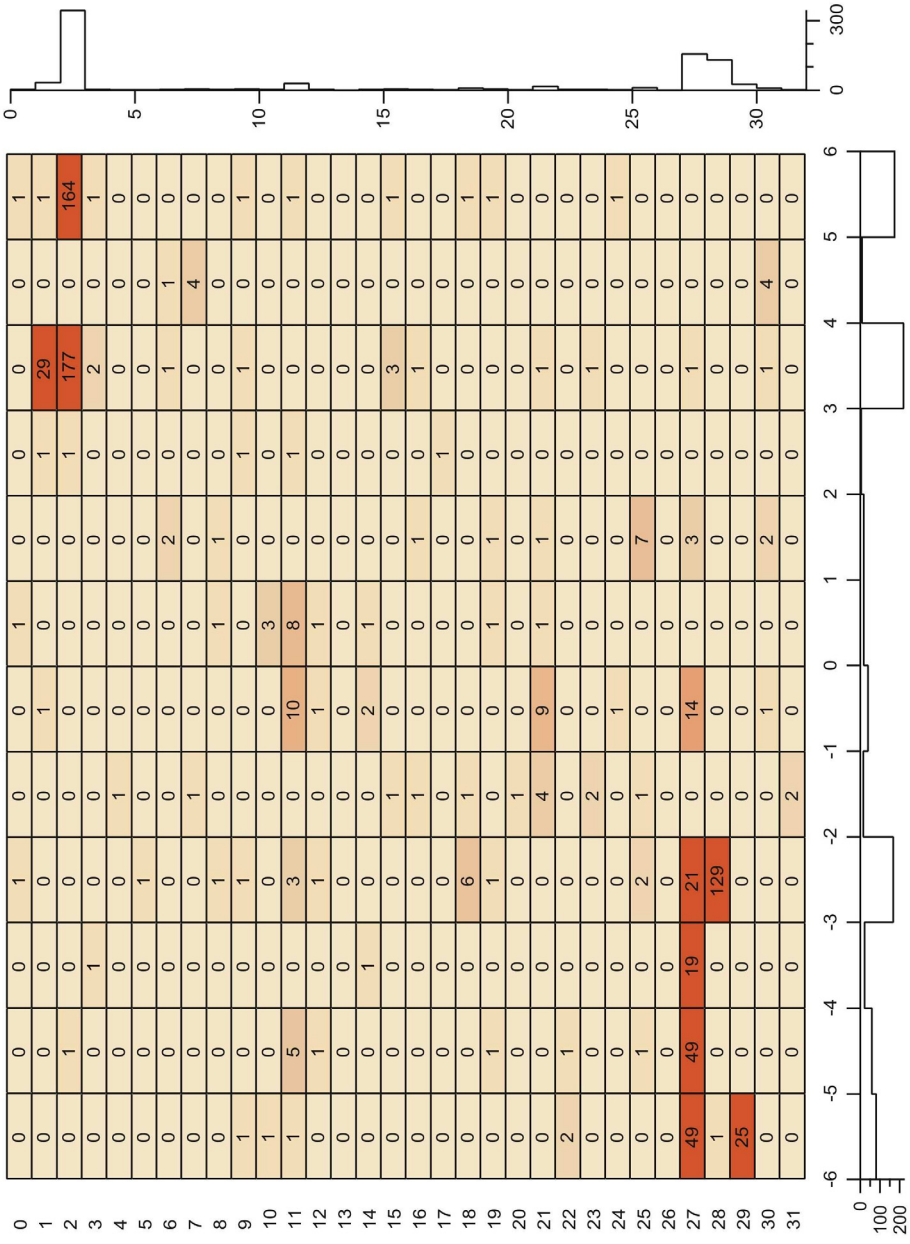

Figure 9.22: Distribution of detector defects for noise occupancy.

9.2.3 DCS Results

Recording of the DCS values through the DAQ was not implemented during most of the warm tests of B3, but a sample set was noted manually. These values were taken at the beginning of testing and are different than the temperature during testing. For this reason only some values are presented here, notably those recorded by the DAQ during the scans. The second set of warm test and the cold tests will have a full set of DCS values (examples in annex B.4).

Figure 9.23 shows the bias voltage read back after setting the voltage to 200 V and the corresponding bias current for the modules recorded during electrical testing (LV on). The voltage is stable at 200 V but the current is quite distributed. Most of the currents are less than 800 μA but some sporadic modules have currents higher than the 850 μA, which is the limit at 350 V. The decision has been taken to not replace these modules because there was no evidence of these modules being damaged.

Figure 9.24 shows left, the temperature distribution of link0 and link1, and right, the difference between the temperatures for the two links. As can be seen the temperature of the link 0 is a bit lower than the one on link 1. The difference is mostly less than 0.5°C which is considered acceptable, even thought the plot of the differences shows values up to 15°C. This is not a real effect, but due to inconsistencies in the measurement software. Not all temperatures and not always the temperatures on both links were stored. From experience, we know that there is good agreement between the temperatures on the two links.

From figure 9.25 one can see the distribution of the digital and analogue voltages and their corresponding currents. The digital, Vcc, and analogue, Vdd, voltages should not be too low for the electrical tests to be working. The left hand figure shows that the Vcc and Vdd values are close to their respective 3.5 V and 4 V operational values. One module shows high Vcc, but this module passed all electrical tests without any problems. The corresponding analogue, Icc, and digital, Idd, currents should be around 900 μA and 500 μA respectively. The plots show good agreement with this value. One module was found with Icc rather low, but it still passed all tests.

In conclusion, the DCS worked satisfactory during testing and permitted to run the barrel in safe operating conditions. Some inconsistencies needs further investigation but the overall performance is well within the expectations.

Geometric Distribution

Figure B.14 shows the distribution of bias current on the barrel. As can be seen three values are higher than 1 μA. Otherwise the distribution over the barrel is quite uniform. The left side of the barrel might have two regions with slightly higher bias current than the rest. The temperature distribution, 9.27, across the barrel is also quite homogeneous. There is no apparent region where the temperature is especially high and thus gives measurements with higher noise values than the rest of the barrel. The difference in temperature between the two links is not higher than 2 degrees difference, which corresponds to around 10 ENC difference in noise.

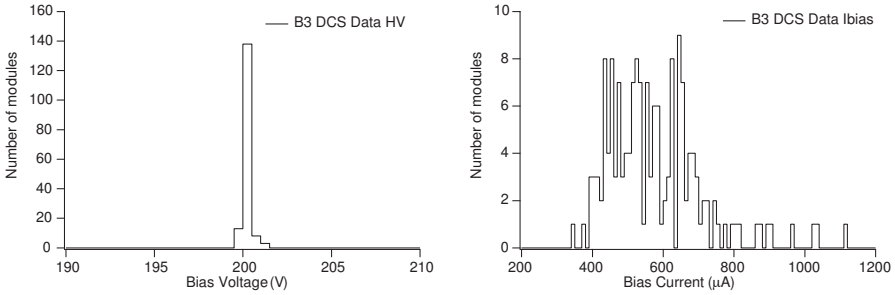

Figure 9.23: Distribution of detector bias voltage (left) and current (right).

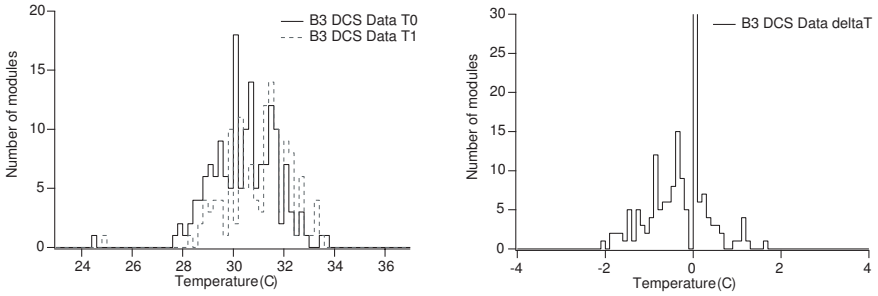

Figure 9.24: Distribution of detector temperature. Left, the temperatures on the two links and right the difference between the temperatures of the two links. The right-hand picture has a peak at 0 degrees for the modules where no temperature sensor was recorded.

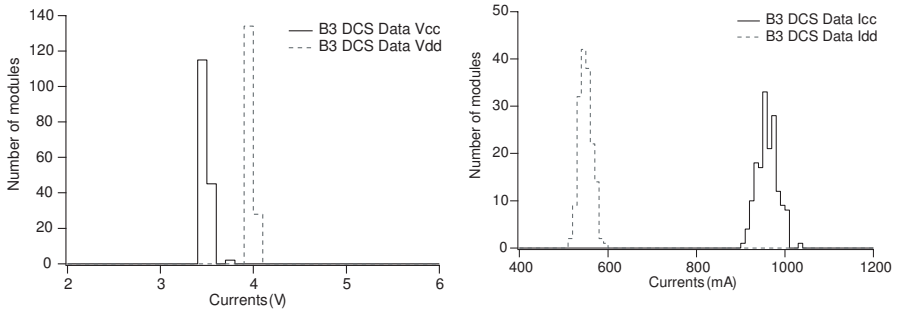

Figure 9.25: Distribution of supply voltages (left) and currents (right).

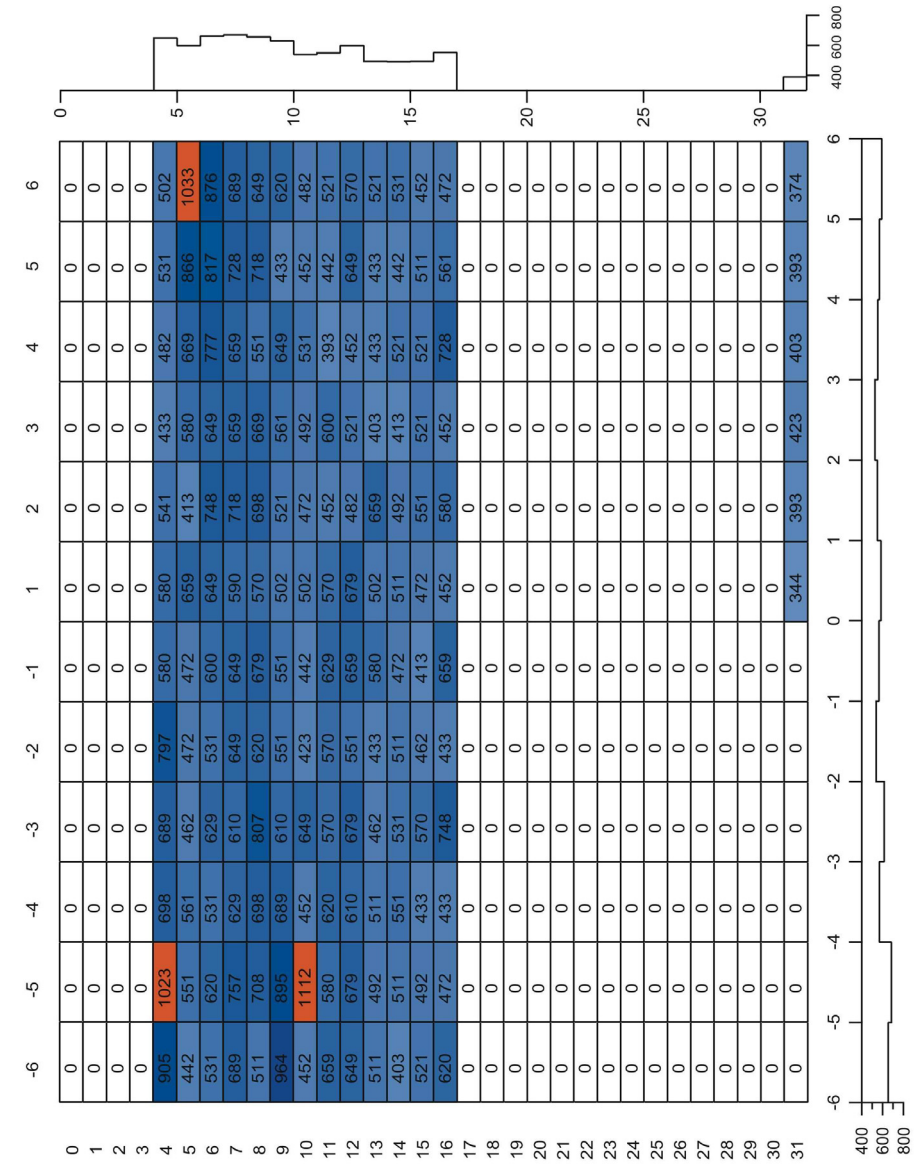

Figure 9.26: Distribution of bias current of the modules. Values in red are those exceeding 1 μA.

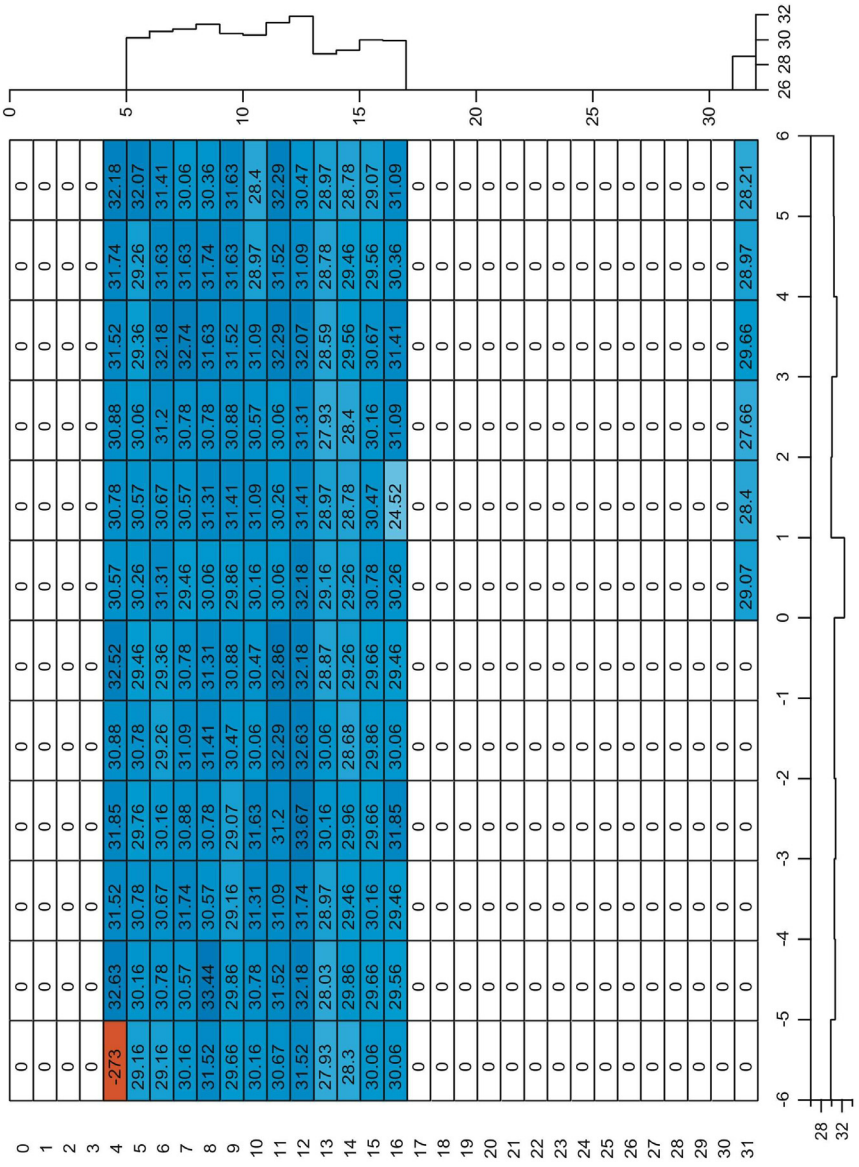

Figure 9.27: Distribution of temperatures (L0) of the B3 modules. Values are missing due to late implementation saving of DCS values. One value is red because of a temperature "glitch".

9.3 B3 Problems

During mounting of the modules onto the barrel surprisingly few problems where detected. However a few potential or real problems are worth mentioning. When it was possible faults were repaired, but in a few cases this was impossible or dangerous to the modules and a minor reduction of the barrel performance had to be accepted. The problems are presented in the following section as they where found during assembly testing. Later tests or repairs have not been included. However, these results gives a first indication of what kind of problems can be seen in future tests and how it will influence the overall barrel 3 performance. However, one needs to emphasise that these are only minor problems and the overall performance of the barrel 3 is very good and the assembly highly successful.

Figure 9.28 shows where these problems were detected on the barrel, both mounting, electronics or DCS problems. Most of the DAQ related problems could be fixed by changing the software parameters but some hardware failures forced the use of redundancy links or the replacement of a module. Only a few of the most serious or frequent problems will be explained as follows.

Two UKB modules were damaged; one in its box before mounting and one was removed because the mounting point on the barrel was initially incorrect. Two USA modules had problems passing the electrical tests. Both modules have subsequently been replaced. One broken fibre was discovered after mounting[5] connected to module 202203800111. Extensive tests and searches did not reveal the location of the breaking point. It was decided that any attempt to repair the fibre would be very dangerous to the module and its neighbours. This results in the loss of link 0 for this module and it will need to be read out by the redundancy link (link 1). This means that only 11 chips can be read of this module, the information from the last chip is lost due to the redundancy implementation.

Due to the individual changes to the optical lines and the optical-electrical conversion both at the BOC and at the module tuning of RX and TX threshold and strobe delay values seems to be needed occasionally. So far the problems seems to occur randomly except for the strobe delay, which sometimes has to be adjusted for a whole harness (blue). Strobe delay can be adjusted by software and is therefore not considered to be a serious problem.

Some of the DCS problems, which were first seen during barrel testing, have proven challenging to eliminate and some of the most important or tricky ones are listed below. Some DCS related problems were discovered during testing which needs more investigation. This mainly concerns the temperature readings and the bias current readings.

Figure 9.29 shows a problem with the DCS readings of temperature where occasionally spikes or bad temperature readings occur. There seems to be two types of spikes one which always goes to -173°C and one which goes to a lower value (for the Oxford set-up) of $\sim$ 8°C. A first investigation by changing the LV card connecting to one silicon module shows that the amount of spikes seemed to change. One of the two crates also had less spikes than the other crate. However this is not conclusive

[5]LMT row 29 Z- dogleg 6

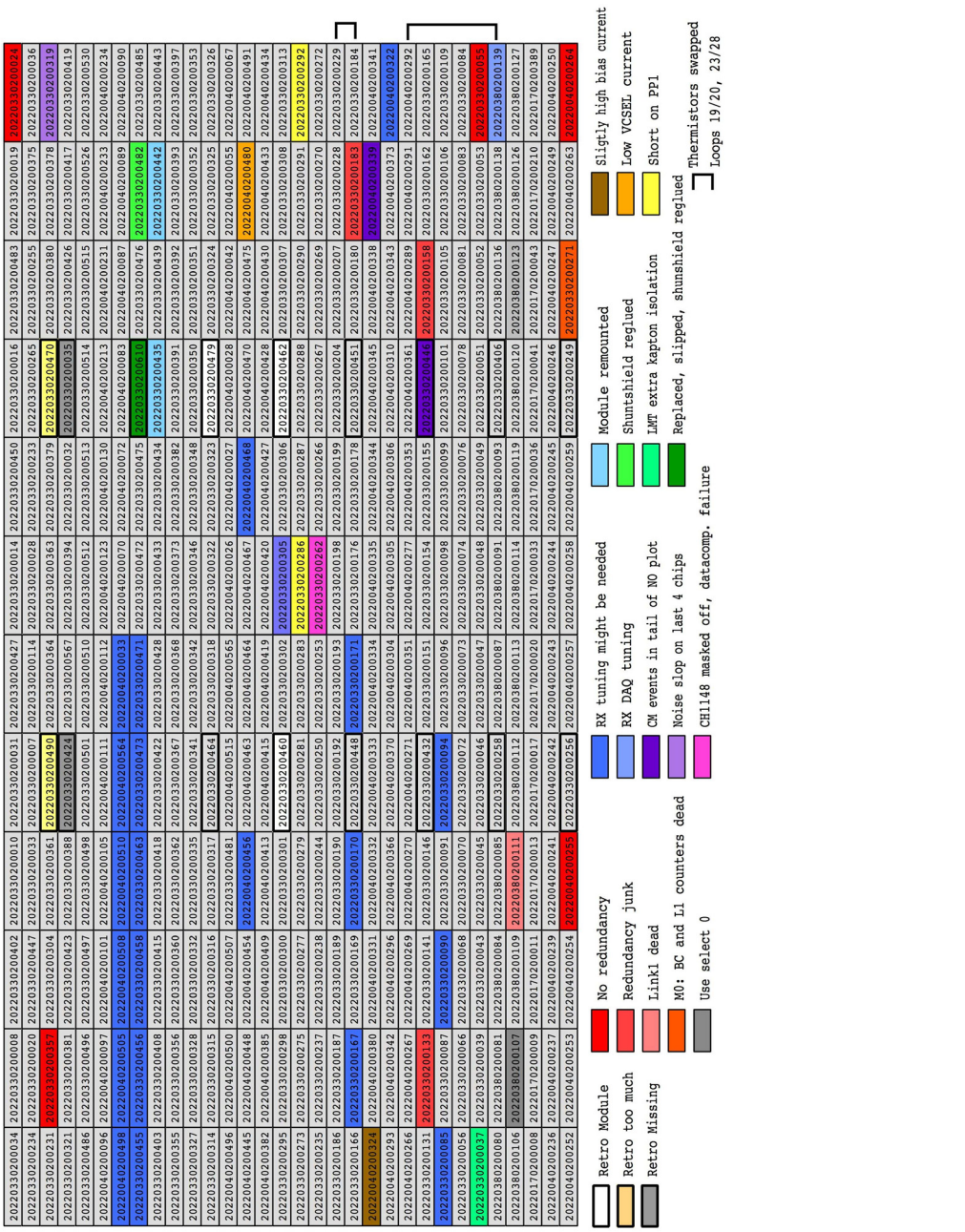

Figure 9.28: Some of the B3 inconsistencies, most of which are tuneable in software, firmware or by changing off-detector hardware [118].

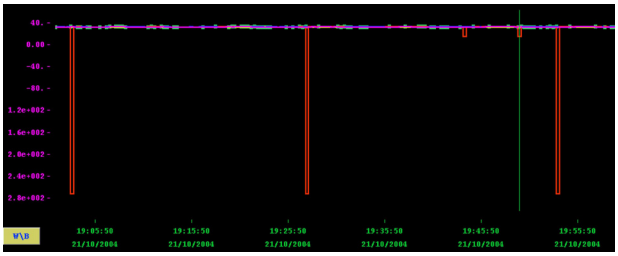

Figure 9.29: During the measurement of temperature several spikes appeared either at -273°C or at some fixed lower value around 12°. This picture shows three spikes to 273°C and two spikes to 8°C.

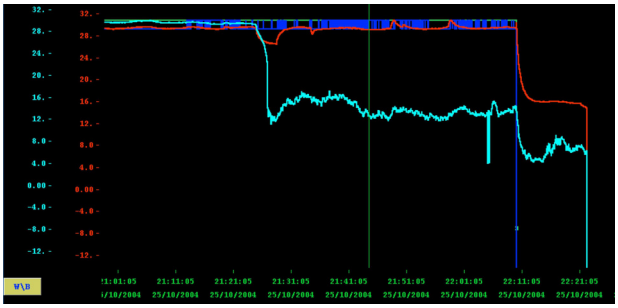

Figure 9.30: Temperatures for two links on one module. Link0 shows stable temperature around 29°C before the module power is being shut off. Link1 has an unstable temperature which drops much before the end of the test sequence down to around 12°C.

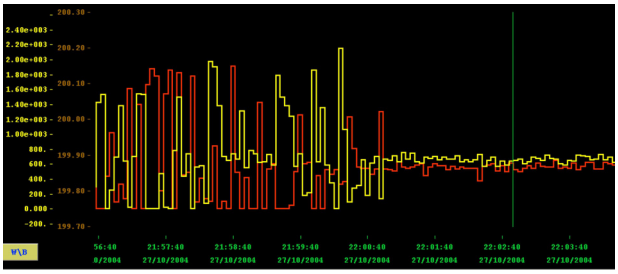

Figure 9.31: This figure shows the bias current of two neighbouring modules (probably also on the same HV card) which shows a region of very unstable bias currents oscillating between $\sim$ 0 - 2 μ A before stabilising at $\sim$ 600 nA. In addition the two modules shows a very dependent behaviour. When the current of one module increases the other one drop.

since the amount of spikes over time seemed to change quite a lot. These spikes have later been seen also at CERN. Further testing will show if this is due to the DCS hardware or some logical communication problem.

Another temperature related problem was found which affected two modules. As can be seen in Figure 9.30 showing the first module with this problem only on link 0, the one temperature sensor show abnormal behaviour and does not follow the pattern of the second sensor. It was also found for the second module that the value of the sensor was inversely coupled to the value of the Vcc sense line. After investigation it was found that the grounding of the two modules were not correct and it was repaired by soldering the Vdd return sense line to the Vdd return on the patch panel on the support wheel (PPB1[6]) via a 0 Ohm resistor. In addition the Vcc return sense line was connected to Vcc return at PPB1 via a wire link. Tests of these modules after repairs show the return to normal behaviour.

A third problem, which was only observed once, was an abnormal behaviour of the bias current. Figure 9.31 shows what happens to two neighbouring silicon modules on the barrel. Normally after setting the bias current it needs a bit time to stabilise from the high ramping values of around 2 μA to the operating values of $\sim$ 6-800 nA. The stabilisation is normally more or less immediate but in this case it took around four minutes to stabilise. This also happened for no apparent reason, there was no ramping going on. Another observation from this figure is a connection between the two bias currents on the two modules seems to depend on each other, when one bias current goes up the other one goes down etc. This coupling between two modules has only been seen once and will need to be reproduced before more investigation can take place. From the power supply development (chapter 6) there is a history of rare couplings observed between two HV channels on the same card and this new problem could be related to this.

In total, the faults found on barrel 3 are few. Most can and will be repaired, however one chip has been lost because of a faulty harness. Nevertheless, the total performance of the barrel is excellent and this is good news for the macro-assembly community.

Conclusion

The assembly of barrel 3 in Oxford have been most successful. Almost four hundred times a module have been picked up and fixed to the barrel structure with more or less no accidents. The amount of defects (with very few exceptions) has been less than 1%, which must be said to be a considerable achievement. In addition both the DCS and DAQ system have been installed and working during all assembly tests, in spite of all initial and occurring problems with both the cooling and the power supplies. This is a major system achievement, since this means it has been used every working day for more than 6 months, for many hours at a time. Later tests of the full barrel, also confirms the successful scale-up of the test system.

[6]Patch Panel Barrel 1

The warm tests presented here, show results that are highly promising. Not only are the warm data within the expected limits for the warm tests, the distribution of noise and gain values per chip even seems slightly better on average than for the reference data. This is a formidable achievement for both the barrel macro-assembly group in Oxford as well as for the SCT community. Already, the results of the cold tests have given an excellent confirmation of the procedure. The next step will be to test barrel 3 at CERN to determine if any degradation has occurred during the shipping. It will be exiting to see if the CERN set-up can meet the excellent results seen in Oxford for the first barrel.

Part III

Physics Simulation

10
Beyond the Standard Model

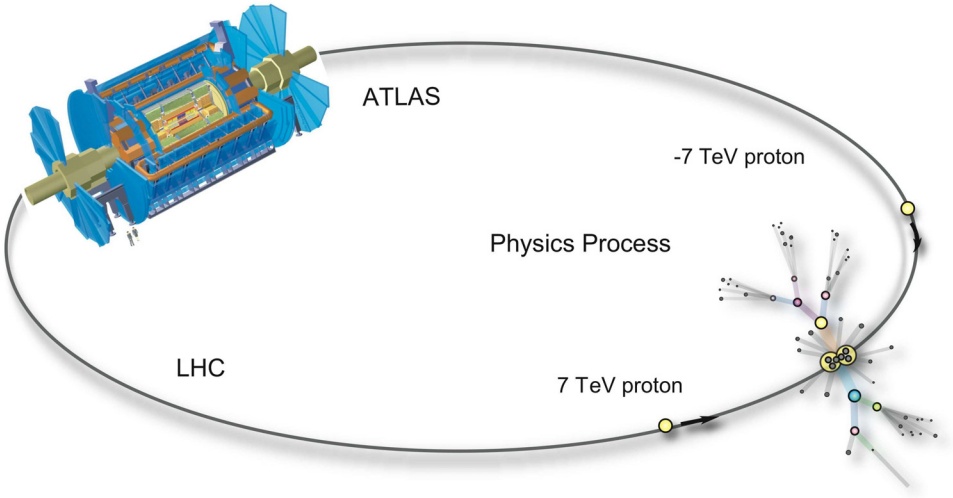

Introduction

Within the next few years, the ATLAS detector will be ready for its first series of physics runs. When this happens, a new energy region will be reached where the Standard Model may no longer be valid. The ATLAS detector not only specialises in finding the remaining unknown quantities of the SM, but it will also probe the new energy range for new physics.

Several theories have been developed, which try to describe the physics beyond the SM and to address the unresolved questions described in chapter 1. This chapter presents the theories and framework behind extra neutral gauge bosons (Z'), one of the main motivations for searches for new physics besides supersymmetry. These bosons are highly interesting in the light of the LHC development, since they could be among the first new particles to be produced and detected by the ATLAS detector even at the initial low luminosity. In addition, the detection of one or more Z' bosons could make it possible to distinguish between the theoretical models due to their different properties.

This chapter will first present briefly the appearance of Z' in different models before discussing the corresponding experimental parameters. Then follows a description of the envisaged Z' production in LHC and the possible ATLAS detection. The chapter ends with a discussion of lower and upper limits for existing and future Z' searches. Simulation results obtained with the ATLAS detector simulation software will be presented in chapter 11.

10.1 Grand Unified Theories

As explained in chapter 1, the Standard Model is a well-proven theory in very good agreement with experimental results [14]. However, it does not explain certain problems such as the unification of strong and electroweak interactions and the hierarchy problem. A larger symmetry could also explain the more than 19 free SM parameters which now have to be determined experimentally, such as coupling constants, mixing angles and particle masses [119]. In addition, there are strong motivations for trying to unify all four fundamental forces, including gravity.

The main aim of the Grand Unified Theories (GUT) is to provide a model at the limit of the SM, which can unify at least the electroweak and strong force into one. This can be done by searching for one new and larger gauge group, which includes all the SM gauge groups. By doing this, new particles are likely to occur. Many of the GUTs [120, 121], most Superstring models [120] and Left-Right symmetric models [121] as well as dynamical symmetry breaking [122] and Little Higgs models [123], predict the existence of one or more heavy neutral gauge boson [11]. It can also arise in certain classes of theories with extra dimensions. Current theories predict that one or more Z' could be found just below the Planck scale, however many models predicts the Z' to be near or at the electroweak scale.

An important feature of new neutral gauge bosons is that they do not spoil the observed electroweak gauge coupling unification. On the other hand, the present

theories do not predict of the mass of these new bosons, as was made for Z^0. It can be either light or heavy. For this reason, a dedicated detector search is excluded, but the particles can be discovered in a number of general-purpose detectors either directly or by indirect searches. The Z′ signature would make it easily detectable in ATLAS at the LHC or by any similar detector and accelerator systems.

10.2 Extra Neutral Gauge Bosons (Z′)

From the many GUT theories, the simplest case is to assume an underlying effective gauge group at low energies of the form $SU(3)_C \times SU(2)_L \times U(1)_Y \times U'(1)$ which results in an extra neutral gauge boson, Z′. The second assumption is that the couplings of the Z′ to fermions are universal for all generations, although it is not the case for all models. This simplified model is in general useful to understand the principle of all GUT's. The following description of the different Z′ arising from several models is taken from [119, 124, 125]. The new particles required by each of these models are presented in table 10.1.

Sequential Standard Model (SSM)

The Sequential Standard Model (SSM) assumes the Z′ to be identical to Z^0, with similar couplings to SM fermions, except for having a higher mass. There is no theoretical motivation for this model, but it has proven useful as a reference when comparing different models and results from different sources. Newer theories state that a model with extra dimensions at an electroweak scale also could produce this Z′ as an excited state, Kaluza-Klein excitations, of the ordinary Z^0 [124]. In the discussion which follows, any sequential standard model Z′ will be denoted Z'_{SSM}.

Grand Unified Theories (E_6)

String theory has been an important motivation to look for additional Z′ - particles. One of the main reasons is that in this theory certain compactifications lead naturally to an E6 gauge group or one of its sub-groups:

$$E_6 \rightarrow SO(10) \times U(1)_\psi \rightarrow SU(5) \times U(1)_\chi \times U(1)_\psi \rightarrow SM \times U(1)_\beta,$$

where SM is the Standard Model group $SU(3)_C \times SU(2)_L \times U(1)_Y$. The breaking of the E_6 gauge group into $SO(10) \times U(1)_\psi$ as well as the breaking of SO(10) into $SU(5) \times U(1)_\chi$ produce two new neutral bosons, Z'_ψ and Z'_χ respectively. The observed Z′ would be a linear combination of a Z'_ψ and Z'_χ, expressed by the mixing angle β:

$$Z' = Z'_\chi \cos\beta + Z'_\psi \sin\beta, \tag{10.1}$$

with β being a free parameter in the range $-\frac{\pi}{2}$ to $\frac{\pi}{2}$. The three most studied models, corresponds to three uniquely defined β values ($\beta_\chi = 0$, $\beta_\psi = \frac{\pi}{2}$ and $\beta_\eta = -\arctan\sqrt{\frac{5}{3}}$) are here presented in more detail as well as in chapter 11 [121, 125, 126]:

- Z'_χ is defined by the breaking of the SO(10) GUT to its maximal subgroup SU(5) × U(1)$_\chi$. The boson is the unique solution to several conditions; e.g. family universality[1], no extra matter other than the right-handed neutrino. If the Z′ is a pure Z'_χ, the mixing angle is equal to $\beta_\chi = 0$.
- Z'_ψ arises from the E_6 GUT which contains the subgroup SO(10) x U(1)$_\psi$. Z'_ψ only has axial-vector couplings to the ordinary fermions and its mass is generally less constrained than for other models. The mixing angle for Z'_ψ is equal to $\beta_\psi = \frac{\pi}{2}$.
- Z'_η appears in superstring theory where E_6 is broken directly into a rank-5 group. The Z'_η is the linear combination of $\sqrt{3/8}\ Z'_\chi - \sqrt{5/8}\ Z'_\psi$ and its mixing angle is equal to $\beta_\eta = -\arctan\sqrt{\frac{5}{3}}$.
- In the past also other models with different mixing angles have been studied, such as Z'_I with a mixing angle $\beta_I = \cos^{-1}\sqrt{\frac{3}{8}}$. However, the models presented above are generally considered the most important today.

Left Right Model (LRM)

Another important group of models are the Left-Right Models appearing from the groups SU(2)$_L$ × SU(2)$_R$ × U(1)$_Y$, where an additional right-handed group has been added. The LRM restores the parity symmetry at high energies. The relation between the left- and right-handed couplings is given by the following expression:

$$\kappa = |\frac{g_R}{g_L}|. \tag{10.2}$$

The electroweak gauge symmetry of this group gives identical right-handed and left-handed couplings if the relation between left and right is symmetric, $\kappa = 1$. Some of the most popular sub-models exists are found by varying the mixing parameter κ:

- Z'_{LRM} with $0.55 \leq \kappa^2 \leq$ 1-2
- Z'_{LRSM}, the Left Right *Symmetric* Model with (LRSM) $\kappa = 1$.

Alternative Left Right Symmetric Model (ALRM)

Derived from the LRM are the Alternative Left-Right Models which arise from the E_6 groups. They are based on the SU(2)$_L$ × SU(2)$_R$ × U(1)$_{B-L}$ gauge group where B and L are the baryon and lepton numbers. The ALRM restores the parity symmetry at high energies by extending the SU(2)$_L$× U(1)$_Y$ SM-gauge group to SU(2)$_L$× SU(2)$_R$× U(1)$_{B-L}$ and by introducing three new gauge bosons W_R^+, W_R^- and Z':

[1] Any known SM family structures will be conserved and any new particles will follow this same family pattern.

Model	Group Structure	Model Specific Particles
SM	$SU(2)_L \times U(1)_Y$	-
SSM	$SU(2)_L \times U(1)_Y \times U'(1)$	W'^{+}, Z'
E_6	$SU(2)_L \times U(1)_Y \times U(1)_{\theta_{E_6}}$	$W'^{+/-}, Z', \nu_R$
LRM	$SU(2)_L \times SU(2)_R \times U(1)_Y$	$H^{++}_{L/R}, W^{+/-}_R, Z^0_R, \nu_R$
ALRM	$SU(2)_L \times SU(2)_R \times U(1)_{B-L}$	$H^{++}_{L/R}, W^{+/-}_R, Z^0_R, \nu_R$
KK		$Z'_0, ..., Z'_n$, ...

Table 10.1: New particles occurring in various Z′ models.

$$LRSM \rightarrow SO(10) \rightarrow SU(3)_C \times SU(2)_L \times SU(2)_R \times U(1)_{B-L}. \tag{10.3}$$

The relation between left and right, α, has been adjusted with respect to κ of the Left Right Model ($\frac{g_R^2}{g_L^2} = \kappa^2$):

$$\alpha = \sqrt{(c_W^2 g_R^2 / s_W^2 g_L^2) - 1},$$

where $c_W = \cos\theta_W$ and $s_W = \sin\theta_W$. By varying the mixing parameter α the following sub-models can be derived:

- Z'_{ALRM} is an asymmetric distribution of left and right helicity and $\sqrt{2/3} \leq \alpha^2 \leq \sqrt{c_W^2/s_W^2 - 1}$.
- For Z'_χ, $\alpha = \sqrt{3/2}$ the E_6-model Z'_χ is retrieved.

Extra Dimensions (KK)

Other relevant models include the recent work on Kaluza-Klein excitation modes leading to extra gauge bosons, Z'^{kk}_i propagating with the graviton in the extra dimensions. A tower of massive gauge bosons, Kaluza-Klein states (KK), appears from the extra dimension of freedom in the higher dimensional theory when compactified to the usual 3+1 dimensions.

10.3 Z′ Parameters

The Z′ parameters can provide important information on new physics either by constraining their experimental limits or by direct measurement. Among the most interesting parameters are the mass (M) and the width (Γ) of the Z′ mass eigenstate as well as the Z′ coupling strength ($g_{Z'}$) and the vector and axial couplings to fermions (v'_f, a'_f). A subset of the Z′ parameters are presented below and are based on descriptions in [121, 119, 125].

Mass Mixing

An extension of the gauge group will result in a new representation of the eigenstates of the electroweak theory of the Standard Model. In the case where the vacuum expectations for the Higgs fields are real, the mass eigenstates Z_1 and Z_2 can be diagonalised by a rotation of the fields Z and Z′ (weak interaction eigenstates) around the mixing angle θ_M, where c_M and s_M are $\cos\theta_M$ and $\sin\theta_M$ respectively [121]:

$$\begin{bmatrix} Z_1 \\ Z_2 \end{bmatrix} = \begin{bmatrix} c_M & s_M \\ -s_M & c_M \end{bmatrix} \begin{bmatrix} Z \\ Z' \end{bmatrix}. \tag{10.4}$$

In some other gauge models, for example in the Left-Right Models, this eigenstate mixing is made in one step through an orthogonal 3×3 matrix. Due to the experimental results of the SM, the mixing angle is severely constrainted and has to be less than $\sin\theta_M < 0.01$, which is very weak [14]. For this reason, it is common to neglect Z-Z′ mixing.

Lagrangian

Using the SM representation of the Lagrangian for neutral currents (NC) and adding the electroweak term in this new gauge group, the new Lagrangian can be written as [127, 121]:

$$\begin{aligned} -\mathcal{L}_{NC} &= e J^\mu_\gamma A^\mu + g_1 J^\mu_Z Z_\mu + g_2 J^\mu_{Z'} Z'_\mu && (10.5)\\ J^\mu_\gamma &= \sum_f \bar{f}\gamma^\mu Q^f f && (10.6)\\ J^\mu_Z &= \sum_f \bar{f}\gamma^\mu [v_f - \gamma_5 a_f] f && (10.7)\\ J^\mu_{Z'} &= \sum_f \bar{f}\gamma^\mu [v'_f - \gamma_5 a'_f] f. && (10.8) \end{aligned}$$

These three neutral currents are weighted by their electroweak coupling constants (e, g_1,g_2), which obey the following relation, where $\sin\theta_W = s_W = \frac{e}{g}$:

$$\begin{aligned} e &= \sqrt{4\pi\alpha} && (10.9)\\ g_1 &= \frac{g}{2c_W} = \frac{e}{2 s_W c_W} && (10.10)\\ g_2 &= \text{model dependent.} && (10.11)\\ & && (10.12) \end{aligned}$$

The vector and axial couplings are defined by the electrical charges, with $Q^f = T_3^f + \sqrt{\frac{5}{3}} Y^f$, Y being the hypercharge and T the weak isospin. The vectorial and axial coupling are defined by the following relations, where $f \in \{d, u, e, \nu\}$:

$$v_f = T_3^f - 2Q^f s_W^2 \tag{10.13}$$
$$a_f = T_3^f \tag{10.14}$$
$$v'_f = g_2\,[(q'_{fL} + q'_{fR}) + \frac{g_{12}}{g_2}\sqrt{\frac{3}{5}}\,(-T_{3f}^f + 2Q^f)] \tag{10.15}$$
$$a'_f = g_2\,[(q'_{fL} - q'_{fR}) + \frac{g_{12}}{g_2}\sqrt{\frac{3}{5}}\,(-T_{3f}^f)]. \tag{10.16}$$
$$\tag{10.17}$$

Z′ couplings

The couplings of fermions to Z′ are gauge model dependent and the vector and axial couplings to fermions for both E6 models and the Left-Right model are shown in table 10.2. Since the Z'_{SSM} has identical couplings as the Z^0, its coupling, g_2, is equal to g_1.

As described in [127], the coupling constants of the E_6 model are defined by the relations:

$$g_{12} = 0 \tag{10.18}$$
$$g_2 = \frac{c_W}{g}\sqrt{\frac{5}{3}}\frac{e}{c_W} = \sqrt{\frac{5}{3}}s_W, \tag{10.19}$$

taking $\sin^2\theta_W = 0.23$. The left and right couplings of Z′ to fermions are described by a linear combination of the $U(1)_\psi$ and $U(1)_\chi$ charges:

$$g_2(Q_\chi \cos\ \beta + Q_\psi \sin\ \beta), \tag{10.20}$$

where $Q' = Q_\chi \cos\ \beta + Q_\psi \sin\ \beta$ is either the left handed, q'_{fL}, or right handed, $q'_{fR} = q'_{f^cL}$ couplings to fermions. The new electroweak charges, Q_χ and Q_ψ, for the different types of fermions are defined by the following relations:

Q'	$2\sqrt{10}Q_\chi$	$2\sqrt{6}Q_\psi$
q'_{qL}	-1	1
q'_{u^cL}	-1	1
q'_{d^cL}	3	1
q'_{lL}	3	1
q'_{e^cL}	3	1

The vectorial and axial couplings for the E_6 model used above are displayed in table 10.2.

For the Left-Right model, the coupling to fermions is given by the following expression where $\kappa^2 = (\frac{g_R}{g_L})^2$ lies between 0.55 and 1-2:

E6	a'_f	v'_f	LR	a'_f	v'_f
ν	$\frac{3\cos\beta}{\sqrt{40}} + \frac{\sin\beta}{\sqrt{24}}$	$\frac{3\cos\beta}{\sqrt{40}} + \frac{\sin\beta}{\sqrt{24}}$	ν	$\frac{1}{2\alpha}$	$\frac{1}{2\alpha}$
e	$\frac{\cos\beta}{\sqrt{10}} + \frac{\sin\beta}{\sqrt{6}}$	$\frac{2\cos\beta}{\sqrt{10}}$	e	$\frac{\alpha}{2}$	$\frac{1}{\alpha} - \frac{\alpha}{2}$
u	$-\frac{\cos\beta}{\sqrt{10}} + \frac{\sin\beta}{\sqrt{6}}$	0	u	$-\frac{\alpha}{2}$	$-\frac{1}{3\alpha} + \frac{\alpha}{2}$
d	$\frac{\cos\beta}{\sqrt{10}} + \frac{\sin\beta}{\sqrt{6}}$	$-\frac{2\cos\beta}{\sqrt{10}}$	d	$\frac{\alpha}{2}$	$-\frac{1}{3\alpha} - \frac{\alpha}{2}$

Table 10.2: Vector and axial couplings of Z′ to fermions for the E_6 and the ALRM models [121]. These values need to be multiplied with the coupling constant g_2.

$$\frac{gz}{\sqrt{\kappa - (1-\kappa)s_W}} \, (s_W T_{3L} + \kappa(1-s_W)T_{3R} - s_W Q), \tag{10.21}$$

T_{3L} is the same as SM weak isospin, T_{3R}= 1/2, -1/2, -1/2, 1/2 for u_r, d_r, e_r, ν_r respectively, and Q is the electric charge. All fermions with a left-handed helicity are equal to zero.

The Z'_{ALRM} couples to a linear combination of the right-handed and B-L currents:

$$J^{\beta}_{LR} = \sqrt{\frac{5}{3}}(\alpha J^{\beta}_{3R} - (1/2\alpha)J^{\beta}_{B-L}), \tag{10.22}$$

where α is expressed by the left- and right-handed couplings and where J^{β}_{3R} and J^{β}_{B-L} are the currents associated with the $SU(2)_R$ and the $U(1)_{B-L}$ group, respectively. B-L are the baryon and lepton numbers given by $B - L = 2(Q - T_{3L} - T_{3R})$.

10.4 Z' Production at LHC

As described in chapter 3, the Large Hardron Collider (LHC) is a proton-proton collider with 14 TeV center of mass energy and 10^{34} cm^{-2}s^{-1} luminosity. At this luminosity, an average of $\sim$ 20 hard collisions will be produced per bunch crossing (every 25 ns). The particles produced by the LHC machine will be detected by four large experiments, of which the two general-purpose detectors CMS and ATLAS can expect to detect extra neutral gauge bosons if they are produced.

At the LHC, any Z′ will be produced by a quark-antiquark annihilation between the valence quark and a sea anti-quark ($pp \rightarrow q\overline{q}X \rightarrow Z'X$) of the two colliding protons. Figure 10.1 shows a Feynman diagram for this process and figure 10.3 the

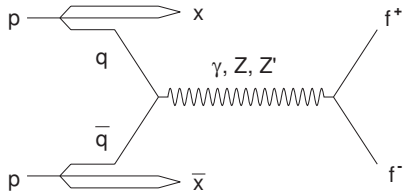

Figure 10.1: Production channels of Z′, decay to leptons or di-jets from produced quarks.

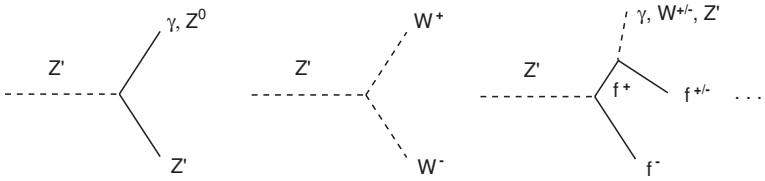

Figure 10.2: Some other Z′ decay modes.

typical cross sections for a $p\bar{p}$ collider at $\sqrt{s} = 4$ TeV and a pp collider at $\sqrt{s} = 14$ TeV.

The observation of Z′ can be made by the detection of Z′ decay to pairs of leptons (see figure 10.1). Other possible decay modes for new neutral gauge bosons are decays to dijets, pairs of SM bosons and leptonic W^+ decay modes (rare decay or associate production, see figure 10.2). The main channel for Z′ observation is the Drell-Yan process with decay of Z′ to an electron-positron or muon-anti muon pair $pp \rightarrow Z', X \rightarrow l^+l^-(l = e,\ \mu,\ \tau)$, X. Even though pp and $p\bar{p}$ collisions differ at low energies, at high energies, such at the LHC energy, the cross section of their processes become similar ($\sigma(pp) \lesssim \sigma(p\bar{p})$).

The main Standard Model process, contributing to the background and interfering with the signal, is Drell-Yan production via an intermediate γ or Z^0. Other possible, but negligible background sources are leptons from γW, $\gamma\gamma$, ZZ, ZW,W^+W^- and $t\bar{t}$ production. In the case where a new model is determined, the decay to exotics can be playing a non-negligible role.

10.5 Z′ Detection in ATLAS

As described in chapter 3, ATLAS is designed not only to search for the Higgs particle but also to search for physics beyond the Standard Model. Already at low luminosity (10 fb^{-1}), during the first year of LHC operation, a heavy Z′ could be detected. If discovered, the first step will be to investigate direct Z′ properties such as its mass, total width and cross-section. Secondly, it will be important to investigate

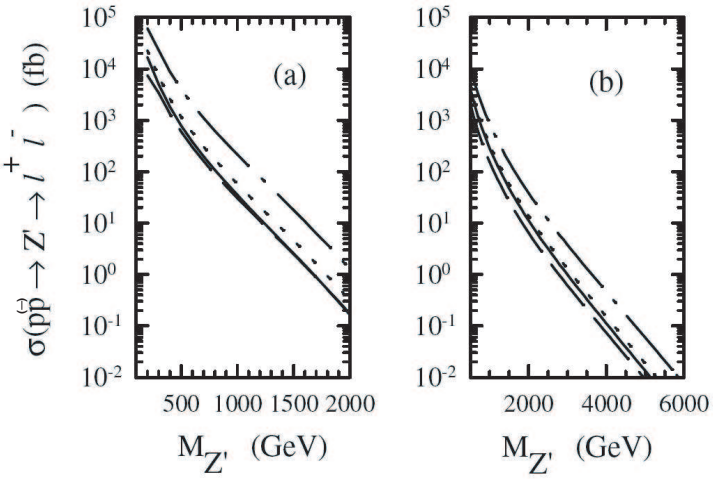

Figure 10.3: The cross section for the process $pp(p\bar{p}) \to Z' \to l^+l^-$ as a function of $M_{Z'}$ for left, a $p\overline{p}$ with $\sqrt{s} = 4$ TeV and right pp with $\sqrt{s} = 14$ TeV. Solid, dashed, dotted and dot-dashed lines displays Z'_χ, Z'_ψ, Z'_{LRM} and Z'_{ALRM} respectively [125].

the couplings to fermions, the nature of symmetry breaking and the coupling to exotic or supersymmetric particles, in order to increase the information about the underlying theoretical model.

In the case where a Z′ is discovered, the ATLAS detector could easily measure the Z′ mass, $M_{Z'}$, its width, Γ_{tot}, and the lepton cross section, σ_l by using the main production channels $pp \to Z' + X \to l^+l^- + X$. The total production cross-section can be calculated to within a few percent for given Z′ couplings. The lepton cross-section permits the determination of Z′ couplings. The lepton branching ratio $B_l = \frac{\Gamma(Z' \to l^+l^-)}{\Gamma_{tot}}$ does not only depend on SM fermions but might also depend on the contribution from exotic fermions and supersymmetric partners to the Z′ width. In this way the branching ratio is a useful indirect probe for the existence of such particles. Moreover, from measurements of Γ_{tot} and σ_{ll} one obtains $\sigma\Gamma(Z' \to l^+l^-) = \sigma\ B\ \Gamma_{tot}$ which probes the absolute magnitude of the gauge couplings. A short description of the main parameters, which could be determined with ATLAS, is as follows:

Cross-Section

The differential Z′ cross section for the process $q\overline{q} \to Z'\ X \to l^+l^-\ X$ is given by the following formula for a Drell-Yan production of lepton pairs with high invariant mass [128]:

$$\frac{d\hat{\sigma}(q\overline{q} \to \gamma, Z^0, Z' \to l^+l^-)}{d\cos\theta^*} = \frac{1}{9}\frac{\pi\alpha^2}{2\hat{s}}[(1+\cos^2\theta^*)Q_1 + 2\cos\theta^* Q_3], \tag{10.23}$$

where $\hat{s} = M_{ll}^2$ and θ^* the angle between the lepton direction, of either the l^- or the l^+, and the quark direction in the Z′ centre of mass frame. The Q's are charges defined in terms of helicity amplitudes with

$$Q_{1(3)} = \left[|Q_{LL}|^2 + |Q_{RR}|^2 + |Q_{RL}|^2 + |Q_{LR}|^2\right]/4, \tag{10.24}$$

Q_{ij} with $i, j =$ L, R are given by:

$$Q_{ij} = \underbrace{g_i^{\gamma,q} g_j^{\gamma,l}}_{\gamma} + \underbrace{\frac{g_i^q g_j^l}{s_W^2 c_W^2}\,\frac{\hat{s}}{\hat{s} - M_Z^2 + \mathrm{i}\Gamma_Z M_Z}}_{Z^0} + \underbrace{\frac{g_i'^q g_j'^l}{c_W^2}\,\frac{\hat{s}}{\hat{s} - M_{Z'}^2 + \mathrm{i}.\Gamma_{Z'} M_{Z'}}}_{Z'} \tag{10.25}$$

(10.26)

As can be seen from relations 10.23 to 10.25 the differential cross section is inversely proportional to the Z′ width. If exotic decay modes are permitted, the decay width will become larger and the branching ratios to conventional fermions smaller.

Decay Width

The partial width for the Z′ decay to massless fermions, $Z' \to f\overline{f}$, is given by the following expression, for the case where no new decay modes are allowed [128]:

$$\Gamma_{Z' \to f\overline{f}} = N_c \frac{\alpha M_{Z'}}{6c_W^2}\left[g_L'^2 + g_R'^2\right], \tag{10.27}$$

where N_c is the colour factor ($N_{l(q)} = 1(3)$) and α the electromagnetic coupling.

Forward - Backward Asymmetry (FB)

As can be seen from the cross-section (10.23) the decay modes are dependent on $\cos\theta^*$, which due to the different vectorial and axial couplings results in a measurable forward backward asymmetry. This forward-backward asymmetry, A_{FB}^l, can be rewritten as:

$$\frac{d\sigma}{d\cos\theta^*} \propto \frac{3}{8}(1+\cos^2\theta^*) + A_{FB}^l \cos\theta^*. \tag{10.28}$$

A_{FB} is defined as a function of either the mass, the rapidity or the θ^*, expressed by the parameter i and where F (forward) and B (backward) are the number of events for a certain parameter i for $\cos\theta^* > 0$ and $\cos\theta^* < 0$, respectively:

$$\left.\begin{array}{l} A_{FB}^l = \dfrac{F(i) - B(i)}{F(i) + B(i)} \end{array}\right\} \quad i = y, M, \cos\theta^*. \tag{10.29}$$

In higher gauge groups, other exotic particles often occur and it will be necessary to distinguish between the cases where Z′ only decays to Standard Model particles and the model depended case where it also decays to other exotic particles.

Interference

Z′ interference with SM neutral gauge bosons is assumed to occur in the same way as for the γZ^0 interference in the Standard Model:

$$|\gamma + Z + Z'|^2 = |\gamma|^2 + |Z|^2 + |Z'|^2 + 2\gamma Z^\dagger + 2\gamma Z'^\dagger + 2ZZ^\dagger. \tag{10.30}$$

To be able to get information about these couplings, several observables have been proposed that are independent of the disintegration mode of Z′ and as insensitive to systematic uncertainties as possible. A subset of these observables is presented below:

- Main production channel
  - Forward-backward asymmetry. The first probe to be recognised for gauge couplings at future hadron colliders. It is the cleanest probe for a particular combination of quark and lepton couplings and can be used to distinguish models up to 2-3 TeV [119].
  - Ratio of cross-sections in different rapidity bins. Useful complementary probe separating the Z′ couplings to the u and d quarks due to the harder valence u-quark distribution in the proton relative to the d-quark.
  - Corresponding asymmetries due to proton polarisation if available at future hadron colliders. An increased knowledge of the polarised spin distribution functions for quarks would be needed.
- Other two fermion final state channels (could have large background)
  - Measurements of the τ polarisation in the $pp \to Z', X \to \tau^+\tau^-$, X channel to address the Z′ lepton couplings.
  - Measurements of the cross section in the $pp \to Z', X \to jet\ jet$, X channel. QCD background may be overcome by kinematical cuts, excellent di-jet mass resolution etc. It is the only probe available for left handed quark couplings.
- Other decay modes. One example is the decay to four fermions, which have suppressed rates compared to the two fermion channels. Any discovery in this channel would rely on receiving enough statistics.

10.6 Z′ Discovery Limits

Until now, there has been no experimental evidence for extra neutral gauge bosons. Both pp, $p\bar{p}$ as well as ep colliders have been used in the search for Z′. These various colliders permit different types of searches resulting in four primary sets of constraints on the existence of Z′:

- (I) Precision measurements of neutral current processes at low energies. For instance, the determination of the angle of the Z and Z′ mixing gives lower boundaries on the Z′ mass. Current bounds on the mixing angle, mainly from LEP, requires it to be $\xi << 1$ since $\sin\theta_M < 0.01$.

- (II) Z′ pole constraints on Z-Z′ mixing. Electroweak measurement both at LEP and SLC, while sitting on the Z resonance are generally sensitive to Z′ physics only through the mixing with Z unless the Z and Z′ are very nearly degenerate. Typical Z′ pole searches have been done by LEP.

- (III) Indirect constraints from precision electroweak measurements off the Z′ pole at high energy. At $\sqrt{s} < M_{Z'}$, but off the Z-pole, strong constrains on new Z′ physics can be found by comparing measurements of asymmetries and leptonic and hadronic cross-section with their SM predictions. Information on the Z′ couplings and mass can be extracted which is not accessible via Z-Z′ mixing alone. Typical experiments are e^+e^- colliders at low energies ($\sqrt{s} < M_{Z^0}$) and at LEP-II ($M_{Z^0} < \sqrt{s} < 209$ GeV).

- (IV) Constraints from direct searches at very high energies (on-shell production and decay). Searches can be classified by the initial state from which the Z′ is produced and the final state into which the Z′ decays (exotic decays not included). Experiments up to date have been sensitive to Z′ production via their coupling to quarks ($p\bar{p}$ colliders), or electrons (e^+e^-) or to both (ep). CDF and D0 at Tevatron are two experiments which can currently perform direct searches. In the future, ATLAS plans to extend the search up to even higher energies.

Table 10.3 presents the lower limits from [11] as of 2004 from searches at the main experiments capable of detecting a Z′ if it exist. Lower limits from different types of measurements exclude the energy regions below $\lesssim 1$ TeV. Direct searches in e^+e^- colliders have ruled out the existence of any light Z′ ($M_{Z'} < M_{Z^0}$). In addition, indirect searches from e^+e^- colliders have constrained the mass for a heavy Z′. Measurements from the LEP excludes a Z'_{SSM} up to 1787 GeV [14].

For a heavy Z′, the best direct limits come from $p\bar{p}$ machines via Drell-Yan production with decay to the main channel (di-leptons). Direct measurements at Tevatron (Run-I) exclude a SSM neutral gauge bosons with masses less than 690 GeV (CDF) or 670 (D0) [11]. Recent preliminary results from Tevatron Run-II show that the lower limit from direct searches have increased utterly. Figure 10.5 shows the preliminary dilepton mass distribution from Run-II. The new limit from the CDF experiment for a Z'_{SSM}-model is of 815 GeV [130]. Together, these different lower limits imply that new Z′ bosons must be rather heavy and with very small Z^0-Z′ mixing.

The Z′ search limits are shown in figure 10.6. It shows the current and future detectors which could detect a Z′ and the upper energy limit for which it can be found. The limits from hadronic colliders are less model dependent than the ones from leptonic factories. The Tevatron experiment (Run II) is the largest operating

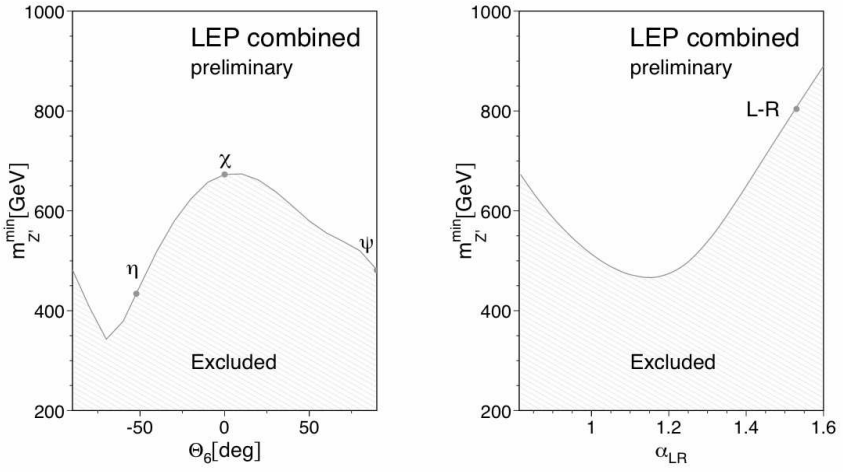

Figure 10.4: LEP limits for the detection of extra gauge bosons (95% CL). Left, the limits for the E_6 models and right, for the Left-Right model. Taken from [14].

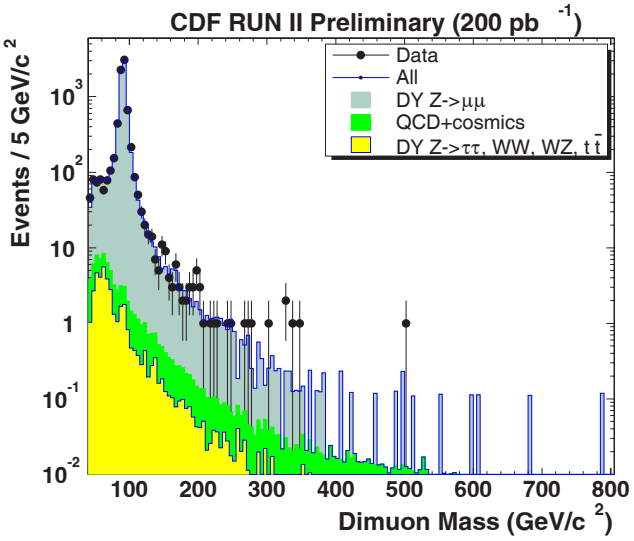

Figure 10.5: The dilepton mass distribution from the Tevatron (Run-II) taken during the winter 2004. From [129].

Model	CDF	CDF (Run II)	D0	DELPHI	ALEPH	LEP II	Cheung
Methode	direct	direct	direct	indirect	indirect	total	electroweak
SSM	690	815	670	710	898	1787	1500
X	595	670	-	440	533	673	680
ψ	590	690	-	350	284	481	-
η	620	640	-	310	329	434	-
LR	630	-	-	380	436	804	860

Table 10.3: Lower limits of Z' searches with 95% CL [11]. The CDF (Run II) preliminary limits are taken from [130].

proton-proton collider today, and provides currently collisions with 1.96 TeV protons, with a typical luminosity of 10^{32} cm^{-2}s^{-1}. The current integrated luminosity is $\sim$ 500 pb^{-1} but up to 4.4 fb^{-1} is expected by the end of 2009. By this time, the LHC is expected to provide competition with its 7 TeV collisions and its design luminosity of 10^{34} cm^{-2}s^{-1}. In addition, ATLAS will have slightly lower selection criteria than the Tevatron experiments, which use $E_T > 25$ GeV for di-electron and $p_T > 20$ GeV for di-muon, and the $|\eta|$ coverage is expected to be better.

10.7 Simulation Tools

Before ATLAS and LHC start operation, valuable information about the future physics searches is gained by the use of software tools. A particle generator, which produces virtual particles as close as possible to the LHC conditions is used together with a detector simulation tool. The objective of the generator is to provide events as detailed as could be experienced by a perfect detector. The purpose of the detector simulator is to reduce these perfectly generated signals into as realistic as possible ATLAS measurements. For the Z′ studies, the PYTHIA and ATLFAST software have proven useful.

PYTHIA, described in [132, 133, 134], is a general purpose particle physics generator (e.g. $p\bar{p}$, pp, e^+e^-, ep), which from two incoming particles creates all the outcoming particles, as can be seen in figure 10.7. A set of parton distributions, defining the parton sub-structure and the energy of the two incoming particles, is the starting point of the generation. When these two particles approach each other, an initial shower is being built from the branching of the two initial particles (e.g. $q \rightarrow qg$). Both QED and QCD process comes into play. The resulting shower is called the initial state radiation (IRS).

The actual reaction between the two incoming particles is the hard process (HP). The main characteristics of the event are defined from this process. In our case of Z′ generation, the hard process is equal to $q\bar{q} \rightarrow Z' \rightarrow l^+l^-$, where the Z′ is a short-lived resonance which decays into two leptons with opposite charge. Similar as for the incoming partons, the two outgoing leptons may branch and build up a final state radiation (FSM). This radiation is governed by QED processes if only decay to leptons is permitted, or by both QCD and QED processes when more decay modes

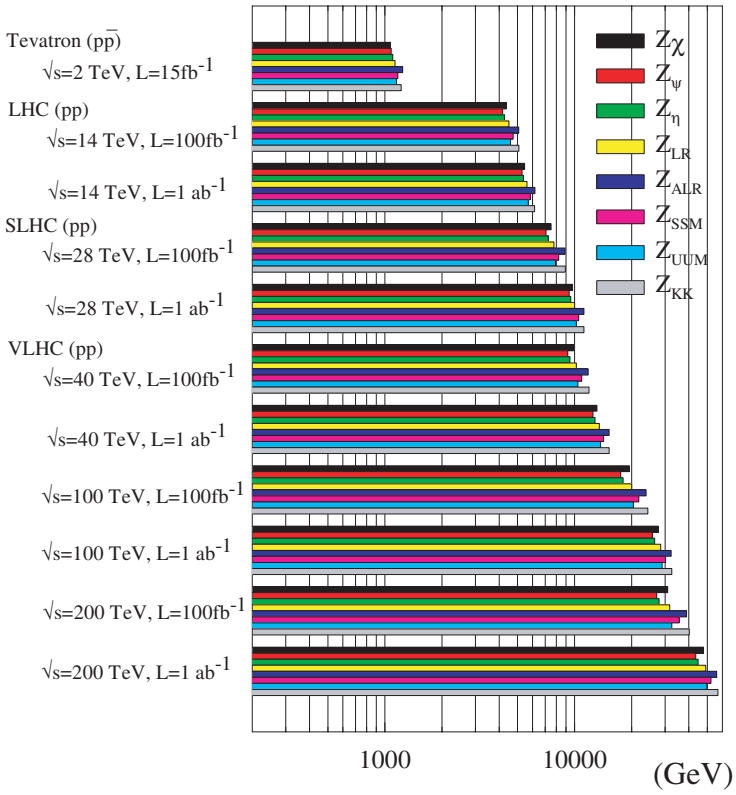

Figure 10.6: Discovery reach for extra neutral gauge bosons (Z′) for some popular models at various existing or planned detectors. Each limit are for ten discovered events in the $e^+e^- + \mu^+\mu^-$ channel [131].

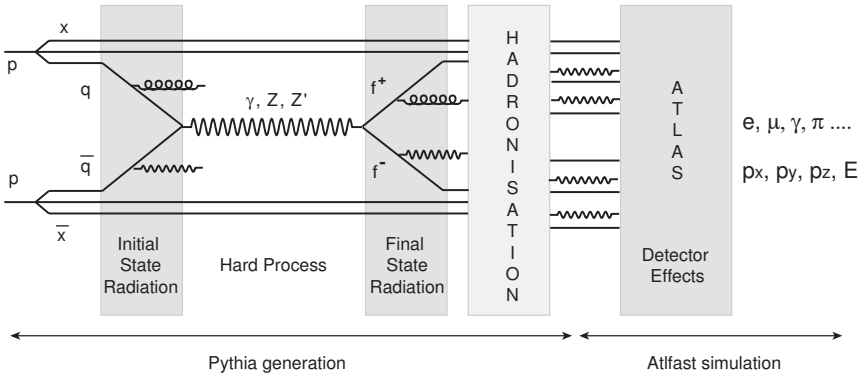

Figure 10.7: The generated and simulated chain of processes. PYTHIA produces the hard process as well as initial and final state radiation and fragments the particles before they enter the ATLFAST routine. ATLFAST simulates a simplified ATLAS detector and provides similar detector and trigger conditions.

are enabled ($e \to e\gamma$, $q \to qg$, $q \to q\gamma$, $g \to gg$ and $g \to q\bar{q}$).

Several additional processes which play a role for proton-proton collision and contributes to the final state. The partons from the initial two hadrons, which do not interact in the hard process, may be subject to semi-hard interactions. Also the beam remnant contributes to the final state for proton-proton collisions producing multiple interactions (MI). As many as 20 events may be produced in each collisions. Finally, all generated coloured particles are subject to hadronisation (H), which produces colour neutral hadrons due to the QCD confinement mechanism.

ATLFAST [135] is a fast detector simulation program which propagates the particles generated by PYTHIA through the ATLAS detector. It was originally written in Fortran77 but is also available within the ATHENA framework written in C^{++} [136]. Fast simulation presents an intermediate step between simple analysis of the event topology after hadronisation. It is not as sophisticated and CPU consuming as a full simulation of the complete detector. It gives a rapid and approximate estimation of signals and background rates for specific channels and reproduces the expected experimental mass resolutions, as well as the energy and momentum measurements, based on the following simplification of the ATLAS detector:

- Leptons and photons are isolated and smeared in momentum and energy, photons according to a gaussian energy resolution, electrons according to the mass resolution and muons according to a resolution depending on p_T, $|\eta|$ and ϕ. Detection efficiencies are not taken into account.

- The jet reconstruction in the calorimeter part of ATLAS is simulated and labelling of b-, c- and τ-jets provided.

- The missing transverse energy of the system is calculated by summing all transverse momenta of identified particles and jets, smeared, and compared to the expected "theoretical" value.
- The presence of a magnetic field is taken into account and its effect is simulated by the smearing of un-decayed particles with $p_T > 0.5$ GeV in the calorimeter.
- A simplified trigger response is provided. The default trigger settings are close to the ones used by the ATLAS detector and are explained in chapter 11.

ATLFAST reproduces the expected ATLAS detector mass resolution for important physics signal comparable to full simulation. It does not reproduce the expected efficiencies for lepton and photon isolation or the background. Only very basic aspects are used to simulate the detector geometry,

Conclusion

As described in this chapter, the search for extra neutral gauge bosons in existing and new experiments will provide an important tool for the search for, investigation and determination of new physics beyond the Standard Model. Not only would the detection of a Z′ boson indicate the existence of new physics, but the determination of the bosons parameters could indicate which models could be valid beyond the SM. Secondly, as will be shown in the following chapter the detection of Z′ could be made even at low luminosities and could be among the first particles detected by ATLAS. For higher luminosities, the exclusion possibilities up to Z′-masses of around 1 TeV, makes this signature highly interesting for the LHC and ATLAS operation. If not already found by the Tevatron experiments, ATLAS will have good opportunities to search for this particle. Chapter 11 will discuss what the signals in ATLAS would look like, what discovery reach (Z′ mass) one can expect to obtain with ATLAS and how the different models can be distinguished.

11

ATLAS Search for Exotic Particles - Fast Simulation

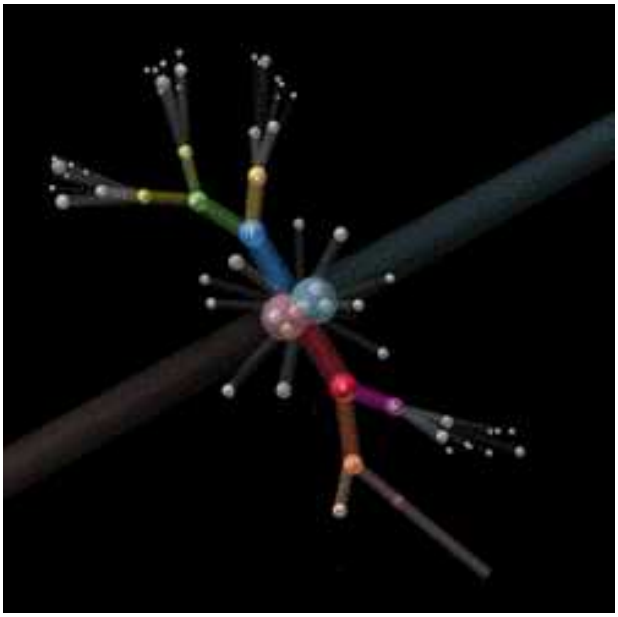

3D event from [8].

Introduction

Since extra neutral gauge bosons could be among the first particles to be discovered in ATLAS, it is interesting to have a closer look at this particle's parameters. Before the start of ATLAS in 2007, several simulation tools are used to prepare for the physics run and to test the off-line software. One part of these preparations is to define certain particle searches and the necessary cuts needed to separate the signal from the abundant background to get the best possible result. It is also important to start preparing analysis tools and to determine the detector reach and how to discriminate between beyond-standard models.

This chapter presents the result of a study of the Z′ boson, for different models, by the use of fast simulations as described in chapter 10. Only Drell-Yan production of Z′ will be considered and its decay to two leptons, electrons or muons. Decay to exotic particles has so far been excluded under the presumption that the gauge bosons would be first seen directly or as SM deviations. The results from this study is presented in three sections, the first presenting the conditions and the basic Z′ characterisation for one model (e.g. cross-sections, lepton kinematics, signal and background). The second part presents the Z′ discovery reach for various models and the third and last part describes the model discrimination possibilities.

11.1 Z′ Generation and Simulation

The specific aim of this analysis is to present data from fast simulation, which are as close as possible to the expected data from the ATLAS detector. This gives a first indication about the Z′ performance and the detector reach as well as being a guideline for the full simulations. Moreover, the simulations are kept as simple as possible to be able to clearly distinguish between the effects from different generation modes and between the different gauge models. This study includes the following aspects:

- A presentation of the generation of the full interaction chain, including initial and final state radiation.
- Fast simulation, providing more realistic measurements than for some of results presented previously [128] except where first results from full simulations have been presented [137].
- Both decay to electrons and muons are presented together for comparison, whereas most of the earlier studies have presented only one channel.

The Z′ particles in this study have been generated with the PYTHIA software, version 6.224, and simulated with ATLFAST, version 2.51. Five Z′ models have been studied, the sequential SM model (Z'_{SSM}), three superstring inspired E_6 models (Z'_{χ}, Z'_{ψ} and Z'_{η}) and one symmetric Left Right model originating from extensions of SM gauge groups (Z'_{LR} with $g_R = g_L$) . The main easy channel, for the generation of

extra gauge bosons at a centre of mass energy of 14 TeV in a p-p collider, is the decay of Z′ to a lepton pair:

$$p\ p \rightarrow q\bar{q} + X \rightarrow Z' + X \rightarrow e^+e^-/\mu^+\mu^- + X. \tag{11.1}$$

As described in more detail in chapter 10, the background consists of Standard Model decay to the same particles, mostly from the following Drell-Yan production:

$$p\ p \rightarrow q\bar{q} + X \rightarrow \gamma/Z^0 + X \rightarrow e^+e^-/\mu^+\mu^- + X. \tag{11.2}$$

From the many Z′ generation possibilities provided by PYTHIA there are three cases, which have been used for this study:

$$q\bar{q} \rightarrow Z' \rightarrow e^+e^-, \mu^+\mu^- \text{ (other decays off)} \tag{11.3}$$

$$q\bar{q} \rightarrow \gamma, Z^0, Z' \rightarrow e^+e^-, \mu^+\mu^- \text{ (other decays off)} \tag{11.4}$$

$$q\bar{q} \rightarrow \gamma, Z^0, Z' \rightarrow \textit{all decays on}\ . \tag{11.5}$$

Both in relation 11.3 and 11.4 only decay to e^+e^- or $\mu^+\mu^-$ is permitted and all other particle decays are turned off. In the case of 11.5 all possible decay modes are enabled. The PYTHIA parameters used for the Z′ generation are presented below together with the ATLFAST predefined cuts, which simulate the ATLAS trigger environment. Some additional software cuts are needed, especially for the asymmetry analysis. Together this defines the overall simulation environment used in this study.

11.1.1 PYTHIA Parameters

Table 11.1 shows the main PYTHIA parameters and switches needed for the Z′ generation of the SSM and E_6 models. The Left-Right model is defined by similar parameters as described in [132]. The first set of switches defines the hard process generation and its decay modes. The couplings to leptons are defined by the parameters PARU and PARJ for the different fermion couplings and for each of the three families. The couplings need to be set in accordance with the model to be studied. The calculated couplings from equation 10.2 in chapter 10 for the E_6 models need to be multiplied by two before being used in PYTHIA [138]. This is due to a different normalisation factor used in the equation compared to the PYTHIA implementation.

Since there is no prediction of the Z′ mass it is very useful to probe different masses, which can be made by scanning the PMAS parameter. In the simulations presented here, the Z′ mass will be varied between 1 - 5 TeV. Additional kinematic cuts on the dilepton mass are used, typically 800 and 1000 GeV on the centre of mass energy of the hard process ($\sqrt{\hat{s}}$), to limit the number of events to be simulated and to reduce the number of low-mass background events.

Finally, PYTHIA provides useful switches for turning on and off initial and final state radiation as well as multi-interactions and hadronisation. In the following sections all plots are generated with initial and final state radiation, hadronisation

and multi-interactions, in addition to the hard process, except where it is explicitly stated otherwise. As described in chapter 10 the initial and final state radiation contains QCD and QED interactions if the process contains coloured or charged objects. The multi-interaction takes into account that more than one shower-initiator may be present in the beam, which would cause additional interaction in one event. As the distance increases between the particles created, the QCD becomes strongly interacting and coloured partons are transformed into colourless hadrons. This process is called hadronisation. The following combination of radiation processes has been investigated:

HP	Hard process
ISR+	Hard process, initial state radiation and multi-interaction
FSR+	Hard process, initial state radiation, multi-interaction, final state radiation and hadronisation.

11.1.2 ATLFAST Parameters

The ATLFAST default parameters [135] are chosen to be close to the ATLAS conditions as described in the ATLAS trigger Technical Design Report [43], but can be changed if needed. Switches for turning on and off the smearing or magnetic field as well as access to the pseudorapitiy and p_T cuts are made available via a text file. One of the most important ATLFAST switches is the luminosity switch, for which the ATLAS trigger conditions can be automatically changed between the ones for low luminosity and the ones for high luminosity. The trigger conditions during the first year of operation will be less stringent than the design parameters to increase the statistics of rare processes during this initial data-taking period.

The different p_T and η cuts can be seen in table 11.2. The pseudorapidity is taken to be equal to $\eta = 2.5$ for electrons and 2.4 for muons. The p_T cuts are harder for high luminosity than for low luminosity and hardest for the electron and muon with the highest momentum. The selection of ATLAS trigger cuts are made to cover efficiently the ATLAS physics program and to provide the required reduction in the event rate for the high level trigger. In addition, ATLFAST does not include the particle identification efficiency, but according to [135], a suitable choice would be to multiply the number of electron and muon events with an efficiency of $\epsilon_{corr} \sim 0.953$ and 0.978 respectively. This ϵ_{corr} consists of a part of the overall efficiency which will be used in the formula $\mathrm{N} = \sigma\ L\ \epsilon$.

11.1.3 Additional Cuts and Conditions

Some additional cuts have is needed to optimise the signal to background ratio and to get better performance for certain parameters. Two regions have been defined for the analysis of asymmetries that permit to distinguish between the off-peak and the on-peak asymmetry. When used, these cuts will be stated explicitly. The two regions are defined as follows, with $M_l^{peak}l$ being the generated dilepton mass:

Command	Value	Operation	Description
MSEL	0		User control
MSUB (141)	1	$f\bar{f} \to \gamma, Z^0, Z'$, int	Enabling the hard process
MSTP(44)	1	$f\bar{f} \to \gamma$	Decay only to γ
	2	$f\bar{f} \to Z^0$	Decay only to Z^0
	3	$f\bar{f} \to Z'$	Decay only to Z'
	4	$f\bar{f} \to \gamma, Z^0$, int	Decay to γ, Z^0 with interference
	5	$f\bar{f} \to \gamma, Z'$, int	Decay to γ, Z' with interference
	6	$f\bar{f} \to Z^0, Z'$, int	Decay to Z^0, Z' with interference
	7	$f\bar{f} \to \gamma, Z^0, Z'$, int	Main interaction with interference
PARU(121-128)	nb	$v_d, a_d, v_u, a_u, v_l, a_l, v_\nu, a_\nu$	First generation couplings
PARJ(180-187)	nb	$v_d, a_d, v_u, a_u, v_l, a_l, v_\nu, a_\nu$	Second generation couplings
PARJ(188-195)	nb	$v_d, a_d, v_u, a_u, v_l, a_l, v_\nu, a_\nu$	Third generation couplings
PMAS(32,1)	1500	GeV	Setting the Z′ mass
CKIN(1)	800	GeV	Cut on $\sqrt{\hat{s}}$
MDME(KF, 1)	1	particle (KF) on	Particle decay is turned on
	0	particle (KF) off	Particle decay is turned off
	-1	particle (KF) off	Opens a non SM decay mode
MSTP(61)	1/ 0	on / off	Initial state radiation switch
MSTP(71)	1/ 0	on / off	Final state radiation switch
MSTP(81)	1/ 0	on / off	Multi-interaction switch
MSTP(111)	1/ 0	on / off	Hadronisation switch

Table 11.1: PYTHIA parameters for Z′ production of the E_6 model. The LRSM is defined in similar fashion.

Luminosity		low L	high L
Particle	$\|\eta\|$	min p_T	min p_T
Isolated electron/photon trigger			
1st. electron	<2.5	20.0	30.0
1st. photon	<2.5	40.0	60.0
2nd. electron or photon	<2.5	15.0	20.0
Muon trigger			
1st. muon	<2.4	20.0	20.0
2nd. muon	<2.4	6.0	10.0

Table 11.2: A subset of the ATLFAST trigger values, based on the expected performances of the real ATLAS triggers.

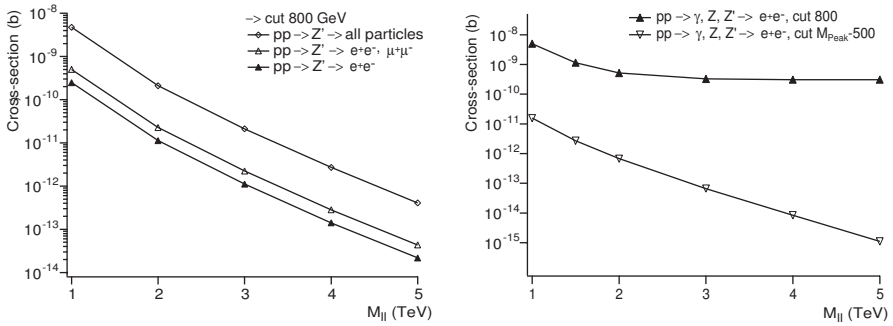

Figure 11.2: The cross section as a function of different dilepton masses. Right, the different cross-sections are shown for different decay modes. Left, one curve shows the result using a fixed kinematic cut of 800 GeV the other with a variable cut equal to the M_{ll} - 500 GeV.

- *On-peak region:* M_{ll}^{peak} - 50 GeV $< M_{ll}^{peak} < M_{ll}^{peak}$ + 50 GeV. For a mass of 1.5 TeV this gives a peak region between 1450 and 1550 GeV.
- *Off-peak region:* This region is in the tail of the signal to include interference effects, and is defined as M_{ll}^{peak} - 500 GeV $< M_{ll}^{peak} < M_{ll}^{peak}$ - 50 GeV. For a mass of 1.5 TeV this region would be between 1000 and 1450 GeV.

According to [139], for the asymmetry analysis based on the dilepton mass, the result can be improved by applying a cut on the rapidity. The details of this cut is explained in section 11.5:

- *Rapidity cut:* A cut for $|Y_{ll}| > 0.8$ permits to eliminate the excess of leptons coming from low energy quarks or gluons and which results in the production of a Z′ with a different direction than the incoming quark.

11.1.4 Cross-Section and Branching Ratio

A brief investigation of the cross-section behaviour, as generated by PYTHIA, is summarised in figure 11.2 for different modes of generation and Z′ masses between 1 and 5 TeV. The left hand plot shows the change in cross-section due to the decay to different final state particles for different Z′ masses ($pp \rightarrow Z'$). The decays studied are those relevant for this analysis: e^+e^-, $e^+e^-, \mu^+\mu^-$ and the case where decay to all possible particles is permitted. The branching ratio for the leptons pairs are $\sim 5.4 \times 10^{-2}$. The cross section for decay to both lepton pairs are twice as large as for the electron-positron pair only. Decay to all particles is approximately ten times larger than the decay to the two lepton pairs.

The right hand plot shows the effect that different lower kinematic cuts ($\sqrt{\hat{s}}$) have on the cross sections for the generation of $pp \rightarrow \gamma, Z^0, Z' \rightarrow e^+e^-$. A comparison between a scan over Z′ masses with a fixed cut or with a cut equal to the mass-500

GeV is shown. In the latter case most of the γ, Z^0 Drell-Yan background could be avoided. It is however important to keep enough statistics to be able to determine its shape under the Z′ peak. A harder cut would also lower the statistics necessary for the asymmetry evaluation. For this reason a static kinematic cut of 800 GeV has been chosen for this analysis.

11.2 Lepton Kinematics - χ-model

This section describes the lepton kinematics, for the individual leptons and for the reconstructed Z′ (dilepton system) and both for the generated and simulated signal. The difference in number of events is due to the effects of the detector efficiency and the initial and final state radiation. The basic kinematic cut at 800 GeV, as discussed previously, has been applied, but not the additional cuts.

A particle's momentum can be described by its z-component, p_z, and its transverse momentum, p_T, which is perpendicular to the beam direction. For a 4-vector $p = (E, p_x, p_y, p_z)$, p_z is read directly from the vector and and p_T is given by the following expression:

$$p_T = \sqrt{p_x^2 + p_y^2}. \tag{11.6}$$

The momentum of the dilepton system (Z′) is found by summing the two lepton vectors, where the components of $\vec{p}_{l1}$ and $\vec{p}_{l1}$ are given by PYTIHA in the laboratory frame:

$$\vec{p}_{ll} = \vec{p}_{l1} + \vec{p}_{l2}. \tag{11.7}$$

Figure 11.3 shows the p_z momentum distributions of the lepton and dilepton system both for the generated signal directly (dashed line) and the simulated signal (solid line). The momentum of the two single leptons shows a symmetric p_z distribution around zero. The $p_{ll,z}$ momentum of the dilepton system, is also symmetric around zero but with a broader width than the lepton momentum, which tells that the Z′ is neither produced at rest ($p_{ll,z} \sim 0$) nor very boosted ($p_{ll,z}$ peaks at large values, $p_{ll,z} \sim 2p_{l,z}$).

Figure 11.4 shows the p_T momentum distribution of both leptons and dileptons. The transverse momentum of the two single leptons is positive and peaking around 750 GeV, which corresponds to half of the generated Z′ mass. The momentum distribution also has a small tail towards higher energies due to the initial and final state radiation. An additional peak at around 400 GeV comes from the application of a kinematic cut of 800 GeV at the generation level and is due to interference effects. The corresponding $p_{ll,T}$ values are positive and peak at low values.

Figure 11.5 shows two plots of the lepton p_T for different models, both with the same cut at 800 GeV. However, whereas the left-handed plot shows only decay to $pp \to Z'$ (no interference effects) the right-handed plot was generated with decay to $pp \to \gamma, Z^0, Z'$ (including interference effects). The proportion of events in the peak at 400 GeV compared to the peak at half the Z′ mass is model dependent,

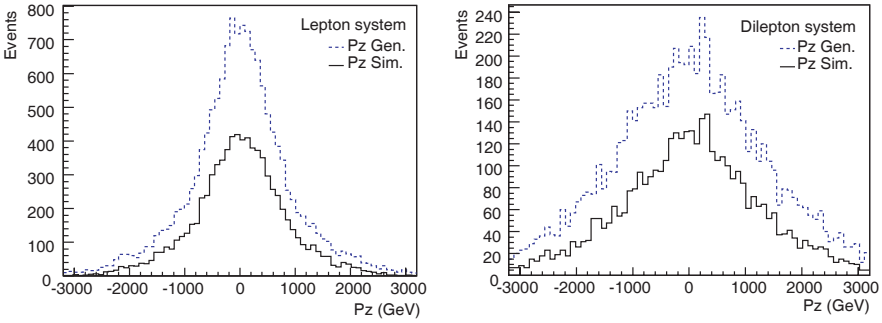

Figure 11.3: $Z' \to e^+e^-$ (Z'_χ, 100 fb^{-1}): The momentum distribution in the z direction, p_z. Left, the lepton momentum, right, the momentum of the dilepton system.

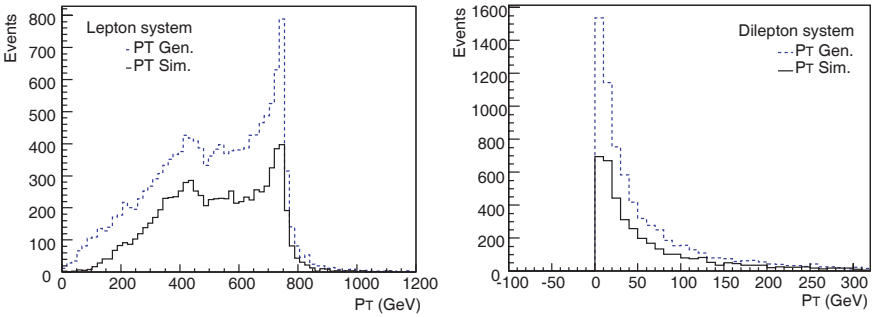

Figure 11.4: $Z' \to e^+e^-$ (Z'_χ, 100 fb^{-1}): The transverse momentum distribution, p_T. Left, the lepton momentum, right, the momentum of the l^+l^--system.

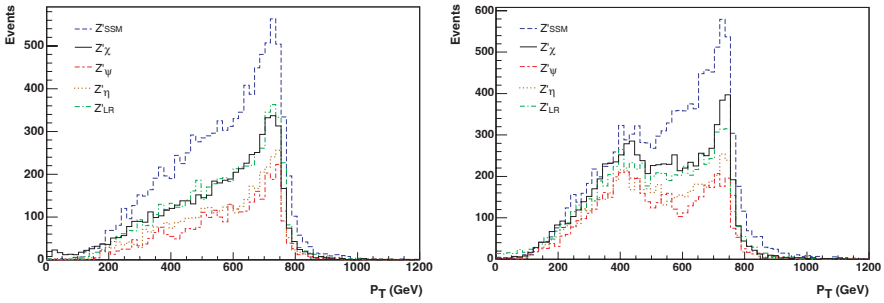

Figure 11.5: $Z' \to e^+e^-$ (Z'_χ, 100 fb^{-1}): The lepton transverse momentum for different models. Left, with no kinematic cut and right, with a cut of 800 GeV.

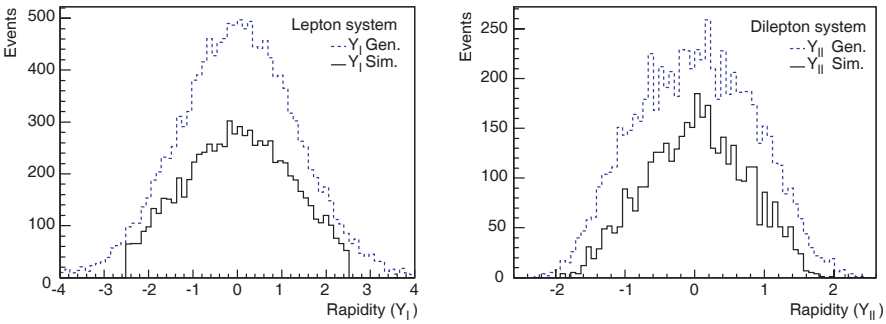

Figure 11.6: $Z' \rightarrow e^+e^-$ (Z'_χ, 100 fb^{-1}): Left, the rapidity distribution for the leptons. Right, the rapidity of the dilepton system. Both rapidities are centred around zero and the ATLFAST lepton pseudorapidity cut is visible.

and diminish for models where the cross-section dominates above the Drell-Yan cross-section.

Figure 11.6, left, shows the lepton rapidity, Y_l, and right, the dilepton system, $Y_{ll} = Y(\vec{l^+} + \vec{l^-})$. Again both the generated rapidity signal (dashed line) as well as the simulated signal (solid line) are shown. The rapidity, Y, is described by the following relation, expressed as a function of the energy and the momentum in the z-direction of the observed particle:

$$Y = \frac{1}{2} \log \frac{E + p_z}{E - p_z}. \tag{11.8}$$

The single lepton system shows a rapidity distribution symmetric around $Y_{ll} = 0$, with an ATLFAST cut for the simulated signal at $Y_l = 2.5$. This corresponds to the overall ATLAS pseudorapidity coverage. The dilepton rapidity has similar features with a symmetric distribution around $Y_{ll} = 0$.

11.3 Signal and Background - χ-model

The Z′ signal is the number of events as a function of the e^+e^- invariant mass. This invariant mass is a function of the dilepton momentum, p_{ll}, and energy, E_{ll}, where $\vec{p}_{ll} = \vec{p}_{l1} + \vec{p}_{l2}$ and $E_{ll} = E_{l1} + E_{l2}$. The invariant mass is expressed by the following relation, where c is the speed of light set equal to 1:

$$M^2 = E^2/c^4 - p^2/c^2 = (E_{l1} + E_{l2})^2 - (\vec{p}_{l1} + \vec{p}_{l2})^2.$$

For Z′, this distribution is expected to have a large signal peak above a small background, leading to a large signal to background ratio. Figure 11.7 and figure 11.8 show typical $Z' \rightarrow e^+e^-, \mu^+\mu^-$ distributions for different Z'-model. The simulated distribution for muon decay has a much broader width than the generated signal. This is due to the detector simulation, which smears the generated

Z'_χ (GeV)	Gen. Mass	Gen. Γ	Sim. Mass	Sim. Γ
(1) BW + E	1499 ± 0.2	17.65 ± 0.78	1499 ± 0.3	24.88 ± 0.92
(2) BW + Q	1499 ± 0.1	17.37 ± 0.84	1499 ± 0.3	25.33 ± 1.17
(3) BW*E + E	1500 ± 0.2	18.96 ± 0.77	1500 ± 0.3	26.56 ± 1.06

Table 11.3: $q\bar{q} \to \gamma, Z^0, Z' \to e^+e^-$ (Z'_χ, 100 fb^{-1}): Fit results for three types of fits for a Z′ of mass 1.5 TeV, both for the generated and the simulated invariant mass.

signal to simulate the expected muon signal in ATLAS. At high energies the energy resolution for muons is worse than that for electrons. This resolution is dominated by the performance of the tracking detectors within ATLAS. The electron resolution is given by the Inner Detector (including the SCT detector) and the muon resolution is given by the muon tracker. The relations for the detector resolution for different particles are given in chapter 3, table 3.2 and is $\sigma/p_T \simeq 5 \times 10^{-4} p_T(\text{GeV}) + 1\%$ for the ID and $\sigma/p_T \simeq 10\%$ at $p_T \sim 1$ TeV for the muon spectrometer. Figure 11.7 and figure 11.8 also shows the Drell-Yan distribution for decay to electrons and muons, respectively (bottom left picture).

By fitting the invariant mass distribution one can determine the "measured" total decay width, Γ, and the Z′ mass, $M_{Z'}$. The width depends on the specific Z′ model and the mass being generated. Several fitting methods have been used. In particluar the Breit-Wigner fit has proven suitable for the signal part of the invariant mass distribution. The Breit-Wigner formula is given by the following expression as a function of x, the mass bin, where Γ is the width of the distribution, M is the Z′ mass and a the normalisation factor:

$$BW(x) = \frac{a}{(x^2 - M^2)^2 - \Gamma^2 M^2}. \tag{11.9}$$

The background has been simulated using the following exponential, E(x), or polynomial, Q(x), expressions:

$$E(x) = e^{c_0 + c_1 x} \tag{11.10}$$

$$Q(x) = b_0 + b_1 x + b_2^2 x^2. \tag{11.11}$$

The effect of the final state radiation, the shift of events towards lower invariant masses, can be modelled by multiplying the Breit-Wigner fit of the signal with another exponential. Table 11.3 shows the different width and mass of a fit of both the generated and simulated signal for three different types of fits. Out of the three, the fit which combines a multiplication of the Breit-Wigner function with an exponential with another exponential for the background (3), seems to be the most suitable for this analysis. As can be seen from figure 11.7 this function seems to fit rather well for decays to electrons, including the effect of the initial and final state radiation. This radiation causes the leptons to loose momentum, which causes the shift to the left of the invariant mass. At low invariant masses some small

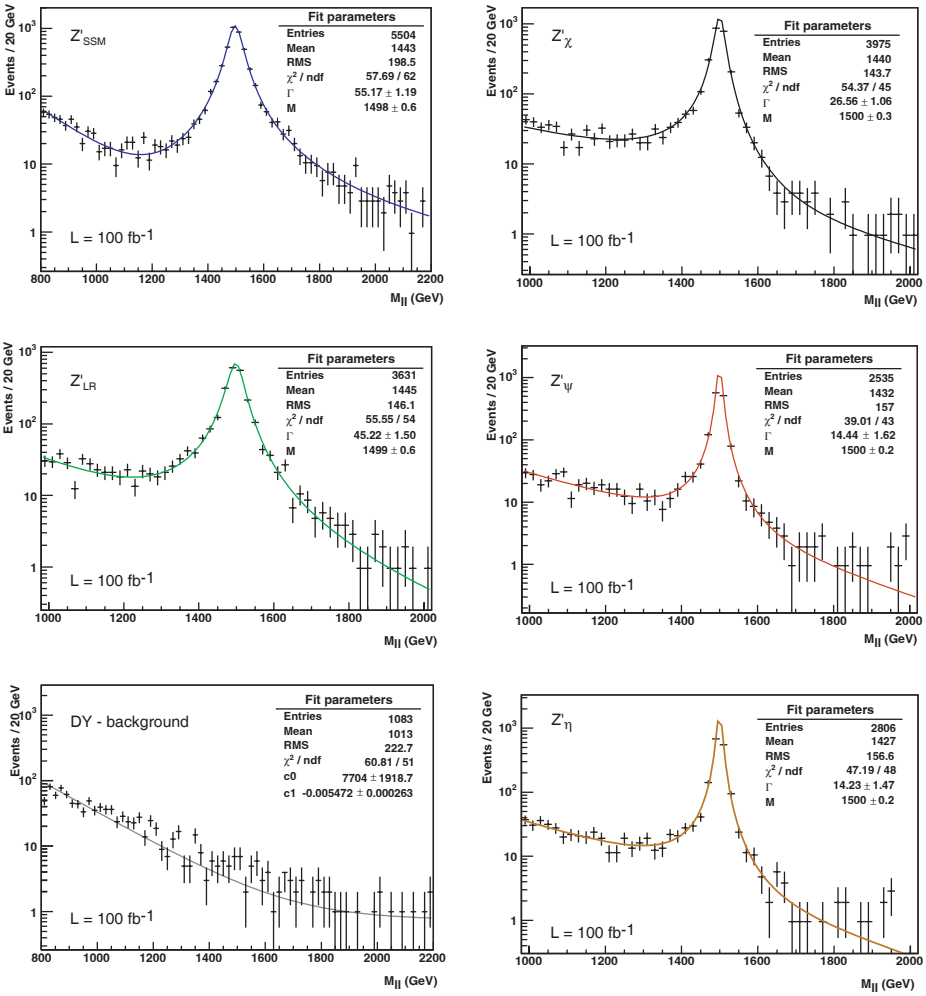

Figure 11.7: $q\bar{q} \to \gamma, Z^0, Z' \to e^+e^-$ (Z'_χ, 100 fb^{-1}): The simulated Z′ distribution for different models including the corresponding Drell-Yan background. The distributions are fitted with a modified Breit-Wigner function at the peak and an exponential for the background (3).

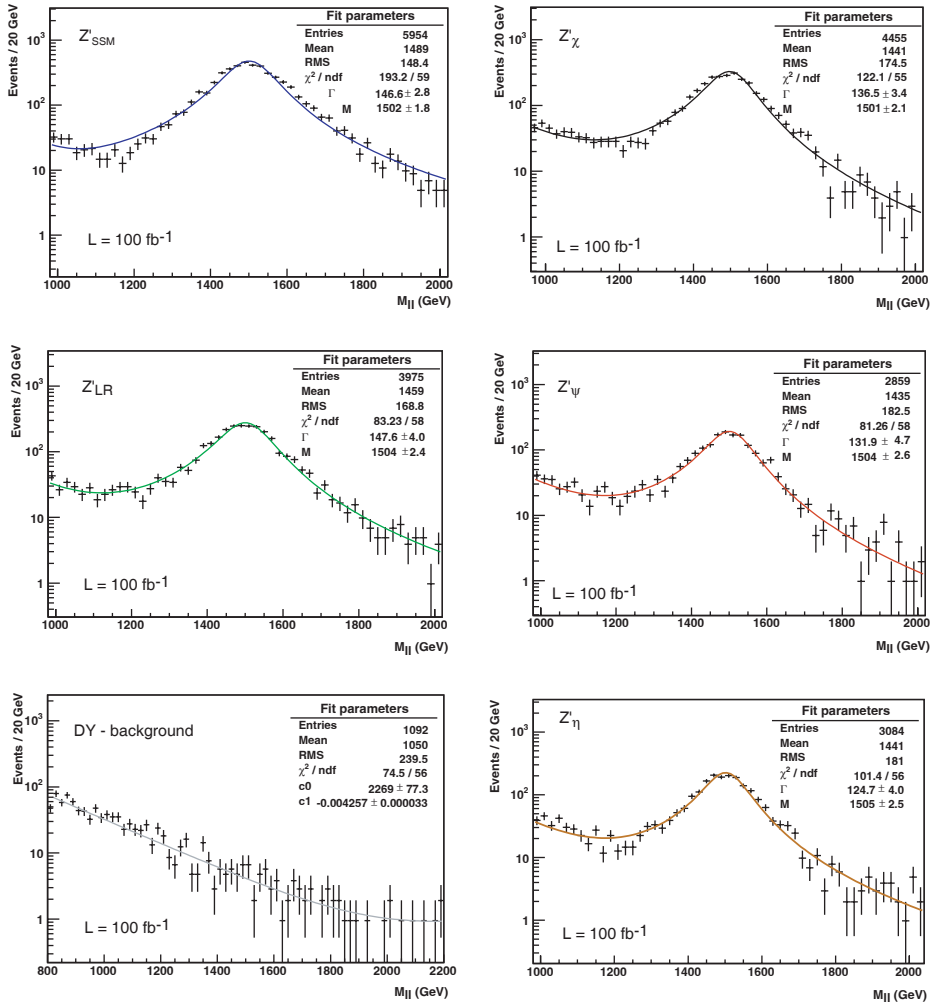

Figure 11.8: $q\bar{q} \to \gamma, Z^0, Z' \to e^+e^-$ (Z'_χ, 100 fb^{-1}): The simulated Z′ distribution for different models including the corresponding Drell-Yan background. The distributions are fitted with a modified Breit-Wigner function at the peak and an exponential for the background (3). The fit would be improved by using two gaussians for the peak instead of a Breit-Wigner.

$Z'_\chi \rightarrow$	e^+e^-	Mass (fit) GeV	Γ (fit) GeV	3Γ Events	Frac. %	Total Events	Frac. %
HP	Gen.	1500 ± 0.2	19.8 ± 0.8	4302		7184	
	Sim.	1500 ± 0.2	24.5 ± 0.8	3641	85	6076	85
ISR+	Gen.	1500 ± 0.2	18.1 ± 0.8	3823		6328	
	Sim.	1501 ± 0.2	22.8 ± 0.9	3133	82	5218	83
FSR+	Gen.	1498 ± 0.3	17.7 ± 0.8	3937		6377	
	Sim.	1498 ± 0.3	25.8 ± 1.1	2114	54	3636	57

$Z'_\chi \rightarrow$	$\mu^+\mu^-$	Mass (fit) GeV	Γ (fit) GeV	3Γ Events	Frac. %	Total Events	Frac. %
HP	Gen.	1500 ± 0.2	19.45 ± 0.77	5260		7186	
	Sim.	1505 ± 1.7	134.4 ± 2.7	4507	86	6362	89
ISR+	Gen.	1500 ± 0.2	20.67 ± 0.79	4727		6392	
	Sim.	1503 ± 2.3	140 ± 3.3	3580	76	5014	78
FSR+	Gen.	1499 ± 0.2	18.55 ± 0.80	4613		6343	
	Sim.	1487 ± 1.9	129.8 ± 3.5	2666	58	3926	62

Table 11.4: $q\bar{q} \rightarrow \gamma, Z^0, Z' \rightarrow l^+l^-$ (Z'_χ, 100 fb^{-1}): Results from three different radiation modes (HP, ISR+, FSR+) using fit (3) for both signal and background of a simulated Z′ with a mass of 1.5 TeV. The mass and the width of the signal are determined from the fit parameters. The total number of events is the number reconstructed events.

discrepancy in some of the plot between the fit and the simulation is due to a few low statistic bins. At very high masses the small inaccuracy of the fit is due to low statistics. Figure 11.7 shows the corresponding plots for decay to muons. For some models this seems to fit well, such as for the Z'_{LR} and the Z'_ψ model, but the other fits would need to be improved. This is due to the difference in detection methods between the calorimeter and the muon spectrometer, and the invariant mass distribution for decay to muons would be best fitted with two gaussians in addition to an exponential for the background events.

The detector influence on the generated signal can be determined by comparing the number of events in the simulated distribution and comparing them to the number of events of the generation, taken directly from PYTHIA. As described earlier, from the initial signal generated by PYTIHA, several radiation effects reduce the number of events and influences the signal shape if switched on. To approach a real situation, it is necessary to generate in addition to the first order hard process: initial state radiation, final state radiation, multi-interaction and hadronisation.

Table 11.4 shows the values for some of these sub-processes both for the generated and the simulated signal. Looking at the hard process, the application of a detector simulator reduces the total number of events to 85% for electrons and 89% for muons of the number of generated events. The application of initial state radiation reduces the number of events for electrons and muons to 83% and 78% respectively. Finally,

the generation of final state radiation reduces the total number of events to 57% and 62% for decay to electrons and muons. The values in the 3Γ region are also shown in the table with percentages equal or slightly less than the total ones. Both the values for the 3Γ region and the total number of events include the background. The higher number of events for the muons compared to the electrons is due to the $\sim 3\%$ difference in particle identification efficiency within ATLFAST. When looking at the numbers within the 3Γ region and comparing the values to the generated hard process only, one finds that the loss due to the simulation is around 15% for electrons and 14% for muons. The losses due to addition of the ISR+ radiation and the FSR+ radiation are around 12% and 23% for the electrons and 18% and 17% for muons, respectively. Figures 11.9 and 11.10 shows both the generated and simulated signals as well as the simulated signal with full radiation effects included (FSR+).

11.4 Z′ Discovery Potential in ATLAS

The Z′ discovery potential in ATLAS, as for any Drell-Yan process, is considered to be very good because of the large signal over relatively small background. However, the discovery reach depends on the Z′-model. Results will be given for five of the most popular models, Z'_{SSM}, Z'_{χ}, Z'_{ψ}, Z'_{η}, Z'_{LR}. Figures 11.11 and 11.12 show the invariant mass for each of these models for comparison, for decay to electrons and muons, respectively. The characteristics for each model, such as cross-section, mass and width, are listed in table 11.5. The Z'_{SSM} and the Z'_{LR} models have the broadest widths for both types of decay, with $\sim$ 55 GeV and 45 GeV for decay to electrons. The difference in width between these two models are even less for decay to muons. The Z'_{χ} follows with a width of $\sim$ 27 GeV for electrons and 137 GeV for muons. The Z'_{ψ} and Z'_{η} have the smallest width with around 14 GeV for decay to electrons and 132 GeV and 125 GeV for muons, respectively.

To determine the Z′ discovery potential it is necessary to examine the significance within the fitted region of $\pm 3\Gamma$ around the Z′ mass using the relation $\sigma = \frac{S}{\sqrt{B}}$, where S is the number of signal events and B that of background events. The chosen interval $\pm 3\Gamma$ is considered sufficient for this simulation and are in some sources taken to be $\pm 4\Gamma$. The number of events must not be lower than 5σ or 10 events for it to be statistically insignificant.

The results from a 3Γ fit are presented with the fit parameters in table 11.5 and are shown in figure 11.13 and 11.14 for decay to electrons and 11.15 for the decay to muons. All plots shows the invariant mass distributions with DY background only. From the table it can be seen that the different models have characteristic width different from each other. By determining the width of the simulated (or later the reconstructed) data one can thus have an indication of which model is valid. The higher number of muon events are mainly due to the higher particle identification efficiency within ATLFAST.

Figure 11.13 shows the difference in reach between the generated and the simulated signal. The reach is found by fitting the invariant mass distribution at different

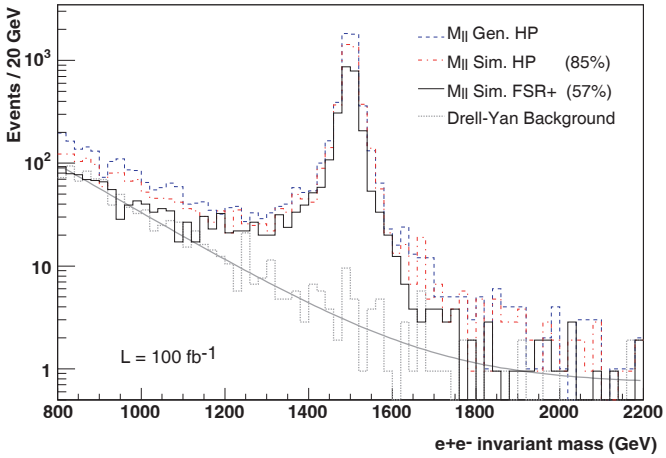

Figure 11.9: $q\bar{q} \to \gamma, Z^0, Z' \to e^+e^-$ (Z'_χ, 100 fb^{-1}): The Z′ distribution for different simulation modes. The loss due to the addition of the initial, final state radiation, multi-interaction, hadronisation as well as the losses due to the ATLAS simulation can be seen.

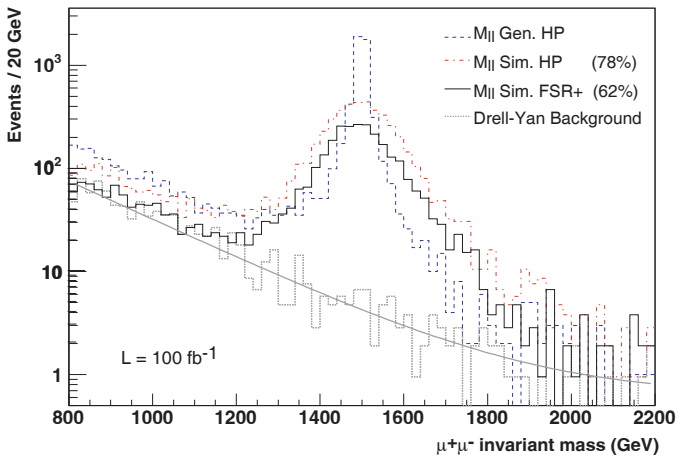

Figure 11.10: $q\bar{q} \to \gamma, Z^0, Z' \to \mu^+\mu^-$ (Z'_χ, 100 fb^{-1}): The Z′ distribution with decay to muons. The loss due to the addition of the initial, final state radiation, multi-interaction, hadronisation as well as the losses due to the ATLAS simulation can be seen.

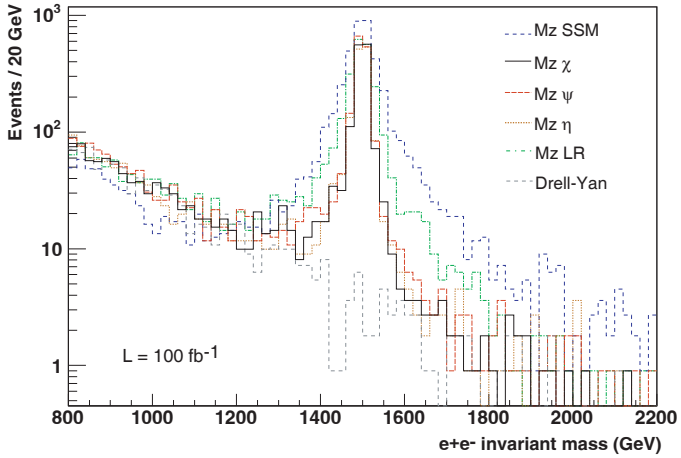

Figure 11.11: $q\bar{q} \to \gamma, Z^0, Z' \to e^+e^-$ (100 fb^{-1}): Simulated invariant mass for different Z′-models.

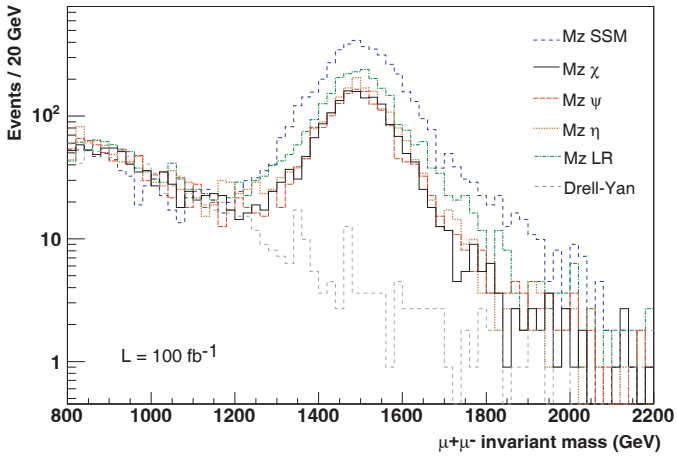

Figure 11.12: $q\bar{q} \to \gamma, Z^0, Z' \to \mu^+\mu^-$ (100 fb^{-1}): Simulated invariant mass for different Z′-models.

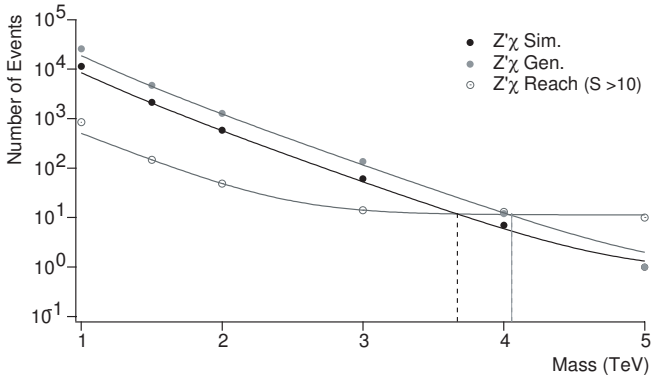

Figure 11.13: $Z' \rightarrow e^+e^-$ (100 fb^{-1}): The difference in reach between the generated and simulated number of events.

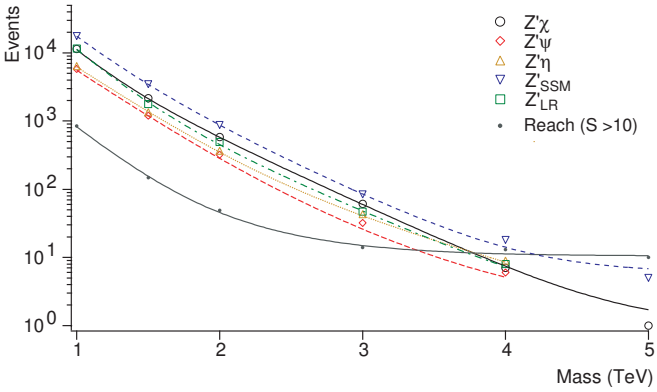

Figure 11.14: $Z' \rightarrow e^+e^-$ (100 fb^{-1}): The difference in reach between the different models. The Z'_{SSM} model has the highest reach whereas the Z'_{ψ} model the lowest.

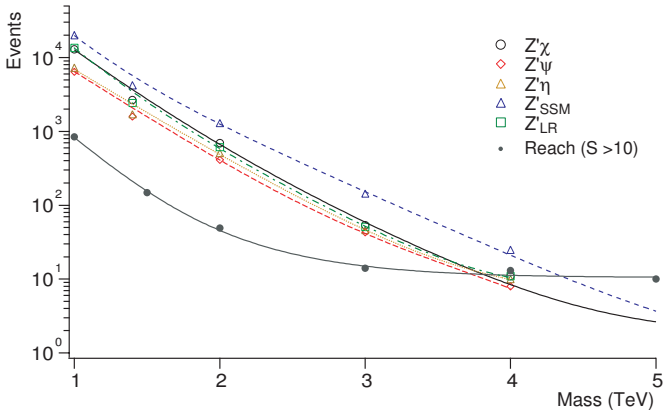

Figure 11.15: Z′ → $\mu^+\mu^-$ (100 fb^{-1}): The difference in reach between the different Z′ models. The Z'_{SSM} model has the highest reach whereas the Z'_{ψ} model the lowest.

$Z' \to e^+e^-$	σ_c (Gen.) fb	Mass (Fit) GeV	Γ (Fit) GeV	S(3Γ) events	B(3Γ) events	σ $\frac{S}{\sqrt{B}}$
Z'_{SSM}	55.04	1498 ± 0.6	55.16 ± 1.19	4003	39	641
Z'_{χ}	39.74	1500 ± 0.3	26.56 ± 1.06	2275	18	536
Z'_{ψ}	25.35	1500 ± 0.2	14.44 ± 1.62	1176	15	304
Z'_{η}	28.06	1500 ± 0.2	14.23 ± 1.47	1341	15	346
Z'_{LR}	36.31	1499 ± 0.6	45.22 ± 1.50	2083	29	387
$Z' \to \mu^+\mu^-$	σ_c (Gen.) fb	Mass (Fit) GeV	Γ (Fit) GeV	S(3Γ) events	B(3Γ) events	σ $\frac{S}{\sqrt{B}}$
z Z'_{SSM}	59.54	1502 ± 1.8	146.6 ± 2.8	4743	120	433
Z'_{χ}	44.55	1501 ± 3.4	136.5 ± 3.4	3057	107	296
Z'_{ψ}	28.59	1504 ± 2.6	131.9 ± 4.7	1706	102	169
Z'_{η}	30.84	1505 ± 2.5	124.7 ± 4.0	1908	97	194
Z'_{LR}	39.75	1504 ± 2.4	147.6 ± 4.0	2711	121	246

Table 11.5: Z′ → l^+l^- ($M_{Z'}$ = 1500 GeV, 100 fb^{-1}) : The generated cross sections, number of events (3Γ) and the width for different model, together with the number of background events and the calculated significance $\sigma = \frac{S}{\sqrt{B}}$.

mass values and to compare the number of events within the 3Γ region (solid circles) and compare it to a discovery criteria (empty circles). In this case the criteria has been that if the number of events in this region is more than 10 above the background then a Z′ can be detected. Another useful choice of criteria is to check if $\frac{S}{\sqrt{B}} = 5$ or more. When comparing the generated and simulated signals of figure 11.13 one find that the reach of a simulated Z′ is around 0.5 TeV less than the reach of the generated signal. Figure 11.14 shows the same type of plot but comparing the reach for different Z′ masses for different models at high luminosity. Figure 11.15 shows the same plot only for muons. One can see that some of the models, such as the Z'_{SSM} can be detected up to higher masses than others. The models with the shortest reach are the Z'_{η} and Z'_{ψ}-models.

Table 11.6 shows the value of the highest particle mass for which the different models can be detected, both for high and low luminosity as well as for decay to electrons and muons. At high luminosity and for decay to electrons only, a Z'_{SSM} could be discovered with a mass up to 4.3 TeV and between 3.5 and 4 TeV for the other models. At low luminosity, and for decays to two electrons, the results show that it will be possible to discover a Z′ in ATLAS with up to 3.1 TeV mass for the Z'_{SSM}-model, around 2.6 for a Z'_{χ}, Z'_{LR} and Z'_{η}, and 2.5 for the Z'_{ψ}-model. For muons the results are similar, a Z'_{SSM} could be found up to 3.2 or 4.4 TeV at 10 and 100 fb^{-1} respectively. The other models could be found between 3.5 and 4.0 TeV for high luminosity and 2.6 and 3.0 TeV for low luminosity. The difference between the electron and muon reach at high luminosity is within the statistical errors and the effect of the different efficiency in ATLFAST. The difference is larger at low luminosity, where the effects of more relaxed muon triggers are visible.

The results presented here are less optimistic than previous determinations of the ATLAS Z' reach, as in [128] where the ATLAS simulation was a less complex one. In addition, the results are well compatible with the expected CMS result, as presented in [140].

Particle	Luminosity (fb^{-1})	SSM	χ	ψ	η	LR
Z′ → e^+e^-	10	3.10	2.67	2.50	2.57	2.66
	100	4.28	3.89	3.53	3.73	3.73
Z′ → $\mu^+\mu^-$	10	3.15	3.05	2.59	2.70	2.76
	100	4.38	3.91	3.53	3.76	3.79

Table 11.6: The Z′ discovery reach of ATLAS.

11.5 Z′ Model Discrimination in ATLAS

If the Z′ is discovered, either in ATLAS or in another experiment, it will be interesting to extract as much information as possible from this particle about the new physics. The main task will be to identify from which model the observed Z′ comes from. To do this several observables will be useful.

- *Total decay width:* As already discussed in the previous section the different models have different total decay widths, found by a Breit-Wigner fit to the invariant mass distribution of the dilepton system. This can be used as a first indication of which model the Z′ might comes from.

- *Asymmetry*: Another useful tool is the forward-backward lepton charge asymmetry as described in chapter 10 (section 10.5), determined by the relation:

$$\left.\begin{array}{l} A^l_{FB}(i) = \dfrac{F(i) - B(i)}{F(i) + B(i)} \end{array}\right\} \quad i = Y, M, \cos\theta^*. \tag{11.12}$$

  The asymmetry information in the Z′ peak region (on-peak) as well as in the interference region (off-peak) will be of interest, since only the on-peak region might not provide a good model discrimination alone. The asymmetry can be looked at for different parameters and the ones of main interest are the following:

  - Decay angle, $|\theta^*|$.
  - Dilepton mass, $A^l_{FB}(M_{ll})$.
  - Dilepton rapidity, $A^l_{FB}(Y_{ll})$.

- *Rapidity distribution:* The Z′ couplings are sensitive to the up or down type quarks. Depending on which model is investigated, the fraction of certain quarks in the rapidity distribution will be different. For this reason, the shape of the dilepton rapidity distribution could be used to distinguish between the models provided one could find a way to "tag" flavour.

11.5.1 Angular Distribution - $\cos\theta^*$

The angular distribution of the lepton system, $\cos\theta^*$, is described by the angle between the direction of the negatively charged lepton (e^- or μ^-) and the corresponding quark direction in the centre of mass system of the Z′ (rest frame), as seen in figure 11.16, left. In reality, the original quark direction can not be determined from $p - p$ collisions, but the quark direction can be approximated by the Z′ direction, as will be demonstrated later. In this analysis, both the angle between the electron and the dilepton (Z') system as well as the angle between the electron and the original quark have been studied. The information about the quark is taken directly from the PYTHIA output. In addition, the angle between the dilepton vector and the beam-axis (z-axis) has been calculated and used as a reference since it has a symmetric distribution.

To determine the angle θ^* in the Z′ centre of mass system the electron and quark need to be boosted in the direction $\vec{b} = -\frac{\vec{p}_{ll}}{E_{ll}} = (-p_x/E, -p_y/E, -p_z/E)$. The boost transformation is standard Lorentz transformation of type:

$$p_x = p_{x'} + \frac{\gamma - 1}{\beta^2}(b\ p_{x'})b + \gamma E' b \tag{11.13}$$

$$E = \gamma(E' + b\ p_{x'}), \tag{11.14}$$

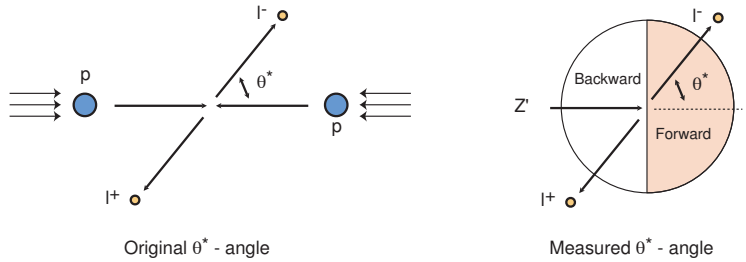

Figure 11.16: Left, θ^* is the angle between the produced negatively charged lepton (e^- or μ^-) and the incoming quark direction. Right, an illustration of the measured θ^*. Since the quark direction can not be measured, $\cos\theta^*$ is taken as the angle between the negative charged lepton and the Z′ direction of flight. The forward and backward direction is the one towards positive $\cos\theta^*$ or negative $\cos\theta^*$, respectively.

where $\beta = \frac{v}{c}$ is the speed of the centre of mass frame and $\gamma = \frac{1}{\sqrt{1-\beta^2}}$. The three different angular distributions are then found by the following relations:

$$\angle(e^-, q) = \frac{\vec{p}_{e^-}^{\,Z'cms} \cdot \vec{p}_q^{\,Z'cms}}{|\vec{p}_{e^-}^{\,Z'cms}|\ |\vec{p}_q^{\,Z'cms}|} \tag{11.15}$$

$$\angle(e^-, Z') = \frac{\vec{p}_{e^-}^{\,Z'cms} \cdot \vec{p}_{ll}^{\,lab}}{|\vec{p}_{e^-}^{\,Z'cms}|\ |\vec{p}_{ll}^{\,lab}|} \tag{11.16}$$

$$\angle(e^-, z) = \frac{\vec{p}_{e^-}^{\,Z'cms} \cdot \vec{p}_z^{\,lab}}{|\vec{p}_{e^-}^{\,Z'cms}|\ |\vec{p}_z^{\,lab}|} \tag{11.17}$$

were $\vec{p}_z^{\,lab} = (0,\ 0,\ 1)$. Figure 11.17 shows these three different angular distributions, $\cos\theta^*$, for the Z'_χ model. The angle between the lepton and the quark direction shows a maximum of asymmetry (dashed line). The angle between the lepton and the Z′ direction is not as good (solid line) since events with the wrong directions are also present, but still an asymmetry is recognisable. Finally, the angle between the lepton and the beam direction is symmetric (dotted-dashed line). Figure 11.18 shows the angular distribution with respect to the Z' direction (+z) for different models normalised to 100 fb^{-1} luminosity. As can be seen from this figure, some of the models can be distinguished by this distribution since the asymmetry is different. This is true especially for the Z'_χ model where the slope of the distribution is opposite of the others due to having different signs of the coupling constants. However, for other model having similar angular distributions, like the Z'_ψ and Z'_η - model, any discrimination will be difficult.

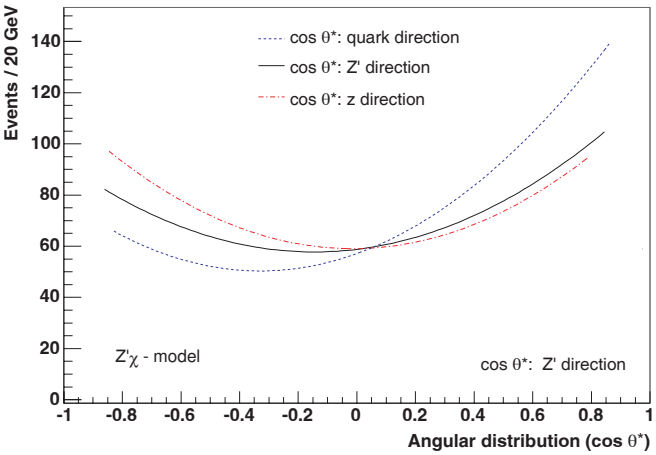

Figure 11.17: $q\bar{q} \to \gamma, Z^0, Z' \to \mu^+\mu^-$ (Z'_χ, 100 fb^{-1}): The angular distribution using different "quark" directions in the centre of mass frame, showing a reduced but still recognisable asymmetry for the Z′ direction.

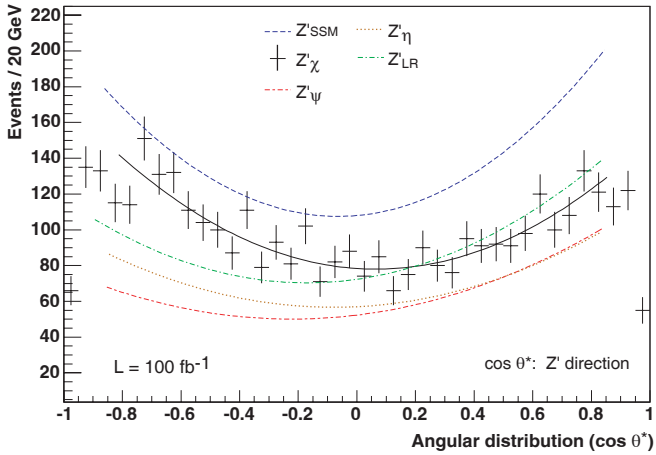

Figure 11.18: $q\bar{q} \to \gamma, Z^0, Z' \to e^+e^-$ (100 fb^{-1}): The angular distribution with respect to the Z′ direction for different Z′ models.

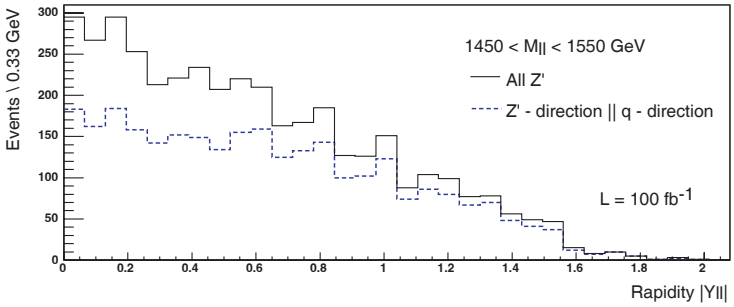

Figure 11.19: $q\bar{q} \to \gamma, Z^0, Z' \to e^+e^-$ (100 fb^{-1}): The total number of Z' and the number of Z' moving in the same direction as the quark are shown as a function of the dilepton rapidity. A cut on low $|Y_{ll}|$ would limit the fraction of Z' with the wrong direction with respect to the quark direction.

11.5.2 Mass Distribution of the Asymmetry - $A^l_{FB}(M)$

The asymmetry with respect to the mass distribution (equation 11.12) is found by comparing the different numbers of events in the forward and backward direction with respect to the quark direction, which again is approximated by the direction of the reconstructed Z' particle (see figure 11.16, right). The validity of this assumption is described in [139]. Figure 11.19 shows the number of simulated Z' with the correct quark direction in comparison with the total number and as a function of the absolute value of the dilepton rapidity. One can see that for low rapidities the fraction of Z' with the correct direction decreases towards $\sim 50\%$ of the total number of events. At larger rapidities the fraction of events with correct direction increases.

Figure 11.20 shows the p_z distribution of the lepton system, p_{ll}, for different rapidity cuts, for the on-peak region ($M_{Z'}$ - 50 GeV $\leqslant M_{l^+l^-} \leqslant M_{Z'}$ + 50 GeV). The Z' events are sorted out according to whether they stem from a quark emitted along the forward hemisphere (F, $p_{z,q} > 0$, white area) or the backward hemisphere (B, $p_{z,q} < 0$, shaded area). With harder rapidity cuts the amount of events with the wrong direction is reduced significantly. Table 11.7 shows in one column the fraction of remaining events with the wrong quark direction for various rapidity cuts. It also shows the fraction of remaining events for the different cuts compared to the total number of events without the rapidity cut applied. Taking the example of the Z'_χ-model, for a cut of $|Y_{ll}| > 0.2$ the wrong events are reduced to 24% of the total number, whereas the number of events itself has been reduced to 78%. With increasing cut the number of events with the wrong direction is reduced significantly but so is the total number of events as well. For a cut of $|Y_{ll}| > 0.4$, 0.6, 0.8 and 1.0, the fractions kept are 61%, 44%, 30% and 19%, respectively. A cut of $|Y_{ll}| = 0.8$ has been chosen in this analysis to be able to compare this results with previous ones, and will be used in the following asymmetry discussion. It corresponds to an efficiency of around 30 % having only $\sim 10\%$ events with incorrect directions for

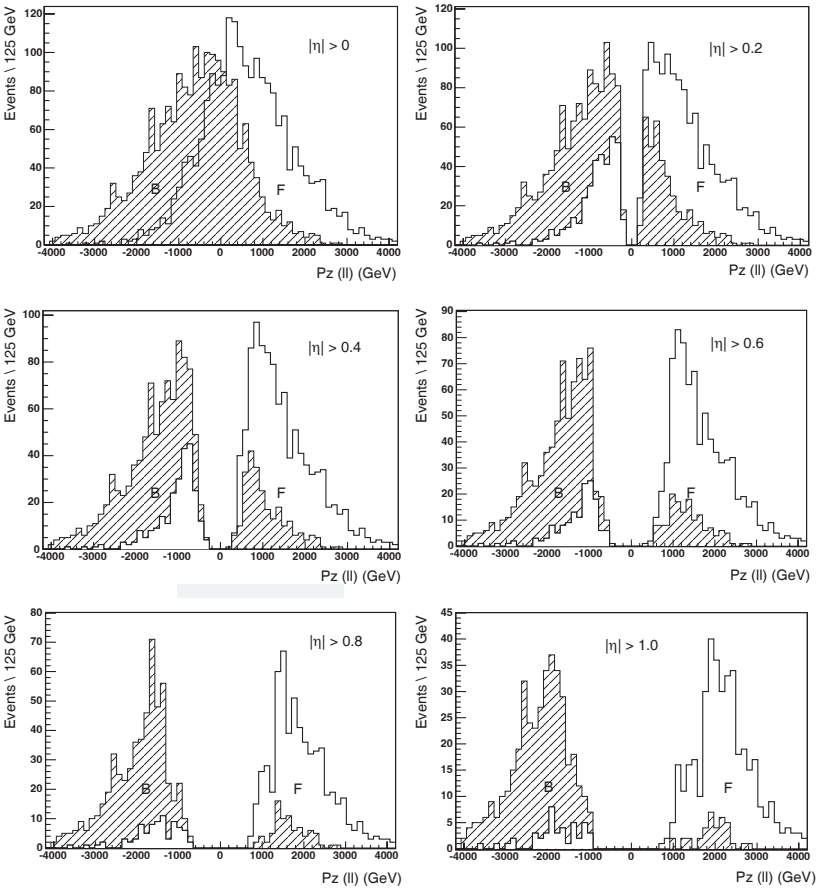

Figure 11.20: $q\bar{q} \to \gamma, Z^0, Z' \to e^+e^-$ (Z'_χ, 100 fb^{-1}): The P_z^{ll} distribution for $P_z^q < 0$ (striped area, B) and $P_z^q > 0$ (white area, F) with different pseudorapidity cuts. The number of electrons with the wrong direction decreases as the cut increases. However the reduction of the number of correct events also decreases rapidly.

$Z' \to e^+e^-$	Z'_{SSM}		Z'_χ		Z'_ψ		Z'_η		Z'_{LR}	
$\lvert Y\rvert$	Dir.	Frac.	Dir.	Frac.	Dir.	Frac.	Dir.	Frac.	Dir.	Frac.
> 0.2	21%	81%	24%	78%	20%	82%	20%	83%	24%	82%
> 0.4	17%	63%	20%	61%	15%	65%	15%	65%	20%	63%
> 0.6	14%	47%	15%	44%	11%	49%	12%	50%	17%	47%
> 0.8	11%	32%	13%	30%	10%	34%	7%	34%	13%	31%
> 1.0	7%	19%	10%	19%	8%	23%	4%	22%	9%	19%

Table 11.7: $Z' \to e^+e^-$: The fraction of Z′ in the peak region with a direction different from that of the quark. The influence of the rapidity requirements on various Z′ models is shown. The column marked Dir. shows the fraction of events with the wrong quark direction, the column marked Frac. shows the fraction of the total number of events after the cut.

the different models. Approximately the same values are achieved for the off-peak region. However, at low luminosity, a less hard cut on the rapidity may be favourable to increase the observed statistics.

Since the γ-Z^0 interference results in large forward backward asymmetries it is expected that this will be the case for the γ-Z^0-Z' interferences too (γZ^0, $\gamma Z'$ and Z^0Z'). The γ-Z^0 interference is large even for masses much higher than the Z^0-peak and in this region essentially asymmetries around 61% are expected for up- and down- type reactions according to [139]. When approaching the Z' peak the additional interference with Z′ is expected to modify this asymmetry value. Figure 11.21 shows the simulated charge asymmetry for a partial interference only, for different M_{ll} ranges and for decay to muons. The processes $q\bar{q} \to \gamma Z^0$ (DY), $q\bar{q} \to \gamma Z'$ and $q\bar{q} \to Z^0Z'$ has been generated separately, with a dilepton cut of $|Y_{ll}| > 0.8$, and their asymmetry calculated within different dilepton mass regions. The DY background (circles) contributes with an approximately constant asymmetry values of ~ 0.6, which is conform to the expected value. The contributions from the $\gamma Z'$ contribution is more approaching zero towards higher mass values and the Z^0Z' contribution is approximately symmetric around the peak value.

The asymmetry for the Z'_{SSM}-model with respect to different flight directions and with decay to muons is shown in figure 11.22. The dashed line shows the generated asymmetry with respect to the quark direction and the dotted-dashed line the generated asymmetry with respect to the Z′ direction. Finally, the solid line shows the simulated signal with respect to the Z′. Both the latter distributions have been made with a rapidity cut of $|Y_{ll}| > 0.8$. One can see that the approximation of the direction is valid with this particular cut. However, the minimum seems to be shifted to the left when compared to the quark direction. The simulated signal shows less asymmetry and an even larger shift of the minimum towards lower masses. For high masses the asymmetry values goes towards 0.6 but are distorted due to the low statistics in this region. At low masses the increasing dominance of the Z^0 peak changes the interference pattern.

Figures 11.23 and 11.24 show the $M_{e^+e^-}$ distribution for a Z′ mass of 1.5 TeV

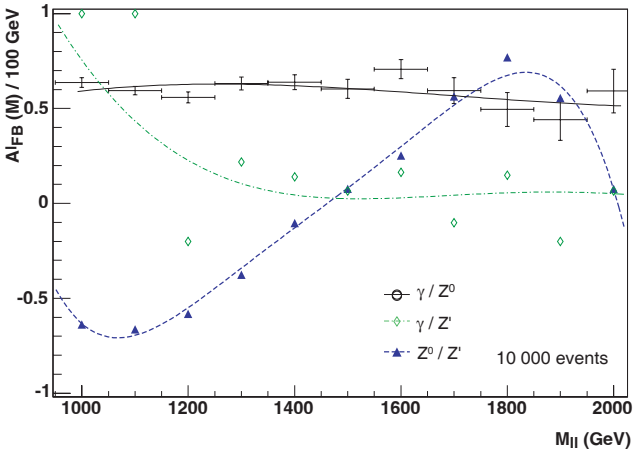

Figure 11.21: $q\bar{q} \rightarrow \gamma Z^0$ *or* $\gamma Z'$ *or* $Z^0 Z' \rightarrow \mu^+\mu^-$ (10 000 events): The asymmetry plotted as a function of dilepton mass regions to study the different interferences. The DY interference is seen to be relatively flat at a values ~ 0.6.

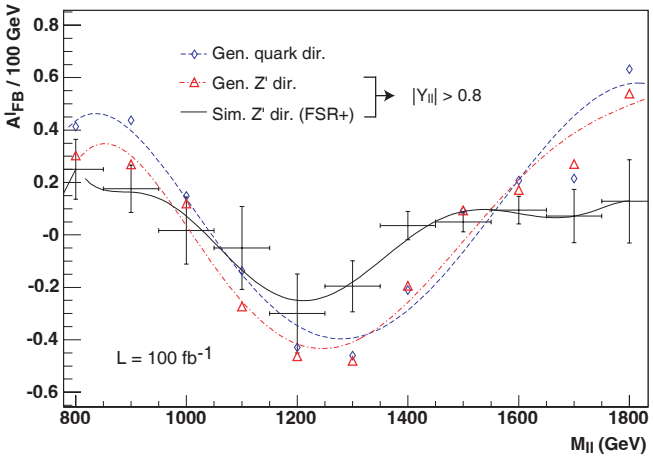

Figure 11.22: $q\bar{q} \rightarrow \gamma, Z^0, Z' \rightarrow \mu^+\mu^-$ (Z'_{SSM}, 100 fb^{-1}): The $A^l_{FB}(M_{ll})$ values for different sub-regions of the mass distribution, both in the on- and off- peak region. Three cases are studied, the generated asymmetry with respect to the quark direction (dashed lines), the generated asymmetry with respect to the Z' direction (dotted- dashed line) and the simulated asymmetry with respect to the Z' direction (solid line and points including error bars).

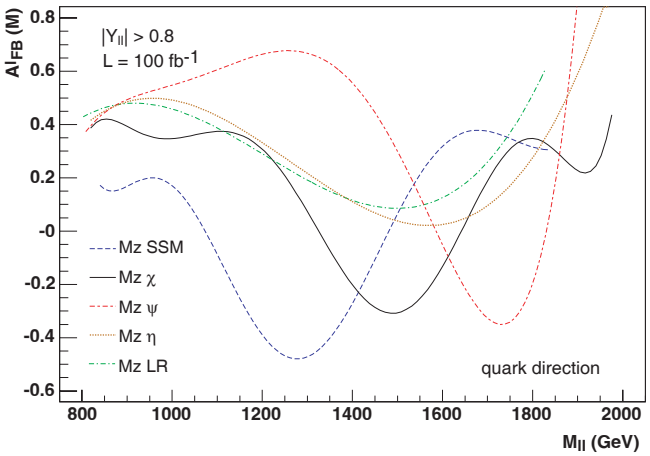

Figure 11.23: $q\bar{q} \to \gamma, Z^0, Z' \to e^+e^-$ (100 fb^{-1}): The $A^l_{FB}(M_{ll})$ values with respect to the quark direction in the on and off Z' peak region for different models.

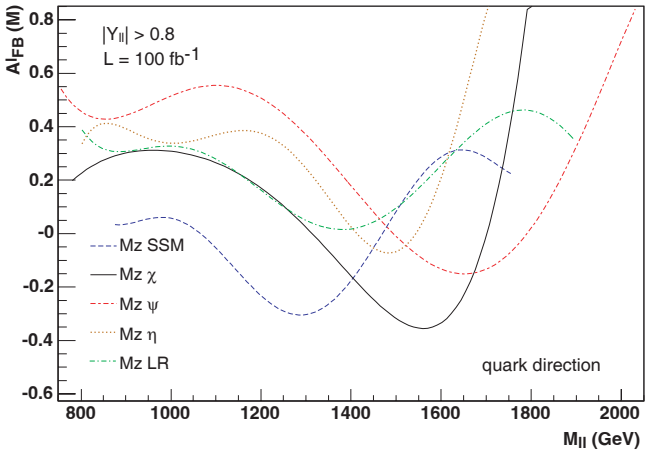

Figure 11.24: $q\bar{q} \to \gamma, Z^0, Z' \to e^+e^-$ (100 fb^{-1}): The $A^l_{FB}(M_{ll})$ values with respect to the Z′ direction in the on and off Z' peak region for different models.

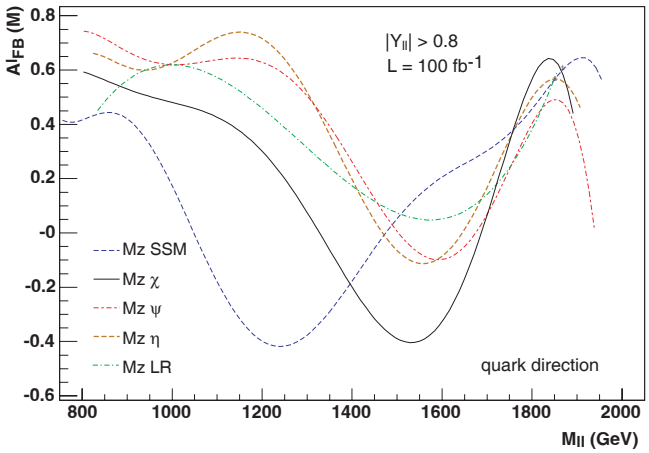

Figure 11.25: $q\bar{q} \to \gamma, Z^0, Z' \to \mu^+\mu^-$ (100 fb^{-1}): The $A^l_{FB}(M_{ll})$ values with respect to the quark direction in the on and off Z' peak region for different models.

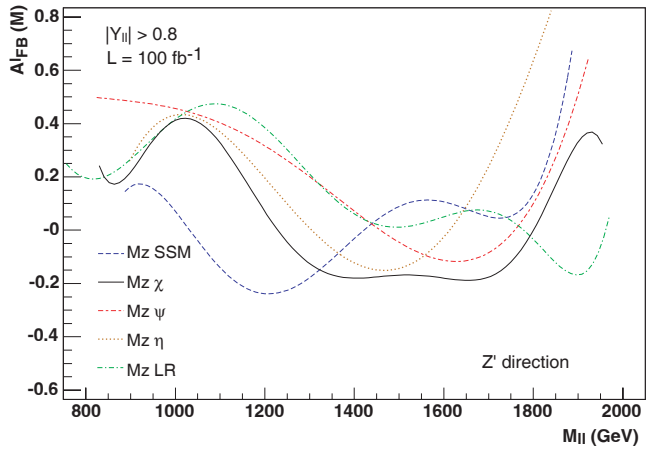

Figure 11.26: $q\bar{q} \to \gamma, Z^0, Z' \to \mu^+\mu^-$ (100 fb^{-1}): The $A^l_{FB}(M_{ll})$ values with respect to the Z$'$ direction in the on and off Z' peak region for different models.

$Z' \to e^+e^-$	Z'_{SSM}	Z'_{χ}	Z'_{ψ}	Z'_{η}	Z'_{LR}
On peak					
Quark dir.	0.08 ± 0.01	0.35 ± 0.01	-0.03 ± 0.02	-0.07 ± 0.02	0.12 ± 0.02
Z′ dir.	0.05 ± 0.02	0.14 ± 0.02	0.00 ± 0.05	-0.05 ± 0.03	0.04 ± 0.02
Z′ dir./$\|Y\|$ >0.8	0.08 ± 0.03	0.21 ± 0.04	-0.01 ± 0.05	-0.06 ± 0.04	0.13 ±0.04
Off peak					
Quark dir.	-0.21 ± 0.03	0.58 ± 0.02	0.64 ± 0.03	0.56 ± 0.03	0.30 ± 0.03
Z′ dir.	-0.08 ± 0.03	0.19 ± 0.04	0.31 ± 0.04	0.20 ± 0.04	0.16 ± 0.04
Z′ dir./$\|Y\|$ >0.8	-0.07 ± 0.06	0.28 ± 0.07	0.25 ± 0.08	0.12 ± 0.08	0.21 ± 0.06

$Z' \to \mu^+\mu^-$	Z'_{SSM}	Z'_{χ}	Z'_{ψ}	Z'_{η}	Z'_{LR}
On peak					
Quark dir.	0.09 ± 0.01	0.38 ± 0.01	-0.03 ± 0.02	-0.07 ± 0.02	0.08 ± 0.02
Z′ dir.	-0.01 ± 0.02	0.17 ± 0.03	0.01 ± 0.03	-0.00 ± 0.03	0.03 ± 0.03
Z′ dir./$\|Y\|$ >0.8	0.05 ± 0.04	0.24 ± 0.05	-0.08 ± 0.06	-0.06 ± 0.06	-0.03 ± 0.05
Off peak					
Quark dir.	-0.23 ± 0.03	0.56 ± 0.03	0.58 ± 0.03	0.56 ± 0.03	0.36 ± 0.03
Z′ dir.	-0.01 ± 0.02	0.16 ± 0.03	0.09 ± 0.03	0.11 ± 0.03	0.18 ± 0.03
Z′ dir./$\|Y\|$ >0.8	-0.03 ± 0.04	0.32 ± 0.04	0.24 ± 0.05	0.11 ± 0.05	0.25 ± 0.05

Table 11.8: $q\bar{q} \to \gamma, Z^0, Z' \to e^+e^-$ (100 fb^{-1}): The on and off peak asymmetry values, A^l_{FB} for $M_{Z'} = 1.5$ TeV for various models. The values are shown for both the quark or Z′ direction and with or without the rapidity cut of $|Y_{ll}| > 0.8$.

and 100 fb^{-1} for different models, for the quark direction and the Z′ direction, respectively. Figures 11.25 and 11.26 show a similar plot but for decay $M_{\mu^+\mu^-}$. As one can see from all four plots the shape and the on- and off- peak values are characteristic for the model and may be used for model discrimination. The curves have a characteristic minimum close to the generated mass but on which side it lays and for which value the minimum is found, will give an indication of the model. At high GeV and close to the 800 GeV the fit is no longer valid since it approaches a region with either low statistics or a kinematic cut, respectively. For the Z'_{SSM} model the minimum is around 1300 GeV and for the Z'_{χ} model the minimum is close to the mass peak itself $\sim$ 1500 GeV for the generated asymmetry but shifted towards $\sim$ 1600 GeV for the simulated asymmetry. The Z'_{SSM} is also characteristic with a minimum around 1750 GeV for the generated asymmetry and shifted towards 1650 GeV for the simulated asymmetry. Both the Z'_{η} and the Z'_{LR} model are rather similar both in shape and minimum but the first tends towards a minimum of 1400 GeV and the latter 15 GeV in the case of the simulated asymmetry. Z'_{LR} is much broader then the other models. Z'_{η} and Z'_{χ} have similar minima in the simulated mode but the asymmetry is much larger in the case of Z'_{χ}. To determine and quantify the discrimination possibilities due to this plot another more detail analysis is needed taking into account the statistical errors and the quality of the fit.

Table 11.8 shows the asymmetry values both in the on-peak region and the off-

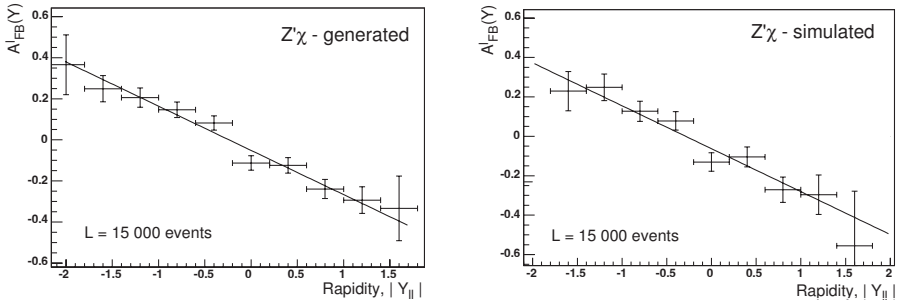

Figure 11.27: $q\bar{q} \rightarrow \gamma, Z^0, Z' \rightarrow e^+e^-$ ($Z'\chi$, 100 fb^{-1}): Left the generated asymmetry for different rapidity distribution region. Right, the simulated asymmetry. One can see from the generated asymmetry that apart from the edges where there are large error bars, the values are rather linear and symmetric around zero.

peak region ($M_{Z'}$ - 500 GeV $\leqslant M_{l^+l^-} \leqslant M_{Z'}$ - 50 GeV) for different Z' models, as well as with a dilepton rapidity cut of $|Y_{ll}| > 0.8$. When comparing the values for the decay of electrons with respect to the Z′ direction and with the rapidity cut, both regions provide a possibility of model discrimination already at 100 fb^{-1}. By looking at the values in the on-peak region Z'_χ and Z'_{LR} can not be distinguished from each other since they both have values around 0.2 with overlapping error regions. However these two models can be distinguished from the other models by having a large positive asymmetry value. Next the Z'_{SSM}- model can be distinguished from all other models since by having a positive value around 0.1. The Z'_ϕ and Z'_η-models can be distinguished from the other models by having a negative value close to -0.05, but not from each other. The same discrimination possibilities are available for the off-peak region, however, the values for each model changes and become more characteristic. With higher statistics the errors bars will decrease and the off-peak region will provide a useful tool for model discrimination in addition to the on-peak values. The discrimination possibilities for Z′ decay to muons provide equally a tool for model discrimination.

11.5.3 Asymmetry of the Rapidity Distribution - $A^l_{FB}(Y_{ll})$

Another possibility to discriminate between models can be made by comparing the asymmetry in different rapidity bins for the on-peak distribution in a similar fashion as done for the mass distribution of the asymmetry. However, in this case the angular distribution is taken with respect to the z-direction and not the flight direction of the Z′. The on-peak region is this time taken as M_{peak} - 30 GeV ¡ M_{peak} + 30 GeV to improve the result. Figure 11.27 shows an example of the asymmetry distribution for the $Z'\chi$- model. The left plot shows the generate distribution, which a part from the edges where the error bars are very large, shows a linear distribution approximately

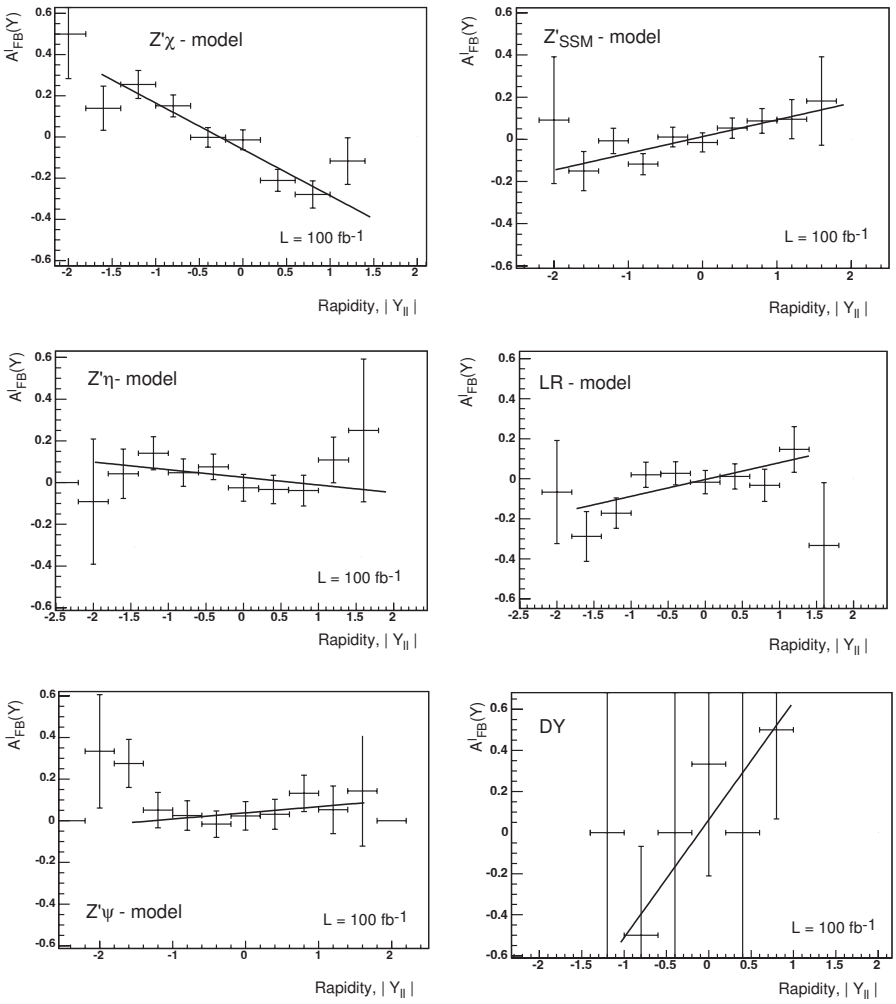

Figure 11.28: $q\bar{q} \to \gamma, Z^0, Z' \to e^+e^-$: The $A^l_{FB}(Y_{ll})$ values for different models for $M_{Z'} = 1.5$ TeV. The variations in slope between the models permits discrimination.

symmetric around zero. The simulated distribution, as shown in the right-hand plot, is less linear, but still the shape is recognisable. At higher statistics the distribution becomes more linear.

Figure 11.28 shows the rapidity distribution of the simulated asymmetry for different models. The distributions are all more or less symmetric around zero. The

$Z' \to e^+e^-$	Gen.	Sim.	$Z' \to \mu^+\mu^-$	Gen.	Sim.
Z'_{SSM}	0.08 ± 0.02	0.08 ± 0.03	Z'_{SSM}	0.06 ± 0.02	0.03 ± 0.04
Z'_{χ}	0.21 ± 0.03	0.21 ± 0.04	Z'_{χ}	-0.19 ± 0.05	-0.19 ± 0.03
Z'_{ψ}	0.02 ± 0.03	0.03 ± 0.04	Z'_{ψ}	-0.04 ± 0.03	-0.05 ± 0.06
Z'_{η}	-0.03 ± 0.02	-0.04 ± 0.03	Z'_{η}	-0.06 ± 0.02	0.02 ± 0.06
Z'_{LR}	0.07 ± 0.03	0.07 ± 0.04	Z'_{LR}	-0.04 ± 0.03	- 0.01 ± 0.02
DY	0.48 ± 0.04	0.57 ± 0.04	DY	-0.05 ± 0.02	- 0.05 ± 0.02

Table 11.9: $q\bar{q} \to \gamma, Z^0, Z' \to l^+l^-$: The slope values of a linear fit to $A^l_{FB}(Y_{ll})$ for a simulated Z′ at $M_{Z'} = 1.5$ TeV (from figure 11.28).

Z'_{SSM}- and $Z'\chi$- models are more linear than the others but are also the model with most simulated events. To be able to discriminate between the models it is possibly to compare the values of the slope of a linear fit. The results of this fit for a simulated Z′ of mass 1.5 TeV is presented in table 11.9 together with the values for the generated signal. Compared with the mass distribution it will be more difficult to distinguish between most models at 100 fb^{-1} using the rapidity distribution. The Z'_{SSM}- and $Z'\chi$-models are easy to distinguish due to their rather steep and characteristic slope. The values of the slope are rather different, ~ 0.1 and ~ 0.2 respectively, so the two models could be distinguished even from each other. The three other models have slopes with values very close to zero and the uncertainty at the present low statistics makes it difficult to distinguish between them.

11.5.4 Quark Distribution - $R_{u\bar{u}}$

For the different models the number of events coming from a collision involving $u\bar{u}$ and $d\bar{d}$ quark - antiquark pairs varies due to their different couplings. The fraction of $u\bar{u}$ or $d\bar{d}$ events in the inital state may allow to distinguish between models. As for the asymmetry the quark direction is not known, but the shape of the Z′ rapidity distribution differs according to which of the two quark types are dominating. Assuming that the W$^{\pm}$ and Z^0 rapidity distributions have been measured in detail the relative parton distribution functions for u and d quarks as well as for the corresponding sea quarks and antiquarks are well known. Thus the rapidity spectra can be calculated separately for $u\bar{u}$ and $d\bar{d}$ as well as for the sea quark antiquark annihilation and for the mass region of interest. Using these distributions a fit can be performed to the Z′ rapidity distribution, which permits to obtain the corresponding fractions of the Z′ bosons produced.

Figure 11.29 and figure 11.30 show the quark distribution for the Z'_{χ} model for e^+e^- and the Z'_{ψ} model for $\mu^+\mu^-$, respectively. The quark distributions are taken from the output of the PYTHIA generator. As one can see, for the Z'_{χ} the $d\bar{d}$ quarks dominate at low rapidities. Equivalently, the Z'_{ψ} model, plotted for muons, shows a domination of $u\bar{u}$ quarks in the high rapidity region. Comparing the shape of the two distributions one can estimate which quark-flavour dominates, a rather flat rapidity distribution points to a majority of $u\bar{u}$ quarks, while a more pointy distribution

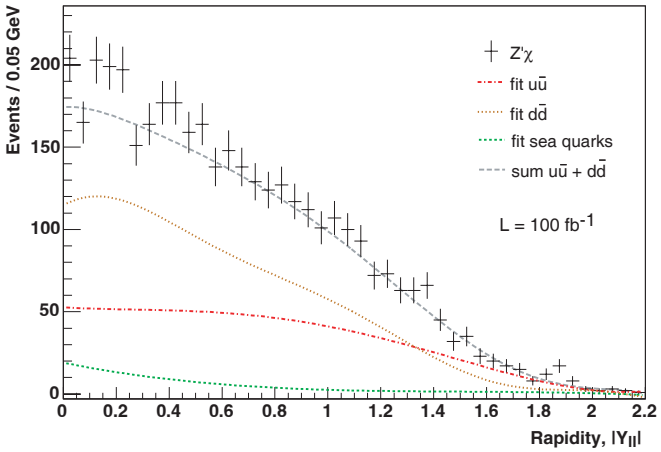

Figure 11.29: $q\bar{q} \to \gamma, Z^0, Z' \to e^+e^-$ (Z'_χ, 100 fb^{-1}): The quark fraction as a function of the rapidity. This model shows a high fraction of $d\bar{d}$ quarks, which increases the number of events close to zero.

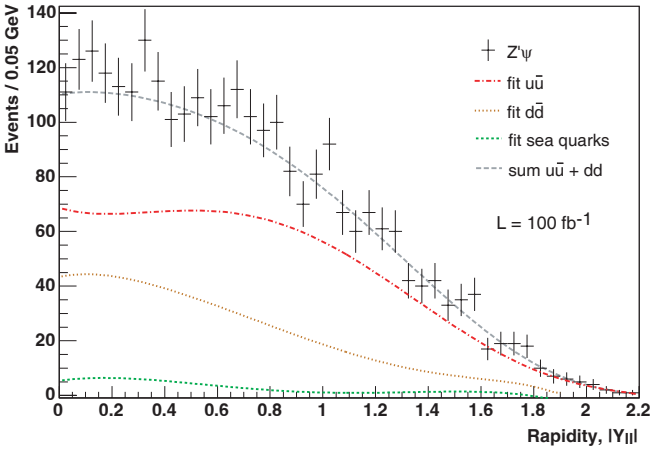

Figure 11.30: $q\bar{q} \to \gamma, Z^0, Z' \to \mu^+\mu^-$ (Z'_ψ, 100 fb^{-1}): The quark fraction as a function of the rapidity. This model shows a high fraction of $u\bar{u}$ quarks, which increases the number of events at high rapidities.

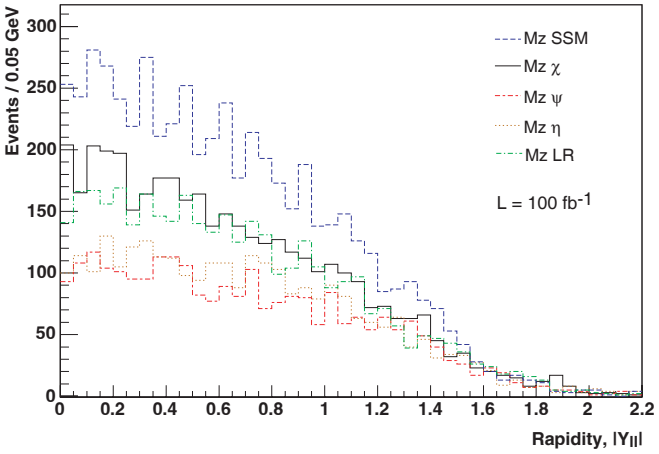

Figure 11.31: $q\bar{q} \to \gamma, Z^0, Z' \to e^+e^-$ (100 fb^{-1}): Comparison of the rapidity distribution for different models, models with flat rapidity distributions such as Z'_ψ and Z'_η can be distinguished.

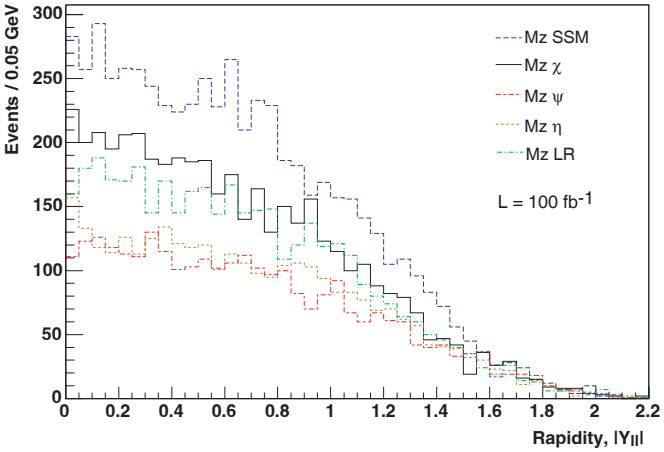

Figure 11.32: $q\bar{q} \to \gamma, Z^0, Z' \to \mu^+\mu^-$ (100 fb^{-1}): Comparison of the rapidity distribution for different models. Models with flat rapidity distributions such as Z'_ψ and Z'_η can be distinguished.

$Z' \to e^+e^-$	Z'_{SSM}	Z'_χ	Z'_ψ	Z'_η	Z'_{LR}	DY
$u\bar{u}$	57%	36%	66%	71%	52%	72%
$d\bar{d}$	39%	58%	30%	26%	44%	23%
Sea quarks	4%	6%	4%	3%	4%	5%

$Z' \to \mu^+\mu^-$	Z'_{SSM}	Z'_χ	Z'_ψ	Z'_η	Z'_{LR}	DY
$u\bar{u}$	57%	36%	66%	69%	52%	75%
$d\bar{d}$	39%	58%	30%	27%	43%	21%
Sea quarks	4%	6%	4%	4%	5%	4%

Table 11.10: $q\bar{q} \to \gamma, Z^0, Z' \to l^+l^-$ (100 fb^{-1}): The fraction of quarks of a certain type with respect to the total number of events, $\frac{N_q}{N_{tot}}$, for decay to muons and electrons. No cut on the dilepton mass has been applied.

around zero has a majority of $u\bar{u}$ quarks. Figure 11.31 and 11.32 shows the rapidity distribution for the different models at 100 fb^{-1}, where it is seen that the models Z'_ψ and Z'_η are rather flat and could have large $u\bar{u}$ quarks fraction, whereas the Z'_χ rapidity looks pointy and could have a large $d\bar{d}$ fraction.

From the PYTHIA data one can extract the quark information and evaluate theoretically which models are dominated by which quark flavour. This information can be used as a comparison for any measured distribution. Table 11.10 shows the quark fraction, R_q, for all dilepton events:

$$R_q = \frac{N_q}{N_{tot}}. \tag{11.18}$$

From this table it becomes clear that the models Z'_{SSM}, Z'_ψ and Z'_η has a majority of events from $u\bar{u}$ collisions, the model Z'_{chi} has a majority from $d\bar{d}$ collisions and the Z'_{LR} has more or less equal distribution. The proportion of sea quarks is around 4-6 %. In comparison the Drell-Yan background is mostly produced by $u\bar{u}$ collisions ($\sim 70\%$)

The differences between the different models can be improved by looking at the rapidity distribution in the on-peak region only (1450 GeV $< M_{ll} <$ 1550 GeV). Table 11.11 gives the $u(\bar{u})$ fraction, $R_{u\bar{u}}$, in this region for different:

$$R_{u\bar{u}} = \frac{N^{on-peak}_{u,\bar{u}}}{N^{on-peak}_{tot}}. \tag{11.19}$$

Conclusion

The simple and clean Z′ signal will allow the search of a heavy neutral gauge boson to be efficiently performed, even in early ATLAS data acquisition runs. The expected reach as determined by fast simulation lies between 2.5 and 3.2 TeV for decay to electrons or muons at 10 fb^{-1} and around 3.5 to 4.4 TeV for 100 fb^{-1}. If a Z' exists

$Z' \to e^+e^-$	$R_{u\overline{u}}$ (Sim.)	$Z' \to \mu^+\mu^-$	$R_{u\overline{u}}$ (Sim.)
Z'_{SSM}	0.48 ± 0.004	Z'_{SSM}	0.572 ± 0.002
Z'_{χ}	0.248 ± 0.005	Z'_{χ}	0.358 ± 0.004
Z'_{ψ}	0.625 ± 0.005	Z'_{ψ}	0.659 ± 0.003
Z'_{η}	0.715 ± 0.003	Z'_{η}	0.689 ± 0.002
Z'_{LR}	0.450 ± 0.005	Z'_{LR}	0.523 ± 0.003

Table 11.11: $q\bar{q} \to \gamma, Z^0, Z' \to l^+l^-$ (100 fb^{-1}): $R_{u\overline{u}} = \frac{N_{u,\bar{u}}}{N_{tot}}$, the fraction of u and $u\bar{u}$ quarks in the on-peak region (1450 GeV $< M_{ll} <$ 1550 GeV) for muons and electrons for a simulated Z′ at 1.5 TeV and for 100 fb^{-1}.

in this mass range it should be possible to be discovered within the first two years of operation.

The discrimination possibilities at 100 fb^{-1} makes it possible to determine the Z′ model at least up to 1.5 TeV. It will also be possible to distinguish between models by not only the examination of the width and amplitude of the resonance peak, but also the forward-backward asymmetry both on- and off- peak will simplify this work. In addition, although less powerful, the rapidity distribution may confirm the choice of model.

Part IV

Conclusions

12
Achievements and Outlook

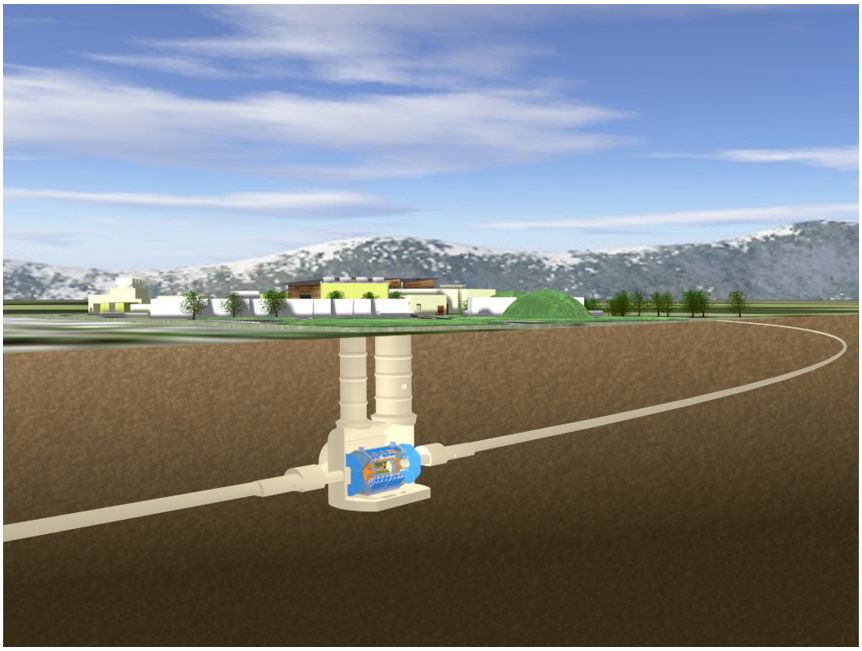

Figure 12.1: Conceptual drawing of the final ATLAS [8].

Introduction

During this work, the SCT detector has gone from the stage of building prototype modules to finishing approximately 1/3 of the detector. Module production sites have completed more than 2112 modules needed for the barrels and almost all of the 1976 end-cap modules. At this moment two full barrels and around six disks for the end-cap have been finished. At my arrival at CERN, the pit was empty, now four of the toroid magnets have been installed and the central barrel of both TileCal and ECAL calorimeters have been built, with the solenoid mounted inside. From the prototype and testing stage, ATLAS is now taking shape as the end of installation is approaching. The first beam is scheduled for 2007.

This thesis shows a slice of many aspects needed when building a large-scale particle detector, from the production of modules to the assembly of larger detector parts and development and scale up of off-detector electronics. It also includes tests of most parts of the SCT, including calibration of the detectors and their data-taking in testbeams. It includes the determination of the best SCT operating conditions as well as the different error modes and corrective actions. Also work on the analysis of simulated ATLAS data has been done to complete the detector cycle from construction to final results.

12.1 Achievements

The main part of my work has been to contribute to the construction of the SCT detector. In completing a detector of the size and complexity as the SCT, many areas of development and expertise are needed. In addition, the work includes important efforts to integrate the SCT into the Inner Detector and into ATLAS. A summary of the contributions made in the different fields is presented below.

Detector Production

The production of SCT barrel modules was finished in 2004 and approximately 320 modules have been produced and tested by the SCAND cluster. Several test setups needed for the module production in Oslo were realised during the scope of this work and consists of the following sub-systems:

- An IV-curve measurement system was successfully constructed and used to validate and qualify the modules after mechanical assembly.
- A production DCS system, including cooling and environmental sensors, was constructed, verified and used during tests of pre-production modules.
- A set-up of a production DAQ system was realised and verified by testing pre-production modules.
- Successful electrical tests on two pre-production modules were made with the complete. measurement system.

Off-detector Electronics

For the SCT to be operated, the modules need to be powered with a set of high and low voltages and initialised with a set of slow commands, which are all provided by the SCT power supplies. During this work, an important contribution to the development of the power supplies has been made, in the form of continuous testing and analysis of the system performance of both the hardware and firmware of HV-cards, LV- cards, CC and backplane. As a consequence, both the internal power supply communication and the CAN communication with the DCS system was extensively tested. This work resulted in finding several problems in different parts of the power supply system, in addition to noise comparison tests and tests of basic functionalities. Solved by both hardware and firmware modification and new designs, this has resulted in more stable and efficient power supplies. Some of the main findings are:

- Detection of glitches on the backplane, disturbing the communication and resulting in power trips.
- Detection of the HV transistor failure.
- Current probe malfunctioning was detected.
- LV busy problem was detected.
- Various LV communication problems were detected and solved.
- A failure with the temperature readings were detected during tests of barrel 3.

In addition, a defined start-up procedure was discussed due to LV and DORIC design crashes as well as the implementation of CC and PP reset functions.

Another major accomplishment of the power supply system has been the successful implementation and scale-up for the macro-assembly in Oxford (barrel) as well as in Liverpool and NIKHEF (end-cap). After initial debugging the system has proven stable and have been running safely for the several months. This includes the assembly of the first barrels and their full tests, both warm and cold. More than 380 modules have been powered and run at the same time. Installation of a power supply system in SR1 sufficient for 700 modules is on going. The power supplies were also used successfully during the combined testbeam of 2004, where high reliability over time was important.

Detector Read-out

Another major part of this work is the construction and implementation of a SCT DCS system. Starting more or less from scratch, a DCS software has been developed, which has been important to the power supply development and essential to the macro-assembly tests of both barrels and disks. The macro-assembly could not have functioned safely without this DCS. Developing the PSS DCS together with the

power supply development made the system very robust and tolerant. It has been installed and used successfully at NIKHEF, Oxford, Liverpool as well as in SR1 and in testbeam at CERN and the feedback from users has been positive. In SR1, the full close-to-final SCT DCS system is operating and is currently used for the barrel acceptance tests. Preparations are being made for the insertion of the SCT barrels into each other and the inner detector integration. Both are tasks where the SCT DCS will be used to confirm the SCT functionality. A summary of the main development achievements is as follows:

- Construction of a DCS for the operation of power supplies and slow commands (including the proper communication) resulting in a stable and robust system.
- Definition and implementation of SCT operational states (run state transitions).
- Defining and implementing all SCT operational error conditions and failure states as well as the actions to be taken in each case.
- A reliable communication between SCT DCS parts (environmental monitoring, thermal enclosure, and ID cooling) has been established. It is controlled by the power supply DCS acting as a global control stations, while all other projects are defined as local control stations, providing a safe startup/shutdown procedure as well as safe transitions between the run states.
- Implementation of a reliable communication between the DAQ and the DCS to be able to issue DCS command from DAQ and to integrate the DCS run states into the DAQ operation.
- A first integration of the SCT DCS into the ATLAS DCS framework has been made, where commands for operating ATLAS also affects the SCT and where transmission of errors back to the ATLAS DCS gives feedback to the user.

Barrel Macro-Assembly

One of the main SCT achievements of 2004-2005 has been the barrel macro-assembly. I have contributed both to the installation of the test-system and to the warm assembly test sequence qualifying the assembly process. The analysed data shows a very promising result of the performance of the SCT, no degradation of the modules was detected. This has been confirmed later by cold tests. The main achievements of the barrel macro-assembly, which are described in this thesis, are as follows:

- Confirmation of a successful production of the SCT modules.
- Successful mechanical assembly of modules onto barrels. Tests of the modules on the barrel showed no major problems and no new defects.
- Implementation of a full and safe supply of power and cooling, a success for all off detector electronics such as power supplies and interlocks etc.

- A successfully working DAQ over time.
- Successful interaction between the two readout systems, DAQ and DCS.
- 380 modules (for B3) were successfully tested. Never have so many modules been tested at the same time, a great achievement of both the final DAQ and DCS.
- The cooling of 380 modules has been accomplished. Never before had so many module been cooled with a close to final evaporative cooling system.

In conclusion, the barrel tests shows that the macro-assembly has been a great success for the module and barrel design as well as the design of the off-detector electronics, mechanics and software.

ATLAS Integration

The main SCT goal of the 2004 testbeam was to integrate this detector as much as possible into the Inner Detector and the overall ATLAS. Another main goal was to run the SCT with all final components and to run both in calibration as well as in data-taking mode. Some of the SCT realisations, which include or follows from my contributions:

- Demonstration of the full SCT readout chain, running SCT in testbeam with both final DAQ and DCS.
- Calibration and operation taking data in calibration mode and data taking mode.
- Efficiency and resolution of the SCT detector were demonstrated to be conform with previous testbeam results.
- Operation and taking data in combined detector mode.
- SCT calibrated data was used for the alignment and the tracking of particles.

Preparation for Physics Data

As part of the preparation for the taking of physics data, a fast simulation of extra neutral gauge bosons has been performed. One of the main motivations for this work has been their clear signal over background and the early discovery potential in ATLAS. Simulations are useful to investigate different aspects of the detector performance and their affects on the physics results. In addition, they are also an important tool for tests of the final off detector software to be used when ATLAS is running. The following results for the Z' detection by ATLAS have been performed:

- An analysis has been performed which will be useful for the first years of ATLAS operation concentrating on 10 and 100 fb^{-1} luminosity.

- The generation of particles has been made with a maximum of decays possible, including initial and final state radiation, multi-interaction and hadronisation.
- The simulation included detector effects and a reduced efficiency, which is more realistic than earlier results, where not full simulation results have been presented.
- The Z′ discovery reach has been determined in ATLAS for 10 fb^{-1} and 100 fb^{-1} to be 2.5 TeV for electrons and 3.2 TeV for muons in the first case and 3.5 TeV for electrons and 4.4 TeV for muons in the latter case.
- The model discrimination possibilities have been successfully investigated at 100 fb^{-1} for a Z′ of mass 1.5 TeV, where it will be possible to early discriminate between different models using asymmetry results of both rapidity and mass distributions and by the shape of the rapidity distribution.

Interdependencies

The different parts of this thesis are dependent on each other and form a logical sequence of work. The contributions are made to the three main areas needed in most particle physics experiments: the construction of a detector (chapters 4, 5, 9), the operation of the detector (6, 7) and data-taking (either in testbeam, chapter 8, or by simulation, chapter 10 and 11, since real data is not yet available).

Each of these three areas could not function without the other. Without the success of the module production there would be no macro-assembly, and if the macro-assembly would go wrong then there would be detector defects, which might reduce the performance and the later physics results. Without the work done in testbeam, the implementation of the SCT in ATLAS would be poorer, which again would alter the physics results due to reductions in detector efficiency and the tracking results.

On the other hand, final ATLAS can not take data if the SCT modules are not properly powered and cooled, with a functioning DCS. If the modules are not supplied correctly, the modules might not be read out or return corrupted data. During operation, if the detector has a problem, it is the task of the SCT DCS to ensure the safety of the detector and to inform the user that the data taken will eventually not be valid, or will have reduced quality, for this particular run. As seen during the testbeam sessions, serious errors of the SCT might even make the whole of ATLAS stop. It is important for the later operation that all the sub-detector supplies, controls and read-out work correctly.

The simulation and off-line analysis are very useful not only to test the off-line software tools, but has been and will be important when it comes to select the right trigger options and to focus the physics searches for particles and in regions where there could be discoveries. By optimising the online and offline software in advance, time and effort can be spared. The physics analysis can also be used on real data in the future, if the code permits it, thus saving time in the reconstruction and analysis process of the ATLAS data.

12.2 Outlook

Although many accomplishments have been made during the last years, it still needs a considerable effort to finish ATLAS and start the first physic runs. The next few years with ATLAS development and the first years of operation will be most interesting and exciting when it comes to detector construction. The four barrels of the SCT will be inserted into each other to form a completed barrel. After insertion into the thermal enclosure it will then go into the TRT barrel. The same will be done for the two end-caps, which arrive fully mounted from Liverpool and NIKHEF. After testing the Inner Detector barrel, a combined run will be made using cosmic radiation to test the operation and read-out of the both SCT and TRT, which will take place during autumn 2005. After the solenoid field mapping has been completed in February 2006, the SCT and TRT will be lowered into the pit and installed into the inner part of ATLAS. Finally the Pixel detector, with the beam pipe will be installed inside the SCT barrel. In 2007 ATLAS will be finished and the first complete tests can be made.

Towards Physics Data

During the first year of operation, tuning of the machine parameters will be necessary. While a possible start up luminosity for the first collisions could be 6×10^{31} $\mathrm{cm}^{-2}\mathrm{s}^{-1}$, the goal of the first year is to arrive of a luminosity of up to 2×10^{33} $\mathrm{cm}^{-2}\mathrm{s}^{-1}$ during a first physics run. However, already for one day of LHC operation at 10^{33} $\mathrm{cm}^{-2}\mathrm{s}^{-1}$ one expects to supersede the amount of SM processes taken during 10 years of operation by previous machines. The crucial factor during the first years is the machine luminosity performance, but work must be done also on detector and trigger commissioning to reach the performance necessary for the envisaged physics searches. Background studies will also be important during this first initial operation. In spite of this, new physics might be discovered at an early stage. Even though it might be difficult to detect Higgs at these low luminosities, SUSY particles or extra gauge bosons may appear. It will be a very interesting time at ATLAS during the next few years.

Conclusion

My time in the ATLAS collaboration has been a most interesting and rewarding experience, both scientifically and personally. It has been a privilege to work with so many experienced physicists with a high interest in sharing their knowledge. It has been both a challenging and exciting time to be present, with many critical steps successfully completed. I am very pleased that I have been permitted to contribute in such a delicate phase of the detector construction. It has also been very satisfactory to see how my contributions have been integrated into the whole and used by many collaborators. I hope my next few years in physics will be just as rewarding as this past ones have been.

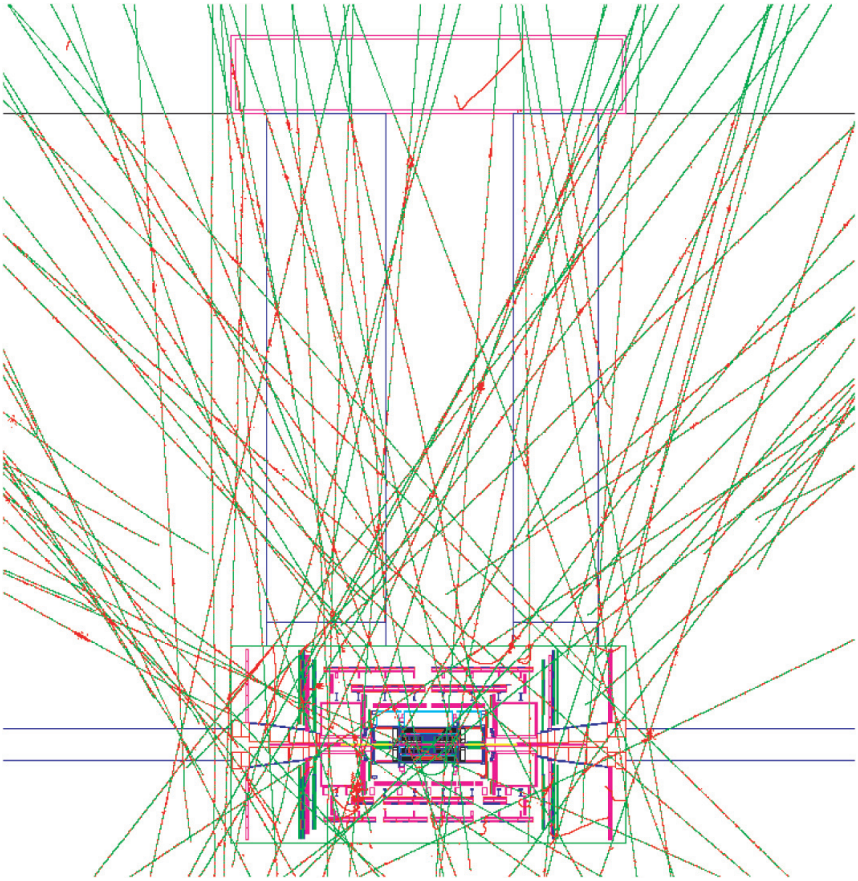

Figure 12.2: Simulation of cosmic muons in the ATLAS pit during a time of 10 μs [141]. Maybe the first particles to be detected by ATLAS.

Bibliography

[1] H. Sandaker on behalf of the SCT collaboration. The readout & control system for the ATLAS SemiConductor Tracker. *NIMA5517*, 2005.

[2] J. Bohm et al. Multiprocessor system controlling power supply distribution for the ATLAS SCT. *CERN-2004-010*, 2004.

[3] A. Sfyrla et al. The Detector Control System for the ATLAS SemiConductor Tracker Assembly Phase. *IEEE*, 2005, in print.

[4] M. Chamizo Llatas et al. The Control and Monitoring System for the ATLAS Semi-Conductor Tracker. *NIMA*, 2005, in print.

[5] P. Ferrari et al. SCADA Detector Control System for SCT Modules in ATLAS 2004. *Atlas Note*, 2005, in preparation.

[6] G. Moorhead et al. Beam test of ATLAS SCT silicon strip detector modules. *NIM A 538*, (384-407), 2005.

[7] H. Sandaker. Extra Gauge Bosons - Search for Z' at ATLAS (poster). *Physics at LHC, Vienna*, 2004.

[8] From the CERN photolibrary.

[9] ATLAS Detector and Physics Performance, Technical Design Report (part I and part II). Technical report, ATLAS TDR 14/15, CERN/LHCC/99-14/-15,, 1999.

[10] J. Iliopoulos. Beyond the Standard Model. *European School of High-Energy Physics, Pylos*, 2002.

[11] S. Eidelman et al. (Particle Data Group Collaboration). Review of Particle Physics. *Phys. Lett. B592*, Issue 1-4, 2004.

[12] S. Pokorski. *Gauge Field Theories*. Cambridge University Press, (1987) 2000.

[13] C. Quigg. The Electroweak Theory. *TASI lectures on Electroweak Theory, hp/0204104,*, 2002.

[14] The LEP Collaborations ALEPH, DELPHI, L3, Opal, the LEP Electroweak Working Group, the SLD Electroweak and Heavy Flavour Groups. A Combination of Preliminary Electroweak Measurements and Constraints on the Standard Model. *CERN-PH-EP/2004-069, hep-ex/0412015*, 2004.

[15] http://lepewwg.web.cern.ch/LEPEWWG/plots/winter2005/.

[16] Joseph D. Lykken. Introduction to Supersymmetry, in Fields, Strings, and Duality. *TASI 96*.

[17] M. Green, J. Schwarz and E. Witten. *Superstring Theory*. Cambridge Univ. Press, 1988.

[18] P. Langacker. Status and Phenomenology of the Standard Model. *Czechoslovak Journal of PhysicS*, Vol. 55, Suppl. A,, 2005.

[19] S. Weinberg. *Phys. Rev. D13*, (974), 1976.

[20] R. Cashmore, L. Maiani, J-P. Revol et al. Prestigious Discoveries at CERN. *Eur.Phys. J. C. Vol. 34/1*, 2004.

[21] W.R. Leo. *Techniques for Nuclear and Particle Physics Experiments*. Springer-Verlag, 1994.

[22] S. Stapnes. Instrumentation for High Energy Physics. *European School of High-Energy Physics, Pylos*, 2002.

[23] C. Grupen. *Particle Detectors*. Cambridge University Press, 1996.

[24] C. Joram. Particle Detectors. *CERN summer student lectures (Talks)*, 2002.

[25] B. G. Streetman, S. Banerjee. *Solid State Electronic Devices*. Prentice Hall International, 2000.

[26] H. Mathieu. *Physique des semiconducteurs et des composants e'lectroniques*. Masson, 1996.

[27] From the ATLAS Outreach Group.

[28] Incandela. Hadron collider detectors. *NIM A 453*, pages 17–24, 2000.

[29] LHC Design Report, Vol. 1 The LHC Main Ring. Technical report, 2004.

[30] F. Gianotti. Collider Physics LHC. *Lectures given at the European School of High-Energy Physics, Casta Papiernicka*, 1999.

[31] ATLAS Trigger Performance Status Report. Technical report, CERN/LHCC/98-15, 1998.

[32] ATLAS Technical Proposal for a General-Purpose pp Experiment at the Large Hadron Collider at CERN. Technical report, CERN/LHCC/94-43, 1994.

[33] The case for mini black holes. *CERN courier*, Vol. 44(Nb. 9), 2004.

[34] V. A. Mitsou. QCD studies with ATLAS at the LHC. *hep-ph/0411147*, 2004.

[35] T. Lani. TOT calibration and spatial resoultion, Testbeam results on Pixel spatial resolution. *http://troncon.home.cern.ch/troncon/resolution.html*, 2001.

[36] Inner Detector Technical Design Report. Technical report, ATLAS TDR 5, CERN/LHCC/97-17, 1997.

[37] http://atlas.web.cern.ch/Atlas/GROUPS/INNER_DETECTOR/PIXELS-/pixel.html.

[38] S. Beranov et al. Estimation of Radiation Background, Impact on Detectors, Activation and Shielding Optimization in ATLAS, Atlas Radiation Background Task Force Summary Document. *ATL-GEN-2005-001*, 2005.

[39] From the ATLAS magnet group web-pages. http://atlas-magnet.web.cern.ch/atlas-magnet/.

[40] Calorimeter Performance TDR, CERN. Technical report, CERN/LHCC/96-40, 1996.

[41] ATLAS Muon Spectrometer, Technical Design Report. Technical report, CERN/LHCC 97-22, 1997.

[42] R. Hauser. The ATLAS Trigger System. *APJdirect A1*, pages 1–11, 2003.

[43] ATLAS High-Level Trigger Data Acquisition and Controls, Technical Design Report. *ATLAS TDR 016, CERN/LHCC/2003-022*, 2003.

[44] The SCT Community. SCT Barrel Module FDR documents, SCT-BM-FDR-1 to 9. 2001.

[45] The SCT Community. SCT Endcap FDR documents, ATL-IS-ES-0041, -0017, -0016, -0034, -0021, -0051.

[46] A. Chilingarov D. Campbell and T. Sloan. Frequency and temperature dependence of the depletion voltage from CV measurements for irradiated Si detectors. *NIMA 492*, (402-410), 2002.

[47] Technical Specifications, Supply of Silicon Microstrip Detectors for the ATLAS SemiConductor Tracker (SCT). *from EDMS*, 1999.

[48] J. A. J. Matthews et al. Bulk Radiation Damage in Silicon Detectors and Implications for ATLAS SCT. *ATLAS Internal Note, INDET-95-118*, 1995.

[49] The ATLAS semiconductor tracker collaboration. Design and Performance of the ABCD3TA ASIC for Readout of Silicon Strip Detectors in the ATLAS Semiconductor Tracker. *in preparation.*

[50] Project Specification, Project Name: ABCD3T ASIC, Version V1.2. *ATLAS Technical Note*, 2000.

[51] N. Spencer. ATLAS SCT/Pixel Grounding and Shielding Note. *ATL-IC-EN-0004*, 1999.

[52] M. Morrissey and T. Weidberg. Grounding and Shielding for the Barrel SCT. *ATL-IS-ES-0056*, 2005.

[53] A. Robson and P. W. Phillips. The Temperature Dependence of the Electrical Performance of ABCD2T readout chips in Prototype ATLAS SCT Barrel Modules. 2000.

[54] http://hepunx.rl.ac.uk/atlasuk/sct/engineer/modules.html.

[55] The ATLAS semiconductor tracker collaboration. ATLAS SCT barrel modules. in preparation.

[56] Y, Unno. ATLAS silicon microstrip Semiconductor Tracker (SCT). *NIMA 453*, pages 109–120, 2000.

[57] T. Kondo et al. Construction and performance of the ATLAS silicon microstrip barrel module. *NIM A 485*, pages 27–42, 2002.

[58] A. Kugel. Design of the ATLAS Trigger/DAQ Readout-Buffer input (ROBIN) device. *ATL-DAQ-CONF-2005-009, ATLAS Internal Note*, 2005.

[59] H.C. van der Bij et al. A Prototype of the ATLAS Read-out Link. *Fourth Workshop on Electronics for LHC Experiments, Rome*, 1998.

[60] ATLAS High-Level Trigger Data Acquisition and Controls. Technical report, CERN/LHCC/2003-022, 2003.

[61] R. Spiwoks et al. VMEbus Application Program Interface. *ATLAS Internal Note, ATL-D-ES-0004*, 2005.

[62] J. Butterworth et al. TTC Interface Module for ATLAS Read-Out Electronics: Final production version based on Xilinx FPGA devices. *LECC*, 2004.

[63] From the SctRodDaq group (taken from talk by P. Phillips).

[64] B. J. Gallop. Thesis at the University of Birmingham. in preparation.

[65] L. Eklund, D. Ferrère, B. Gallop, P.W. Phillips. Electrical tests of SCT hybrids and modules. *ATLAS internal note ATL-COM-INDET-2003-004*, 2003.

[66] A. Barr. Calibration the ATLAS Semiconductor Tracker Front End Electronics. *IEEE conference Rome*, 2004, in print.

[67] From the KEK web-pages. http://atlas.kek.jp/sub/photos/Silicon/module-nobg.jpg.

[68] T. Huse. PhD Thesis at the University of Oslo. 2005, in preparation.

[69] J. Butterworth et al. Timing, trigger and control interface module for ATLAS SCT read out electronics, http://www.hep.ucl.ac.uk/atlas/sct/cloac/Welcome.html.

[70] M. Goodrick and M. Morrissey. The SLOG slow command generator, http://hepwww.rl.ac.uk/atlas-sct/mm/slog/slog.ps.

[71] M. Morrissey. MuSTARD, the multi-channel semiconductor tracker ABC(D) readout device, http://hepwww.rl.ac.uk/atlas-sct/mm/mustard/MUSTARD.PS.

[72] J. Bohm et al. SCT LV3, http://www-hep2.fzu.cz/Atlas/WorkingGroups-/Projects/MSGC.html.

[73] Proposal for Barrel Module Categories, http://atlas.web.cern.ch/Atlas-/GROUPS/INNER_DETECTOR/ SCT/module/SCTSGmod/mod03/030304 /SQ/ModuleCategories030303.pdf.

[74] B. Hallgreen et al. The Embedded Local Monitoring Board (ELMB) in the LHC Front-End I/O Control System. *7th Workshop on Electronics for LHC Experiments, Stockholm*, 2001.

[75] J. R. Cook, G. Thomas. ELMB128 Documentation. 2004.

[76] B. Hallgren and H.J. Burckhart. Frontend I/O via Canbus of the ATLAS Detector Control System. *Fourth Workshop on Electronics for LHC Experiments, Rome, Italy*, 1998.

[77] J. Bohm et al. Crate Controller Specifications. *ATLAS technical note, ATL-IS-ES-0083 to ATL-IS-ES-0089*, 2003.

[78] J. Stastny. SCT Low Voltage Power Supply, Requirements and Specifications. *ATLAS Internal Note, ATL-IS-ES-00.*

[79] E. Górnicki, S. Koperny. SCT High Voltage Power Supply, Requirements and Specifications. *ATLAS Internal Note, ATL-IS-ES-0084.*

[80] R. Brenner. SCT interlock specifications. *ATL-IS-ES-0067*, 2003.

[81] E. Górnicki, S. Koperny. Backplane. *ATLAS Internal Note, ATL-IS-ES-0088.*

[82] Technical specification for the manufacture and supply of low-mass tapes for the ATLAS SCT detector. *ATL-IS-CS-0014.*

[83] M. Olcese et al. Inner detector thermal management and environmental gas. *ATL-IC-ES-0006.*

[84] P.Bonneau. ATLAS detector cooling work package - Evaporative cooling system for ATLAS inner detector silicon trackers, external part. *ATC-TL-EP-0001*.

[85] M. Olcese, M. Stodulski, H. Niewodniczanski. Inner Detector Evaporative Cooling System, Requirements and general design issues. *ATLAS Internal Note, ATL-IC-ES-0006*.

[86] S. Kersten and P. Kind. The BBIM crate, Pixel Patch Panel PP3 Design. *ATL-IP-ES-0075*.

[87] S. Kersten and P. Kind. Technical Description of the Interlock Circuit and System of the ATLAS Pixel Detector. *ATL-IP-ES-0041*.

[88] S. Kersten and P. Kind. Requirements for Interlock Circuit and System of the ATLAS Pixel Detector. *ATL-IP-ES-0040*, 2004.

[89] www.jtag.com.

[90] A. Daneels and W. Salter. Selection and Evaluation of Commercial SCADA System for the Controls of the CERN LHC Experiments. *ICALEPCS, Trieste*, 1999.

[91] http://www.pvss.com.

[92] V. Filimonov. OPC CANopen server User guide. 2004.

[93] http://itcowww.cern.ch/jcop.

[94] H.J. Burckhart et al. The Supervisor of the ATLAS Detector Control System. *Proceedings of ICALEPCS2003, Gyeongju, Korea*, 2003.

[95] R. Hart, V. Khomoutnikov. ATLAS DAQ - DCS Communication Software, High Level Design and performance of the ABCD chip for the binary readout of silicon strip detectors in the ATLAS Semiconductor Tracker. *ATLAS note number 165*, 2001.

[96] CAN in Automation (CiA). http://www.can-cia.de.

[97] http://www.kvaser.com.

[98] H. Boterenbrood. CANopen, high-level protocol for CAN-bus, Version 3.0. *NIKHEF, Amsterdam*, 2000.

[99] The SCT DCS group. SCT Detector Control System. *ATLAS internal note*, 2005, ready for submission.

[100] LHL Computing Grid Project (LCG). http://lcg.web.cern.ch/LCG.

[101] F. Varela Rodriguez. Systems of ELMB buses using the Kvaser PCI CAN card. *ATLAS internal working Node DCS-IWN17*, 2002.

[102] F. Varela Rodriguez, J. Cook, V. Filimonov, B. Hallgren. ELMB Full Branch Test:Behaviour and Performance. *ATLAS Internal Working Node DCS-IWN13*, 2001.

[103] http://atlas.web.cern.ch/Atlas/GROUPS/GENERAL/TESTBEAM/2004/.

[104] F. Campabadal et al. Beam tests for ATLAS SCT silicon strip detector modules. 2003.

[105] The ATLAS Inner Detector Community, Inner Detector Technical Design Report. Technical report, ATLAS TDR 4, CERN/LHCC97-16, 1997.

[106] S. Gonzales C. Escobar. SCT results in the CTB04. *talk in the SCT week 14th Dec.*, 2004.

[107] H. P. Beck et al. The base-line DataFlow system of the ATLAS Trigger & DAQ. *ATL-DAQ-2004-006*, 2004.

[108] S. Gonzalez. various talks. *SCT and ID weeks*, 2004-2005.

[109] http://atlas.web.cern.ch/Atlas/GROUPS/DAQTRIG/ROS/ros.htm.

[110] M. Jose Costa. various talks. *SCT and ID weeks*, 2004-2005.

[111] M. Barczyk et al. ATLAS TDAQ/DCS Online software, Online Software Architecture. *ATLAS Internal Note, ATLAS-TDAQ-2002-*, 2002.

[112] G. Moorhead. various talks. *SCT and ID weeks*, 2004-2005.

[113] Technical specification - Supply of a prototype composite cylinder for ATLAS. *Technical documentation*, 1996.

[114] http://www.physics.ox.ac.uk/atlas/detector/Overview.htm.

[115] From the Oxford Barrel Group, http://www-pnp.physics.ox.ac.uk /ṽiehhaus/pictures/.

[116] H. Pernegger. Construction and Integration of the ATLAS SemiConductor-Tracker. *9th Pisa Meeting on Advanced Detectors, Isola d'Elba (talk)*, 2003.

[117] Private communication with S. Roe.

[118] G. Viehhauser, B3 feature document taken just after the assembly tests finished. *http://www-pnp.physics.ox.ac.uk/ viehhaus/*.

[119] F. Ould-Saada. Une excursion a travers la physique des particules. *UIO-PHYS-2000-02*.

[120] J. Hewett and T. Rizzo, Phys. Rep. 183 (1989) 193; A. Leike, Phys. Rep. 317 (1999) 143; M. CvetiÀác and P. Langacker, hep-ph/9707451.

[121] A. Leike. The Phenomenology of Extra Neutral Gauge Bosons. *Phys. Reports 317*, pages 143–250, 1999.

[122] R. S. Chivukula. An Introduction to dynamical electroweak symmetry breaking. *Advanced School on Electroweak Theory, hepph/9701322*, 1998.

[123] N. Arkani-Hamed A. G. Cohen and H. Georgi. *Phys. Lett. B 513*, page 232, 2001.

[124] J. Erler and P. Langacker. Constraings on Extended Neutral Gauge Structures. *hep-ph/9903476 v1*, 1999.

[125] M. Cvetic and S. Godfrey. Discovery and Identification of Extra Gauge Bosons. *hep-ph/9504216*, 1995.

[126] P. Langacker et al. New heavy gauge bosons in pp and ppbar collisions. *Phys. Rev. D13*, page 1470, 1984.

[127] F. del Aguila. The Physics of Z' bosons. *Lectures at the XVII International School of Theoretical Physics "Standard Model and Beyond", Szczyrk, hep-ph/9404323*, 1993.

[128] M. Dittmar, A. Nicollerat, A. Djouadi. Z' studies at the LHC: an update. *ETHZ-IPP PR-2003-01*, 2003.

[129] http://www-cdf.fnal.gov/physics/exotic/exotic.html.

[130] M. Carakoz Unel. Exotic explorations: experiences using CDF dileptons. *talk in the ATLAS exotic meeting (february)*, 2005.

[131] S. Godfrey. Update of Discovery Limits for Extra Neutral Gauge Bosons at Hadron Colliders. *hep-ph/0201093*, 2002.

[132] T. Sjostrand et al. PYTHIA 6.301 Physics and Manual. *hep-ph/0308153*, 2003.

[133] T. Sjostrand et al. PYTHIA 6.154. *Computer Phys. Commun. 135 238, hep-ph/0010017*, 2001.

[134] T. Sjostrand et al. CERN physics lectures. 2005.

[135] E. Richter-Waas, D. Froidevaux and Luc Poggioli. ATLFAST 2.0 a fast simulation package for ATLAS. *ATLAS Internal Note, ATL-PHYS-98-131*, 1998.

[136] http://www.hep.ucl.ac.uk/atlas/atlfast/UserGuide.html.

[137] M. Schafer. Study of $Z' \to e^+e^-$ in full simulation with regard to discrimination between models beyond the Standard Model, ATLAS @ CERN. Master's thesis, 2004.

[138] From private communication with T. Sjostrand.

[139] M. Dittmar. Neutral current interference in the TeV region:The experimental sensitivity at the CERN LHC. *Phys. Rev. D13*, Vol 55, 1997.

[140] I. Golutvin et al. Search for TeV-scale bosons in the dimuon channel with the CMS detector. *Physics a LHC, Czech. J. Phys. 54*, 2004.

[141] F. Gianotti. LHC physics: the first year... (talk). *Physics at LHC, Vienna*, 2004.

A
Parameters

Speed of light in vacuum [c]	= 299 792 458 m s^{-1}
Planck constant [h = 2 π $\hbar$]	= 6.626 0693(11) $\times$ 10^{-34} J s
Electron charge [e]	= 1.602 176 53(14) x 10^{-19} C
Electron mass [m_e]	= 0.510 998 918(44) MeV/c^2
Proton mass [m_p]	= 938.272 029(80) MeV/c^2
Permittivity of free space [$\epsilon_0 = 1/\mu_0 c^2$]	= 8.854 187 187 $\times$ 10^{-12} F m^{-1}
Permeability of free space [μ_0]	= 12.566 370 614 $\times$ 10^{-7} N A^{-2}
Fine structure constant [$\alpha = e^2/4\pi\epsilon_0\hbar c$]	= 1/137.035 999 11(46) ($Q^2 = 0$)
Classical electron radius [$r_e = e^2/4\pi\epsilon_0 m_e c^2$]	= 2.817 940 325(28) $\times$ 10^{-15} m
Avogadro constant [N_A]	= 6.022 1415(10) $\times$ 10^{23} mol^{-1}
Boltzman constant [k]	= 1.380 6505(24) $\times$ 10^{-23} J K^{-1}
Fermi coupling constant [$G_F/(\hbar c)^3$]	= 1.16637(1) $\times$ 10^{-5} GeV^{-2}
$W^{\pm}$ mass [m_W]	= 80.425(38) GeV/c^2
Z mass [m_Z]	= 91.1876(21) GeV/c^2
Weak mixing angle [$\sin^2\hat{\theta}(m_z)$ ($\overline{MS}$)]	= 0.23120(15)
Effective weak mixing angle [$\sin^2\theta$]	= 0.23149(15)
Strong coupoling contstant [$\alpha_s(m_z)$]	= 01187(20)
Z full width [Γ_Z]	= 2.4952 $\pm$ 0.0023 GeV
Z lepton width [$\Gamma_Z(l^+l^-)$]	= 83.984 $\pm$ 0.086 MeV
Z coupling to leptons [g_V^l]	= -0.03783 $\pm$ 0.00041
Z coupling to leptons [g_A^l]	= -0.50123 $\pm$ 0.00026
Z coupling to μ_e [g^{μ_e}]	= 0.502 $\pm$ 0.009
Asymmetry e [A_e]	= 0.1515 $\pm$ 0.00019
Asymmetry μ [A_μ]	= 0.142 $\pm$ 0.015
Lepton asymmetry at Z pole [A_{FB}^{0l}]	= 1.71 $\pm$ 0.10

A.1 Bethe-Block Parameters

z	charge of incident particle in units of the elementary charge
Z, A	atomic number and atomic weight of the absorbing material
m_e	electron mass
r_e	classical electron radius ($r_e = \frac{1}{4\pi\epsilon_0}\frac{e^2}{m_e c^2}$) with ϵ_0 the permittivity of free space
N_A	Avogadro constant
I	ionisation constant, characterisctic of the absorber material.
δ	density correction $\delta = 2\ln\gamma + \zeta$
ρ	density of absorbing material
β	v/c of the incident particle
γ	$1/\sqrt{1-\beta^2}$
C	shell correction
W_{max}	maximum energy transfer in a single collision

Table A.2: The Bethe-Block parameters.

A.2 Silicon Sensor Characteristics

Parameter	Value
Intrinsic density	1.45×10^{10} cm^{-3}
No. of intrinsic charge carriers	4.5×10^8
Band gap, E_g	1.12 V
E (e^--hole pair)	3.6 eV
Specific density	2.33 g/cm^3
Mobility - μ_e	1450 cm^2/Vs
Mobility - μ_h	450 cm^2/Vs
Charge collection	< 10 ns
e-h pairs in 300 μm thickness (average)	3.2×10^4

Table A.3: Typical silicon semiconductor parameters [24].

B
SCT Characteristics

B.1 SCT Composition

Barrels	Radius (mm)	Number of Modules
B3	300	384
B4	373	480
B5	447	576
B6	520	672
Total		2112

Disks	z (mm)	Number of Modules
2 × D1	± 835	264
2 × D2	± 925	184
2 × D3	± 1072	264
2 × D4	± 1260	264
2 × D5	± 1460	264
2 × D6	± 1695	264
2 × D7	± 2135	184
2 × D8	± 2528	184
2 × D9	± 2778	104
Total		1976

SCT total	4088

Table B.1: SCT barrel and disks with their radius or z-distance and their number of modules [56].

B.2 SCT Module Parameters

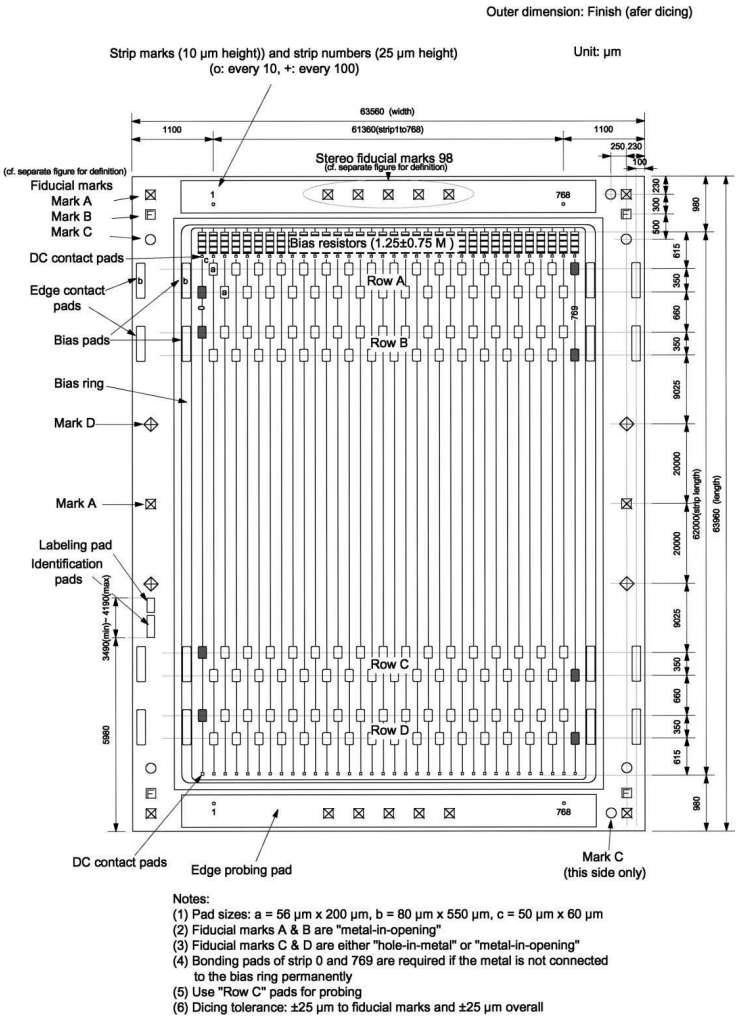

Figure B.1: A schematic drawing of the SCT sensor.

Paramters	Design value	Tolerance
Dowel hole, mhx (μm)	-6500	30
Dowel hole, mhy (μm)	-37.000	30
Dowel slot, msx (μm)	38.500	100
Dowel slot, msy (μm)	-37.000	30
Mid-point of front pair, midxf (μm)	0	10
Mid-point of front pair, midyf (μm)	0	5
Separation of front pair, sepf (μm)	64.090	10
Separation of back pair, sepb (μm)	64.090	10
Sensor1 angle, a1 (mrad)	0	0.13
Sensor2 angle, a2 (mrad)	0	0.13
Sensor3 angle, a3 (mrad)	0	0.13
Sensor4 angle, a4 (mrad)	0	0.13
Half-stereo angle, half-stereo (mrad)	-20	0.13

Table B.2: Module in-plane geometry parameters [57].

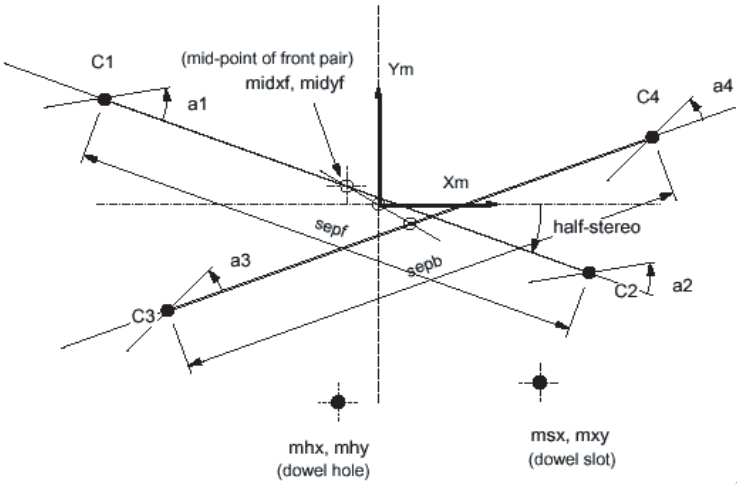

Figure B.2: Drawing of the module in-plane geometry parameters [55].

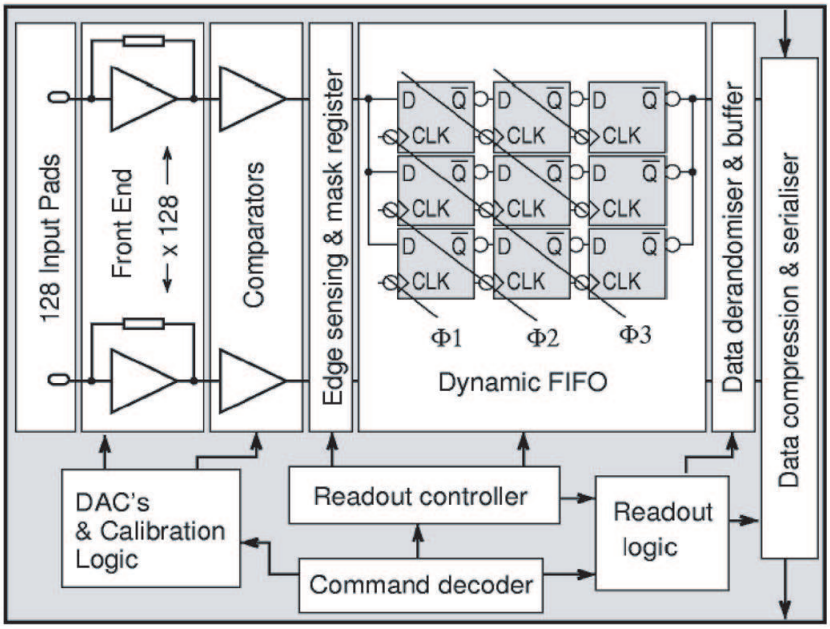

Figure B.3: A simplified schematic block diagram of the ABCD3TA chip [55].

B.3 DCS Variables

Channel Parameters	DCS name	Range	Limits	Read/Write
HV Channel status	HVchStat	8 bit	-	R
Bias voltage	HVchVolt	0-500V	dev.	R/W
Bias current	HVchCurr	10nA - 10mA	5.8 mA (1ms)	R
Ramping speed	HVchRamp	0-3	-	W
Current limit	HVchITrp	5-50V/s	-	W
Card Parameters	DCS name	Range	Limits	Read/Write
HV Card status	HVcaStat	8 bit	-	R
Mask	HVcaMask	0 - 255	-	W

Table B.3: Parameters for control and monitoring of the module high voltage supply. Dev. stands for under development. The HV high limit depends on the new changes to the circuitry to account for problems described in chapter 6.

Channel Parameters	DCS name	Nominal/Range	Limits	Read/Write
LV Channel status	LVchStat	8 bits	-	R
Analogue voltage hybrid	LVch_Vcc	3.323-3.675 V	10 V at PS	R/W
Analogue voltage at PS	LVps_Vcc	-	10 V	R
Analogue voltage return	LVretVcc	-	-	R
Analogue current	LVch_Icc	900 mA	1300 mA	R
Analogue current limit	LVch_ITrp	2-510 ms	510 ms	W
Digital voltage hybrid	LVch_Vdd	4.0 V	10 V at PS	R/W
Digital voltage at PS	LVps_Vdd	-	10 V	R
Digital voltage return	LVretVdd	-	-	R
Digital current	LVch_Idd	572 mA	1300 mA	R
Digital current limit	LVch_DTrp	2-510 ms	510 ms	W
VCSEL voltage	LVchVCSV	1.6-6.6 V	9.6V	R/W
VCSEL current	LVchVCSI	4.0 mA	10.0 mA	R
PINV voltage	LVchPINV	5.0-10.0 V	13.0V	R/W
PINV current	LVchPINI	0.5 mA	2.5 mA	R
Temperature link0	MOch_Tm0	-29-70°C	80 uA/8 V	R
Temperature link1	MOch_Tm1	-29-70°C	80 uA/8 V	R
Temperature warning	LVchTLim	-	-	W
Temperaure trip limit	LVchTTrp	-	-	W
Clock Select line	LVchCLKS	H:Vdd/L:-0.7 V	1.4 mA	W
Hard Reset	LVchCLKR	H:Vdd/L:-0.7 V	-0.42 mA	W

Output on	LVchVOut	0 or 1	-	W
Card Parameters	DCS name	Range	Limits	Read/Write
LV Card status	LVcaStat	8 bit	-	R
Card temperature	LVcaTemp	20/10-40°C	40	R
Card Power	LVcaPowr	-	-	R
Mask	LVcaMask	0-15	-	W
Over current	LVcaTrip	-	-	W

Table B.4: Parameters for control and monitoring of the module low voltage supply.

I-V Parameters	DCS name	Range	Limits	Read/Write
Voltage for first scan point	IVchStrt	0-500 V	500 V	W
Voltage for last scan point	IVchStrt	0-500 V	500 V	W
Step between scan points	IVchStrt	0-500 V	$\sim$ 100 V max	W
Set the voltage to this level after test	IVchStrt	0-500 V	500 V	W
Software current trip (μA)	IVchStrt	1-10 μA	10 μA	W
Software current warning (μA)	IVchStrt	-	-	W
Time interval (seconds)	IVchStrt	-	$>$ 5s	W
Acknowledgement	IVchStrt	-	-	R

Table B.5: Parameters defining I-V curve used by crate controller.

CC Parameters	DCS name	Range	Limits	Read/Write
Status	CCchStat	-	-	R
Reset	CC_Reset	-	-	W
		-	-	
Read channel parameters	CCchRead	-	-	W
Set channel parameters	CCch_Set	-	-	W
Set configuration	CCcf_Set	-	-	W
Set run state transition	CCcf_RST	-	-	W
Start IV curve measurement	StartIVCurve	-	-	W
Acknowledgement	CCcf_Ack	-	-	R/W

Table B.6: Parameters for control and monitoring of the power supply crate used by the crate controller.

B.4 Barrel Data - Cold

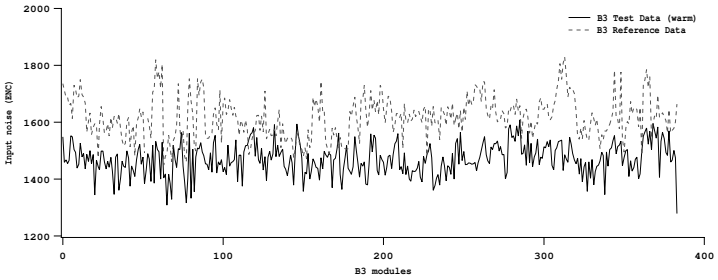

Figure B.4: Distribution of module noise occupancy for B3 COLD data.

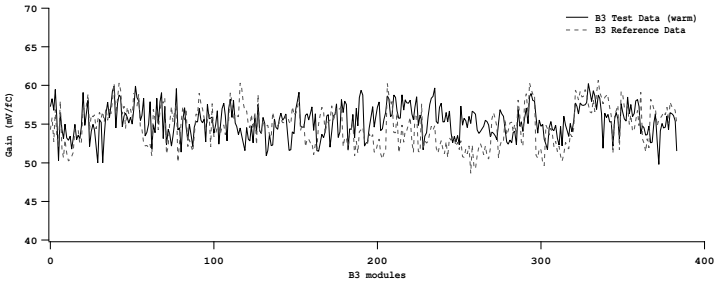

Figure B.5: Distribution of module noise for B3 COLD data.

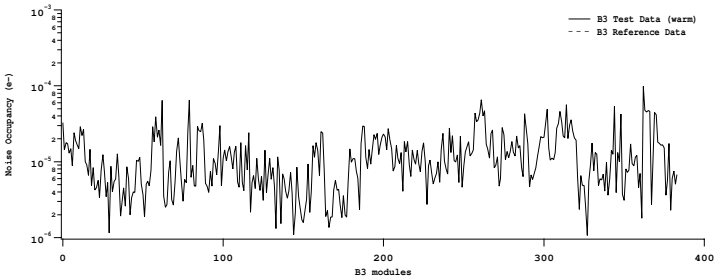

Figure B.6: Distribution of module gain for B3 COLD data.

Figure B.7: Geometric distribution of detector noise for B3 COLD data.The axes show the average distribution along the beam and vertical to the beam.

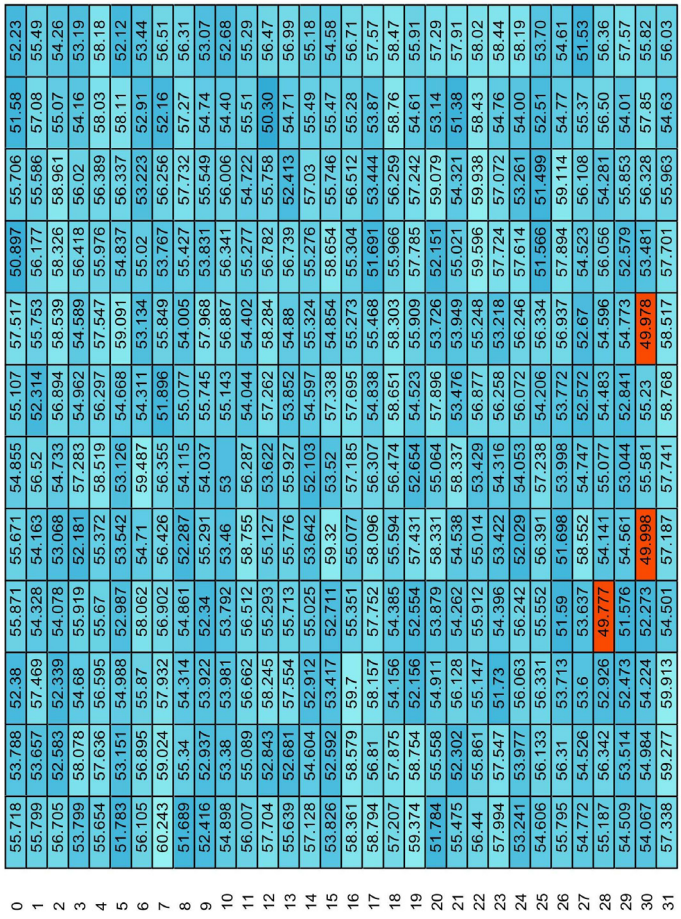

	-6	-5	-4	-3	-2	-1	1	2	3	4	5	6
0	55.718	53.788	52.38	55.871	55.671	54.855	55.107	57.517	50.897	55.706	51.58	52.23
1	55.799	53.657	57.469	54.328	54.163	56.52	52.314	55.753	56.177	55.586	57.08	55.49
2	56.705	52.583	52.339	54.078	53.068	54.733	56.894	58.539	58.326	58.961	55.07	54.26
3	53.799	58.078	54.68	55.919	52.181	57.283	54.962	54.589	56.418	56.02	54.16	53.19
4	55.654	57.636	56.595	55.67	55.372	58.519	56.297	57.547	55.976	56.389	58.03	58.18
5	51.783	53.151	54.988	52.987	53.542	53.126	54.668	59.091	54.837	56.337	58.11	52.12
6	56.105	56.895	55.87	58.062	54.71	59.487	54.311	53.134	55.02	53.223	52.91	53.44
7	60.243	59.024	57.932	56.902	56.426	56.355	51.896	55.849	53.767	56.256	52.16	56.51
8	51.689	55.34	54.314	54.861	52.287	54.115	55.077	54.005	55.427	57.732	57.27	56.31
9	52.416	52.937	53.922	52.34	55.291	54.037	55.745	57.968	53.831	55.549	54.74	53.07
10	54.898	53.38	53.981	53.792	53.46	53	55.143	56.887	56.341	56.006	54.40	52.68
11	56.007	55.089	56.662	56.512	58.755	56.287	54.044	54.402	55.277	54.722	55.51	55.29
12	57.704	52.843	58.245	55.293	55.127	53.622	57.262	58.284	56.782	55.758	50.30	56.47
13	55.639	52.681	57.554	55.713	55.776	55.927	53.852	54.88	56.739	52.413	54.71	56.99
14	57.128	54.604	52.912	55.025	53.642	52.103	54.597	55.324	55.276	57.03	55.49	55.18
15	53.826	52.592	53.417	52.711	59.32	53.52	57.338	54.854	58.654	55.746	55.47	54.58
16	58.361	58.579	59.7	55.351	55.077	57.185	57.695	55.273	55.304	56.512	55.28	56.71
17	58.794	56.81	58.157	57.752	58.096	56.307	54.838	55.468	51.691	53.444	53.87	57.57
18	57.207	57.875	54.156	54.385	55.594	56.474	58.651	58.303	55.966	56.259	58.76	58.47
19	59.374	58.754	52.156	52.554	57.431	52.654	54.523	55.909	57.785	57.242	54.61	55.91
20	51.784	55.558	54.911	53.879	58.331	55.064	57.896	53.726	52.151	59.079	53.14	57.29
21	55.475	52.302	56.128	54.262	54.538	58.337	53.476	53.949	55.021	54.321	51.38	57.91
22	56.44	55.861	55.147	55.912	55.014	53.429	56.877	55.248	59.596	59.938	58.43	58.02
23	57.994	57.547	51.73	54.396	53.422	54.316	56.258	53.218	57.724	57.072	54.76	58.44
24	53.241	53.977	56.063	56.242	52.029	54.053	56.072	56.246	57.614	53.261	54.00	58.19
25	54.606	56.133	56.331	55.552	56.391	57.238	54.206	56.334	51.566	51.499	52.51	53.70
26	55.795	56.31	53.713	51.59	51.698	53.998	53.772	56.937	57.894	59.114	54.77	54.61
27	54.772	54.526	53.6	53.637	58.552	54.747	52.572	52.67	54.523	56.108	55.37	51.53
28	55.187	56.342	52.926	49.777	54.141	55.077	54.483	54.596	56.056	54.281	56.50	56.36
29	54.509	53.514	52.473	51.576	54.561	53.044	52.841	54.773	52.579	55.853	54.01	57.57
30	54.067	54.984	54.224	52.273	49.998	55.581	55.23	49.978	53.481	56.328	57.85	55.82
31	57.338	59.277	59.913	54.501	57.187	57.741	58.768	58.517	57.701	55.963	54.63	56.03

Figure B.8: Geometric distribution of detector gain for B3 COLD data.

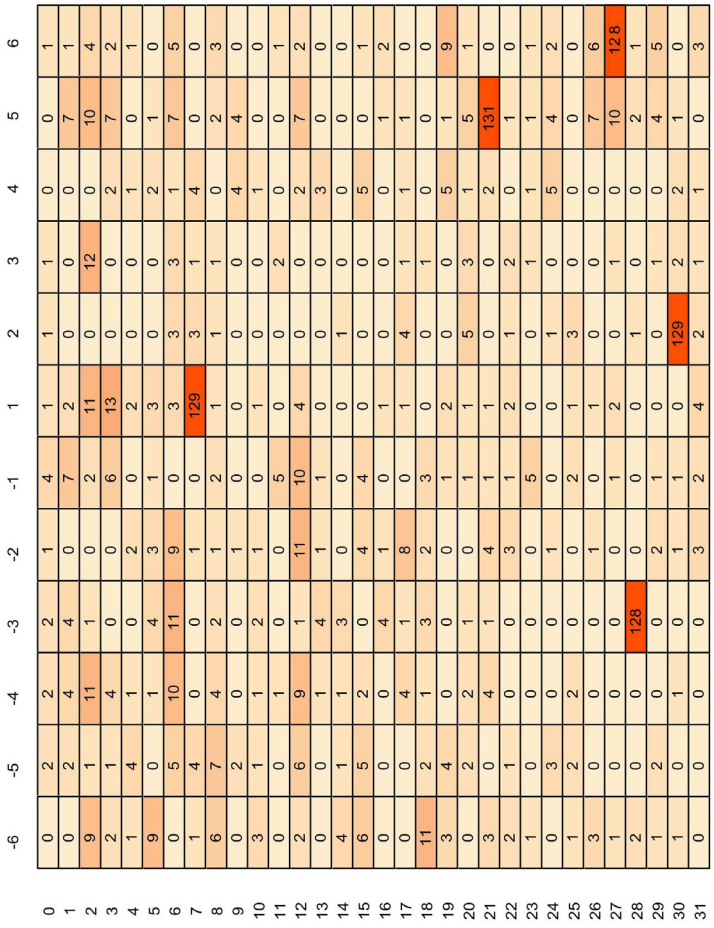

Figure B.9: Distribution of detector defects for 3Pt gain for B3 COLD data

Figure B.10: Distribution of noise occupancy (ENC) for B3 COLD data.

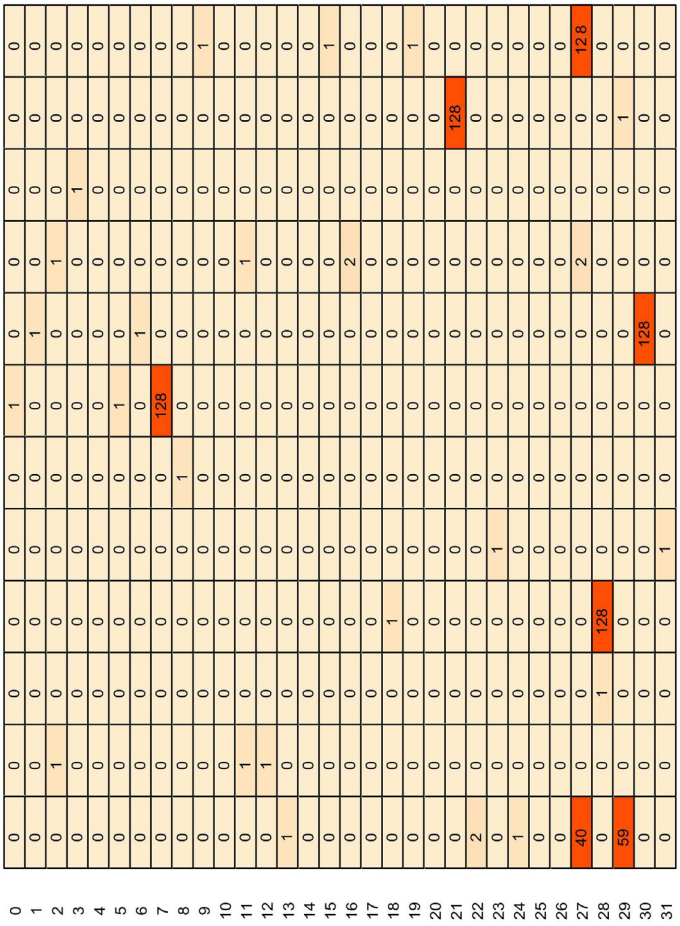

Figure B.11: Distribution of detector defects for noise occupancy for B3 COLD data.

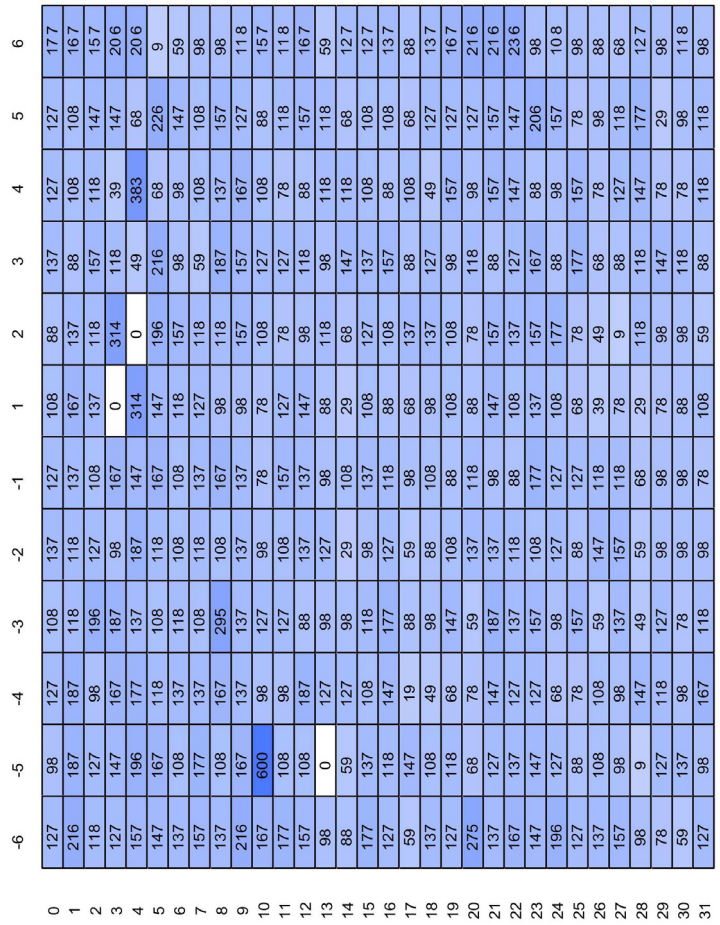

Figure B.12: Distribution of bias current of the modules for B3 COLD data. Values in red are those exceeding 1 uA. Zero values are faulty readings.

	-6	-5	-4	-3	-2	-1							
0	11.04	12.06	12.06	11.67	11.33	11.5	11.54	12.64	10.26	12.32	11.24	9.9	
1	11.67	12.15	12.82	12.19	11.67	13.14	11.84	12.55	13	12.24	12.32	12.24	
2	11.58	10.54	12.32	11.41	10.42	11.04	11.46	11.2	11.71	10.95	11.04	12.96	
3	12.06	11.5	11.46	13.19	10.38	13.89	11.24	11.63	11.5	12.96	11.84	10.62	
4	12.15	12.91	12.55	12.19	12.55	13.42	12.24	11.93	12.77	12.37	13.19	14.53	
5	12.59	12.77	13.47	11.67	13.33	11.84	13.05	12.96	13.09	10.46	11.29	13.33	
6	11.54	12.24	10.42	11.41	10.91	10.91	13.14	12.1	13.42	13.28	13.33	12.77	
7	11.12	11.8	13.56	11.71	12.02	11.58	11.12	11.84	11.8	14.09	12.5	11.5	
8	15.38	13.94	13.05	12.68	13.75	13.14	12.28	12.64	12.91	12.68	13.19	11.46	
9	12.64	12.24	12.68	12.37	14.04	13.89	13.51	13.75	14.77	11.71	13.05	12.06	
10	13.47	12.96	12.91	12.91	11.89	12.1	12.68	11.33	13.28	11.24	9.55	11.54	
11	12.59	12.96	12.59	13.05	13.84	14.57	10.14	11.97	11.93	12.96	12.28	12.41	
12	12.77	13.23	13.05	13.99	13.99	13.14	11.12	12.64	12.96	13.84	12.37	11.97	
13	11.93	11.67	12.06	12.73	13.05	11.97	12.15	11.8	8.72	11.37	8.98	9.24	
14	10.5	12.24	11.41	11.8	10.79	11.58	11.37	11.08	11.04	9.24	11.46	11.2	
15	11.12	10.54	11.33	10.83	10.91	11.08	12.19	11.71	11.71	12.06	11.04	10.22	
16	12.06	11.46	11.33	12.96	11.04	10.83	11.71	9.05	11.97	12.37	10.79	12.1	
17	10.66	10.87	10.14	11.89	5.92	10.22	11.33	13.09	12.41	11.37	11.8	10.34	
18	10.71	10.75	10.22	10.14	10.46	9.78	10.62	11.08	9.75	10.87	10.18	10.75	
19	10.5	10.62	10.1	10.95	11.67	10.22	10.79	10.26	9.67	9.4	11.2	10.1	
20	11.04	11.8	12.06	10.75	11.33	10.75	11.54	11.71	11.37	11.97	12.86	11.76	
21	11.97	12.32	12.06	11.54	12.59	11.33	11.33	11.8	11.5	11.8	12.19	11.29	
22	12.5	11.08	10.34	11.41	11.67	11.29	11.2	11.71	11.29	11.41	11.16	11.41	
23	10.91	10.75	12.28	11.33	11.8	10.95	10.71	10.34	11.63	11.8	10.83	10.95	
24	9.32	9.9	9.71	8.98	10.14	12.19	8.61	9.17	9.13	8.83	8.94	8.5	
25	9.4	7.71	8.24	8.21	7.88	7.99	8.39	9.28	9.94	8.83	9.75	9.09	
26	8.75	8.94	7.85	8.75	8.1	7.32	8.1	8.24	7.39	7.95	7.85	10.38	
27	8.83	7.78	8.42	7.92	9.21	8.53	7.67	7.88	7.67	8.06	7.92	7.64	
28	10.75	10.3	11.04	10.95	10.87	11.37	10.71	11.16	11.54	12.19	11.37	12.06	
29	11.12	11.08	11.33	11.97	11.46	10.99	10.71	10.58	10.71	11.46	10.1	11.04	
30	12.06	11.04	10.42	11.46	10.79	10.38	10.79	10.58	9.9	10.62	10.18	10.54	
31	10.5	9.71	10.87	9.63	10.46	10.54	11.71	10.58	10.22	11.46	10.95	9.82	

Figure B.13: Distribution of temperatures (T0) of the modules for B3 COLD data.

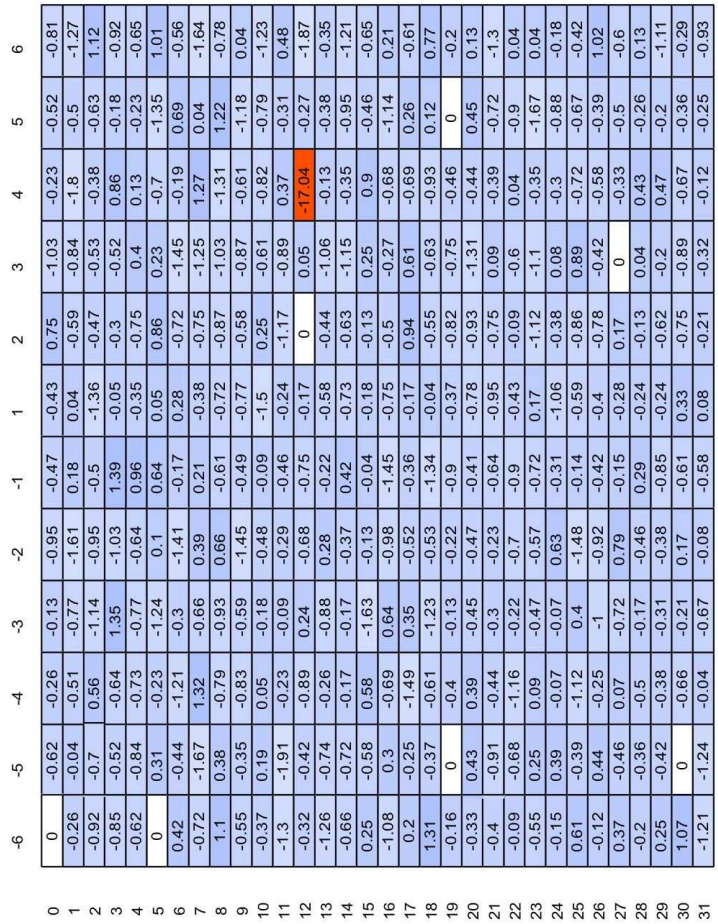

Figure B.14: Distribution of temperature differences of the modules for B3 COLD data. Zero values are when the temperature readings for both sensors are the same within 0.1°C.

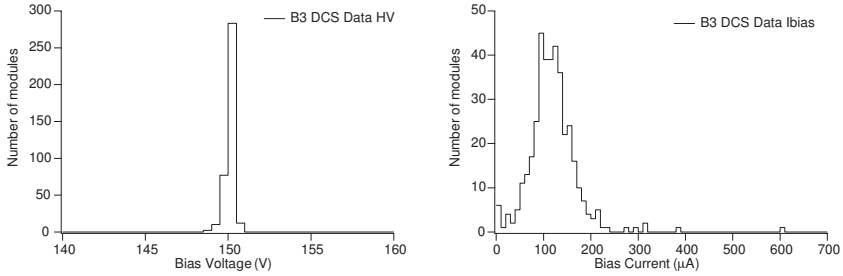

Figure B.15: Distribution of detector bias voltage (left) and current (right).

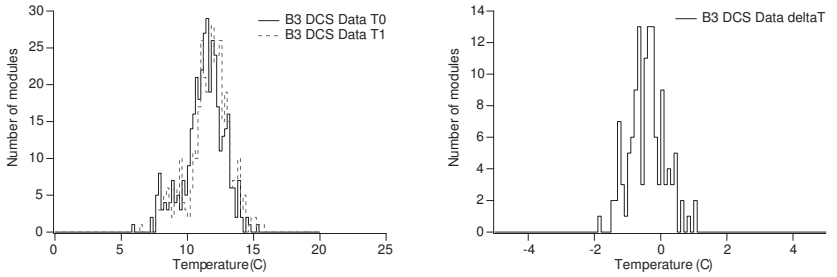

Figure B.16: Distribution of detector temperature. Left, the temperatures on the two links and right the difference between the temperatures of the two links.

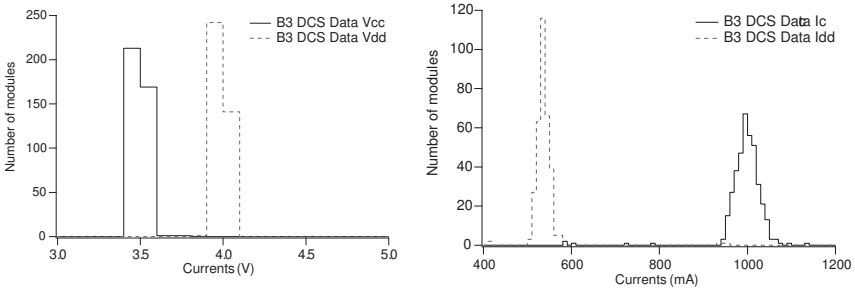

Figure B.17: Distribution of supply voltages (left) and currents (right).

C
Picture Gallery

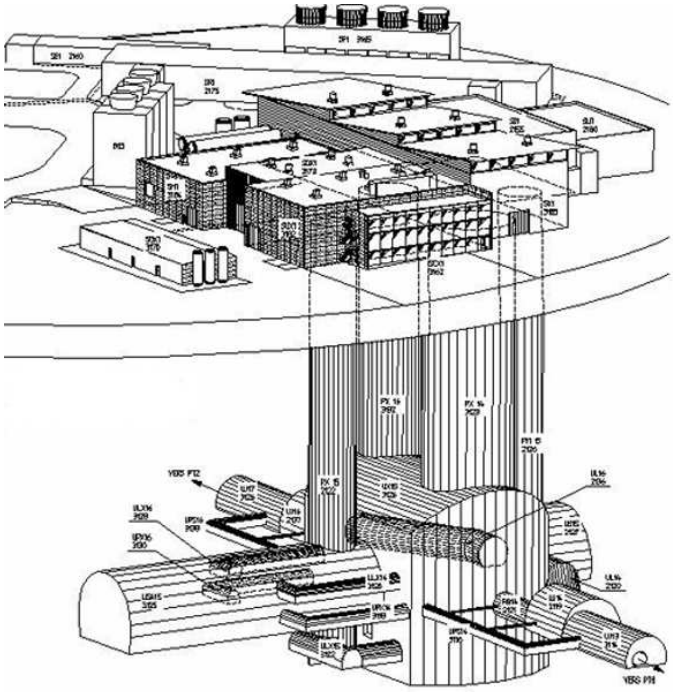

Figure C.1: Drawing of the ATLAS surface building and the pit area, including the main cavern and support chambers.

Figure C.2: The ATLAS cavern as in September 2004. The first detector parts, the TileCal has been lowered and are being completed. In the front, rails can be seen for the horisontal movement of detector parts.

Figure C.3: Tile Calorimeter being lowered into the ATLAS Cavern. The TileCal will be completed in the Cavern into a cylinder.

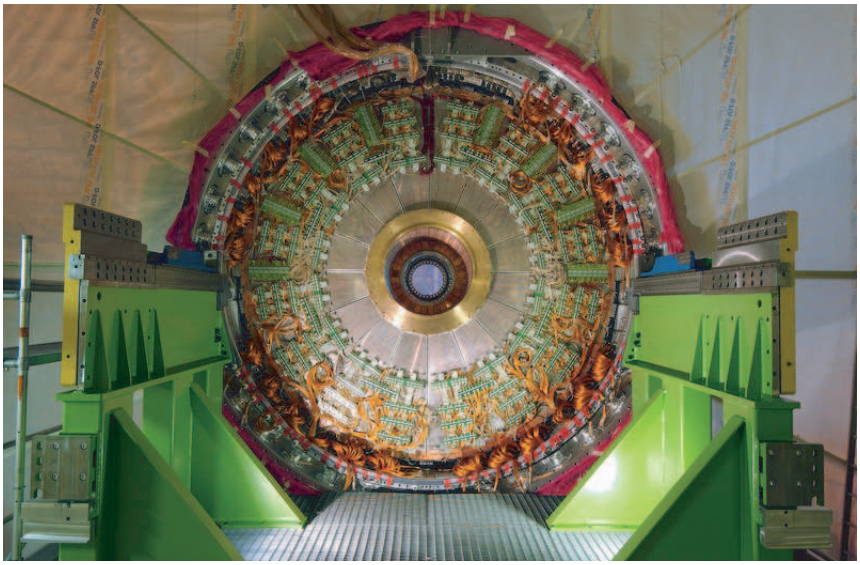

Figure C.4: LAr Hadronic Calorimeter, End-Cap, finished and waiting for instllation in the Cavern.

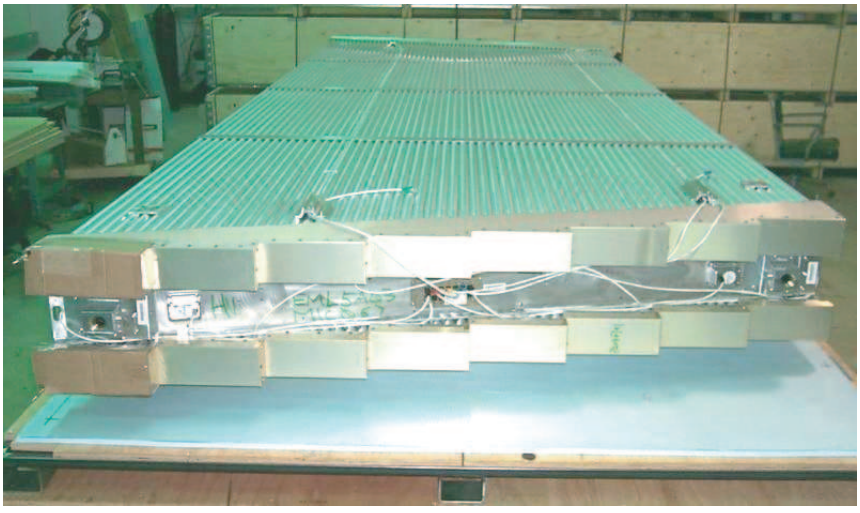

Figure C.5: A Muon Chamber ready for installation.

Figure C.6: The TRT detector, Barrel section, with two rings of modules installed and tested.

List of Figures

List of Tables

Nomenclature

ABCD3TA ATLAS Binary Chip produced in DMILL technology, version 3 with Trim DACs, revised version

ACK Acknowledgement

ADC Analogue Digital Converter

ALEPH Apparatus for LEP PHysics

ALICE A Large Ion Collider Experiment

AlN Aluminium Nitride

API Application Programming Interface

AS Address Strobe

ATLAS A Toroidal LHC ApparatuS

B3 Barrel 3

BA Board Address

BBIM Building Block Interlock Monitoring

BeO Beryllium Oxide

BOC Back Of Crate card

Brookhaven Brookhaven National Laboratory

BT Barrel Toroid

CAN Controller Area Network

CC Crate Controller

CDF The Collider Detector at Fermilab

CERN The European Centre of Nuclear Research

CIC Common Infrastructure Control

CKM Cabbibo-Kobayashi-Maskawa

CLOAK CLOck And Control

CMS Compact Muon Solenoid detector

CS Cooling System

CSC Cathode Strip Chambers

CTF Command Transfer Facility

DAQ Data Acquisition system

DCS Detector Control System

DELPHI DEtector with Lepton, Photon and Hadron Identification

DORIC4 Digital Optical Receiver Integrated Circuit

DS Data Strobe

ECAL Electromagnetic CALorimeter

ECT End-Cap Toroid

EF Event Filter

ELMB Embedded Local Monitor Box

ENV ENVironmental system

EPR Error Reporting Service

FB Forward-Backward

Fermilab Fermi National Accelerator Laboratory

FET Field-Effect Transistor

FSI Frequency Scanning Interferometry

FSM Finite State Machine

FSR Final State Radiation

GCS Global Control Station

GIM Glashow-Iliopoulos-Maiani mechanism

GPIB General Purpose Interface Bus

GUI Graphical User Interface

GUT Grand Unified Theories

H Hadronisation

HLT High-Level Trigger system

HP Hard Process

HV High Voltage

I/O Input / Output

IBOX Interlock BOX

ID Inner Detector

IMatrix Interlock Matrix

IRQ Interrupt ReQuest

IRS Initial State Radiation

IS Information Service

IS Interlock System

IV Current-Voltage

JCOP The Joint COntrols Project

LAr Liquid Argon Calorimeter

LCS Local Control Station

LEIR Low Energy Ion Ring, previously the Low Energy Antiproton Ring

LEP Large Electron and Positron collider

LHC Large Hadron Collider

LHCb The Large Hadron Collider beauty experiment

LINAC2 Linear Accelerator 2

LMT Low Mass Tapes

LV Low Voltage

LVL1 Low level 1 trigger

LVL2 Low Level 2 trigger

MDT Monitored Drift Tubes

MI Multi-interaction

MTR Message Transfer Facility

MUSTARD MUltichannel Semiconductor Tracker ABC(D) Readout Device

MWPC Multi-Wire Proportional Chamber

NTC Negative Temperature Coefficient

PMT Photo Multiplier Tubes

PPB1 Patch Panel Barrel 1

PPS Power Pack System

PRTD Platinum Resistance Temperature Detectors

PS Proton Synchrotron

PSS Power Supply System

PVSS ProzessVisualisierungs- und Steuerungs-System

QCD Quantum Chromodynamics

QED Quantum Electrodynamics

QM Quantum Mechanics

R/W Read/Write

RCC Rod Crate Controlle

ROB Read Out Buffers

ROD Read Out Drivers

ROS Read Out System

RPC Resistive Plate Chambers

SCADA Supervisory Control and Data Acquisition

SCS Sub-detector Control Station

SCT SemiConductor Tracker

SCT SemiConductor Tracker

SCTLV3 SCT Low Voltage 3

SIC System Interlock Card

SLAC Stanford Linear Accelerator Center

SLC SLAC Linear Accelerator

SLOG SLow Command Generator

SM Standard Model

SPEAR Stanford Positron Electron Accelerating Ring

SPS Super Proton Synchrotron

SR1 Surface building 1

TDR Technical Design Report

TE Thermal Enclosre

TGC Thin Gap Chambers

TileCal Tile Calorimeter

TIM Timing Interface Module

TPC Time Projection Chamber

TPG Thermo Pyrolytic Graphite

TRD Transition Radiation Detector

TRT Transition Radiation Tracker

TTL Transistor-Transistor Logic

VCSL Vertical Cavity Surface Emitting Laser

VDC VCSL Driver Chip

WLS WaveLength Shifting fibres

Index